AMPK signaling in dendritic cells: a metabolic sensor controlling the balance between immunity and tolerance

Brombacher, E.C.

AMPK Signaling in Dendritic Cells

A metabolic sensor controlling the balance between immunity and tolerance

Eline C. Brombacher

AMPK Signaling in Dendritic Cells

A metabolic sensor controlling the balance between immunity and tolerance

Eline C. Brombacher

ISBN:	978-94-93289-42-0
Cover design:	Designed by Eline Brombacher, colored by Sare Jansma (5 years old)
Layout:	Eline Brombacher and TOSAM
Printing:	PrintSupport4U

The work described in this thesis was performed at the department of Parasitology at the Leiden University Medical Center, Leiden, The Netherlands. The work was supported by the LUMC (grant awarded to dr. B. Everts).

Printing of this thesis was financially supported by Bio X Cell and ChipSoft, which is gratefully acknowledged.

AMPK Signaling in Dendritic Cells

A metabolic sensor controlling the balance between immunity and tolerance

Proefschrift

ter verkrijging van
de graad van doctor aan de Universiteit Leiden,
op gezag van rector magnificus prof.dr.ir. H. Bijl,
volgens besluit van het college voor promoties
te verdedigen op donderdag 7 maart 2024
klokke 13.45 uur

door

Eline Constance Brombacher
geboren te Monnickendam
in 1993

Promotor:	Prof. dr. M. Yazdanbakhsh
Co-promotors:	Dr. B. Everts Dr. B.G.A. Guigas
Leden promotiecommissie:	Prof. dr. J.G. Borst Dr. ir. R. Stienstra (Wageningen University) Prof. dr. B. Viollet (Université Paris Cité) Prof. dr. C.R. Berkers (Utrecht University)

Table of contents

Part 1

Introduction


AMPK

1

General introduction

Introduction

All living organisms need energy for survival, development, and growth. Nutrients are a major energy source and therefore sufficient nutrient availability is indispensable for life. The capacity to adapt intracellular processes to extracellular nutrient levels is crucial to ensure optimal growth and survival. Even prokaryotes have receptors and enzymes that respond to fluctuating extra- and intracellular nutrient levels. The engulfment of oxidative bacteria and the capacity to store nutrients in subcellular compartments required more complex metabolic regulation in eukaryotes (1). One of the pathways involved in metabolic control that is absent in prokaryotes, but conserved among all eukaryotes is the AMP-activated protein kinase (AMPK) signaling axis (2). AMPK is activated upon a variety of metabolic stimuli and acts through phosphorylation of key metabolic enzymes and regulators of cellular growth, thereby adapting intracellular metabolism and processes to energy levels and nutrient availability. AMPK consists of a catalytic α-subunit, and regulatory β- and γ-subunits. This heterotrimeric structure is conserved among eukaryotes, but upstream and downstream regulators can differ. For example, canonical AMPK activation in mammals is facilitated by binding of adenine nucleotides AMP and ADP to the γ-subunit, while only ADP can activate *S. cerevisiae* AMPK homolog Snfl (sucrose nonfermenting). However, similar to mammalian AMPK, Snfl also promotes a switch to oxidative metabolism (3,4). Plant homolog SnRK1 (SNF1-related kinase) is not activated by adenine nucleotides, but inhibition by sugar-phosphates (e.g. glucose-6-phosphate) plays a major role in regulating its activity. Interestingly, SnRK1 is also activated in the dark, which could be considered an energy-deprived condition for plants (5). This indicates that the AMPK signaling pathway evolved to tailor the needs of an organism, also evidenced by a role for AMPK in the hypothalamus of animals, where it controls whole-body homeostasis by promoting food intake and body weight (6). Despite the regulatory differences between species, the main purpose of AMPK signaling is conserved from unicellular eukaryotes to more evolved species: maintaining energy homeostasis during metabolic stress.

Canonical AMPK activation, mediated by adenine nucleotide binding, involves three mechanism: allosteric activation, promotion of phosphorylation of Thr183 (α1-subunit) or Thr172 (α2-subunit) by liver kinase B1 (LKB1) (7), and inhibition of Thr183/Thr172 dephosphorylation (4,8). AMPK can additionally be phosphorylated by other kinases, including Ca2+/calmodulin-dependent kinase kinase β (CaMKKβ) upon $Ca2^{+}$ accumulation (9) and transforming growth factor-β-activated kinase 1 (TAK1) upon lysosomal damage (10) (Fig. 1). Non-canonical modulation of AMPK activity mediated by fluctuating nutrient levels. High glucose levels (11) and potentially glycogen levels can inhibit AMPK (8), while long-chain fatty acid (LCFA)-CoA esters (the activated, soluble form of LCFAs) (12) and microbiota derived short-chain fatty acids (SCFA) (13) can function as AMPK activator.
Over a 100 AMPK target proteins have been reported, that impact a wide variety of metabolic pathways and cellular functions. Promoting glucose uptake, induction of fatty acid oxidation, and boosting mitochondrial biogenesis are among the best-studied downstream effects of AMPK signaling, as well as autophagy and inhibition of protein synthesis (Fig. 1) (8,14). Altogether, these processes aim to maintain sufficient cellular energy levels during metabolic stress.

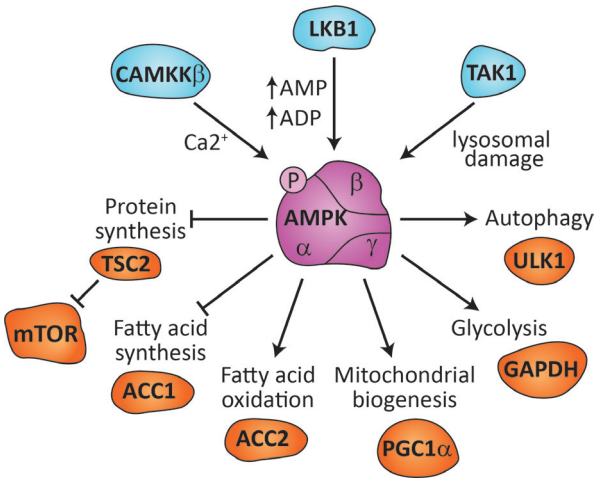

Figure 1: AMPK signaling pathway. $Ca2^+$/calmodulin-dependent kinase kinase β (CaMKKβ), Liver kinase B1 (LKB1), and transforming growth factor-β-activated kinase 1 (TAK1) activate AMPK in response to rising $Ca2^+$ levels, increases in ADP or AMP levels, and upon lysosomal damage respectively. Key targets of AMPK include Tuberous Sclerosis 2 (TSC2), Acetyl-CoA Carboxylase (ACC) 1 and ACC2, PPARγ Coactivator 1 Alpha (PGC1α), glyceraldehyde 3-phosphate dehydrogenase (GAPDH) and Unc-51 like autophagy activating kinase (ULK1).

During the past decade it has become clear that cellular metabolism directly affects the function of immune cells, including that of dendritic cells (DCs) (15,16). DCs are antigen presenting cells that upon activation can promote inflammatory as well as anti-inflammatory immune responses by governing the priming and polarization of T cell responses (17). A number of DC subsets, including conventional DCs, plasmacytoid DCs, monocyte-derived DCs, and skin-resident Langerhans cells are recognized, that differ in their tissue distribution, function, and ontogeny (18). These DC subset-defining characteristics, as well their activation status, are associated with distinct metabolic profiles (15,16). Generally speaking, induction of pro-inflammatory T cell responses are associated with anabolic metabolism in DCs, including upregulating glycolysis and fatty acid synthesis (19,20), while DCs conditioned to prime T cells towards a regulatory phenotype (21,22), as well as DCs in the immunosuppressive tumor-micro environment (23), display a catabolism-centered metabolism, characterized by increased glycolysis, oxidative phosphorylation, and fatty acid oxidation (FAO) (Fig. 2).
Several studies point towards a key role for AMPK signaling in DC-driven immune responses. For instance, AMPK activation in DCs dampens LPS-mediated activation (19) and loss of AMPK in DCs has been shown to promote LPS-induced activation (24). Furthermore, AMPK signaling in $CD11c^+$ myeloid cells contributes to Th2-driven control of hookworm infection (25). Yet, although the metabolic phenotype observed in tolerogenic DCs is similar to AMPK-induced metabolic changes (14), it remains unknown whether AMPK signaling in DCs shapes their ability to orchestration of regulatory immune responses and what the underlying (metabolic) mechanisms are through which AMPK shapes DC-driven T cell responses.
Within the framework of this thesis, we aim to address the hypothesis that DC-intrinsic AMPK signaling governs the balance between inflammatory and tolerogenic immune responses by controlling cellular metabolism. In addition, we question whether AMPK in DCs serves a

key nutrient sensing role that functionally connects metabolic conditions of the local micro-environment to changes in T cell priming properties of DCs (Fig. 2). Our goal is to contribute to provide a better understanding of how this metabolic sensor in DCs controls the balance between immunity and tolerance and how ultimately targeting AMPK in DCs may contribute to improved treatment of inflammatory and metabolic diseases.

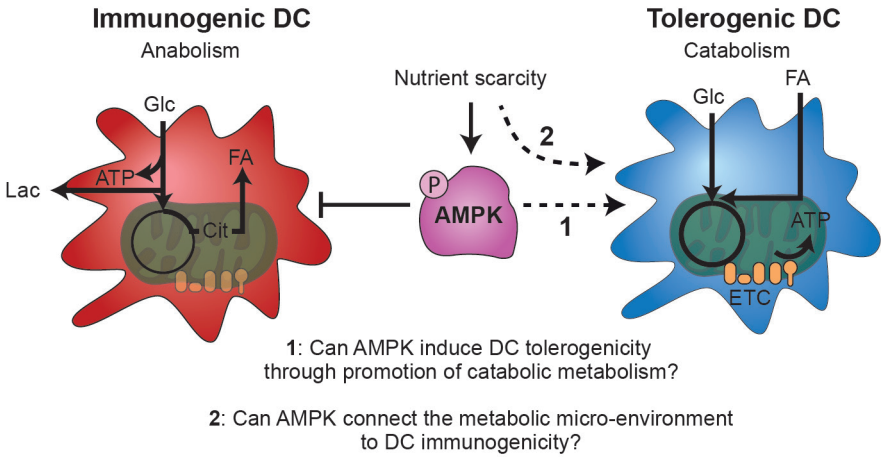

Figure 2: AMPK signaling in dendritic cells: research questions. Metabolic pathways associated with immunogenic and tolerogenic DCs, and research questions addressed in this thesis, regarding the role of AMPK in driving DC metabolism and immunity.

Thesis outline

Chapter 2 and chapter 3 constitute a theoretical and practical introduction to this thesis. In **chapter 2** a background is provided on DC subsets, function, and metabolism, and the current knowledge about the effects of the metabolic micro-environment on DC biology is described. In **chapter 3** a protocol to study intracellular metabolism in DCs using flow cytometry is given. The described methods are used in all research chapters of this thesis and are essential tools to perform research in the field of immunometabolism.
In **chapter 4** the role of the AMPK signaling axis in an inflammatory context is addressed. Obesity causes chronic low-grade inflammation in metabolic organs (26) and here we showed an important role for the LKB1-AMPK/SIK signaling axis in hepatic DCs, in controlling metabolic homeostasis during obesity.

The next section focusses on the role of AMPK in DCs as regulator of tolerance. In **chapter 5** we described how drug-induced AMPK activation induces metabolic changes that lead to RALDH^{high} tolerogenic DCs. In **chapter 6** we examined the tumor micro-environment as physiological activator of AMPK and showed that AMPK activation in tumor-associated DCs compromises the control of tumor growth. In **chapter 7** we described how the effects of

tolerogenic compound retinoic-acid depends on AMPK signaling and how AMPK activity in DCs *in vivo* induces regulatory T cell responses.
In **chapter 8** the main findings of this thesis are summarized, novel insights are discussed in a broader perspective, and future research suggestions are provided to expand our knowledge on the role of AMPK signaling in dendritic cells.

References

1. Chantranupong L, Wolfson RL, Sabatini DM. Nutrient-sensing mechanisms across evolution. Vol. 161, Cell. 2015. p. 67–83.
2. Craig PM, Moyes CD, LeMoine CMR. Sensing and responding to energetic stress: Evolution of the AMPK network. Comp Biochem Physiol B Biochem Mol Biol. 2018;224:156–69.
3. Hedbacker K, Carlson M. SNF1/AMPK pathways in yeast. Vol. 13, Frontiers in Bioscience. 2008.
4. Hardie DG, Schaffer BE, Brunet A. AMPK: An Energy-Sensing Pathway with Multiple Inputs and Outputs. Vol. 26, Trends in Cell Biology. 2016. p. 190–201.
5. Broeckx T, Hulsmans S, Rolland F. The plant energy sensor: evolutionary conservation and divergence of SnRK1 structure, regulation, and function. Vol. 67, Journal of Experimental Botany. 2016. p. 6215–52.
6. López M, Nogueiras R, Tena-Sempere M, Diéguez C. Hypothalamic AMPK: A canonical regulator of whole-body energy balance. Vol. 12, Nature Reviews Endocrinology. 2016. p. 421–32.
7. Woods A, Johnstone SR, Dickerson K, Leiper FC, Fryer LGD, Neumann D, et al. LKB1 Is the Upstream Kinase in the AMP-Activated Protein Kinase Cascade. Current Biology. 2003;13(22):2004–8.
8. Steinberg GR, Hardie DG. New insights into activation and function of the AMPK. Nature Reviews Molecular Cell Biology. 2022.
9. Hawley SA, Pan DA, Mustard KJ, Ross L, Bain J, Edelman AM, et al. Calmodulin-dependent protein kinase kinase-β is an alternative upstream kinase for AMP-activated protein kinase. Cell Metab. 2005;2(1):9–19.
10. Jia J, Bissa B, Brecht L, Allers L, Choi SW, Gu Y, et al. AMPK, a Regulator of Metabolism and Autophagy, Is Activated by Lysosomal Damage via a Novel Galectin-Directed Ubiquitin Signal Transduction System. Mol Cell. 2020;77(5):951-969.e9.
11. Zhang CS, Hawley SA, Zong Y, Li M, Wang Z, Gray A, et al. Fructose-1,6-bisphosphate and aldolase mediate glucose sensing by AMPK. Nature. 2017;548(7665):112–6.
12. Pinkosky SL, Scott JW, Desjardins EM, Smith BK, Day EA, Ford RJ, et al. Long-chain fatty acyl-CoA esters regulate metabolism via allosteric control of AMPK β1 isoforms. Nat Metab. 2020;2(9):873–81.
13. Donohoe DR, Garge N, Zhang X, Sun W, O'Connell TM, Bunger MK, et al. The microbiome and butyrate regulate energy metabolism and autophagy in the mammalian colon. Cell Metab. 2011;13(5):517–26.
14. Hardie DG, Ross FA, Hawley SA. AMPK: A nutrient and energy sensor that maintains energy homeostasis. Vol. 13, Nature Reviews Molecular Cell Biology. 2012. p. 251–62.
15. Møller SH, Wang L, Ho PC. Metabolic programming in dendritic cells tailors immune responses and homeostasis. Vol. 19, Cellular and Molecular Immunology. 2022. p. 370–83.
16. Wculek SK, Khouili SC, Priego E, Heras-Murillo I, Sancho D. Metabolic Control of Dendritic Cell Functions: Digesting Information. Vol. 10, Frontiers in immunology. 2019. p. 775.
17. Kapsenberg ML. Dendritic-cell control of pathogen-driven T-cell polarization. Vol. 3, Nature Reviews Immunology. 2003. p. 984–93.
18. Guilliams M, Ginhoux F, Jakubzick C, Naik SH, Onai N, Schraml BU, et al. Dendritic cells, monocytes and macrophages: A unified nomenclature based on ontogeny. Vol. 14, Nature Reviews Immunology. 2014. p. 571–8.
19. Krawczyk CM, Holowka T, Sun J, Blagih J, Amiel E, DeBerardinis RJ, et al. Toll-like receptor-induced changes in glycolytic metabolism regulate dendritic cell activation. Blood. 2010;115(23):4742–9.

20. Everts B, Amiel E, Huang SCC, Smith AM, Chang CH, Lam WY, et al. TLR-driven early glycolytic reprogramming via the kinases TBK1-IKKε supports the anabolic demands of dendritic cell activation. Nat Immunol. 2014;15(4):323–32.

21. Malinarich F, Duan K, Hamid RA, Bijin A, Lin WX, Poidinger M, et al. High Mitochondrial Respiration and Glycolytic Capacity Represent a Metabolic Phenotype of Human Tolerogenic Dendritic Cells. The Journal of Immunology. 2015;194(11):5174–86.

22. Ferreira GB, Kleijwegt FS, Waelkens E, Lage K, Nikolic T, Hansen DA, et al. Differential protein pathways in 1,25-dihydroxyvitamin D 3 and dexamethasone modulated tolerogenic human dendritic cells. J Proteome Res. 2012;11(2):941–71.

23. Zhao F, Xiao C, Evans KS, Theivanthiran T, DeVito N, Holtzhausen A, et al. Paracrine Wnt5a-β-Catenin Signaling Triggers a Metabolic Program that Drives Dendritic Cell Tolerization. Immunity. 2018;48(1):147-160.e7.

24. Carroll KC, Viollet B, Suttles J. AMPKα1 deficiency amplifies proinflammatory myeloid APC activity and CD40 signaling. J Leukoc Biol. 2013;94(6):1113–21.

25. Nieves W, Hung LY, Oniskey TK, Boon L, Foretz M, Viollet B, et al. Myeloid-Restricted AMPKα1 Promotes Host Immunity and Protects against IL-12/23p40–Dependent Lung Injury during Hookworm Infection. The Journal of Immunology. 2016;196(11):4632–40.

26. Gregor MF, Hotamisligil GS. Inflammatory mechanisms in obesity. Annu Rev Immunol. 2011;29:415–45.


AMPK

2

Shaping of Dendritic Cell Function by the Metabolic Micro-Environment

Eline C. Brombacher[1], B. Everts[1]

[1]Department of Parasitology, Leiden University Medical Center, Leiden, The Netherlands

Frontiers in Endocrinology
DOI: 10.3389/fendo.2020.00555

Abstract

Nutrients are required for growth and survival of all cells, but are also crucially involved in cell fate determination of many cell types, including immune cells. There is a growing appreciation that the metabolic micro-environment also plays a major role in shaping the functional properties of dendritic cells (DCs). Under pathological conditions nutrient availability can range from a very restricted supply such as seen in a tumor micro-environment, to an overabundance of nutrients found in for example obese adipose tissue. In this review we will discuss what is currently known about the metabolic requirements for DC differentiation and immunogenicity and compare that to how function and fate of DCs under pathological conditions can be affected by alterations in environmental levels of carbohydrates, lipids and amino acids as well as by other metabolic cues, including availability of oxygen, redox homeostasis and lactate levels. Many of these insights have been generated using *in vitro* model systems, which have revealed highly diverse effects of different metabolic cues on DC function. However, they also stress the importance of shifting towards more physiologically relevant experimental settings to be able to fully delineate the role of the metabolic surroundings in its full complexity in shaping the functional properties of DCs in health and disease.

1 Introduction

DCs are crucial for the regulation of immunity and tolerance during infections as well as during immune homeostasis in steady state, by governing the activation and maintenance of different $CD4^+$ T helper subsets and $CD8^+$ cytotoxic T cell responses. DCs are a heterogenic population of cells that comprise several lineages, including conventional DCs (cDCs), plasmacytoid DCs (pDCs), Langerhans cells (LCs), and inflammatory monocyte-derived DCs (infDCs) (1). Two main lineages can be identified within the cDCs, IRF8-dependent cDC1 and IRF4-dependent cDC2 (2). These different DC subsets have specialized largely non-redundant functions in priming and regulation of T cell responses (2). For instance, cDC1s and cDC2s are considered to be the most potent activators of T cells, that are particularly well equipped to prime $CD8^+$ and $CD4^+$ T cell responses, respectively. pDCs, on the other hand, play an important role in the viral defense by producing large amounts of type I interferons. infDCs develop from monocytes during inflammation and have been described to have a role in innate inflammatory responses as well as in T cell priming (3). Given the scarcity of DCs *in vivo*, several experimental models have been developed to study DC biology. In this respect monocyte-derived DCs (moDCs), obtained from monocytes cultures supplemented with granulocyte-macrophage colony-stimulating factor (GM-CSF) and IL-4 are a widely used model to study human DC biology and metabolism (4). moDCs have phenotypical and functional similarities as cDCs, but closely resemble infDCs on transcriptional level (5, 6). *In vitro* generated murine DCs are commonly derived from GM-CSF-stimulated bone marrow (BMDCs), which bear resemblance to antigen presenting monocyte-derived murine inflammatory DCs. Flt3L-stimulated bone marrow cultures (Flt3L-DCs) give rise to equivalents of multiple steady state splenic DC subsets, including cDC1s, cDC2s and pDCs (7-9). Regulation of the functional properties of DCs is dictated by their ontogeny, but also strongly influenced by their micro-environment. While the effects of danger signals, cytokines and chemokines are extensively reviewed elsewhere, we will focus on the role of metabolic cues in tuning DC function (10-12).

Over the last decade it has become increasingly clear that immune cell activation, proliferation, fate and function are closely linked to, and dependent on activation of specific metabolic pathways (13). Since these metabolic shifts are largely fueled and dependent on nutrients present in the immune cell niche it is becoming evident that the metabolic micro-environment is a vital factor in shaping the outcome of an immune response (14, 15). This review describes the latest insights into the nutritional requirements for DCs to drive an effective immune response and how altered nutrient availability in diseased states may affect the immunogenic or tolerogenic properties of DCs. In this context we will particularly focus on nutrient-limiting and excessive nutrient conditions as found in cancer and diabetes, respectively. Overall we here aim to provide an overview of how the metabolic micro-environment affects the functional properties of DCs.

2 Metabolic demands of DCs during an immune response

During homeostasis DCs reside in peripheral tissues in a relatively quiescent state. However, upon sensing of changes in this homeostatic state, either due to invading pathogens or tissue-derived inflammatory signals, DCs undergo a well-defined activation program that involves increased capturing and processing of antigens for presentation in major histocompatibility complex I (MHC-I) and MHC-II and the induction of expression of chemokine receptors,

cytokines, and costimulatory molecules. This enables DCs to traffic, via tissue-draining lymphatic vessels, to T cell zones of secondary lymphoid organs to efficiently prime and control effector T cell responses. Here, we discuss how the availability of carbohydrates (glucose), amino acids and lipids influences these functions of DCs during an immune response.

2.1 Glucose

A well described phenomenon in immune cells, including DCs, is the switch from catabolic metabolism, characterized by fatty acid oxidation and mitochondrial respiration (Fig. 1A) to anabolic metabolism, with enhanced glycolytic rates and lowered oxidative phosphorylation following activation (Fig. 1B). BMDCs increase glycolytic rates within minutes after stimulation with LPS (TLR4), Poly(I:C) (TLR3) and CPG (TLR9) and also for moDCs a rapid glycolytic increase has been observed upon LPS stimulation (16-20). Likewise, human myeloid $CD1c^+$ DCs and human pDCs show a similar metabolic reprogramming upon pRNA (TLR7/8) stimulation or viral infection (TLR7), respectively (21, 22). Although this points towards increased glucose utilization to fuel glycolysis as a conserved metabolic response to TLR stimulation by DCs, the function of this metabolic reprogramming and fate of glucose-derived carbons can change over time after activation, as discussed below.

For LPS-induced BMDCs the switch to enhanced glycolysis is essential, given that inhibition of glycolysis using 2-deoxyglucose (2-DG) interferes with activation and their capacity to induce T cell proliferation *in vitro* and *in vivo* (16, 23). Correspondingly, changing glucose concentrations in culture media from 10mM to 0mM diminished the upregulation of co-stimulatory markers CD40 and CD86, and production of p40, subunit of IL-12 and IL-23 in LPS-stimulated murine BMDCs (16). In the presence of glucose, LPS stimulation enhances glycolysis via activation of the PI3K/Akt pathway and promotes loss of mitochondrial respiration via stabilization of Hypoxia-inducible factor 1-alpha (HIF1a) and expression of Inducible nitric oxide synthase (iNOS) in BMDCs (16, 17, 24). iNOS is involved in production of nitric oxide (NO) which in an autocrine manner poisons oxidative phosphorylation (17, 24). These TLR-induced events are largely absent in BMDCs activated by LPS in the absence of glucose, due to impaired mTOR activation, thereby further establishing the crucial role for glucose in supporting TLR-induced DC activation (Fig. 1B). Mechanistically, BMDCs require glucose as a carbon source for fatty acid synthesis (FAS) to support ER and Golgi membrane expansion that is needed to accommodate the increased demands for protein translation during activation (23). To this end, glucose is metabolized in the TCA cycle to citrate, which is used as a carbon substrate for FAS (Fig. 1B). In contrast to this anabolic role that glucose-derived carbon plays during BMDC activation, once activated, glucose is used in glycolysis by BMDCs purely for bioenergetic purposes (e.g synthesis of ATP) to compensate for loss of OXPHOS due to the autocrine effects of NO derived from iNOS that poisons the ETC (17). Apart from direct usage of extracellular glucose, BMDCs and moDCs can also utilize intracellular glycogen stores to fuel glycolysis. These glycogen stores are formed prior to TLR stimulation and essential for activation and subsequent T cell stimulation in both moDCs and BMDCs by directly contributing to FAS (Fig. 1A+B) (19).

Upon TLR-ligation, DCs upregulate CCR7 and are attracted towards lymphatic vessels that secrete CCR7 ligand CCL21 (25). In BMDCs the presence of glucose in the medium and subsequent activation of glycolysis are required for CCR7 oligomerization and cytoskeletal changes that support the mobility of DCs. Correspondingly, glucose depletion reduced migration of splenic DCs towards CCL21 ex vivo and 2-DG administration in an experimental

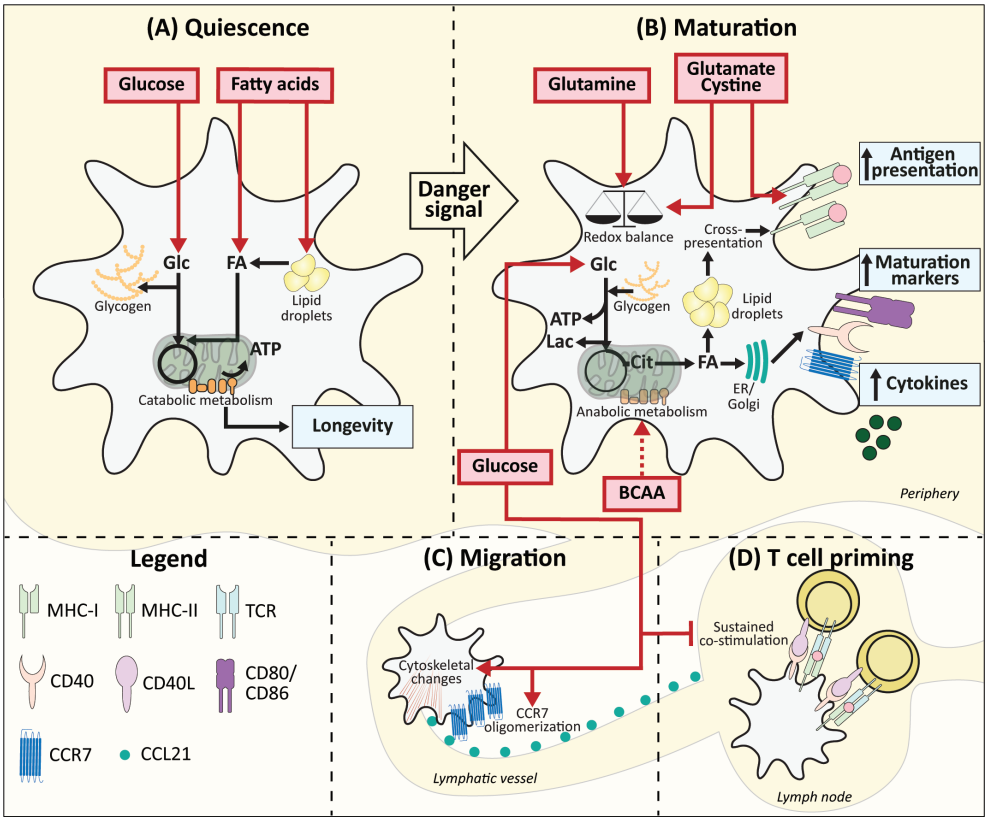

Figure 1: metabolic demands of conventional DCs during homeostasis. (A) Quiescent DCs in peripheral tissues require, glucose and lipids as fuel for mitochondrial ATP generation and to build up intracellular storage of lipids and glycogen. **(B)** After TLR ligation uptake of glucose and BCAAs increases and together with glucose derived from glycogen this supports the switch from catabolic to anabolic metabolism, which is required for DC maturation. During this process, lipid bodies support cross-presentation. Glutamine, cystine and glutavmate promote DC activation via maintaining redox homeostasis and promoting antigen presentation. **(C)** Glucose also promotes migration via stimulating CCR7 oligomerization and inducing cytoskeletal changes. **(D)** In the lymph nodes local glucose availability may be reduced due to glucose consumption by T cells, which may allow for more sustained expression of costimulatory markers and thereby more potent T cell priming. Red boxes: nutrients. Blue boxes: Functional consequences. Dotted arrow: presumed mechanism. ER: Endoplasmatic reticulum. Golgi: Golgi apparatus.

model of allergic asthma, reduced migration of $CD11c^{+}MHCII^{hi}$ DCs to the lung (26). Similarly, BMDCs pulsed ex vivo with OVA plus LPS in the presence of 2-DG, displayed impaired migration towards skin-draining lymph nodes following subcutaneous injection. Altogether this points towards an important role for glucose in DC migration *in vivo* (Fig. 1C) (16).

Interestingly, there are indications that the role of glucose in priming of T cell responses by DCs changes once the cells interact with T cells. It has been shown that the T cell-priming capacity of BMDCs declines after 24h following TLR stimulation, which was associated with a reduction in expression of costimulatory molecules (27). However, this reduction in expression

was prevented when 8h after stimulation glucose was replaced with galactose, a carbohydrate that cannot be efficiently used in glycolysis. These data indicate that after the initial need for glucose, sustained high glycolytic rates repress BMDC activation (Fig. 1D). Hence a local glucose-limiting micro-environment when DCs interact with T cells, may actually support T cell priming and an active immune response (24). Interestingly, both *in vitro* and *in vivo* data suggest that reduction of glucose availability may occur naturally during T cell priming in lymph nodes, due to scavenging of glucose by T cells that are being activated by DCs (24).

Many studies addressing the role of glycolysis, use glucose analog 2-DG to mimic glucose starvation. 2-DG can reduce mitochondrial metabolism independently of reducing glycolysis (28). Moreover, treatment of LPS-activated moDCs with 2-DG has been documented to result in ER-induced upregulation of IL-23 expression, while glucose depletion did not. These data indicate that the effects of 2-DG are not always connected to glycolysis and warrant caution when interpreting data from studies that have used 2-DG to interrogate the role of glycolysis in DC biology (29). In addition, most of the studies described above have been performed in BMDCs, in which iNOS plays a major role in the suppression of mitochondrial respiration in response to TLR stimulation. Most other DC subsets, including moDCs and primary human DCs, do not express iNOS (30). Hence, the role of oxidative phosphorylation during an immune response in human DCs may be underestimated and in physiological settings DCs may rely less on glucose as predicted based on BMDC experiments. Thus far it has not been addressed whether other nutritional carbohydrates shape DC function, but it is worth investigating given that an immunosuppressive role for D-mannose was found in T cells (31). In conclusion, there is clear evidence that many aspects of DC activation are dependent on availability of glucose in the micro-environment. Glucose initiates metabolic reprogramming required for activation and boosts DC migration towards lymph nodes, while during T cell interaction glucose may have an immunosuppressive effect on DCs.

2.2 Amino acids

Amino acids are important for fueling mitochondrial respiration, for protein synthesis, as well as acting as a source of carbon and nitrogen for the synthesis of various other macromolecules. There are clear indications that amino acids in the environment of DCs play an important role in regulating their function. For example, lowering the supraphysiological amino acid concentrations commonly found in standard culture media to ones found in human plasma, increased the efficiency of moDC differentiation. (32, 33). Conversely, moDCs in media containing imbalanced amino acid concentrations, as found in plasma of liver cirrhosis patients, showed impaired expression of maturation markers, secretion of IL-12 and migratory capacity in response to LPS stimulation, compared to moDCs stimulated in control medium (32, 33). The amino acid imbalance interfered with mitochondrial metabolism of immature DCs, causing a reduction in ATP levels and an increase in glucose consumption, which could not be further increased by LPS stimulation. This together supports the idea that several aspects of DC biology, including differentiation, activation and core metabolism, are sensitive to changes in amino acid concentrations in their environment (33).

In addition to the aforementioned work implicating amino acids in general in regulating DC function, there are several studies that have specifically interrogated the role of individual amino acids in this context. LPS stimulation of moDCs has been shown to enhance the uptake of aspartate, cystine, glutamate and branched chain amino acids (BCAAs) valine, leucine and isoleucine (33). Depletion of BCAAs and in particular valine from culture media of

moDCs impairs maturation upon LPS stimulation, characterized by lowered CD83 levels and decreased ability to induce T cell proliferation. Additionally, mTOR signaling was impaired, which raises the possibility that BCAAs may affect DC maturation through modulation of metabolism via the mTOR pathway (Fig. 1B) (34). Of note, as the above mentioned studies were performed in serum-free media with high glucose concentrations (25mM), the relevance of these results under more physiological settings remains to be established. BCAAs are also important for maturation of moDCs stimulated with TLR7/8 ligand protamine-RNA (pRNA). In contrast to LPS stimulation, pRNA ligation boosts fatty acid oxidation (FAO)-dependent mitochondrial respiration and high intracellular levels of BCAAs are required to induce moDC maturation via FAO (20). BCAA leucine may play a key role in supporting FAO, as leucine can promote mitochondrial biogenesis (35). LPS treatment also increases uptake of glutamate and cystine in moDCs and inhibition of the cystine/glutamate antiporter in these cells reduced glutathione synthesis, but did not change the expression of maturation markers. Nevertheless, treating murine splenic DCs with the cystine/glutamate antiporter inhibitor resulted in lowered antigen presentation to both class I and class II MHC-restricted T cells (Fig. 1B) (36). Hence, cystine and glutamate may be crucial metabolites for DC maturation via their role in redox homeostasis and antigen presentation.

As mentioned before, FAS is upregulated in BMDCs following LPS-stimulation. In cancer cells glutamine can contribute to lipogenesis via NADPH production that takes place when glutamine is metabolized to lactate or when glutamine is converted to citrate, facilitated by reductive carboxylation (37, 38). However, depleting glutamine (from 2mM to 0mM) from BMDC culture media did not affect CD40 and CD86 levels and inhibition of glutaminolysis had no effect on the metabolic alterations 6h after LPS stimulation (19, 23). Interestingly, in BMDCs stimulated with TLR7/8 ligand imiquimod, glutamine deprivation or disruption of glutaminolysis enhanced mitochondrial reactive oxygen species (ROS) production and subsequently IL-23 expression. This may suggest that glutamine, by supporting NADPH production, may contribute to scavenging of ROS in BMDCs, rather than to FAS-dependent activation (Fig. 1B) (39). In addition, glutamine may fuel the TCA cycle to support oxidative phosphorylation in DCs as human pDCs increased oxidative phosphorylation following pRNA stimulation and inhibition of glutaminolysis in these cells caused a significant decrease in activation, IFNα secretion and mitochondrial respiration (21). Since activation of human $CD1c^+$ myeloid DCs using pRNA resulted in reduced oxidative phosphorylation and as immunogenicity remained unaffected by inhibition of glutaminolysis, this effect of glutamine may be associated with DC subsets that depend on mitochondrial respiration upon activation, such as pDCs (21).

Apart from glutamine, the importance of availability of different amino acids on DC biology are still poorly defined and are mainly addressed in moDCs. Possibly, due to the low proliferative capacity of differentiated DCs and therefore expected relative little dependency on anabolic metabolism, general amino acid availability may be less of critical factor for DC function than for other more proliferating cells. Nonetheless, as studies exploring the role of glutamine on DC function suggest, specific amino acids may be important in regulation of certain metabolic properties of DCs that are essential for their functional output. Hence, single amino acid depletion studies under more physiological nutrient levels may unravel novel roles of amino acids in DC function.

2.3 Lipids

In contrast to activated DCs, in which glycolysis is often the main bioenergetic pathway, immature quiescent BMDCs and Flt3L-induced cDC1s rely on FAO for energy generation, which would support a longer lifespan for these immature cells (Fig. 1A) (16, 17, 40). Lipids from the local micro-environment may function as important nutrients for FAO in resting DCs. In human Lin-HLA-DR$^+$ and murine CD11c$^+$ hepatic DCs, high lipid content is associated with a stronger immune response (41). These lipids derived from both fatty acid (FA) uptake and synthesis and are stored in lipid bodies. Short term priming with triacyl glycerides of murine DCs containing few lipid bodies did not boost their immunogenic capacities, suggesting that pre-stored lipids rather than direct lipid availability in the micro-environment is important for hepatic DC immunogenicity (41). Mechanistically, lipid bodies in murine BMDCs and splenic CD11c$^+$ DCs have been shown to boost CD8$^+$ T cell priming by supporting cross-presentation, a process by which peptides from exogenous antigens are presented in MHC-I (42). It is therefore tempting to speculate that resting DCs may not only utilize FAs from the extracellular environment to fuel FAO for their bioenergetic homeostasis, but also to store in lipid bodies to help prepare them for potent T cell priming after activation (Fig. 1A).

In contract to conventional DCs, FAO can increase upon TLR7/8/9 stimulation of pDCs (20, 43). Interestingly, FAO in murine bone marrow-derived pDCs is fueled with FAs that are synthesized de novo (43). LPS is also known to increase FAS in BMDCs, possibly suggesting that FAO during an immune response predominantly depends on de novo synthesis and not on the FA availability in the micro-environment (Fig. 1B) (18, 23). Correspondingly, in rats it was found that lipid content between different cell types in the same micro-environment was more similar than lipid content between DCs from distinct lymph nodes. Additionally, *in vivo* LPS stimulation diminished the differences observed between distinct DCs, supporting the notion that lipid accumulation during inflammation is independent of FA availability, while lipid storage during homeostasis does appear to be determined by the micro-environment (Fig. 1A) (44).

In summary, it appears that during homeostasis lipid availability influences the types and amount of lipids stored in DCs and at least in some tissues this is important for their immunogenic potential. During an immune response, both conventional and pDCs accumulate lipids, most likely independent of the FA availability in the local micro-environment, but fueled by FAS. For cDCs the reduced ability of activated DCs to burn FAs by FAO may also contribute to lipid accumulation (16). Cultures in lipid-restricted conditions, 13C-labeled lipid metabolic flux analysis and lipid profiling of DCs during homeostasis and upon activation can further elucidate the role of extracellular lipids on DC function.

2.4 Concluding remarks

The metabolic demands of DCs in non-pathological conditions are dependent on the subset, their location and the maturation stage, as summarized in Fig. 1. Given that most of these data are obtained from *in vitro* studies it is important to realize that *in vitro* nutrient availability is often not limiting and exceed the levels that occur *in vivo*. Furthermore, nutrient competition with cells in the proximity of DCs and metabolites secreted by these surrounding cells are metabolic settings that are hard to mimic *in vitro* and hard to measure *in vivo*, but likely to affect the metabolic micro-environment. Nevertheless, it is evident that nutrient availability is of great importance for the functional output by DCs.

3 Effects of the metabolic environment on DCs in cancer

3.1 Metabolic properties of the tumor micro-environment

Disturbance of nutrient homeostasis is a cause and consequence of many pathologies. A well-studied and complex disease is cancer, which is characterized by a wide range of local metabolic alterations, including nutrient deficiency, hypoxia and oxidative stress. Cancer is a heterogenous disease that arises from cells with traits that allow uncontrolled proliferation. One of these traits, or hallmarks, is avoiding immune detection, required to prevent elimination by the immune system (45). Cells within the tumor micro-environment (TME), including tumor cells, fibroblasts, endothelial cells and immune cells secrete immunomodulatory signals that regulate the anti-tumor immune response (46). Among these factors are cytokines, growth factors and metabolites. During the initial phases of tumor growth, tumor-associated DCs (TADCs) are able to recognize tumor antigens and initiate an anti-tumor T cell response. However, during tumor progression DCs gain tolerogenic rather than pro-inflammatory properties (47-49). A major contributor to immune suppression and another hallmark of cancer is deregulated cellular metabolism (45). The best known metabolic adaptation of cancer cells is the Warburg effect, the conversion of glucose to lactate under aerobic conditions, which allows for rapid production of ATP and biosynthetic precursors (50). In addition, tumors also use amino acids and lipids to fuel the TCA cycle, which promotes ATP generation via oxidative phosphorylation and synthesis of macromolecules to support cell growth and proliferation (51-53). Another cancer-specific metabolic feature is the accumulation of oncometabolites due to mutations in metabolic enzymes. L- or D-2-hydroxyglutarate (L- or D2-HG) is a well-known oncometabolite that promotes tumor growth by regulating DNA and histone modifying enzymes (54). Finally, malignancies are often characterized by unusually high concentrations of extracellular ATP and adenosine, hypoxia and by large quantities of ROS in poorly vascularized regions (52, 55). The above mentioned metabolic changes and stressors do not only affect tumor cells, but also reach stromal cells residing in the TME. Here we will describe how these metabolic cues affect DCs.

3.2 Nutrient starvation

The excessive utilization of carbohydrates, amino acids and lipids by cancer cells results in a limited nutrient supply for cells residing in the TME. Although there are several seminal papers showing how nutrient limitation in the TME impairs $CD8^+$ T cell function, there are few studies that have directly interrogated the contribution of nutrient starvation to the known suppressive effects of the TME on DCs (56, 57). Initially upon entering of DCs into the TME, one could imagine that TADCs may be able to utilize internal stores of glycogen and lipids to support the metabolic demands for their survival and immunogenic activation(19, 41). However, sustained limited access to glucose may impair metabolic rewiring and thereby DC maturation and migration to tumor draining lymph nodes (16, 24, 26). Likewise, based on *in vitro* studies, as discussed in section 2.2, it stands to reason that also insufficient access to amino acids may compromise TADC function by affecting mitochondrial respiration, redox homeostasis and antigen presenting capacity (33, 36, 39). However, to date no studies have directly addressed this. On the other hand, the effects of lipids on the function of TADCs has been studied more extensively and hence will be discussed in a separate section.

Tolerogenic properties of DCs have been linked to increased FAO and mitochondrial respiration (18, 58). These processes are both stimulated by activation of AMPK, an energy-

sensing enzyme that is activated under nutrient limiting conditions (59). AMPK has been shown to be inactivated in DCs upon LPS-induced activation (16). Conversely, in TADCs of mice inoculated with MC38 colon adenocarcinoma cells, activation of LKB1, one of the main activating kinases of AMPK, was elevated (60). Hence, the nutrient-poor TME may boost AMPK signaling in DCs to induce catabolic metabolism that favors tolerogenic properties. Although no study to date has examined it directly, it is likely that limited nutrient access in the TME contributes to immune suppression of DCs (table 1). Addressing the influence of tumors with different bioenergetic profiles on DC activation *in vivo* and *in situ* will provide more insights into the effects of nutrient deprivation on DC-driven immune suppression.

3.3 Lipid accumulation in tumor-associated DCs

Although tumor cells are generally characterized by high lipid uptake, TADCs can also take up large amounts of FAs from the TME (61). Acquisition of lipids by TADCs is facilitated by the upregulation of genes involved in lipid uptake, including lipoprotein lipase (LPL), fatty acid binding protein 4 (FABP4) and macrophage scavenger receptor (Msr1). The lipids are stored in large lipid droplets, which are associated with a reduced capacity to activate T cells (62-64). As discussed earlier, high lipid content in hepatic DCs is associated with higher immunogenicity and LPS stimulation of BMDCs stimulates lipid droplet formation (23, 41). However, in contrast to lipid droplets of these DCs, lipid droplets from TADCs contain high levels of oxidized polyunsaturated FAs. These oxidized FAs cause accumulation of peptide-bound MHC-I complexes in late endosomes and lysosomes via capturing of heat shock protein 70, an important mediator of cross-presentation (65, 66). This limits cross-presentation and thereby priming of cytotoxic T cell responses (table 1). Given the importance of FAO in supporting a tolerogenic phenotype by DCs it is tempting to speculate that perhaps oxidation of these lipids in the mitochondria contributes to DC tolerogenicity within the TME (table 1) (18, 58). What signals trigger the initial increase in lipid uptake by DCs in the TME remains to be determined.

3.4 Hypoxia

Rapid tumor growth results in poorly vascularized regions where oxygen supply is limited. The main metabolic response to hypoxia is stabilization of HIF1a and subsequent activation of glycolysis, which can also occur independently from HIF1a activation during DC activation (16, 17, 67). This may explain why some studies did not find changes in expression of maturation markers or T cell priming capacity when moDCs were stimulated with LPS after differentiation in a 1% O2 hypoxic chamber (table 1) (68, 69). Also differentiation itself of moDCs is mostly unaffected by hypoxic conditions (68-71). Nonetheless there is also some evidence that 1% oxygen can impair LPS-induced moDC maturation and T cell priming potential (table 1) (70, 72). In addition, hypoxia impaired migration of *in vitro* cultured LPS-treated moDCs and human primary myeloid DCs. Mouse $CD34^{+}$-derived myeloid DCs injected in the footpad of mice after they were treated with LPS and deferoxamine (DFX), a drug that mimics hypoxia, showed reduced migration to the draining lymph node compared to untreated cells, indicating that hypoxia reduces migration both *in vitro* and *in vivo* (68, 72). Interestingly, enhanced expression of migratory genes was found in immature moDCs cultured under low oxygen conditions (71). This could indicate that the hypoxic TME has immunosuppressive effects via capturing mature DCs and elimination of immature DCs. Interestingly, immature moDCs cultured under hypoxic conditions had increased expression of genes involved in sensing

chemotactic signals from pro-inflammatory sites and induced secretion of chemotactic factors that attract neutrophils (69, 70, 72). Additionally, murine myeloid DCs treated with DFX increased local leukocyte infiltration *in vivo* (72). Altogether these data obtained from moDCs, may indicate that an oxygen-poor environment triggers DCs to boost innate rather than adaptive immune responses. However, contrary to human moDCs, murine BMDCs cultured in hypoxic conditions enhanced expression of costimulatory molecules, pro-inflammatory cytokine secretion and T cell proliferation upon LPS stimulation (table 1) (73). Additional studies are needed to determine whether these discrepancies are due to inherent differences between human and murine DCs in their response to hypoxia or caused by differences in experimental setup. In addition, the metabolic context in which DCs are exposed to hypoxia may also affect how DCs respond. For instance, under nutrient replete conditions hypoxia may not compromise DC function, such as in lymph nodes in which hypoxic region have been described (74). In contrast, under pathological conditions such as in the TME where hypoxia may be also accompanied by nutrient restriction, hypoxia may have anti-inflammatory effects on DCs. Studies addressing the effects of hypoxia on DC biology particularly *in vivo* during homeostasis as well as in pathological settings are needed to fully understand the role of oxygen availability on DC function *in situ*.

3.5 Oxidative stress

The main sources of ROS in tumor cells are dysfunctional mitochondria and NADPH oxidases. This is further enhanced by intracellular ROS production of stromal cells, as a consequence of the metabolic alterations within the TME (75, 76). Intracellular ROS production in DCs during an immune response can have both pro-inflammatory and anti-inflammatory effects, via modulation of cross-presentation and as modulator of signaling pathways (39, 76-80). In general, extracellular ROS seems to have a pro-inflammatory effect, although data is limited (table 1). Treatment of immature moDCs with hydrogen peroxide enhanced maturation and their capacity to induce T cell proliferation upon LPS stimulation (81). The inflammatory response of primary DCs to the malaria parasite Plasmodium falciparum also increased upon exposure to cells treated with xanthine oxidase, a malaria-induced enzyme that increases extracellular ROS levels (82). However, while transient ROS exposure following DC activation may have pro-inflammatory effects, what the functional consequences are of chronic ROS exposure, a situation DCs presumably have to deal within the TME, remains unclear. Possibly, the highly oxidized lipids that are found in TADCs, are one of the byproducts of chronic ROS exposure (83). Through this mechanism long-term ROS exposure in the TME could lead to impaired DC immunogenicity. Studies addressing the functional consequences of transient versus chronic ROS exposure as well as of the different types of ROS on DCs, will be required to better define what role tumor-associated ROS and oxidative stress play in DC function in the TME.

3.6 Lactate

Tumor cells are known for the Warburg effect, which goes along with secretion of high levels of lactate. Lactate has a major influence on the immune-priming efficiency of DCs. Lactate derived from tumor spheroids, mesenchymal stromal cells or endogenously produced, affects the differentiation and maturation of moDCs. High concentrations of lactate reduce the differentiation capacity of moDCs, as higher numbers of monocyte like $CD14^{+}/CD1a^{-}$ cells were detected at the end of the cultures (84-86). This was accompanied by a lactate-dependent

Effects associated with the TME	Effects associated with diabetes	References
Glucose		Krawczyk et al. 2010, Guak et al. 2018, Everts et al. 2014, Thwe et al. 2017, Loomans et al. 2009, Gilardini Montani et al. 2015, Vuckovic et al. 2007, Nam et al. 2018, Lu et al. 2013, Musili et al. 2011, Peng et al. 2003, Seifarth et al. 2008, Blank et al. 2012, Bertola et al. 2012, Chen et al. 2014
Local depletion	Hyperglycemia	
Impaired anabolic metabolism »↓ Activation »↓ Migration *AMPK activation* »↓ *Activation*	<u>Blood DCs</u> ↓/↑DC counts = Activation ↑*Migration to metabolic tissues* <u>*In vitro* DCs</u> ↓/= Differentiation ↑Activation »↑*Th17 T cell priming*	
Lipids		Herber et al. 2010, Gao et al. 2015, Gardner et al. 2015, Veglia et al. 2017, Cao et al. 2014, Nicholas et al. 2017, Stelzner et al. 2016, Mogilenko et al. 2019, Reynolds et al. 2012, Miyake et al. 2010, Miyake et al. 2010, Wang et al. 2007, Carlsson et al. 2015, Zeyda et al. 2005
High intracellular storage	Hyperlipidemia	
<u>Oxidized lipids</u> ↓Cross-presentation ↑*Fatty acid oxidation* » ↓*Activation*	<u>PA</u> ↑ NFκB signaling Metabolic rearrangements »↑Activation <u>SA</u> ↓ Activation <u>OA</u> = Activation	
Oxygen levels		Riccardi et al. 2008, Mancino et al. 2008, Yang et al. 2009, Zhao et al. 2005, Elia et al. 2008, Jantsch et al. 2008
Low		
= Differentiation ↑Innate immunity (immature DCs) ↑Migration (immature DCs) =/↓/↑ Activation ↓Migration (mature DCs)		
ROS		Rutault et al. 1999, Gotz, Ty 2019
High		
<u>Short term ROS</u> ↑Activation <u>Long term ROS</u> *Lipid oxidation* »↓*Activation*		
Lactate		Gottfried et al. 2006, Nasi et al. 2013, Selleri et al. 2016, Puig-Kroger et al. 2003, Caronni et al. 2018
High		
Impaired mitochondrial respiration »↓Differentiation ↓Cross-presentation *Epigenetic modifications* »↓Activation		
ATP and adenosine		Sáez et al. 2017, Di Virgilio et al. 2018, Aymeric et al. 2010, Ghiringhelli et al 2009, Lecciso et al. 2017, Wennerberg et al. 2020, Chen et al. 2020, Kayhan et al. 2019
High		
<u>ATP</u> ↑ Migration NLRP3 inflammasome activation »↑ $CD8^+$ T cell priming ↑regulatory T cell priming <u>Adenosine</u> ↓Activation		
2-Hydroxyglutarate		Ugele et al. 2019
High		
↓IL-12 ↑Catabolic metabolism » = Activation *Epigenetic modifications*		

Table 1: Metabolic determinants from pathological environments that influence DC function. Overview of extracellular metabolic cues observed in cancer and diabetes that affect DC function. ↑/↓/=: increased, decreased or equal effect compared to control conditions. » Consequence of aforementioned mechanism. Italics: presumed effect.

reduction of oxidative phosphorylation, but enhanced respiratory capacity in immature moDCs (86). Also maturation of DCs is affected by high lactate levels, reflected by lower levels of maturation markers, an increase in immunosuppressive cytokine secretion, a decrease in pro-inflammatory cytokine secretion and reduced ability to induce T cell proliferation (84, 85, 87). The latter can be caused by detrimental effects of lactate on cross presentation. Using tumor conditioned Flt3L-DCs stimulated with CpG/PolyI:C and OVA-peptide, it was found that high lactate concentrations accelerate antigen processing via lowering the endosomal pH, resulting in impaired preservation of MHC-I epitopes. Thus high concentrations of lactate in the local environment of differentiating or maturing DCs induces tolerance in DCs, via altering metabolism and antigen processing (table 1). Extracellular lactate can mediate its anti-inflammatory function via binding to lactate receptor Gi-protein–coupled receptor 81 (GPR81) as was recently shown in DCs derived from murine mammary gland tumors (88). Alternatively, lactate can enter the cells via monocarboxylate transporter 1 (MCT1) as was shown in moDCs (84). Intracellular lactate may also hamper the immune response via a recently discovered epigenetic modification termed lactylation. In M1 macrophages endogenously produced lactate promoted lactylation of lysine residues, thereby promoting M2-like gene expression (89). Whether histone lactylation is another immunosuppressive feature of lactate in DCs is an interesting question that warrants further study.

3.7 ATP and adenosine

Whereas during homeostasis extracellular ATP levels are negligible, ATP is highly abundant in the TME where it functions as a signaling molecule that provokes inflammation (55, 90). It has been proposed that diffusion of ATP out of the TME recruits DCs to the TME, given that BDMCs treated with 500uM ATP increased migratory speed (table 1) (91, 92). Moreover, extracellular ATP released by tumor cells after chemotherapy can promote anti-tumor immunity via signaling through ATP-receptors P2RX7 on DCs, thereby activating the NLRP3 inflammasome, enhancing IL-1β secretion and boosting $CD8^+$ T cell priming (93, 94). In contrast, moDCs co-cultured with acute myeloid leukemia cells treated with chemotherapy drugs displayed increased potency to expand regulatory T cells in an extracellular ATP-dependent manner (table 1) (95). Hence, there is great value in understanding what factors determine the balance between the pro- and anti-inflammatory effects by extracellular ATP after chemotherapy, as it may be an important predictor for treatment efficacy.

Paradoxically, immunosuppressive nucleoside adenosine, derived from conversion of ATP by membrane-bound ectonucleosides CD39 and CD73, is also abundantly present in the TME (96, 97). Adenosine interacts with four different receptors, of which A2AR and A2BR are most highly expressed on immune cells (98). Irradiation of mouse breast tumors caused upregulation of CD73 expression in tumor cells and increased local adenosine concentrations. Anti-CD73 treatment enhanced cDC1 tumor infiltration, increased the antitumor T cell response and reduced tumor growth (99). Additionally, in mice in which adenosine receptor A2BR was selectively knocked out in $CD11c^+$ DCs, the growth of B16-melanoma was delayed, supporting a role for adenosine signaling in rendering DCs immunosuppressive (100). Furthermore, LPS-stimulated BMDCs treated with adenosine analogue NECA increased intracellular cAMP levels, which lowered secretion of IL-12 and TNF-α secretion and enhanced IL-10 release via protein kinase A (PKA) and exchange protein directly activated by cAMP (Epac) signaling (101). Overall most studies indicate that extracellular ATP enhances immunogenicity of DCs and anti-tumor immune responses, while adenosine does the opposite (table 1) (92, 102).

Shifting the balance in favor of ATP by blocking CD73, CD39 or adenosine receptors is therefore a promising immunotherapy.

3.8 2-Hydroxyglutarate

In various tumors the oncometabolite 2-HG accumulates, which in non-malignant tissues is found at low concentrations (54). 2-HG has been shown to contribute to immune suppression in the TME via anti-inflammatory effects on T cells (103, 104). Immature moDCs cultured for 24 hours with LPS and 2-HG secreted reduced levels of IL-12, enhanced mitochondrial respiration and lowered lactate secretion, indicating that accumulation of 2-HG affects moDCs via metabolic reprogramming. However, the ability of DCs to induce T cell proliferation remained the same, suggesting that the 2-HG-induced metabolic rearrangement in DCs does not affect their T cell priming capacity (table 1) (105). However, in this context 2-HG was added simultaneously with the TLR ligand, while in the TME immature DCs may reside in a 2-HG-rich environment without immediate activation. Long-term exposure to 2-HG may have a stronger effect on the immunogenic capacities of DCs, potentially via the changes in gene expression, given that 2-HG affects activity of DNA and histone modifying enzymes, but this remains to be determined (54).

3.9 Concluding remarks

Thus far the effects of metabolic perturbations characteristic of the TME on DC biology have been primarily studied in *in vitro* systems using moDCs. However, we have still limited knowledge about the real contribution of those metabolic changes on the functional properties of conventional as well as inflammatory DCs residing in the TME *in situ*. Likewise, if and to what extent these different metabolic perturbations interact and synergize to affect the functional properties of DCs remains to be determined. For successful activation of the immune system via DC-based therapy it is important to know how DCs deal with these metabolic rearrangements in the TME. For instance, how do DCs respond to adjuvants in the metabolic context of the TME? Is there a way to make these cells less vulnerable to potential immunosuppressive metabolic cues from the TME? And once out of the immunosuppressive metabolic TME, how quickly can DCs regain immunogenic function, if at all possible? To answer these questions and to gain better understanding of the immunosuppressive effects of the metabolic TME on DCs, in depth characterization of the metabolic TME and DC phenotype in primary tumors will be key.

4 Effects of the metabolic environment on DCs in diabetes

4.1 Interplay between metabolic disturbances and inflammation leading to diabetes

Not only nutrient deprivation, but also excessive amounts of nutrients can disturb immune homeostasis and DC function. A well-known example of a disease that is characterized by elevated concentrations of glucose and lipids is diabetes. The two main types of diabetes are type I and type II Diabetes Mellitus (T1D/T2D), both characterized by dysfunctional insulin regulation and subsequent hyperglycemia. While T1D develops as a consequence of an auto-immune reaction against beta-cells, common causes for T2D are aging and obesity. Obesity causes hyperglycemia, elevated levels of free fatty acids, hypoxia, oxidative stress and an imbalance in many other metabolites, hormones and cytokines (106-109). This causes

a switch in the composition and phenotype of immune cells in metabolic tissues from an anti-inflammatory to a more pro-inflammatory profile and thereby induces chronic low-grade inflammation, which ultimately drives insulin resistance (110-112). cDCs and pDCs are among the immune cells present in adipose tissue and there is a clear correlation between insulin resistance and number of $CD11c^+$ DCs present in adipose tissue (113-116). Moreover, several studies have shown that in response to high-fat diet DCs present in murine adipose tissue transition from Th1- to Th17-priming cells, an inflammatory profile linked to the pathogenesis of diabetes (114, 117, 118).

We will describe how DCs are affected by the metabolic changes in their environment and focus on hyperglycemia and elevated levels of free fatty acids. Oxidative stress and hypoxia are also major metabolic players in diabetes, but to our knowledge there is no data available looking at the effects of these conditions on DC function in diabetic context (108, 109). Hence, we refer to the previous section for the effects of oxygen deprivation and excessive ROS levels on DC function.

4.2 Hyperglycemia

Decreased insulin secretion by beta-cells and lowered sensitivity to insulin signaling reduces the uptake of glucose by cells, which subsequently results in elevated blood glucose levels. As glucose availability plays a major role in DC activation it is conceivable that this glucose imbalance affects DC function. Several studies addressed the effects of hyperglycemia on primary dendritic cells from blood. Both a reduction and an increase in myeloid and pDC counts in blood of patients with T1D and T2D have been reported (table 1) (119-123). Reduced counts seems to be stronger in patients with poor glycemic control (121). Pro- and anti-inflammatory cytokine secretion by DCs from diabetic patients was not altered following ex vivo TLR stimulation, indicating that high blood glucose levels do not directly affect the function of circulating DCs, but primarily their numbers (120, 122, 124). It should be noted that hyperglycemia is not the only (metabolic) difference in blood from diabetic patients and other factors may also influence DC frequencies and function. Since a study in mice showed that hyperglycemia does not influence $CD11c^+$ DC differentiation in the bone marrow, it is unlikely that the decrease in circulating DCs is a consequence of impaired DC generation. (125). Instead, lower numbers of circulating DCs are possibly a reflection of enhanced migration of DCs to metabolic tissues, where DCs are known to accumulate and contribute to the low-grade inflammation observed in metabolic tissues of T2D patients. As previously mentioned DCs in obese adipose tissue drive a Th17 inflammatory response (114, 117). Interestingly, moDCs exposed to 5.5mM, 15 mM and 30mM glucose for 24 hours increase CD83 and CD86 expression and secretion of IL-6 and IL-12 in a dose-dependent manner (78). IL-6 is involved in Th17 differentiation of naïve T cells and was also found to be highly secreted by $CD11c^+$ DCs from obese adipose tissue, suggesting that high glucose levels in adipose tissue may contribute to conditioning DCs for Th17 priming (table 1) (117, 126). However, *in vivo* data connecting glucose levels to DC function in metabolic tissues is currently lacking. *In vitro* generation of tolerogenic moDCs was less efficient with monocytes derived from T1D patients with poor glycemic control in comparison to patients who maintained glycemic control, supporting the hypothesis that a hyperglycemic environment promotes a more pro-inflammatory profile (127). On the other hand, moDCs derived from T2D donors compared to healthy control donors expressed lower levels of maturation markers (119). Moreover, moDC differentiation in high-glucose medium (25mM) or media supplemented with sera from

hyperglycemic T2D patients reduced the number of moDCs, expression of maturation markers and the capacity to induce T cell proliferation after LPS stimulation. In addition, glucose-rich micro-environments increase ROS production and promote activation of the p38 MAPK and Wnt/b-catenin pathways, which are associated with tolerogenic properties of DCs (128-131). Together these *in vitro* studies may indicate that over-abundance of glucose drives monocyte differentiation towards less-proinflammatory DCs, while differentiated moDCs and potentially $CD11c^+$ DCs residing in adipose tissue may become more immunogenic in a hyperglycemic environment (table 1).

4.3 Free fatty acids

A cause and consequence of obesity and insulin resistance in T2D is the release of free fatty acids by expanding fat mass (107, 132). FAs are well-known regulators of the immune response. Polyunsaturated FAs (PUFAs) often have anti-inflammatory effects while many saturated fatty acids (SFAs) serve as pro-inflammatory molecules (133, 134). Examples of the latter are palmitic acid (PA) and stearic acid (SA), which are together with unsaturated oleic acid (OA) among the most abundant dysregulated FFAs in obese and T2D patients (106, 135). Especially PA is known for its pro-inflammatory effects and detrimental role in T2D pathogenesis (136). This is partly caused via its effects on DCs. PA in combination with LPS can enhance Th1-associated inflammation, which is driven by TLR4-dependent activation of the NFkB pathway and ROS in moDCs (77, 137, 138). PA also boosts inflammatory properties of activated BMDCs in a TLR4-independent manner, via inhibition of hexokinase (HK) during the late stages of metabolic reprogramming. This inhibition of HK and thereby glycolysis resulted in enhanced mitochondrial respiration, increased mitochondrial ROS levels, elevated activation of the unfolded protein response (UPR) and subsequent induction of IL-23 expression. UPR-dependent IL-23 expression was also confirmed in mice fed a high fat diet (39). BMDCs derived from obese mice additionally increased IL-1β secretion in a NLRP3 inflammasome-dependent manner following stimulation with PA (139). IL-1β and IL-23 are key cytokines involved in promoting Th17 responses and hence PA is a potential driver of insulin resistance (118). However, a direct causal link between enhanced pro-inflammatory cytokine secretion by DCs and Th17 induction in settings of FA exposure still needs to be established as for instance DCs isolated from human blood displayed a reduced capacity to prime T cell responses upon stimulation with PA, despite having increased IL-1β and TNF secretion (140). In contrast to PA, SA does not seem to affect DC function. SA treatment of LPS-stimulated moDCs did not affect expression of maturation markers nor the capacity to induce T cell proliferation (141). Although data on the effects of SA treatment of DCs is still limited, this appears to be different from what is known for macrophages, where SA and PA have been reported to have a similar pro-inflammatory effect (142, 143). OA is a mono-unsaturated FA that has beneficial effects on insulin resistance. In macrophages, this is partly mediated by counteracting the pro-inflammatory effects of SFA (136). Thus far, there is no data available indicating an anti-inflammatory role for OA in DCs. OA treatment had either no effect, or boosted a pro-inflammatory immune response, but has never been tested in combination with SFA stimulation (137, 140, 144, 145).

The balance in dietary intake of SFAs and PUFAs can have great influence on the clinical outcome of diabetes. A comparison of 6%, 12% and 24% of SFA in the diet of mice without changing the total dietary fat contribution had a profound effect on macrophage function and insulin resistance, with 12% SFA as the greatest contributor to inflammation and

insulin resistance (146). Human data is however inconsistent about the beneficial effects of PUFA-rich and SFA-poor diets on glycemic control of T2D patients (147). Therefore, studies in humans and mice with a focus on the composition in dietary fat and profiling of DCs in metabolic tissues may tell us whether DCs contribute to PUFA-mediated protection against diabetes and/or SFA-mediated development of diabetes, potentially via a PA-induced Th17 response.

In conclusion, compared to other immune cells, there is still little known about the effects on DCs of the FFAs that are most abundant in obesity and T2D patients. While PA stimulation of DCs seems to have the expected pro-inflammatory effects, it is remains unclear if SA and OA influence insulin resistance via DCs (table 1).

4.4 Concluding remarks

T1D is characterized by an active immune response against beta-cells, while T2D is associated with chronic low-grade inflammation. Hence, it is perhaps somewhat surprising that ex vivo data indicate that hyperglycemia has minimal effect on the function of DCs, that most *in vitro* studies describe a tolerogenic effect of excessive glucose levels on DC differentiation, and that only *in vitro* mature DCs are likely to become more pro-inflammatory. Although currently it cannot be excluded that the latter observations may be due the use of *in vitro* model systems such as, *in vitro* generated moDCs that possibly cannot sufficiently mimic the metabolic alterations and glucose-rich environment that cDCs and pDCs are exposed to *in vivo*, it may in fact indicate that hyperglycemia is not a major driver of the pro-inflammatory profiles of DCs observed in diabetes and that other metabolic and/or immunological cues are more important (113-116). This idea would be consistent with the fact that hyperglycemia is generally associated with impaired immune response against for example infections and tumors (148, 149). A better understanding of how overabundance of various nutrients may act in concert to modulate DC function and to thereby contribute to local inflammation in the context of diabetes will be important for identification of the pathways that lead to inflammation-driven insulin resistance that could be targeted to control diabetes.

5 Perspectives and outlook

It is becoming evident that the metabolic micro-environment has a major influence on DC function and that disturbance of metabolic homeostasis can impact immune responses. We aimed to provide an overview of key metabolites that influence DC phenotype and function. Cancer and diabetes are examples of highly prevalent disorders in which metabolic homeostasis is disturbed, but many more pathologies are associated with dysregulated metabolism. Eating disorders alter nutrient availability, organ-specific pathologies such as hepatic steatosis impair systemic metabolism and oxidative stress is associated with many diseases including atherosclerosis, cardiovascular diseases and neurodegenerative disorders. Hence, understanding the impact of nutrient availability on the function of immune cells, including DCs, is relevant for a broad range of diseases. Reprogramming the metabolic state of DCs by intervening with nutrient availability can be an effective way to control inflammation. This could be achieved by systemic approaches, including nutritional interventions which are commonly used to control inflammation (150). For instance, lowering caloric intake, by reducing fat and glucose content, can improve glycemic control and subsequently reduce diabetes-associated low-grade inflammation (151-153). Given the pro-inflammatory effects of high glucose and SFA concentration on tissue-associated DCs, it is reasonable to assume

that dietary interventions that lead to normalization of glucose and SFA concentrations in the tissue that these cells reside in, will render them less pro-inflammatory, thereby contributing to reduction of local tissue inflammation and eventually improvement of metabolic homeostasis. Alternatively, molecular approaches that directly target cellular nutrient uptake or bioenergetic pathways can make DCs potentially less vulnerable to extracellular nutritional changes and intervention with energy-sensing enzymes like AMPK can also control inflammation (154). In addition, targeting metabolism of non-immune cells can also have a beneficial effect on the metabolic micro-environment of DCs. For example, therapies that interfere with cancer metabolism to directly impair tumor growth could also have indirect anti-tumor effects by potentially creating a TME with higher nutrient availability that would be more permissive to effective anti-tumor immune responses (155).

Current studies addressing the effects of the metabolic micro-environment on DCs are mostly performed *in vitro* using human moDCs or murine BMDCs. While these studies have provided us important new insights into how nutrient availability can shape DC function, *in vitro* culture conditions often do not fully mimic the complexity and concentrations of various nutrients and metabolites these cells are exposed to *in situ*. For instance, *In vitro*-generated DCs are commonly cultured in media supplemented with 10% fetal calf serum (FCS) and glutamine. Serum is a source for lipids, vitamins, hormones, growth factors and other compounds, but the exact amounts of these compounds are unknown, differ per batch and may not correspond with concentrations found in tissues that DCs reside in (156). Moreover, commonly used culture media such as RPMI 1640 and DMEM contain supraphysiological levels of glucose (11mM and 25mM, respectively, versus ~5,5mM *in situ*) and lower levels of electrolytes including calcium and magnesium (157). The effects of nutrient availability on the function of DC subsets in a more physiological environment, with other metabolic and non-metabolic immunomodulatory signals around, need to be further evaluated, to be able to better assess what the *in vivo* contribution of the metabolic micro-environment is on the functional properties of DCs. To tackle this issue, there have been recent efforts to develop human plasma-like, physiological medium, which contains components such as amino acids, metabolites, salt ions and vitamins that are absent from standard media and holds physiologically relevant concentrations of common media components. To minimize the effects of FCS-derived components, medium can be supplemented with either a low percentage (2.5%) of FCS or dialyzed FCS (158-160). Studies using these media found enhanced *in vitro* T cell activation and increased biological similarity between cultured breast cancer cells and primary mammary tumors, providing promising first evidence that these types of media could be used to better mimic physiological setting *in vitro* than classically used culture media. (159, 160). These tools will likely also be key to further the field of DC metabolism and to better delineate the interplay between DC function and extra- or intracellular metabolism. In addition, various novel mass-spectrometry, high dimensional flow cytometry and transcriptomics platforms have been developed in recent years that enable one to assess metabolic profiles in tissues at high spatial resolution as well as to characterize metabolic and immunological phenotypes of immune cells present in those tissues at the single cell level. These novel techniques will no doubt greatly improve our understanding of how nutrients shape DC function *in situ*.

Even though many open questions remain, recent work has revealed profound effects of the metabolic micro-environment on DC function in health and disease, which may pave the way for developing DC metabolism-based approaches to treat metabolic and inflammatory disorders.

Author Contributions

All authors declare no conflict of interest and approval of the final version.

Funding

This review is supported by an LUMC fellowship awarded to B.E.

References

1. Guilliams M, Ginhoux F, Jakubzick C, Naik SH, Onai N, Schraml BU, et al. Dendritic cells, monocytes and macrophages: a unified nomenclature based on ontogeny. Nat Rev Immunol. 2014;14(8):571-8.
2. Murphy TL, Grajales-Reyes GE, Wu X, Tussiwand R, Briseno CG, Iwata A, et al. Transcriptional Control of Dendritic Cell Development. Annual review of immunology. 2016;34:93-119.
3. Collin M, Bigley V. Human dendritic cell subsets: an update. Immunology. 2018;154(1):3-20.
4. Sallusto F, Lanzavecchia A. Efficient Presentation of Soluble Antigen by Cultured Human Dendritic Cells Is Maintained by Granulocyte/Macrophage Colony-stimulating Factor Plus Iuterleukin 4 and Downregulated by Tumor Necrosis Factor a. J Exp Med. 1994;179(4):1109-18.
5. Schultze JL, Aschenbrenner AC. Systems immunology allows a new view on human dendritic cells. Semin Cell Dev Biol. 2019;86:15-23.
6. Sander J, Schmidt SV, Cirovic B, McGovern N, Papantonopoulou O, Hardt AL, et al. Cellular Differentiation of Human Monocytes Is Regulated by Time-Dependent Interleukin-4 Signaling and the Transcriptional Regulator NCOR2. Immunity. 2017;47(6):1051-66 e12.
7. Inaba BK, Inaba M, Romani N, Aya H, Deguchi M, Ikehara S, et al. Generation of Large Numbers of Dendritic Cells from Mouse Bone Marrow Cultures Supplemented with Granulocyte/Macrophage Colony-stimulating Factor. J Exp Med. 1992;176:1693-702.
8. Guo X, Zhou Y, Wu T, Zhu X, Lai W, Wu L. Generation of mouse and human dendritic cells in vitro. J Immunol Methods. 2016;432:24-9.
9. Naik SH, Proietto AI, Wilson NS, Dakic A, Schnorrer P, Fuchsberger M, et al. Cutting edge: generation of splenic CD8+ and CD8- dendritic cell equivalents in Fms-like tyrosine kinase 3 ligand bone marrow cultures. J Immunol. 2005;174(11):6592-7.
10. Joffre O, Nolte MA, Spörri R, Reis e Sousa C. Inflammatory signals in dendritic cell activation and the induction of adaptive immunity. Immunol Rev. 2009;227(1):234-47.
11. Eisenbarth SC. Dendritic cell subsets in T cell programming: location dictates function. Nat Rev Immunol. 2019;19(2):89-103.
12. Tiberio L, Del Prete A, Schioppa T, Sozio F, Bosisio D, Sozzani S. Chemokine and chemotactic signals in dendritic cell migration. Cell Mol Immunol. 2018;15(4):346-52.
13. O'Neill LA, Kishton RJ, Rathmell J. A guide to immunometabolism for immunologists. Nat Rev Immunol. 2016;16(9):553-65.
14. Buck MD, Sowell RT, Kaech SM, Pearce EL. Metabolic Instruction of Immunity. Cell. 2017;169(4):570-86.
15. Kedia-Mehta N, Finlay DK. Competition for nutrients and its role in controlling immune responses. Nature Communications. 2019;10(1).
16. Krawczyk CM, Holowka T, Sun J, Blagih J, Amiel E, DeBerardinis RJ, et al. Toll-like receptor-induced changes in glycolytic metabolism regulate dendritic cell activation. Blood. 2010;115(23):4742-9.
17. Everts B, Amiel E, van der Windt GJ, Freitas TC, Chott R, Yarasheski KE, et al. Commitment to glycolysis sustains survival of NO-producing inflammatory dendritic cells. Blood. 2012;120(7):1422-31.
18. Malinarich F, Duan K, Hamid RA, Bijin A, Lin WX, Poidinger M, et al. High mitochondrial respiration and glycolytic capacity represent a metabolic phenotype of human tolerogenic dendritic cells. J Immunol. 2015;194(11):5174-86.
19. Thwe PM, Pelgrom L, Cooper R, Beauchamp S, Reisz JA, D'Alessandro A, et al. Cell-Intrinsic Glycogen Metabolism Supports Early Glycolytic Reprogramming Required for Dendritic Cell Immune Responses. Cell Metab. 2017;26(3):558-67 e5.

20. Basit F, de Vries IJM. Dendritic Cells Require PINK1-Mediated Phosphorylation of BCKDE1alpha to Promote Fatty Acid Oxidation for Immune Function. Front Immunol. 2019;10:2386.
21. Basit F, Mathan T, Sancho D, de Vries IJM. Human Dendritic Cell Subsets Undergo Distinct Metabolic Reprogramming for Immune Response. Front Immunol. 2018;9:2489.
22. Bajwa G, DeBerardinis RJ, Shao B, Hall B, Farrar JD, Gill MA. Cutting Edge: Critical Role of Glycolysis in Human Plasmacytoid Dendritic Cell Antiviral Responses. J Immunol. 2016;196(5):2004-9.
23. Everts B, Amiel E, Huang SC, Smith AM, Chang CH, Lam WY, et al. TLR-driven early glycolytic reprogramming via the kinases TBK1-IKKvarepsilon supports the anabolic demands of dendritic cell activation. Nat Immunol. 2014;15(4):323-32.
24. Lawless SJ, Kedia-Mehta N, Walls JF, McGarrigle R, Convery O, Sinclair LV, et al. Glucose represses dendritic cell-induced T cell responses. Nature Communications. 2017;8:15620.
25. Randolph GJ, Ochando J, Partida-Sanchez S. Migration of dendritic cell subsets and their precursors. Annu Rev Immunol. 2008;26:293-316.
26. Guak H, Al Habyan S, Ma EH, Aldossary H, Al-Masri M, Won SY, et al. Glycolytic metabolism is essential for CCR7 oligomerization and dendritic cell migration. Nat Commun. 2018;9(1):2463.
27. Amiel E, Everts B, Freitas TC, King IL, Curtis JD, Pearce EL, et al. Inhibition of mechanistic target of rapamycin promotes dendritic cell activation and enhances therapeutic autologous vaccination in mice. J Immunol. 2012;189(5):2151-8.
28. Wang F, Zhang S, Vuckovic I, Jeon R, Lerman A, Folmes CD, et al. Glycolytic Stimulation Is Not a Requirement for M2 Macrophage Differentiation. Cell Metab. 2018;28(3):463-75 e4.
29. Marquez S, Fernandez JJ, Teran-Cabanillas E, Herrero C, Alonso S, Azogil A, et al. Endoplasmic Reticulum Stress Sensor IRE1alpha Enhances IL-23 Expression by Human Dendritic Cells. Front Immunol. 2017;8:639.
30. Thwe PM, Amiel E. The role of nitric oxide in metabolic regulation of Dendritic cell immune function. Cancer Lett. 2018;412:236-42.
31. Zhang D, Chia C, Jiao X, Jin W, Kasagi S, Wu R, et al. D-mannose induces regulatory T cells and suppresses immunopathology. Nat Med. 2017;23(9):1036-45.
32. Kakazu E, Ueno Y, Kondo Y, Fukushima K, Shiina M, Inoue J, et al. Branched chain amino acids enhance the maturation and function of myeloid dendritic cells ex vivo in patients with advanced cirrhosis. Hepatology. 2009;50(6):1936-45.
33. Kakazu E, Kondo Y, Kogure T, Ninomiya M, Kimura O, Ueno Y, et al. Plasma amino acids imbalance in cirrhotic patients disturbs the tricarboxylic acid cycle of dendritic cell. Sci Rep. 2013;3:3459.
34. Kakazu E, Kanno N, Ueno Y, Shimosegawa T. Extracellular Branched-Chain Amino Acids, Especially Valine, Regulate Maturation and Function of Monocyte-Derived Dendritic Cells. The Journal of Immunology. 2007;179(10):7137-46.
35. Sun X, Zemel MB. Leucine modulation of mitochondrial mass and oxygen consumption in skeletal muscle cells and adipocytes. Nutr Metab (Lond). 2009;6:26.
36. D'Angelo JA, Dehlink E, Platzer B, Dwyer P, Circu ML, Garay J, et al. The cystine/glutamate antiporter regulates dendritic cell differentiation and antigen presentation. J Immunol. 2010;185(6):3217-26.
37. DeBerardinis RJ, Mancuso A, Daikhin E, Nissim I, Yudkoff M, Wehrli S, et al. Beyond aerobic glycolysis: Transformed cells can engage in glutamine metabolism that exceeds the requirement for protein and nucleotide synthesis. Proc Natl Acad Sci U S A. 2007;104(49):19345-50.
38. Metallo CM, Gameiro PA, Bell EL, Mattaini KR, Yang J, Hiller K, et al. Reductive glutamine metabolism by IDH1 mediates lipogenesis under hypoxia. Nature. 2011;481(7381):380-4.
39. Mogilenko DA, Haas JT, L'Homme L, Fleury S, Quemener S, Levavasseur M, et al. Metabolic and Innate Immune Cues Merge into a Specific Inflammatory Response via the UPR. Cell. 2019;177(5):1201-16 e19.

40. Kratchmarov R, Viragova S, Kim MJ, Rothman NJ, Liu K, Reizis B, et al. Metabolic control of cell fate bifurcations in a hematopoietic progenitor population. Immunol Cell Biol. 2018;96(8):863-71.

41. Ibrahim J, Nguyen AH, Rehman A, Ochi A, Jamal M, Graffeo CS, et al. Dendritic cell populations with different concentrations of lipid regulate tolerance and immunity in mouse and human liver. Gastroenterology. 2012;143(4):1061-72.

42. Bougneres L, Helft J, Tiwari S, Vargas P, Chang BH, Chan L, et al. A role for lipid bodies in the cross-presentation of phagocytosed antigens by MHC class I in dendritic cells. Immunity. 2009;31(2):232-44.

43. Wu D, Sanin DE, Everts B, Chen Q, Qiu J, Buck MD, et al. Type 1 Interferons Induce Changes in Core Metabolism that Are Critical for Immune Function. Immunity. 2016;44(6):1325-36.

44. Mattacks CA, Sadler D, Pond CM. Site-Specific Differences in Fatty Acid Composition of Dendritic Cells and Associated Adipose Tissue in Popliteal Depot, Mesentery, and Omentum and Their Modulation by Chronic Inflammation and Dietary Lipids. Lymphat Res Biol. 2004;2(3):107-29.

45. Hanahan D, Weinberg RA. Hallmarks of cancer: the next generation. Cell. 2011;144(5):646-74.

46. Giovanelli P, Sandoval TA, Cubillos-Ruiz JR. Dendritic Cell Metabolism and Function in Tumors. Trends Immunol. 2019;40(8):699-718.

47. Scarlett UK, Rutkowski MR, Rauwerdink AM, Fields J, Escovar-Fadul X, Baird J, et al. Ovarian cancer progression is controlled by phenotypic changes in dendritic cells. J Exp Med. 2012;209(3):495-506.

48. Monjazeb AM, Zamora AE, Grossenbacher SK, Mirsoian A, Sckisel GD, Murphy WJ. Immunoediting and Antigen Loss: Overcoming the Achilles Heel of Immunotherapy with Antigen Non-Specific Therapies. Frontiers in Oncology. 2013;3(197).

49. Dunn GP, Bruce AT, Ikeda H, Old LJ, Schreiber RD. Cancer immunoediting: from immunosurveillance to tumor escape. 2002;3(11):991-8.

50. Liberti MV, Locasale JW. The Warburg Effect: How Does it Benefit Cancer Cells? Trends in Biochemical Sciences. 2016;41(3):211-8.

51. Cheng C, Geng F, Cheng X, Guo D. Lipid metabolism reprogramming and its potential targets in cancer. Cancer Communications. 2018;38(1).

52. DeBerardinis RJ, Chandel NS. Fundamentals of cancer metabolism. Sci Adv. 2016;2(5):e1600200.

53. Vettore L, Westbrook RL, Tennant DA. New aspects of amino acid metabolism in cancer. Br J Cancer. 2020;122:150-56.

54. Losman JA, Kaelin WG. What a difference a hydroxyl makes: mutant IDH, (R)-2-hydroxyglutarate, and cancer. Genes & Development. 2013;27(8):836-52.

55. Pellegatti P, Raffaghello L, Bianchi G, Piccardi F, Pistoia V, Di Virgilio F. Increased level of extracellular ATP at tumor sites: in vivo imaging with plasma membrane luciferase. PLoS One. 2008;3(7):e2599.

56. Chang CH, Qiu J, O'Sullivan D, Buck MD, Noguchi T, Curtis JD, et al. Metabolic Competition in the Tumor Microenvironment Is a Driver of Cancer Progression. Cell. 2015;162(6):1229-41.

57. Ho PC, Bihuniak JD, Macintyre AN, Staron M, Liu X, Amezquita R, et al. Phosphoenolpyruvate Is a Metabolic Checkpoint of Anti-tumor T Cell Responses. Cell. 2015;162(6):1217-28.

58. Zhao F, Xiao C, Evans KS, Theivanthiran T, DeVito N, Holtzhausen A, et al. Paracrine Wnt5a-β-Catenin Signaling Triggers a Metabolic Program that Drives Dendritic Cell Tolerization. Immunity. 2018;48(1):147-60.e7.

59. Garcia D, Shaw RJ. AMPK: Mechanisms of Cellular Energy Sensing and Restoration of Metabolic Balance. Molecular Cell. 2017;66(6):789-800.

60. Wang Y, Du X, Wei J, Long L, Tan H, Guy C, et al. LKB1 orchestrates dendritic cell metabolic quiescence and anti-tumor immunity. Cell Res. 2019;29(5):391-405.

61. Koundouros N, Poulogiannis G. Reprogramming of fatty acid metabolism in cancer. Br J Cancer. 2019;122(1):4-22.

62. Gao F, Liu C, Guo J, Sun W, Xian L, Bai D, et al. Radiation-driven lipid accumulation and dendritic cell dysfunction in cancer. Sci Rep. 2015;5:9613.

63. Herber DL, Cao W, Nefedova Y, Novitskiy SV, Nagaraj S, Tyurin VA, et al. Lipid accumulation and dendritic cell dysfunction in cancer. Nat Med. 2010;16(8):880-6.

64. Gardner JK, Mamotte CD, Patel P, Yeoh TL, Jackaman C, Nelson DJ. Mesothelioma tumor cells modulate dendritic cell lipid content, phenotype and function. PLoS One. 2015;10(4):e0123563.

65. Veglia F, Tyurin VA, Mohammadyani D, Blasi M, Duperret EK, Donthireddy L, et al. Lipidbodies containing oxidatively truncated lipids block antigen cross-presentation by dendritic cells in cancer. Nat Commun. 2017;8(1):2122.

66. Cao W, Ramakrishnan R, Tyurin VA, Veglia F, Condamine T, Amoscato A, et al. Oxidized lipids block antigen cross-presentation by dendritic cells in cancer. J Immunol. 2014;192(6):2920-31.

67. Hayashi Y, Yokota A, Harada H, Huang G. Hypoxia/pseudohypoxia-mediated activation of hypoxia-inducible factor-1alpha in cancer. Cancer Sci. 2019;110(5):1510-7.

68. Zhao W, Darmanin S, Fu Q, Chen J, Cui H, Wang J, et al. Hypoxia suppresses the production of matrix metalloproteinases and the migration of humanmonocyte-derived dendritic cells. European Journal of Immunology. 2005;35(12):3468-77.

69. Elia AR, Cappello P, Puppo M, Fraone T, Vanni C, Eva A, et al. Human dendritic cells differentiated in hypoxia down-modulate antigen uptake and change their chemokine expression profile. J Leukoc Biol. 2008;84(6):1472-82.

70. Yang M, Ma C, Liu S, Sun J, Shao Q, Gao W, et al. Hypoxia skews dendritic cells to a T helper type 2-stimulating phenotype and promotes tumour cell migration by dendritic cell-derived osteopontin. Immunology. 2009;128(1 Suppl):e237-49.

71. Ricciardi A, Elia AR, Cappello P, Puppo M, Vanni C, Fardin P, et al. Transcriptome of hypoxic immature dendritic cells: modulation of chemokine/receptor expression. Mol Cancer Res. 2008;6(2):175-85.

72. Mancino A, Schioppa T, Larghi P, Pasqualini F, Nebuloni M, Chen IH, et al. Divergent effects of hypoxia on dendritic cell functions. Blood. 2008;112(9):3723-34.

73. Jantsch J, Chakravortty D, Turza N, Prechtel AT, Buchholz B, Gerlach RG, et al. Hypoxia and Hypoxia-Inducible Factor-1 Modulate Lipopolysaccharide-Induced Dendritic Cell Activation and Function. The Journal of Immunology. 2008;180(7):4697-705.

74. Taylor CT, Colgan SP. Regulation of immunity and inflammation by hypoxia in immunological niches. Nature Reviews Immunology. 2017;17(12):774-85.

75. Policastro LL, Ibañez IL, Notcovich C, Duran HA, Podhajcer OL. The Tumor Microenvironment: Characterization, Redox Considerations, and Novel Approaches for Reactive Oxygen Species-Targeted Gene Therapy. Antioxidants & Redox Signaling. 2013;19(8):854-95.

76. Paardekooper LM, Vos W, van den Bogaart G. Oxygen in the tumor microenvironment: effects on dendritic cell function. Oncotarget. 2019;10(8):883-96.

77. Nicholas DA, Zhang K, Hung C, Glasgow S, Aruni AW, Unternaehrer J, et al. Palmitic acid is a toll-like receptor 4 ligand that induces human dendritic cell secretion of IL-1beta. PLoS One. 2017;12(5):e0176793.

78. Lu H, Yao K, Huang D, Sun A, Zou Y, Qian J, et al. High glucose induces upregulation of scavenger receptors and promotes maturation of dendritic cells. Cardiovasc Diabetol. 2013;12(80).

79. Oberkampf M, Guillerey C, Mouries J, Rosenbaum P, Fayolle C, Bobard A, et al. Mitochondrial reactive oxygen species regulate the induction of CD8(+) T cells by plasmacytoid dendritic cells. Nat Commun. 2018;9(1):2241.

80. Chougnet CA, Thacker RI, Shehata HM, Hennies CM, Lehn MA, Lages CS, et al. Loss of Phagocytic and Antigen Cross-Presenting Capacity in Aging Dendritic Cells Is Associated with Mitochondrial Dysfunction. J Immunol. 2015;195(6):2624-32.

81. Rutault K, Alderman C, Chain BM, Katz DR. Reactive Oxygen Species Activate Human Peripheral Blood Dendritic Cells. Free Radic Biol Med. 1999;26(1-2):232-8.

82. Gotz A, Ty MC, Rodriguez A. Oxidative Stress Enhances Dendritic Cell Responses to Plasmodium falciparum. Immunohorizons. 2019;3(11):511-8.

83. Cubillos-Ruiz JR, Silberman PC, Rutkowski MR, Chopra S, Perales-Puchalt A, Song M, et al. ER Stress Sensor XBP1 Controls Anti-tumor Immunity by Disrupting Dendritic Cell Homeostasis. Cell. 2015;161(7):1527-38.

84. Gottfried E, Kunz-Schughart LA, Ebner S, Mueller-Klieser W, Hoves S, Andreesen R, et al. Tumor-derived lactic acid modulates dendritic cell activation and antigen expression. Blood. 2006;107(5):2013-21.

85. Nasi A, Fekete T, Krishnamurthy A, Snowden S, Rajnavolgyi E, Catrina AI, et al. Dendritic cell reprogramming by endogenously produced lactic acid. J Immunol. 2013;191(6):3090-9.

86. Selleri S, Bifsha P, Civini S, Pacelli C, Dieng MM, Lemieux W, et al. Human mesenchymal stromal cell-secreted lactate induces M2macrophage differentiation by metabolic reprogramming. Oncotarget. 2016;7(21):30193-210.

87. Puig-Kroger A, Pello OM, Muniz-Pello O, Selgas R, Criado G, Bajo MA, et al. Peritoneal dialysis solutions inhibit the differentiation and maturation of human monocyte-derived dendritic cells: effect of lactate and glucose-degradation products. J Leukoc Biol. 2003;73(4):482-92.

88. Brown TP, Bhattacharjee P, Ramachandran S, Sivaprakasam S, Ristic B, Sikder MOF, et al. The lactate receptor GPR81 promotes breast cancer growth via a paracrine mechanism involving antigen-presenting cells in the tumor microenvironment. Oncogene. 2020;39(16):3292-304.

89. Zhang D, Tang Z, Huang H, Zhou G, Cui C, Weng Y, et al. Metabolic regulation of gene expression by histone lactylation. Nature. 2019;574(7779):575-80.

90. Allard B, Longhi MS, Robson SC, Stagg J. The ectonucleotidases CD39 and CD73: Novel checkpoint inhibitor targets. Immunol Rev. 2017;276(1):121-44.

91. Sáez PJ, P V, Shoji KF, Harcha PA, Lennon-Duménil AM, Sáez JC. ATP promotes the fast migration of dendritic cells through the activity of pannexin 1 channels and P2X7 receptors. Sci Signal. 2017;10(506).

92. Di Virgilio F, Sarti AC, Falzoni S, De Marchi E, Adinolfi E. Extracellular ATP and P2 purinergic signalling in the tumour microenvironment. Nat Rev Cancer. 2018;18(10):601-18.

93. Aymeric L, Apetoh L, Ghiringhelli F, Tesniere A, Martins I, Kroemer G, et al. Tumor cell death and ATP release prime dendritic cells and efficient anticancer immunity. Cancer Res. 2010;70(3):855-8.

94. Ghiringhelli F, Apetoh L, Tesniere A, Aymeric L, Ma Y, Ortiz C, et al. Activation of the NLRP3 inflammasome in dendritic cells induces IL-1beta-dependent adaptive immunity against tumors. Nat Med. 2009;15(10):1170-8.

95. Lecciso M, Ocadlikova D, Sangaletti S, Trabanelli S, De Marchi E, Orioli E, et al. ATP Release from Chemotherapy-Treated Dying Leukemia Cells Elicits an Immune Suppressive Effect by Increasing Regulatory T Cells and Tolerogenic Dendritic Cells. Front Immunol. 2017;8:1918.

96. Blay J, White TD, Hoskin DW. The Extracellular Fluid of Solid Carcinomas Contains Immunosuppressive Concentrations of Adenosine. Cancer Res. 1997;57(13):2602-5.

97. Longhi MS, Robson SC, Bernstein SH, Serra S, Deaglio S. Biological functions of ecto-enzymes in regulating extracellular adenosine levels in neoplastic and inflammatory disease states. J Mol Med (Berl). 2013;91(2):165-72.

98. Cekic C, Linden J. Purinergic regulation of the immune system. Nat Rev Immunol. 2016;16(3):177-92.

99. Wennerberg E, Spada S, Rudqvist NP, Lhuillier C, Gruber S, Chen Q, et al. CD73 Blockade Promotes Dendritic Cell Infiltration of Irradiated Tumors and Tumor Rejection. Cancer Immunol Res. 2020;8(4):465-78.

100. Chen S, Akdemir I, Fan J, Linden J, Zhang B, Cekic C. The Expression of Adenosine A2B Receptor on Antigen Presenting Cells Suppresses CD8+ T cell Responses and Promotes Tumor Growth. Cancer Immunol Res. 2020.

101. Kayhan M, Koyas A, Akdemir I, Savas AC, Cekic C. Adenosine Receptor Signaling Targets Both PKA and Epac Pathways to Polarize Dendritic Cells to a Suppressive Phenotype. J Immunol. 2019;203(12):3247-55.

102. Silva-Vilches C, Ring S, Mahnke K. ATP and Its Metabolite Adenosine as Regulators of Dendritic Cell Activity. Front Immunol. 2018;9:2581.

103. Bunse L, Pusch S, Bunse T, Sahm F, Sanghvi K, Friedrich M, et al. Suppression of antitumor T cell immunity by the oncometabolite (R)-2-hydroxyglutarate. Nat Med. 2018;24(8):1192-203.

104. Bottcher M, Renner K, Berger R, Mentz K, Thomas S, Cardenas-Conejo ZE, et al. D-2-hydroxyglutarate interferes with HIF-1alpha stability skewing T-cell metabolism towards oxidative phosphorylation and impairing Th17 polarization. Oncoimmunology. 2018;7(7):e1445454.

105. Ugele I, Cárdenas-Conejo Z, Hammon K, Wehrstein M, Bruss C, Peter K, et al. D-2-Hydroxyglutarate and L-2-Hydroxyglutarate Inhibit IL-12 Secretion by Human Monocyte-Derived Dendritic Cells. International Journal of Molecular Sciences. 2019;20(3).

106. Ma Q, Li Y, Wang M, Tang Z, Wang T, Liu C, et al. Progress in Metabonomics of Type 2 Diabetes Mellitus. Molecules. 2018;23(7).

107. Boden G. Obesity and free fatty acids. Endocrinol Metab Clin North Am. 2008;37(3):635-46.

108. Hosogai N, Fukuhara A, Oshima K, Miyata Y, Tanaka S, Segawa K, et al. Adipose tissue hypoxia in obesity and its impact on adipocytokine dysregulation. Diabetes. 2007;56(4):901-11.

109. Giacco F, Brownlee M. Oxidative stress and diabetic complications. Circ Res. 2010;107(9):1058-70.

110. Ferrante AW, Jr. The immune cells in adipose tissue. Diabetes Obes Metab. 2013;15 Suppl 3:34-8.

111. Xu H, Barnes GT, Yang Q, Tan G, Yang D, Chou CJ, et al. Chronic inflammation in fat plays a crucial role in the development of obesity-related insulin resistance. J Clin Invest. 2003;112(12):1821-30.

112. Coope A, Torsoni AS, Velloso LA. Metabolic and inflammatory pathways on the pathogenesis of type 2 diabetes. Eur J Endocrinol. 2016;174(5):R175-87.

113. Patsouris D, Li PP, Thapar D, Chapman J, Olefsky JM, Neels JG. Ablation of CD11c-positive cells normalizes insulin sensitivity in obese insulin resistant animals. Cell Metab. 2008;8(4):301-9.

114. Bertola A, Ciucci T, Rousseau D, Bourlier V, Duffaut C, Bonnafous S, et al. Identification of adipose tissue dendritic cells correlated with obesity-associated insulin-resistance and inducing Th17 responses in mice and patients. Diabetes. 2012;61(9):2238-47.

115. Mraz M, Cinkajzlova A, Klouckova J, Lacinova Z, Kratochvilova H, Lips M, et al. Dendritic Cells in Subcutaneous and Epicardial Adipose Tissue of Subjects with Type 2 Diabetes, Obesity, and Coronary Artery Disease. Mediators Inflamm. 2019;2019:5481725.

116. Stefanovic-Racic M, Yang X, Turner MS, Mantell BS, Stolz DB, Sumpter TL, et al. Dendritic Cells Promote Macrophage Infiltration and Comprise a Substantial Proportion of Obesity-Associated Increases in CD11c+ Cells in Adipose Tissue and Liver. Diabetes. 2012;61(9):2330-9.

117. Chen Y, Tian J, Tian X, Tang X, Rui K, Tong J, et al. Adipose tissue dendritic cells enhances inflammation by prompting the generation of Th17 cells. PLoS One. 2014;9(3):e92450.

118. Abdel-Moneim A, Bakery HH, Allam G. The potential pathogenic role of IL-17/Th17 cells in both type 1 and type 2 diabetes mellitus. Biomed Pharmacother. 2018;101:287-92.

119. Musilli C, Paccosi S, Pala L, Gerlini G, Ledda F, Mugelli A, et al. Characterization of circulating and monocyte-derived dendritic cells in obese and diabetic patients. Molecular Immunology. 2011;49(1-2):234-8.

120. Vuckovic S, Withers G, Harris M, Khalil D, Gardiner D, Flesch I, et al. Decreased blood dendritic cell counts in type 1 diabetic children. Clin Immunol. 2007;123(3):281-8.

121. Seifarth CC, Hinkmann C, Hahn EG, Lohmann T, Harsch IA. Reduced frequency of peripheral dendritic cells in type 2 diabetes. Exp Clin Endocrinol Diabetes. 2008;116(3):162-6.

122. Blank SE, Johnson EC, Weeks DK, Wysham CH. Circulating dendritic cell number and intracellular TNF-alpha production in women with type 2 diabetes. Acta Diabetol. 2012;49 (Suppl 1):25-32.

123. Peng R, Li Y, Brezner K, Litherland S, Clare-Salzler MJ. Abnormal Peripheral Blood Dendritic Cell Populations in Type 1 Diabetes. Ann N Y Acad Sci. 2003;1005(1):222-25.

124. Nam HW, Cho YJ, Lim JA, Kim SJ, Kim H, Sim SY, et al. Functional status of immune cells in patients with long-lasting type 2 diabetes mellitus. Clin Exp Immunol. 2018;194(1):125-36.

125. Loomans CJ, van Haperen R, Duijs JM, Verseyden C, de Crom R, Leenen PJ, et al. Differentiation of bone marrow-derived endothelial progenitor cells is shifted into a proinflammatory phenotype by hyperglycemia. Mol Med. 2009;15(5-6):152-9.

126. Bettelli E, Carrier Y, Gao W, Korn T, Strom TB, Oukka M, et al. Reciprocal developmental pathways for the generation of pathogenic effector TH17 and regulatory T cells. Nature. 2006;441(7090):235-8.

127. Danova K, Grohova A, Strnadova P, Funda DP, Sumnik Z, Lebl J, et al. Tolerogenic Dendritic Cells from Poorly Compensated Type 1 Diabetes Patients Have Decreased Ability To Induce Stable Antigen-Specific T Cell Hyporesponsiveness and Generation of Suppressive Regulatory T Cells. J Immunol. 2017;198(2):729-40.

128. Gilardini Montani MS, Granato M, Cuomo L, Valia S, Di Renzo L, D'Orazi G, et al. High glucose and hyperglycemic sera from type 2 diabetic patients impair DC differentiation by inducing ROS and activating Wnt/beta-catenin and p38 MAPK. Biochim Biophys Acta. 2016;1862(4):805-13.

129. Macdougall CE, Wood EG, Loschko J, Scagliotti V, Cassidy FC, Robinson ME, et al. Visceral Adipose Tissue Immune Homeostasis Is Regulated by the Crosstalk between Adipocytes and Dendritic Cell Subsets. Cell Metab. 2018;27(3):588-601.

130. Oderup C, LaJevic M, Butcher EC. Canonical and Noncanonical Wnt Proteins Program Dendritic Cell Responses for Tolerance. The Journal of Immunology. 2013;190(12):6126-34.

131. Cirone M, Di Renzo L, Trivedi P, Lucania G, Borgia G, Frati L, et al. Dendritic Cell Differentiation Blocked by Primary Effusion Lymphoma-Released Factors is Partially Restored by Inhibition of P38 MAPK. International Journal of Immunopathology and Pharmacology. 2010;23(4):1079-86.

132. Delarue J, Magnan C. Free fatty acids and insulin resistance. Curr Opin Clin Nutr Metab Care. 2007;10(2):142-8.

133. Weatherill AR, Lee JY, Zhao L, Lemay DG, Youn HS, Hwang DH. Saturated and polyunsaturated fatty acids reciprocally modulate dendritic cell functions mediated through TLR4. J Immunol. 2005;174(9):5390-7.

134. Fritsche KL. The science of fatty acids and inflammation. Adv Nutr. 2015;6(3):293S-301S.

135. Staiger H, Staiger K, Stefan N, Wahl HG, Machicao F, Kellerer M, et al. Palmitate-Induced Interleukin-6 Expression in Human Coronary Artery Endothelial Cells. Diabetes. 2004;53(12):3209-16.

136. Palomer X, Pizarro-Delgado J, Barroso E, Vazquez-Carrera M. Palmitic and Oleic Acid: The Yin and Yang of Fatty Acids in Type 2 Diabetes Mellitus. Trends Endocrinol Metab. 2018;29(3):178-90.

137. Stelzner K, Herbert D, Popkova Y, Lorz A, Schiller J, Gericke M, et al. Free fatty acids sensitize dendritic cells to amplify TH1/TH17-immune responses. Eur J Immunol. 2016;46(8):2043-53.

138. Lancaster GI, Langley KG, Berglund NA, Kammoun HL, Reibe S, Estevez E, et al. Evidence that TLR4 Is Not a Receptor for Saturated Fatty Acids but Mediates Lipid-Induced Inflammation by Reprogramming Macrophage Metabolism. Cell Metab. 2018;27(5):1096-110 e5.

139. Reynolds CM, McGillicuddy FC, Harford KA, Finucane OM, Mills KH, Roche HM. Dietary saturated fatty acids prime the NLRP3 inflammasome via TLR4 in dendritic cells-implications for diet-induced insulin resistance. Mol Nutr Food Res. 2012;56(8):1212-22.

140. Miyake T, Akbar SMF, Yoshida O, Chen S, Hiasa Y, Matsuura B, et al. Impaired dendritic cell functions disrupt antigen-specific adaptive immune responses in mice with nonalcoholic fatty liver disease. Journal of Gastroenterology. 2010;45(8):859-67.

141. Wang H, Hao Q, Li QR, Yan XW, Ye S, Li YS, et al. Omega-3 polyunsaturated fatty acids affect lipopolysaccharide-induced maturation of dendritic cells through mitogen-activated protein kinases p38. Nutrition. 2007;23(6):474-82.

142. Zeng J, Zhang Y, Hao J, Sun Y, Liu S, Bernlohr DA, et al. Stearic Acid Induces CD11c Expression in Proinflammatory Macrophages via Epidermal Fatty Acid Binding Protein. J Immunol. 2018;200(10):3407-19.

143. Karasawa T, Kawashima A, Usui-Kawanishi F, Watanabe S, Kimura H, Kamata R, et al. Saturated Fatty Acids Undergo Intracellular Crystallization and Activate the NLRP3 Inflammasome in Macrophages. Arterioscler Thromb Vasc Biol. 2018;38(4):744-56.

144. Carlsson JA, Wold AE, Sandberg AS, Ostman SM. The Polyunsaturated Fatty Acids Arachidonic Acid and Docosahexaenoic Acid Induce Mouse Dendritic Cells Maturation but Reduce T-Cell Responses In Vitro. PLoS One. 2015;10(11):e0143741.

145. Zeyda M, Saemann MD, Stuhlmeier KM, Mascher DG, Nowotny PN, Zlabinger GJ, et al. Polyunsaturated fatty acids block dendritic cell activation and function independently of NF-kappaB activation. J Biol Chem. 2005;280(14):14293-301.

146. Enos RT, Davis JM, Velazquez KT, McClellan JL, Day SD, Carnevale KA, et al. Influence of dietary saturated fat content on adiposity, macrophage behavior, inflammation, and metabolism: composition matters. J Lipid Res. 2013;54(1):152-63.

147. Telle-Hansen VH, Gaundal L, Myhrstad MCW. Polyunsaturated Fatty Acids and Glycemic Control in Type 2 Diabetes. Nutrients. 2019;11(5).

148. Giovannucci E, Harlan DM, Archer MC, Bergenstal RM, Gapstur SM, Habel LA, et al. Diabetes and cancer: a consensus report. Diabetes Care. 2010;33(7):1674-85.

149. Casqueiro J, Casqueiro J, Alves C. Infections in patients with diabetes mellitus: A review of pathogenesis. Indian J Endocrinol Metab. 2012;16 Suppl 1:S27-36.

150. Norling LV, Ly L, Dalli J. Resolving inflammation by using nutrition therapy: roles for specialized proresolving mediators. Curr Opin Clin Nutr Metab Care. 2017;20(2):145-52.

151. Sainsbury E, Kizirian NV, Partridge SR, Gill T, Colagiuri S, Gibson AA. Effect of dietary carbohydrate restriction on glycemic control in adults with diabetes: A systematic review and meta-analysis. Diabetes Res Clin Pract. 2018;139:239-52.

152. Jonasson L, Guldbrand H, Lundberg AK, Nystrom FH. Advice to follow a low-carbohydrate diet has a favourable impact on low-grade inflammation in type 2 diabetes compared with advice to follow a low-fat diet. Ann Med. 2014;46(3):182-7.

153. Vitale M, Masulli M, Rivellese AA, Babini AC, Boemi M, Bonora E, et al. Influence of dietary fat and carbohydrates proportions on plasma lipids, glucose control and low-grade inflammation in patients with type 2 diabetes-The TOSCA.IT Study. Eur J Nutr. 2016;55(4):1645-51.

154. O'Neill LA, Hardie DG. Metabolism of inflammation limited by AMPK and pseudo-starvation. Nature. 2013;493(7432):346-55.

155. Wegiel B, Vuerich M, Daneshmandi S, Seth P. Metabolic Switch in the Tumor Microenvironment Determines Immune Responses to Anti-cancer Therapy. Front Oncol. 2018;8:284.

156. Yao T, Asayama Y. Animal-cell culture media: History, characteristics, and current issues. Reprod Med Biol. 2017;16(2):99-117.

157. McKee TJ, Komarova SV. Is it time to reinvent basic cell culture medium? Am J Physiol Cell Physiol. 2017;312(5):C624-C6.

158. Cantor JR, Abu-Remaileh M, Kanarek N, Freinkman E, Gao X, Louissaint A, Jr., et al. Physiologic Medium Rewires Cellular Metabolism and Reveals Uric Acid as an Endogenous Inhibitor of UMP Synthase. Cell. 2017;169(2):258-72 e17.

159. Vande Voorde J, Ackermann T, Pfetzer N, Sumpton D, Mackay G, Kalna G, et al. Improving the metabolic fidelity of cancer models with a physiological cell culture medium. Sci Adv. 2019;5(1).

160. Leney-Greene MA, Boddapati AK, Su HC, Cantor JR, Lenardo MJ. Human Plasma-like Medium Improves T Lymphocyte Activation. iScience. 2020;23(1):100759.


AMPK

3

Characterization of Dendritic Cell Metabolism by Flow Cytometry

Eline C. Brombacher[1]*, Thiago A. Patente[1]*, Marjolein Quik[1], Bart Everts[1]

* Shared first authorship

[1]Department of Parasitology, Leiden University Medical Center, Leiden, The Netherlands

Methods in Molecular Biology
DOI: 10.1007/978-1-0716-2938-3_16

Abstract

In response to different stimuli dendritic cells (DCs) undergo metabolic reprogramming to support their function. Here we describe how fluorescent dyes and antibody-based approaches can be used to assess various metabolic parameters of DCs including glycolysis, lipid metabolism, mitochondrial activity and the activity of important sensors and regulators of cellular metabolism, mTOR and AMPK. These assays can be performed using standard flow cytometry and will allow for determination of metabolic properties of DC populations at single cell level and to characterize metabolic heterogeneity within them.

1 Introduction

Dendritic cells (DCs) play a key role in orchestration of pro-inflammatory as well as regulatory T cell responses. Classically, DCs undergo an activation program upon sensing of pathogen- or host-derived signals that endow them with the capacity to prime and polarize T cell responses. In recent years, it has become clear that DC activation is accompanied with, and supported by reprogramming of their cellular metabolism, and that their ability to drive different T cell responses is underpinned by distinct metabolic pathways (1, 2). Hence metabolic characterization of DCs provides valuable information about their biology and function in the context of different immune responses. Metabolomics and flux analysis are commonly used methods to assess metabolic properties of immune cells. These techniques generally require high cell numbers as input, which makes their use for metabolic profiling of scarce cell populations, such as DCs, problematic. Moreover, in such approaches information about metabolic heterogeneity within cell populations is lost. This protocol describes how metabolic properties, specifically those related to nutrient uptake, mitochondrial function and activity of key regulators and sensors of cellular metabolism, mTOR and AMPK, can be assessed at single cell level in primary and *in vitro*-cultured DCs using commercially available antibodies, fluorescent dyes and standard flow cytometry.

One of the central regulators of cellular metabolism is AMP-activated protein kinase (AMPK), which is activated in nutrient-poor conditions (1). AMPK controls activity of various metabolic pathways to inhibit anabolism and to promote catabolism. Another crucial metabolic kinase is mammalian target of rapamycin (mTOR), which opposes the functions of AMPK, as it is active in nutrient-rich conditions and drives metabolic processes associated with biosynthesis (1). A commonly used method to study activity of kinases involves assessing phosphorylation status of downstream targets. Here, we provide a flow cytometry protocol for the staining of phosphorylated proteins acetyl-CoA carboxylase (ACC) and S6, as markers for AMPK and mTOR activity, respectively.

Two major nutrient sources for cells are glucose and fatty acids. A shift towards glucose metabolism is commonly observed upon immunogenic DC activation (3), while rewiring of lipid metabolism is associated with tolerogenic DC function (4). The fluorescently labelled glucose-analog 2-(N-(7-Nitrobenz-2-oxa-1,3-diazol4-yl)Amino)-2-Deoxyglucose (2-NBDG) can be used to measure glucose uptake in live cells, while BODIPY™ lipid probes allow for characterization of fatty acid uptake and intracellular lipid accumulation (5, 6). We describe a flow-cytometry based protocol that is applicable for, but not restricted to, staining with 2-NBDG, BODIPY4,4-Difluoro-5,7-Dimethyl-4-Bora-3a,4a-Diaza-s-Indacene-3-Hexadecanoic Acid (BODIPY™ FL C_{16}) and 4,4-Difluoro-1,3,5,7,8-Pentamethyl-4-Bora-3a,4a-Diaza-s-Indacene (BODIPY™ 493/505) to characterize glucose uptake, fatty acid uptake and lipid accumulation, respectively, in live DCs.

Mitochondria serve as central metabolic hubs in cells, including DCs, through citric acid cycle activity, oxidative phosphorylation for ATP production and reactive oxygen species (ROS) production (2). Several fluorescent dyes allow for easy analysis of various mitochondrial parameters. Mitochondrial mass, a measure of overall mitochondrial content in a cell, can be determined through the use of various MitoTracker dyes, which are commercially available in different fluorescence spectra (7). Mitochondrial membrane potential ($\Delta\Psi_m$), the driving force of mitochondrial ATP production and as such an important measure of cellular metabolism, can be stained for with tetramethyl rhodamine methyl (TMRM) (8, 9). Mitochondrial ROS

(mtROS), which are by-products of oxidative phosphorylation, and total cellular ROS production, can be analyzed through the dye MitoSOX™ Red, which fluoresces proportional to mtROS production, and CM-H_2DCFDA, respectively (9-11).

Procedural steps for aforementioned stainings are described below to provide a framework for metabolic characterization of *in vitro*-cultured and primary human and murine DCs by standard flow cytometry as well as options to combine multiple dyes using advanced spectral flow cytometry.

2 Materials

2.1 Cellular systems

This protocol provides detailed information for measurements in primary murine splenic DCs, human blood-derived DCs and *in vitro* cultured DC populations, including murine bone-marrow derived DCs (BMDCs) and human monocyte-derived DCs (moDCs), but may also be applicable to other cell types.

2.2 Flow cytometry reagents and equipment

1. Phosphate buffered saline (PBS).
2. FACS buffer: 1% bovine serum albumin (BSA) in PBS.
3. Lineage-defining antibodies (Table 3-6).
4. αCD16/αCD32 (Fc-Block).
5. Viability dye (see **Note 1**).
6. 96-well V-bottom plate.
7. FACS tubes.
8. Flow cytometer equipped with lasers and emission filters suitable for the analysis of cells stained with the antibodies and dyes listed in the antibody panel (Table 3-7).

2.3 Intracellular staining for metabolic phosphorylated proteins

1. 16% formaldehyde, methanol free, Ultra Pure.
2. Formaldehyde, stabilized with methanol.
3. 100% methanol, stored at -20 °C.
4. 10x eBioscience™ Permeabilization Buffer (Perm buffer).
5. Conjugated antibody or primary and secondary antibodies (Table 2).
6. Complete RPMI: RPMI 1640 Medium GlutaMAX, 10 % fetal calf serum (FCS), 100 IU/ml penicillin, 100 µg/ml streptomycin, and 50 µM 2-mercaptoethanol.
7. 24-well cell culture plate.
8. 96-well flat-bottom plate.
9. 1 mL syringe.
10. 5 ml FACS tubes.

2.4 Metabolic dyes

1. Metabolic dyes (Table 7).

3 Methods

Throughout the protocol, centrifugation is set at 300 x *g* for 4 minutes at 4°C, unless stated otherwise.

3.1 Intracellular staining of phosphorylated metabolic proteins

This protocol describes in detail the staining procedure of phosphorylated ACC and S6, as a direct reflection of AMPK and mTOR activity, respectively. This protocol can be applied to other intracellular and/or phosphorylated proteins as well (*see* **Note 2**).

In brief, the general procedure for intracellular staining for phosphorylated metabolic proteins consists of the following steps:

1. Fixation of cells
    - Phosphorylation is generally an unstable post-translational modification and therefore it is recommended to fix cells prior to any processing (*see* **Note 3**). Live and dead cells can be distinguished by strict gating in the FSC-A vs SSC-A plot (Figure 1A).
    - The fixation protocol is divided in 3 parts: (1) procedure for direct fixation of DCs in in tissues prior to their isolation; (2) fixation procedure of tissue- and blood-derived DCs after their isolation from tissues; (3) fixation procedure for *in vitro*-cultured DCs.
2. Permeabilization of cells.
3. Staining with primary antibody (see Note 4).
4. Staining with secondary antibody.
5. Cell acquisition on flow cytometer.

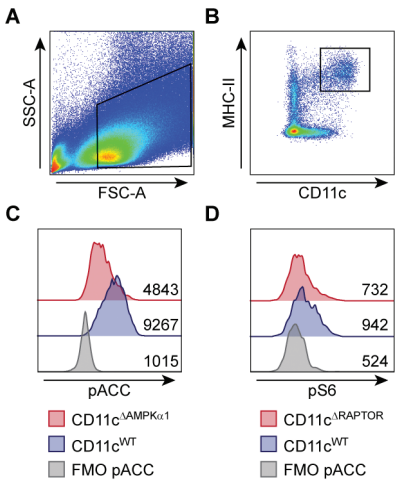

Figure 1: pACC and pS6 staining in murine tissue-derived DCs. (A) Strict gating of the FSC-A is required to remove death cells in a sample without viability staining. **(B)** pACC and pS6 data is shown from MHC-II^{+}CD11c^{+} splenic DCs. The signal of **(C)** pACC and **(D)** pS6 are lost in CD11c$^{\Delta AMPK\alpha1}$ and CD11c$^{\Delta raptor}$ mice, respectively.

3.1.1 Fixation

3.1.1.1 Fixation prior to tissue processing

1. Add 500 µL of 2% formaldehyde/PBS to a 24-wells plate, 1 well per tissue.
2. transfer tissue of interest to 2% formaldehyde/PBS (*see* **Note 5**).
3. Immediately smash the tissue with the back of a 1 mL syringe.
4. Fix the cells for 30 minutes at room temperature (RT).
5. Add 500 µL of RPMI (no additives) to the wells to lower the concentration of the fixative. Continue with the next step if all tissues have been in fixative for at least 30 minutes.
6. Centrifuge the 24-wells plate.
7. Transfer as much supernatant as possible, without transferring pieces of tissue, to a sterile 5 mL FACS tube.
8. Add 1 mL of RPMI (no additives) to the wells of the 24-wells plate and spin down the plate.
9. Repeat step 7-8.
10. After the second centrifugation of the plate, remove supernatant from the well as in step 7 and spin down the 5 ml FACS tubes. In the meantime, add 350 µL of RPMI (no additives) to the wells
11. After centrifugation, remove the supernatant from the tubes by decantation.
12. Resuspend the pellet (may not be visible) in the remaining +/- 150 µL of medium and transfer this solution back to the 24 well plate containing 350 µL of medium.
13. The wells containing the tissues should be now in a total of 500 µL of medium.
14. Process the tissues using your standard protocol to generate single cell suspensions (*see* **Note 6**).
15. After generation of single cell suspensions, store cells in 200 µL FACS buffer at 4 °C for a maximum of 1 week. Continue with step 3.1.2.

3.1.1.2 Fixation of single cell suspensions after tissue or blood processing

1. Process tissues or blood according to your standard protocol to obtain single cell suspensions or PBMCs, respectively.
2. Plate the desired number of isolated cells (Table 2) in a 96-wells V-bottom plate.
3. Fill the wells to 200 µL with PBS.
4. Centrifuge the plate and remove supernatant by flicking.
5. Repeat step 3-4.
6. Stain cells with a viability stain of your choice (*see* **Note 7**).
7. Repeat step 3-4.
8. Add 200 µL of complete medium.
9. Incubate the cells for 1-2 hours at 37 °C (*see* **Note 8**).
10. Take the plate out of the incubator and immediately add 65 µL of 16% ultra-pure methanol free formaldehyde, to reach a final concentration of 4% (*see* **Note 9** and **Note 10**).
11. Fix cells for 15 minutes at RT (*see* **Note 11**).
12. Repeat step 3-4 twice, but use FACS buffer instead of PBS.
13. Store cells in 200 µL FACS buffer at 4 °C for a maximum of 1 week. Continue with step 3.1.2.

3.1.1.3 Fixation of in vitro-cultured DCs

1. Plate the desired number of cells (Table 2) in complete RPMI in a 96-well flat bottom plate. Include wells for the controls: a staining with the secondary antibody only and an unstained sample.
2. Fill the wells to 200 µL with complete RPMI and stimulate cells with your compound of interest.
3. Take the plate out of the incubator and immediately add 65 µL of 16% ultra-pure methanol free formaldehyde, to reach a final concentration of 4% and resuspend.
4. Fix cells for 15 minutes at RT.
5. Put the plate on ice and carefully loosen the adherent cells by scraping with 200 µL pipet tips.
6. Transfer cells to a V-bottom plate.
7. Centrifuge the plate.
8. Discard supernatant by flicking the plate.
9. Add 200 µL FACS buffer.
10. Repeat steps 7-9 twice.
11. Store plate at 4 °C for a maximum of 1 week. Continue with step 3.1.2.

3.1.2 Staining procedure

1. Centrifuge the plate and remove supernatant by flicking.
2. Add 200 µL of 1x eBioscience permeabilization buffer to each well.
3. Centrifuge the plate and remove supernatant by flicking.
4. Repeat steps 2-3.
5. Resuspend cells in 100 µL of 100% methanol for further permeabilization (*see* **Note 12**).
6. Incubate for 20 minutes at -20 °C.
7. Repeat steps 2-3 twice.
8. Resuspend cells in 20 µL of 1x eBioscience permeabilization buffer containing the primary antibody and Fc-Block (αCD16/αCD32) (*see* Table 1).
9. Incubate for 30 minutes at 4 °C.
10. Repeat steps 2-3.
11. Resuspend cells in 30 µL of 1x eBioscience permeabilization buffer containing the secondary antibody and the desired antibody cocktail mix (*see* **Note 13** and Table 3-6).
12. Incubate for 30 minutes at 4 °C.
13. Fill wells up to 200 µL with FACS buffer.
14. Centrifuge the plate and remove supernatant by flicking.
15. Resuspend cells in the appropriate volume of FACS buffer to be acquired in a flow cytometer. A representative example of pACC and pS6 staining is shown in Figure 1.

3.2 Glucose and Lipid Metabolism

Various fluorescent dyes are available to evaluate nutrient uptake and accumulation using flow cytometry. Here, we provide a protocol for assessing glucose uptake (2-NBDG), cellular neutral lipid droplet content (BODIPY™ 493/505) and uptake of long-chain fatty acids (BODIPY™ FL C_{16}).

Table 1: Antibodies used for staining of intracellular (phosphorylated) proteins.

Target	Source	Identifier	Control	Reference for control
Phospho-Acetyl-CoA Carboxylase (Ser79)	Cell Signaling	11818	Metformin	(19)
Phospho-S6 (Ser240) - PE	BD Biosciences	560430	LPS	(20)
Goat anti-Rabbit AF647	ThermoFisher	A-21244	-	-

3.2.1 Staining procedure

1. Plate the desired number of live cells (Table 2) in complete RPMI in 96-wells V bottom plate. Include wells for the controls treated with 2-DG (in case of 2-NBDG, *see* **Note 14**) or incubated in PBS containing 10% FCS (in case of BODIPY™ FL C_{16} and BODIPY™ 493/505, *see* **Note15**)
2. Fill wells with PBS to up to 200 µL.
3. Spin down and remove supernatant.
4. Repeat steps 2-3.
5. Stain cells with the viability dye of your choice and Fc-Block (αCD16/αCD32) in PBS.
6. Incubate cells for 15 minutes at RT.
7. Repeat steps 2-3.
8. Incubate cells with either 50 µM of 2-NBDG, 5 µM of BODIPY™ 493/505 dye or 10 µM BODIPY™ FL C_{16} (diluted in PBS) and incubate cells for 15 minutes at 37 °C in CO_2 incubator. (*see* **Note 16, Note 17, Note 18** and **Note 19**)
9. Add FACS buffer to wells to reach 200 µL.
10. Centrifuge the plate and remove supernatant.
11. Resuspend cells in 30 µL of FACS buffer containing antibody cocktail mix (*see* Table 3-6).
12. Incubate for 30 minutes at 4 °C.
13. Repeat steps 9-10.
14. Resuspend cells in the appropriate volume of FACS buffer to be acquired in a flow cytometer. See Table 7 for information on excitation and emission wavelengths for each dye. A representative example of 2-NBDG and BODIPY™ FL C_{16} staining in DCs is shown in Figure 2.

3.3 Mitochondrial Metabolism

Mitotracker and TMRM are dyes commonly used to measure mitochondrial mass and mitochondrial membrane potential, respectively (*see* **Note 20)**. Due to the positive charge of these probes, they can enter live, polarized mitochondria, but not depolarized mitochondria. While TMRM is a dye available only with a specific emission wavelength, different Mitotrackers are commercially available with fluorescence in different wavelengths (i.e. Mitotracker Green FM and Mitotracker Deep Red FM). The following protocol is optimized for Mitotracker Green FM, but can also be applied to the other available Mitotracker dyes (*see* **Note 21**).

3.3.1 Staining procedure

1. Plate the desired number of cells (Table 2) in complete RPMI in a 96-wells V bottom plate. Include one well for FCCP-treated cells as control (*see* **Note 22**).

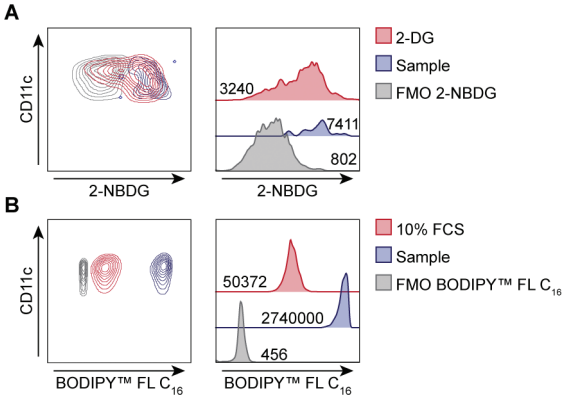

Figure 2: 2-NBDG and BODIPY™ FL C_{16} staining in murine tissue-derived MHCII$^+$CD11c$^+$ DCs. (A) 2-DG functions as a negative control for 2-NBDG staining. **(B)** 10% FCS can be used as a negative control for BODIPY™ FL C_{16} staining.

2. Fill wells up to 200 µL with complete RPMI.
3. Centrifuge the plate and remove supernatant.
4. Repeat steps 2-3.
5. Stain cells with the viability dye of your choice and Fc-Block (αCD16/αCD32) in PBS.
6. Incubate cells for 15 minutes at RT.
7. Repeat steps 2-3.
8. Incubate cells with 10 nM of TMRM and 20 nM of Mitrotracker Green FM for 15 minutes at 37 °C in complete RPMI.
9. Repeat steps 2-3.
10. Incubate control well with 50 µM of FCCP for 15 minutes at 37 °C in complete RPMI.
11. Centrifuge the plate and remove supernatant.
12. Fill wells up to 200 µL with FACS buffer.
13. Centrifuge the plate and remove supernatant.
14. Resuspend cells in 30 µL of FACS buffer containing antibody cocktail mix (*see* Table 3-6).
15. Incubate for 30 minutes at 4 °C.
16. Repeat steps 11-12.
17. Resuspend cells in the appropriate volume of FACS buffer to be acquired in a flow cytometer. See Table 7 for information on excitation and emission wavelengths for each dye. A representative example of Mitotracker Green FM and TMRM staining in DCs is shown in Figure 3.

3.4 ROS Staining

A variety of commercial kits and dyes are available to detect intracellular production of ROS via flow cytometry. Here we describe a staining procedure for CM-H_2DCFDA and MitoSOX™ Red for DCs, that detect total intracellular ROS and mitochondria-derived superoxide, respectively (*see* **Note 23**).

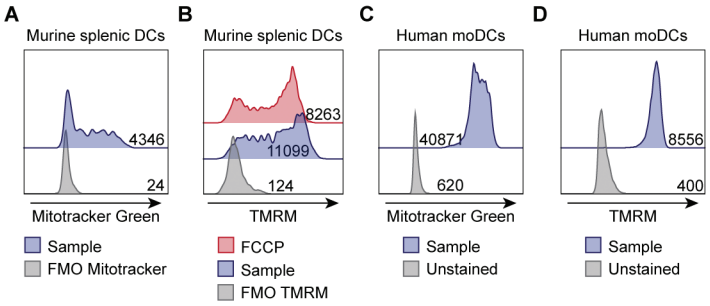

Figure 3: Mitotracker Green FM and TMRM staining. (A+B) Mitotracker Green FM and TMRM staining in murine tissue-derived DCs gives a heterogenous staining. Signal can be quantified using MFI or the frequency of positive cells. **(C+D)** Staining of moDCs, a homogenous population, with the same dyes, gives a single population. In these cells signal can be quantified using MFI.

3.4.1 Staining procedure

1. Plate the desired number of cells (Table 2) in complete RPMI in 96-wells V bottom plate. If desired plate 2 additional wells for positive (H_2O_2) and negative (N-acetyl cysteine (NAC)) control.
2. Fill wells up to 200 µL with complete RPMI.
3. Spin down and remove supernatant.
4. Repeat steps 2-3.
5. Incubate controls well with 0.03 % H_2O_2 or 1 µM of NAC for 1 hour at 37 °C in complete RPMI (*see* **Note 24**).
6. Repeat steps 2-3.
7. Stain cells with the viability dye of your choice and Fc-Block (αCD16/αCD32) in PBS.
8. Incubate cells for 15 minutes at RT.
9. Repeat steps 2-3.
10. Incubate cells with 5 µM of MitoSOX™ Red or 1 µM of CM-H_2DCFDA for 15 minutes at 37 °C in complete RPMI.
11. Fill wells up to 200 µL with FACS buffer.
12. Centrifuge the plate and remove supernatant.
13. Resuspend cells in 30 µL of FACS buffer containing antibody cocktail mix (*see* Table 3-6).
14. Incubate the cells for 30 minutes at 4 °C.
15. Repeat steps 11-12.
16. Resuspend the cells in the appropriate volume of FACS buffer to be acquired in a flow cytometer. See Table 7 for information on excitation and emission wavelengths for each dye. A representative example of MitoSOX™ Red and CM-H_2DCFDA staining in DCs is shown in Figure 4.

3.5 Metabolic panel tested on Cytek Spectral flow cytometer

Metabolic dyes can be measured with standard flow cytometers, but spectral overlap between a number of these dyes makes it difficult to design a panel in which multiple dyes are combined. However, with the Five-laser Cytek Aurora, a spectral flow cytometer, one can combine up to 4 dyes in one panel, namely 2-NBDG, BODIPY™ FL C_{16}, TMRM and Mitotracker Green FM.

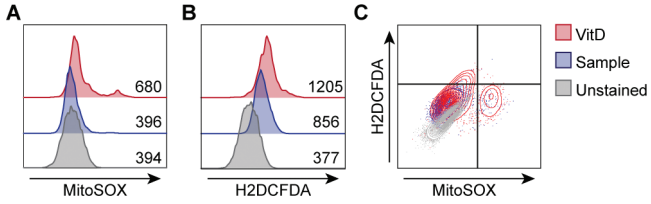

Figure 4: MitoSOX and H2DCFDA staining in *in vitro*-cultured human moDCs. Vitamin D (VitD) was used as positive control (18). **(A)** MtROS and **(B)** total ROS production are increased in VitD-treated DCs. **(C)** MtROS and total ROS can stained together and distinguished from each other. In these cells signal can be quantified using MFI.

Therefore, spectral flow cytometry allows for metabolic profiling using multiple metabolic dyes in parallel when the number of cells is limited, for example in the case of murine tissue-derived DCs (Figure 5).

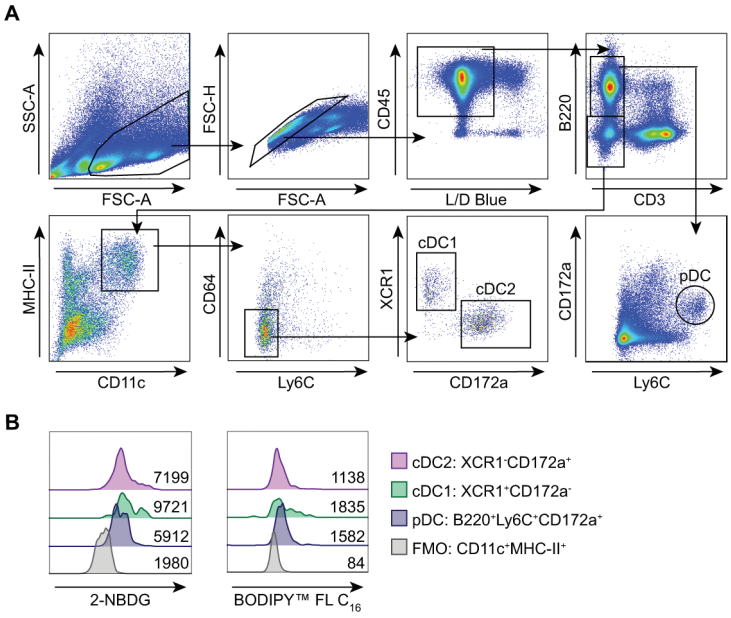

Figure 5: Mitochondrial dye staining using spectral flow cytometry. **(A)** Gating strategy to identify DC subsets in murine splenocytes. **(B)** cDC1s and cDC2s show differences in uptake of 2-NBDG and BODIPY™ FL C_{16}.

Table 2: Recommended number of cells to ensure a proper staining for identification of phosphorylated proteins and metabolic dyes in DCs.

Source of cells	Cells concentration	Minimum number of cells
Pure DC population (from *in vitro* DC cultures)	$1x10^6$/mL	50000
Mixed population (from tissues/PBMCs)	$10x10^6$/mL	1000000

Table 3: Lineage-defining antibodies required for identification of primary murine DC subsets.

Marker	Target population	Clone
CD3	T cells	17A2
B220	B cells/pDCs	RA3-6B2
Ly6C	Monocytes/pDCs	HK1.4
CD64	Macrophages	X54-5/7.1
CD11c	Monocytes/DCs	N418
MHC-II	Monocytes/DCs	M5/114.15.2
XCR1	cDC1	ZET
CD11b	cDC2	M1/70
CD172a	cDC2/pDCs	P84
Siglec-H	pDCs	551
CD16/32	FC-receptors	93

Table 4: Lineage-defining antibodies required for identification of primary human DC subsets.

Marker	Target population	Clone
CD3	T Cells	UCHT1
CD19	B Cells	HIB19
CD56	NK Cells	NCAM16.2
CD11c	Monocytes/DCs	Bu15
HLA-DR	Monocytes/DCs	L243
CD16	Monocytes	3G8
CD14	Monocytes	MΦP9
CD1c	cDC2	L161
CD141	cDC1	AD5-14H12
CD123	pDC	9F5
CD16/32	FC-receptors	polyclonal

Table 5: Lineage-defining antibodies for identification of human *in vitro*-cultured DC populations.

Marker	Clone
CD11c	h: Bu15
HLA-DR	h: L243/
CD14	MφP9
CD1a	HI149

Table 6: Lineage-defining antibodies for identification of mouse *in vitro*-cultured DC populations.

Marker	Clone	Differentiation Protocol
CD11c	N418	GM-CSF/FLT3L
MHC II	M5/114.15.2	GM-CSF/FTL3L
CD11b	M1/70	GM-CSF/FLT3L
CD115	AFS98	GMCSF
CD135	A2F10	GMCSF
CD24	M1/69	FLT3L
CD172a	P84	FTL3L
Siglec-H	551	FTL3L

Table 7: Metabolic dyes.

Dye	Source	Identifier	Concentration	Excitation	Emission
MitoTracker™ Deep Red FM	ThermoFisher	M22426	10 nM	540	595
MitoTracker™ Green FM	ThermoFisher	M7514	20 nM	490	516
TMRM	ThermoFisher	T668	20 nM	548	574
2-NBDG	ThermoFisher	N13195	50 µM	465	540
BODIPYTM FL C16	ThermoFisher	D3821	200 nM	488	508
BODIPYTM 493/503	ThermoFisher	D3922	5 µM	493	503
HCS LipidTOX™ Deep Red	ThermoFisher	H34477	1:200	644	665
MitoSOX™ Red	ThermoFisher	M36008	5 µM	510	580
H2DCFDA (H2-DCF, DCF)	ThermoFisher	D399	1 µM	492-495	517-527

4 Notes

1. Cells can be stained with the viability dye of your choice. We successfully tested LIVE/DEAD™ Fixable Aqua (1:400 dilution when performing experiments on a BD FACSCanto II, BD FACS LSR or BD FACS Fortessa X20 flow cytometer and 1:1000 dilution when performing experiments on a Cytek Aurora Spectral flow cytometer) and LIVE/DEAD™ Fixable Blue and Zombie NIR™ Fixable (both 1:1000 on a Cytek Aurora Spectral flow cytometer).
2. Not all unconjugated antibodies are suitable for flow cytometry. Make sure to have a proper positive and negative control to test if the staining is reliable.
3. To maintain the *in situ* phosphorylation status of the protein of interest it is recommended to fix tissues directly after harvesting. In our hands, this protocol works well for murine spleen, lymph nodes and tumors, but not for lamina propria of the murine small intestine. Furthermore, if a tissue is also used for experiments that require live cells, it is recommended to fix only part of the tissue.
4. If the antibody of interest is already conjugated to a fluorochrome (e.g. pS6-PE (Table 1)), this step can be skipped and the antibody can be included in the antibody cocktail together with lineage-defining antibodies.
5. This protocol is optimized for murine lymphoid tissues such as spleen and lymph nodes. In case of tissues other than spleen or lymph nodes, one can use the standard protocol implemented in your laboratory, replacing the solution normally used to collect the tissue of interest with 2% formaldehyde/PBS. Wash the fixative away with medium or PBS before digesting the tissue.
6. Fixing the samples prior to tissue processing might result in less efficient digestion of the tissues and, as a consequence, reduced number of cells. Digestion of spleen and lymph nodes using DNase I and Collagenase D is still effective when performed on fixed samples.
7. When processing tissue samples before fixing the cells, we recommend to stain the cells with a viability dye before resting the cells in the incubator. Not only the mechanic procedure to obtain the cells can lead to cell death, but the heterogeneity of cells makes it difficult to distinguish live and dead cells by size and complexity. On the other hand, *in vitro*-cultured DCs comprise a more homogenous population when analyzing the samples by size and complexity and the removal of dead cells based on these parameters can be performed easier. Additionally, the viability of *in vitro*-cultured DCs is normally high. However, if working with additional treatments that affect viability DCs, we recommend to include a viability dye staining.
8. The processing procedure to obtain a single cell suspension from tissues can interfere with the *in situ* phosphorylation status of the protein of interest. Therefore, we recommend to leave cells following their isolation for 1-2 hours in an CO_2 incubator. This resting of the cells will help restore phosphorylation status more comparable to their original *in situ* profile.
9. In our experience, adding 22 µL of the standard 37% formaldehyde, which contains methanol as a stabilizer, is also an option. However, this option provides a higher background signal and our advice is to use 16% ultra-pure formaldehyde.
10. 4% ultra-pure formaldehyde can damage epitopes in tissues. Test your panel to see whether binding of your antibodies of interest are affected and perform a titration from

1-4% of ultra-pure formaldehyde if needed to improve staining signal. In our experience XCR1 binding is highly affected by fixation. Staining cells with XCR1 after the fixation might lead to the appearance of false CD172a^{+}XCR1^{+} DC population. To prevent this, stain cells with XCR1 before fixation, for example, together with the viability dye.

11. Fixation can also be performed at 37 °C without affecting the phosphorylation signal. However, in our experience, the recovery of cells is higher when fixation was performed at RT.
12. 100% methanol should be stored at -20 °C and taken out of the freezer right before addition to the cells. Be aware that methanol can damage some epitopes, thereby interfering with cell staining. We observed that CD11c is sensitive to methanol permeabilization, leading to signal loss and making it challenging to identify DCs in tissues. To prevent that, we recommend to stain CD11c prior to methanol permeabilization, for example together with the viability dye. Carefully select your CD11c fluorochrome because some of them are methanol sensitive and cannot be used prior to methanol permeabilization. In our experience, CD11c-BV421 signal is still retained after methanol permeabilization.
13. For staining of *in vitro*-cultured human moDCs, compounds like Vitamin D, retinoic acid or dexamethasone can markedly decrease CD1a expression. In that case, we recommend to stain for only CD11c and HLA-DR. In case of bone marrow-derived DCs differentiated in the presence of GM-CSF, be aware that this is a mixed population of DCs and macrophage-like cells (12) and additional markers might be required depending on your research question.
14. Even though 2-NBDG has been commonly used as a readout for glucose uptake, its use for this purpose was recently questioned (13). Interpret your results carefully and make sure to always include appropriate controls. The following molecules can be used as controls for 2-NBDG staining: (1) 2-DG acts as a substrate for hexokinase to block its activity and directly competes with 2-NBDG; (2) 4,6-O-ethylidene-α-D-glucose (4,6-O) is a glucose analogue that binds to the external site of glucose transporters (GLUTs) but is not transported into cells; (3) cytochalasin B (CytB) diffuses through the cell membrane and binds to the internal site of GLUTs, also preventing entry of glucose into cells (14).
15. Staining cells in PBS 10% FCS serves as a negative control for the uptake of BODIPY™ FL C_{16} and BODIPY™ 493/505. The lipids present in FCS are targets for BODIPY™ 493/505, reducing the availability of the dye for binding to cellular lipid structures. Additionally, lipids present in FCS will directly compete with BODIPY™ FL C_{16} for uptake by cells, thereby reducing BODIPY™ FL C_{16} uptake.
16. As an alternative to BODIPY™ 493/503, HSC LipidTOX is a commercially available dye that stains neutral lipids. This neutral lipid staining can be performed on fixed and permeabilized as well as unpermeabilized cells, which makes this dye an interesting option if cells need to be fixed. According to the manufacturer's instruction, HSC LipidTOX should be diluted 200x and stained in PBS.
17. ThermoFisher provides BODIPY™ lipid probes for multiple purposes, including the staining of membrane lipids, uptake of fatty acids of various lengths and nonpolar probes for neutral lipid staining with different fluorescence. This protocol may be applicable to other BODIPY™ lipid probes as well, but carefully read the manufacturer's instructions.
18. BODIPY™ 493/505 and BODIPY™ FL C_{16} are hydrophobic dyes that do not disperse

readily into aqueous solutions. To ensure proper dissolving of the dye, vigorously vortex them before preparing the staining mix.

19. The metabolic dyes can be stained together with the viability dye. In that case, make sure to stain your cells at 37 °C instead of RT. The viability dyes can resist higher temperatures while most of the metabolic dyes allow less flexibility in this respect and require a specific temperature for optimal staining.
20. Mitotrackers and TMRM are both lipophilic cationic dyes that stain live, polarized mitochondria. However, differently from TMRM, Mitotrackers bind to intramitochondrial protein thiols and remain bound, even after depolarization. Because of these differences, TMRM and Mitotracker are commonly used to measure mitochondrial membrane potential and mitochondrial mass, respectively.
21. Besides Mitotracker Green FM and Mitotracker Deep Red FM, there are also other Mitotrackers options, including Mitotracker Red FM and Mitotracker Red CMXRos. However, these Mitotrackers, in contrast to Mitotracker Green FM and Mitotracker Deep Red FM, accumulate in mitochondria in a membrane potential-dependent manner (in a similar way as TMRM). If one is interested in mitochondrial mass, the preferred choice would be Mitotracker Green FM or Mitotracker Deep Red FM. One important difference between these two dyes is the fact that Mitotracker Deep Red FM is a dye that is well-retained in the mitochondria after fixation of the cells, while Mitotracker Green FM is not.
22. Even though Mitotracker Green FM and Mitotracker Deep Red FM are considered mitochondrial mass dyes, both of their signals seem to be at least partially affected by mitochondrial membrane potential (15). Mitotracker Deep Red FM seems to be more affected than Mitotracker Green FM and the combination of both dyes has been used to identify dysfunctional mitochondria (16, 17). It is important to have an appropriate negative mitochondrial membrane potential control, such as ionophore FCCP, that depolarizes the mitochondrial membrane, to ensure that your Mitotracker staining is not being affected by membrane potential and, also, to properly demonstrate that the TMRM staining is affected by the membrane depolarization.
23. CM-H_2DCFDA (and its derivatives) are non-specific ROS dyes that report general ROS production but cannot be used with fixed cells. If one needs to study ROS production in fixed or permeabilized cells, CellROX™ Green can be used. For more specific ROS detection, one can use dihydroethidium (DHE) (which detects intracellular levels of superoxide) or DAF-FM Diacetate (which detects intracellular levels of NO).
24. Incubation time for the positive control well can be reduced by increasing the percentage of H_2O_2. Be aware that H_2O_2 can be toxic if cells are exposed to high concentrations for a longer period of time.

References

1. Kelly B, O'Neill LA. Metabolic reprogramming in macrophages and dendritic cells in innate immunity. Cell Res. 2015;25(7):771-84.
2. O'Neill LA, Kishton RJ, Rathmell J. A guide to immunometabolism for immunologists. Nat Rev Immunol. 2016;16(9):553-65.
3. Everts B, Amiel E, Huang SC, Smith AM, Chang CH, Lam WY, et al. TLR-driven early glycolytic reprogramming via the kinases TBK1-IKKvarepsilon supports the anabolic demands of dendritic cell activation. Nat Immunol. 2014;15(4):323-32.
4. Zhao F, Xiao C, Evans KS, Theivanthiran T, DeVito N, Holtzhausen A, et al. Paracrine Wnt5a-beta-Catenin Signaling Triggers a Metabolic Program that Drives Dendritic Cell Tolerization. Immunity. 2018;48(1):147-60.
5. Zou C, Wang Y, Shen Z. 2-NBDG as a fluorescent indicator for direct glucose uptake measurement. J Biochem Biophys Methods. 2005;64(3):207-15.
6. Herber DL, Cao W, Nefedova Y, Novitskiy SV, Nagaraj S, Tyurin VA, et al. Lipid accumulation and dendritic cell dysfunction in cancer. Nat Med. 2010;16(8):880-6.
7. Clutton G, Mollan K, Hudgens M, Goonetilleke N. A Reproducible, Objective Method Using MitoTracker® Fluorescent Dyes to Assess Mitochondrial Mass in T Cells by Flow Cytometry. Cytometry Part A. 2018;95(4):450-6.
8. Scaduto RC, Grotyohann LW. Measurement of mitochondrial membrane potential using fluorescent rhodamine derivatives. Biophysical Journal. 1999;76:9.
9. Little AC, Kovalenko I, Goo LE, Hong HS, Kerk SA, Yates JA, et al. High-content fluorescence imaging with the metabolic flux assay reveals insights into mitochondrial properties and functions. Commun Biol. 2020;3(1):271.
10. Kauffman ME, Kauffman MK, Traore K, Zhu H, Trush MA, Jia Z, et al. MitoSOX-Based Flow Cytometry for Detecting Mitochondrial ROS. React Oxyg Species (Apex). 2016;2(5):361-70.
11. Kuznetsov AV, Kehrer I, Kozlov AV, Haller M, Redl H, Hermann M, et al. Mitochondrial ROS production under cellular stress: comparison of different detection methods. Anal Bioanal Chem. 2011;400(8):2383-90.
12. Helft J, Bottcher J, Chakravarty P, Zelenay S, Huotari J, Schraml BU, et al. GM-CSF Mouse Bone Marrow Cultures Comprise a Heterogeneous Population of CD11c(+)MHCII(+) Macrophages and Dendritic Cells. Immunity. 2015;42(6):1197-211.
13. Sinclair LV, Barthelemy C, Cantrell DA. Single Cell Glucose Uptake Assays: A Cautionary Tale. Immunometabolism. 2020;2(4)
14. Holman GD. Chemical biology probes of mammalian GLUT structure and function. Biochem J. 2018;475(22):3511-34.
15. Xiao B, Deng X, Zhou W, Tan EK. Flow Cytometry-Based Assessment of Mitophagy Using MitoTracker. Front Cell Neurosci. 2016;10:76.
16. Yu J, Nagasu H, Murakami T, Hoang H, Broderick L, Hoffman HM, et al. Inflammasome activation leads to Caspase-1-dependent mitochondrial damage and block of mitophagy. Proc Natl Acad Sci U S A. 2014;111(43):15514-9.
17. Ye J, Jiang Z, Chen X, Liu M, Li J, Liu N. The role of autophagy in pro-inflammatory responses of microglia activation via mitochondrial reactive oxygen species in vitro. J Neurochem. 2017;142(2):215-30.
18. Ferreira GB, Vanherwegen AS, Eelen G, Gutierrez ACF, Van Lommel L, Marchal K, et al. Vitamin D3 Induces Tolerance in Human Dendritic Cells by Activation of Intracellular Metabolic Pathways. Cell Rep. 2015;10(5):711-25.

19. Zhou G, Myers R, Li Y, Chen Y, Shen X, Fenyk-Melody J, et al. Role of AMP-activated protein kinase in mechanism of metformin action. Journal of Clinical Investigation. 2001;108(8):1167-74.

20. Amiel E, Everts B, Freitas TC, King IL, Curtis JD, Pearce EL, et al. Inhibition of mechanistic target of rapamycin promotes dendritic cell activation and enhances therapeutic autologous vaccination in mice. J Immunol. 2012;189(5):2151-8.

Part 2

AMPK as Regulator of Immunity


AMPK

4

Dendritic cell-intrinsic LKB1-AMPK/SIK signaling controls metabolic homeostasis by limiting the hepatic Th17 response during obesity

Hendrik J.P. van der Zande[1*], Eline C. Brombacher[1*], Joost M. Lambooij[1], Leonard R. Pelgrom[1], Anna Zawistowska-Deniziak[1,2,3], Thiago A. Patente[1], Graham A. Heieis[1], Frank Otto[1], Arifa Ozir-Fazalalikhan[1], Maria Yazdanbakhsh[1], Bart Everts[1#] and Bruno Guigas[1#]

* Shared first authorship
# Shared senior authorship

[1]Department of Parasitology, Leiden University Medical Center, Leiden, The Netherlands
[2]Department of Parasitology, Institute of Functional Biology and Ecology Faculty of Biology, University of Warsaw, Poland
[3]Department of Immunology, Institute of Functional Biology and Ecology Faculty of Biology University of Warsaw, Poland

JCI Insight
DOI: 10.1172/jci.insight.157948

Abstract

Obesity-associated metabolic inflammation drives the development of insulin resistance and type 2 diabetes, notably through modulating innate and adaptive immune cells in metabolic organs. The nutrient sensor liver kinase B1 (LKB1) has recently been shown to control cellular metabolism and T cell priming functions of dendritic cells (DCs). Here, we report that hepatic DCs from high-fat diet (HFD)-fed obese mice display increased LKB1 phosphorylation and that LKB1 deficiency in DCs ($CD11c^{\Delta LKB1}$) worsened HFD-driven hepatic steatosis and impaired glucose homeostasis. Loss of LKB1 in DCs was associated with increased expression of T helper 17-polarizing cytokines and accumulation of hepatic $IL\text{-}17A^{+}$ T helper cells in HFD-fed mice. Importantly, IL-17A neutralization rescued metabolic perturbations in HFD-fed $CD11c^{\Delta LKB1}$ mice. Mechanistically, deficiency of the canonical LKB1 target AMPK in HFD-fed $CD11c^{\Delta AMPK\alpha 1}$ mice recapitulated neither the hepatic Th17 phenotype nor the disrupted metabolic homeostasis, suggesting the involvement of other and/or additional LKB1 downstream effectors. We indeed provide evidence that the control of Th17 responses by DCs via LKB1 is actually dependent on both AMPKα1 and salt-inducible kinase(s) signaling. Altogether, our data reveal a key role for LKB1 signaling in DCs in protection against obesity-induced metabolic dysfunctions by limiting hepatic Th17 responses.

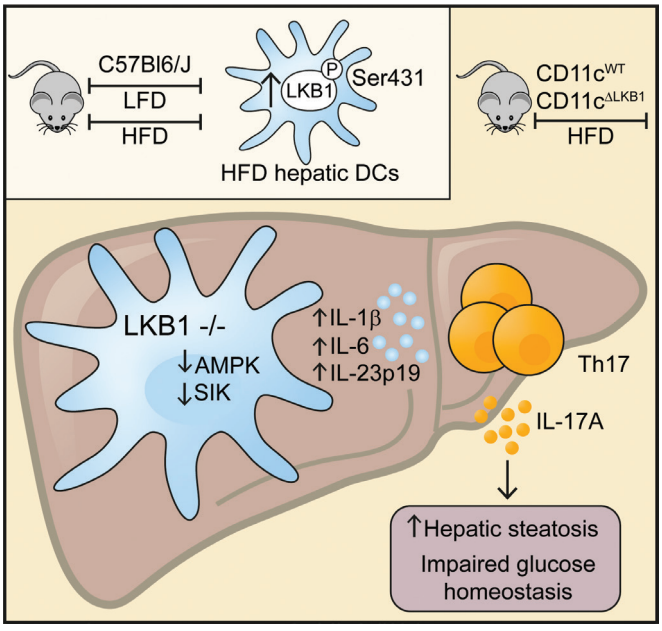

Introduction

Obesity is associated with chronic low-grade inflammation, also known as metabolic inflammation, where continuous overnutrition generates a self-sustained inflammatory loop in metabolic tissues that drives insulin resistance and type 2 diabetes (1). One of the hallmarks of metabolic inflammation is the accumulation of myeloid cells in the main metabolic organs, *i.e.* white adipose tissue (WAT), liver and skeletal muscle (2). Macrophage-related cytokines such as tumor necrosis factor (TNF) and interleukin (IL)-1β were shown to inhibit insulin signaling (3,4) and as such, macrophages are considered key players in the etiology of tissue-specific insulin resistance. However, dendritic cells (DCs) also accumulate in WAT and liver during obesity and are associated with metabolic dysfunctions. Indeed, depletion of the entire DC population or specific conventional DC (cDC) subsets in different genetic mouse models alleviates adipose tissue and/or hepatic inflammation, although the underlying mechanisms are incompletely understood (5-8).

DCs are specialized antigen presenting cells that govern T cell responses depending on the inflammatory and metabolic microenvironment. Moreover, modulation of T helper cell subsets in metabolic tissues has been shown to play a role in the control of immunometabolic homeostasis. For instance, T helper 2 (Th2) cells and regulatory T cells (Tregs) are enriched in lean, insulin sensitive WAT and contribute to maintenance of tissue-specific insulin sensitivity (9-11). On the contrary, Th17 cells accumulate in WAT and liver during obesity, and are associated with hepatic steatosis and insulin resistance (12-16). In addition, preventing CXCR3-dependent hepatic Th17 accrual and blocking IL-17A signaling using neutralizing antibodies both alleviated non-alcoholic fatty liver disease (NAFLD) (15, 16), suggesting an important contribution of hepatic Th17 cells to NAFLD severity. Although both DCs and T helper cell subsets in metabolic tissues have been associated with control of metabolic homeostasis, little is known about the regulation of DC-mediated T helper cell polarization in these organs during the development of obesity, and its impact on whole-body insulin sensitivity.

DC-mediated priming of Tregs and effector Th1, Th2 and Th17 cells is considered to be driven by metabolic rewiring of DCs in response to environmental cues, which controls co-stimulatory molecule and cytokine expression that shape T helper cell polarization (17). For example, *in vitro* Toll-like receptor (TLR)-activated mature DCs depend on glycolysis for fueling their anabolic demands, whereas quiescent DCs mainly rely on fatty acid oxidation and mitochondrial oxidative phosphorylation (18). As such, the obesity-induced changes in the metabolic organ microenvironment in which DCs reside may impact their T cell-polarizing capacities and contribute to metabolic inflammation (19).

Among the bioenergetic sensors that regulate DC intrinsic metabolism and function *in vivo*, liver kinase B1 (LKB1) has recently received considerable attention (20-22). The tumor suppressor LKB1 is a serine/threonine kinase that can phosphorylate and activate AMP-activated protein kinase (AMPK) and 12 other members of the AMPK-related family of protein kinases (23, 24), thereby controlling cell growth, survival, polarity and metabolism (25). In DCs, LKB1 was shown to be a critical regulator of effector T cell and Treg priming, thereby maintaining anti-tumor immunity (21, 22). We therefore hypothesized that LKB1 in DCs may connect the changing metabolic microenvironment during obesity to altered T cell priming, thereby impacting whole-body metabolic homeostasis.

In the present study, we investigated the role of LKB1 signaling in DC-mediated T helper cell priming in metabolic tissues and its impact on metabolic homeostasis. We

demonstrate that obesity increased LKB1 phosphorylation in hepatic DCs, and that loss of LKB1 in DCs exacerbated hepatic steatosis and impaired glucose homeostasis by promoting hepatic Th17 responses in obese mice. Finally, we demonstrate that LKB1 limits DC-mediated Th17 responses through both AMPKα1 and salt-inducible kinase(s) (SIK).

Results

Obesity induces DC activation in metabolic tissues and increases LKB1 phosphorylation in hepatic DCs

To investigate the role of dendritic cells (DCs) in whole-body metabolic homeostasis during obesity, male C57BL/6J mice were fed a high-fat diet (HFD) for 24 weeks, resulting in significant increases in body weight and fat mass when compared to low-fat diet (LFD)-fed control mice (Fig. 1A-C). Using flow cytometry (Fig. S1), we assessed the frequency and phenotype of DCs in metabolic tissues from lean and obese mice. The number of leukocytes per g tissue was found to be significantly increased in WAT but not in the liver from obese mice, likely due to increased liver weight (Fig. S2A-B). Although DC abundance was not affected, DCs from both tissues exhibited increased expression of activation markers (Fig. 1F-G), a feature specific to metabolic tissues as activation status of DCs remained largely unchanged in the spleen (Fig. S2C). These changes in DC phenotypes were associated with alterations in the T helper cell pool in metabolic tissues. In eWAT, interferon (IFN)γ$^+$ Th1 cells were increased at the expense of IL-5$^+$ Th2 cells and FOXP3$^+$ regulatory T cells (Tregs), while in the liver we detected increased Th1 cells, IL-17A$^+$ Th17 cells and Tregs (Fig. 1H-I). Additionally, the frequency of IFNγ$^+$ CD8 T cells was increased in liver but not eWAT of HFD-fed mice (Fig. 1I). In line with unaltered expression of activation markers on splenic DCs, T cell cytokine expression in the spleen was largely unaffected in obese mice (Fig. S2B). These data suggest that the changing microenvironment in metabolic tissues during obesity alters DC activation and, consequently, DC-mediated T cell responses.

As a bioenergetic sensor, LKB1 was recently shown to be a critical regulator of DC biology and T cell responses *in vivo* (20-22). We next investigated LKB1 signaling in spleen, eWAT and liver DCs by flow cytometry to determine its potential role in tissue-specific DC responses to HFD. Interestingly, we found a marked increase in phosphorylation of Ser431-LKB1 specifically in hepatic DCs from obese mice, suggesting that signaling to LKB1 within DCs is altered during high-fat feeding, whereas Ser79-ACC phosphorylation, as a proxy for activity of AMPK, the canonical downstream target of LKB1, was unchanged (Fig. 1J-K; Fig. S2C). Together, these findings indicate that obesity-induced changes in the hepatic microenvironment may affect signaling to LKB1 in DCs which is associated with altered hepatic T cell responses.

LKB1 deficiency in CD11c-expressing cells aggravates obesity-induced metabolic dysfunctions

To study the role of LKB1 in DCs in the context of obesity-induced metabolic inflammation, we crossed *Stk11*$^{flox/flox}$ mice to *Itgax*^{cre} mice to generate mice with CD11c-specific deletion of LKB1. We and others have previously shown that LKB1 RNA and protein is efficiently deleted from CD11c-expressing DCs in this model, and only partially from splenic macrophages (21, 22). Male conditional knockout (CD11c$^{\Delta LKB1}$) and Cre$^-$ littermate control (CD11c^{WT}) mice were fed an HFD for 18 weeks (Fig. 2A), which did not result in differences in body weight gain

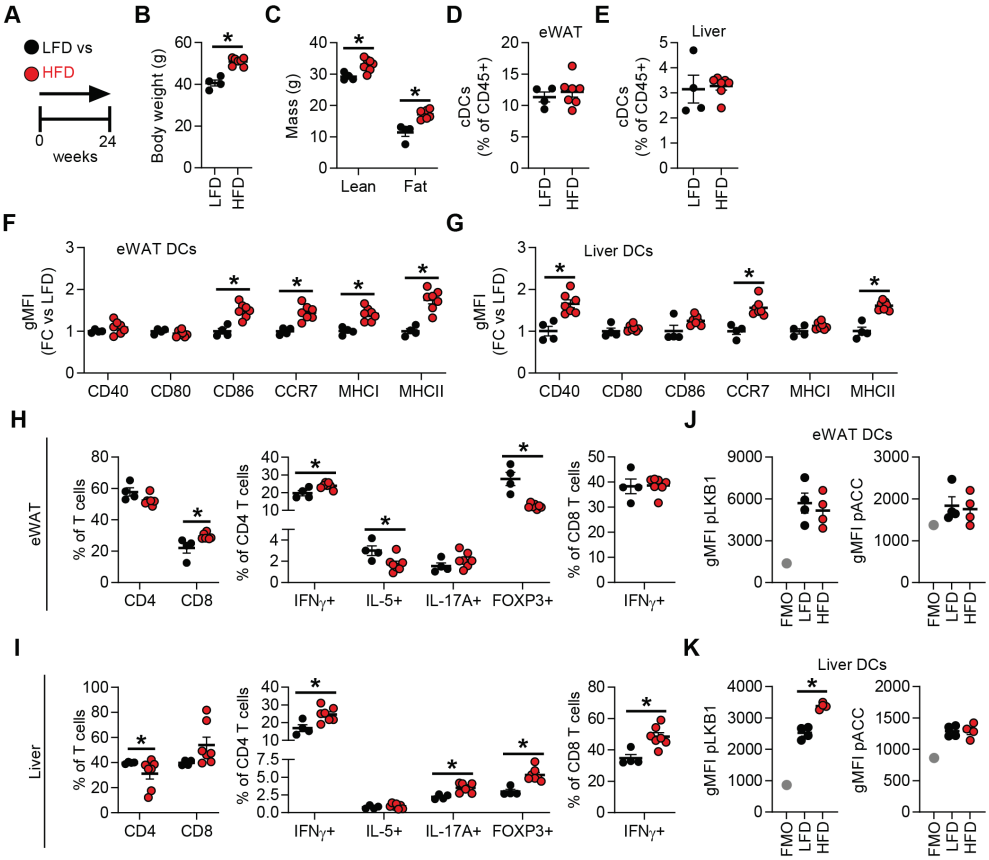

Figure 1. WAT and liver DCs are activated in obese mice. A: Mice were fed a low fat diet (LFD; black symbols) or a high fat diet (HFD; red symbols) for 24 weeks. **B-C:** Body weight **(B)** and body composition **(C)** were measured at the end of the experiment. **D-G:** At sacrifice, epididymal white adipose tissue (eWAT) and liver were collected and immune cells were isolated and analyzed by flow cytometry. Frequencies of DCs within total leukocytes in eWAT **(D)** and liver **(E)**. Relative expression of indicated DC markers by eWAT **(F)** and liver DCs **(G)**. **H-I:** Cells were restimulated with PMA/ionomycin in the presence of Brefeldin A for detection of intracellular cytokines, and were analyzed by flow cytometry. CD4 and CD8 T cell, IFNγ$^+$ (Th1), IL-5$^+$ (Th2), IL-17A$^+$ (Th17) and FOXP3$^+$ (Treg) CD4 T cell and IFNγ$^+$ CD8 T cell percentages in eWAT **(H)** and liver **(I)**. **J-K:** eWAT and liver were immediately formaldehyde-fixed after collection and immune cells were isolated. Phosphorylated LKB1 (Ser431) and ACC (Ser79) were measured in DCs from eWAT **(J)** and liver **(K)** by flow cytometry. Full gating strategies are shown in figure S1. Results are expressed as means ± SEM. Statistical analyses were performed using unpaired t-tests. * P<0.05 vs LFD (n = 4-7 mice per group).

or body composition between genotypes (Fig. 2B-E). Food intake, energy expenditure, and carbohydrate (CHO) and fatty acid (FA) oxidation were also not affected by loss of LKB1 in CD11c-expressing cells (Fig. S3). However, despite similar levels at baseline, CD11c$^{\Delta LKB1}$ mice developed higher fasting blood glucose levels than CD11c^{WT} littermates after 6 weeks on HFD, which was sustained throughout the experiment (Fig. 2F). Furthermore, the glucose excursion

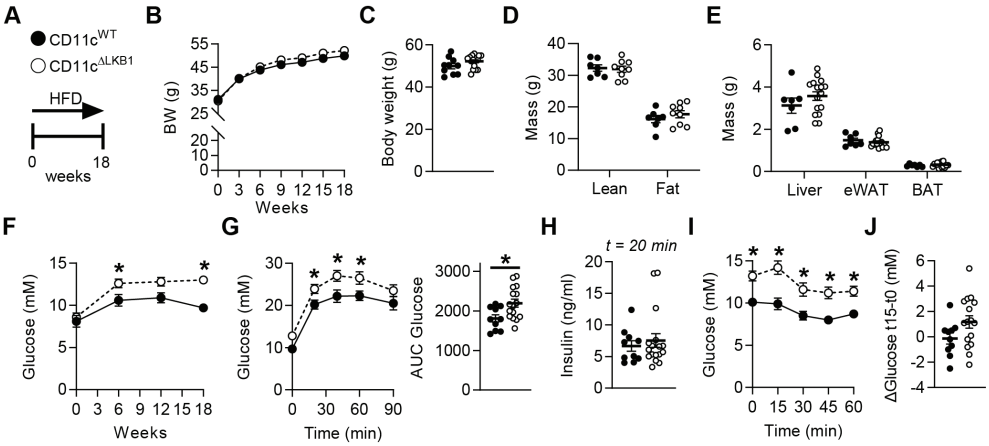

Figure 2. Deletion of LKB1 in DCs aggravates whole-body glucose intolerance and insulin resistance in obese mice.
A: CD11c^{WT} (black symbols) and CD11c$^{\Delta LKB1}$ (open symbols) mice were fed a HFD for 18 weeks. **B-C:** Body weight was monitored throughout the experiment. **D-E:** Body composition **(D)** and weights of liver, eWAT and BAT **(E)** were measured at the end of the experiment. **F:** Fasting blood glucose was measured at the indicated weeks. **G:** An i.p. glucose tolerance test (GTT) was performed 1 week before sacrifice. Blood glucose levels were measured at the indicated time points and the AUC of the glucose excursion curve was calculated. **H:** Plasma insulin was measured at 20 minutes post glucose injection during i.p. GTT. **I:** An i.p. insulin tolerance test was performed 1 week before sacrifice. Blood glucose levels were measured at the indicated time points. **J:** Delta glucose values between timepoints 0 and 15. Data shown are a pool of two independent experiments. Results are expressed as means ± SEM. Statistical analyses were performed using unpaired t-test **(C-E, G-H, J)** or two-way ANOVA followed by Fisher's post-hoc tests **(B, F-G, I)**. * P<0.05 vs CD11cWT (n = 7-17 mice per group).

during glucose tolerance test was larger in CD11c$^{\Delta LKB1}$ than in CD11c^{WT} mice (Fig. 2G), while glucose-induced insulin levels were similar (Fig. 2H), suggesting a stronger impairment in HFD-induced insulin resistance. Although significant differences in glucose levels were already present at baseline, which complexifies the interpretation of the data, similar results were obtained during an insulin tolerance test (Fig. 2I), with a borderline significant (p=0.08) lower glucose drop in the acute response to insulin bolus in CD11c$^{\Delta LKB1}$ compared to CD11c^{WT} mice (Fig. 2J). Altogether, this suggests that LKB1 expression in CD11c^{+} cells is important for restraining metabolic dysfunctions in mice during HFD-induced obesity.

Deletion of LKB1 in DCs promotes hepatic Tregs and Th17 cells and exacerbates hepatic steatosis

We next determined if the exacerbated metabolic dysfunctions observed in obese CD11c$^{\Delta LKB1}$ mice could be driven by tissue-specific immunometabolic changes. In eWAT, total leukocyte count and relative abundances of eosinophils, neutrophils, monocytes and macrophages were unaffected. However, expression of the obesity-associated macrophage marker CD11c was reduced in CD11c$^{\Delta LKB1}$, while the absolute number of CD11c^{+} macrophages per gram eWAT and CD86 expression were unchanged (Fig. S4A-F). In line with our previous findings

that LKB1-deficient DCs are more migratory (22), we found that the relative abundance and numbers of DCs per gram eWAT were decreased in obese CD11c$^{\Delta LKB1}$ mice while frequencies of cDC subsets between genotypes remained similar (Fig. S4G-H). As previous work revealed that LKB1-deficient DCs induced Tregs and effector Th17 cells mostly in lymphoid tissues of lean mice (21, 22), we next assessed whether these T helper subsets are affected in eWAT from obese CD11c$^{\Delta LKB1}$ mice. Despite similar CD4 T cell abundance, frequencies of FOXP3^{+} Tregs and IL-17A^{+} Th17 cells within the CD4 T cell pool were increased in eWAT from obese CD11c$^{\Delta LKB1}$ mice, while IL-5^{+} Th2 cells were not (Fig. S4I-K). However, when expressed as number of cells per gram eWAT, neither Tregs nor Th17 cells were significantly increased (Fig. S4L). Furthermore, adipocyte mean diameter and size distribution were not affected in obese CD11c$^{\Delta LKB1}$ mice (Fig. S4M-O).

In the liver, the abundance of total leukocytes, eosinophils, neutrophils, monocytes and Kupffer cells was unchanged in obese CD11c$^{\Delta LKB1}$ mice when compared to CD11c^{WT} littermates (Fig. 3A; Fig. S5). However, expression of CD11c and CD86 on Kupffer cells was either significantly or tended to be decreased, and numbers of CD11c^{+} Kupffer cells were decreased in CD11c$^{\Delta LKB1}$ mice (Fig. S5E). The frequency and number of DCs per gram liver were reduced in CD11c$^{\Delta LKB1}$ mice, although the relative abundance of DC subsets remained similar (Fig. 3B-C, Fig. S5F-G). Importantly, deletion of *Stk11*, the gene encoding LKB1, was complete in hepatic cDC2s from CD11c$^{\Delta LKB1}$ mice while displaying only a partial deletion in CD11c-expressing Kupffer cells, likely due to lower CD11c expression in these myeloid cells (Fig. S5I-J), as previously reported (21, 22, 26). Strikingly, the proportions of liver Tregs and Th17 cells were significantly increased in mice with LKB1-deficient DCs in comparison to LKB1-sufficient controls (Fig. 3D-G). Moreover, the livers of CD11c$^{\Delta LKB1}$ obese mice exhibited enhanced hepatic steatosis characterized by larger lipid droplets (LDs) when compared to WT littermates (Fig. 3H-I). Consistent with this, triglyceride (TG) and total cholesterol (TC) levels were also higher (Fig. 3J) in the livers of HFD-fed CD11c$^{\Delta LKB1}$ mice and associated with increased expression of genes encoding the FA transporter CD36, the LD coating molecules FSP27 (*Cidec*) and Perilipin-4 (*Plin4*), and some fibrotic markers (Fig. 3K-L).

Taken together, these results show that deletion of LKB1 in DCs induces a potent increase in Tregs and Th17 cells in the liver and exacerbates hepatic steatosis in obese mice.

IL-17A neutralization prevents exacerbated obesity-induced metabolic dysfunctions in CD11c$^{\Delta LKB1}$ mice

WAT and liver Th17 cells have consistently been linked to obesity-induced metabolic dysfunctions (13, 27), and hepatic steatosis in particular (12, 14-16). Accordingly, we observed elevated IL-17A-expressing CD4 T cells in the livers of obese mice lacking LKB1 in DCs, a feature that was associated with enhanced hepatic steatosis. Hence, to investigate the contribution of increased Th17 cells to worsened metabolic dysfunctions in CD11c$^{\Delta LKB1}$ obese mice, we treated them with either neutralizing antibodies for the Th17 effector cytokine IL-17A or isotype control during the first 6 weeks on HFD (Fig. 4A). IL-17A neutralization did not impact body weight gain (Fig. 4B-C) or hepatic Treg and Th17 cell abundances in CD11c$^{\Delta LKB1}$ mice (Fig. S6). However, IL-17A blockade led to significantly improved whole-body insulin sensitivity (Fig. 4D) and reduced hepatic steatosis and LD diameter to comparable levels as CD11c^{WT} littermates (Fig. 4E-G). Interestingly, the increased hepatic gene expression of *Cd36*, LD and fibrotic markers in HFD-fed CD11c$^{\Delta LKB1}$ mice was also rescued following IL-17A neutralization (Fig. 4H-I). Thus, increased IL-17A in CD11c$^{\Delta LKB1}$ mice plays a central role in

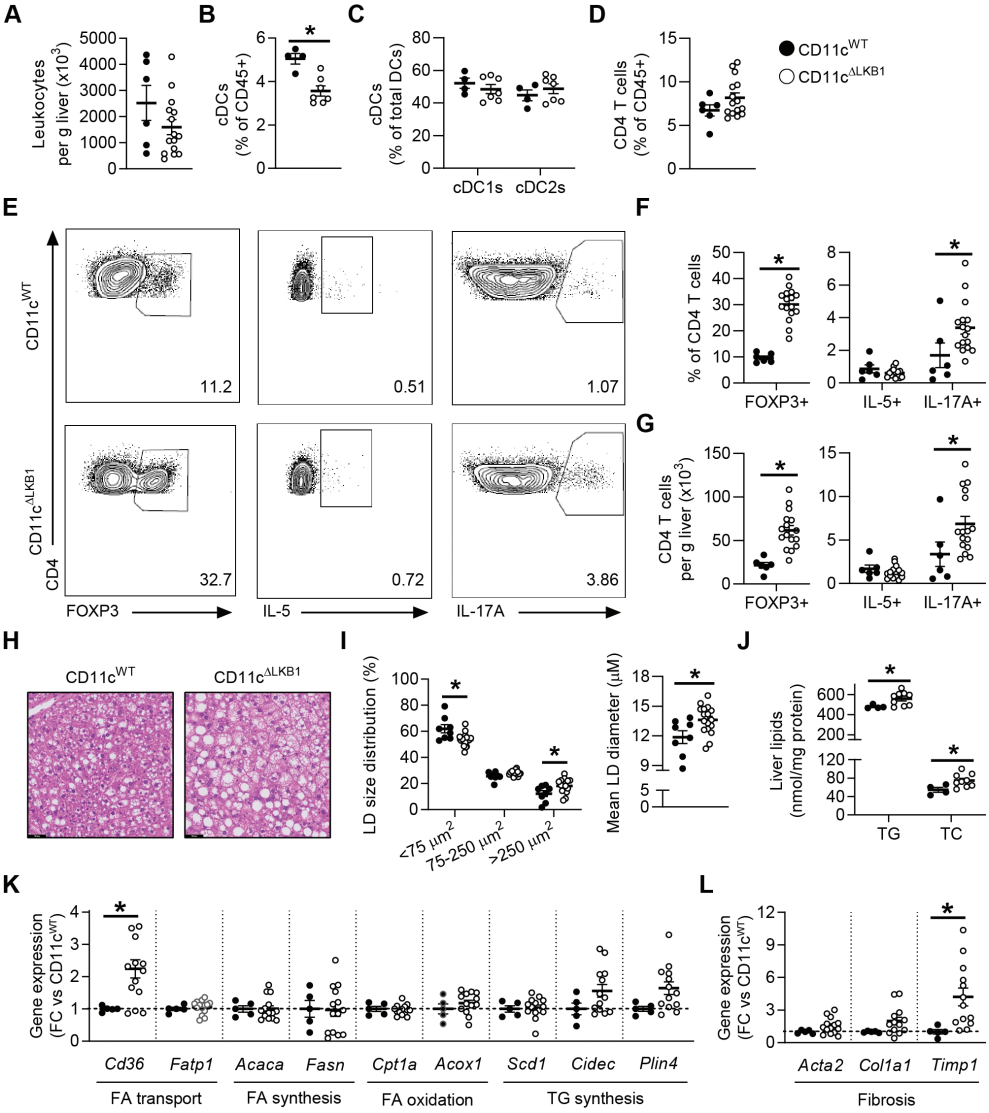

Figure 3. Obese CD11c$^{\Delta LKB1}$ mice are more susceptible to HFD-induced hepatic steatosis and have increased hepatic Treg and Th17 cells. CD11c^{WT} (black symbols) and CD11c$^{\Delta LKB1}$ (open symbols) mice were fed a HFD for 18 weeks. **A-D:** At sacrifice, liver was collected and immune cells isolated. Total leukocytes per gram liver were quantified **(A)**. Percentages of DCs **(B)**, cDC subsets **(C)** and CD4 T cells **(D)** were determined by flow cytometry. E-G: Liver leukocytes were restimulated with PMA and ionomycin in the presence of Brefeldin A for intracellular cytokine detection. Representative plots **(E)** and percentages of FOXP3$^+$ Tregs, IL-5$^+$ Th2 and IL-17A$^+$ Th17 cells were determined as frequencies of CD4 T cells (F) or cells per gram liver **(G)**. **H:** A part of liver was sectioned and H&E stained. **I:** Lipid droplet size distribution and mean lipid droplet diameter were quantified from H&E-stained slides. **J:** Hepatic triglyceride (TG) and total cholesterol (TC) contents were determined. **K-L:** Hepatic gene expression of genes involved in lipid metabolism **(K)** and fibrosis **(L)** was measured by RT-qPCR. Data shown are a pool of two independent experiments, except for **B**, **C** and **J**. Results are expressed as means ± SEM.

Statistical analyses were performed using unpaired t-tests **(A-L)** or two-way ANOVA followed by Fisher's post-hoc tests **(I)**. * P<0.05 vs CD11cWT (n = 6-17 mice per group for **A, D-I**; n = 4-9 mice per group for **B, C** and **J**). The black rectangle at the bottom left of each H&E-stained slides indicates the picture scale (50 μm).

promoting liver steatosis and metabolic dysfunctions during HFD-induced obesity. Altogether our findings suggest that LKB1 in DCs mitigates hepatic inflammation during the development of obesity by restraining Th17 responses.

To explore a direct role for LKB1-deficient DCs in promoting Th17 responses, we sorted hepatic type 2 conventional DCs (cDC2s), the main CD4 T cell-priming subset shown to induce Th17 priming (28), from lean $CD11c^{WT}$ and $CD11c^{\Delta LKB1}$ mice that were subcutaneously injected with Flt3L-secreting B16 melanomas to expand the *in vivo* DC pool (Fig. 5A). Surface expression of activation markers on hepatic cDC2s was largely unchanged during homeostasis (Fig. 5B). LPS-induced expression of the Th17-polarizing cytokines *Il6* and *Il1b* was enhanced in LKB1-deficient hepatic cDC2s when compared to controls, whereas *Il23a* was undetectable and *Tgfb1* unchanged (Fig. 5C). These results show that LKB1 deficiency in DCs promotes production of cytokines known to favor Th17 polarization, suggesting LKB1 in DCs restrains Th17 polarization by limiting IL-1β and IL-6 production.

The LKB1 downstream targets SIK and AMPK in DCs regulate Th17 responses

Having demonstrated that LKB1 loss in DCs exacerbates obesity-induced metabolic dysfunctions in an IL-17A-dependent fashion, we next investigated the signaling mediators downstream of LKB1 involved in the Th17 priming function of DCs. The LKB1-AMPK axis represents a central node in the regulation of cellular energetics, where LKB1 promotes the downstream activation of AMPK though direct phosphorylation of its catalytic α-subunit (25). To assess whether AMPK is involved in the impaired metabolic homeostasis observed in $CD11c^{\Delta LKB1}$ obese mice, we generated $CD11c^{\Delta AMPK\alpha1}$ mice, in which AMPKα1, the main α-subunit expressed by DCs (29), is deleted in these cells (Fig. S7A) (22). We next fed them and their $CD11c^{WT}$ littermates an HFD for 18 weeks (Fig. S7B). Surprisingly, none of the abovementioned detrimental immunometabolic changes observed in $CD11c^{\Delta LKB1}$ obese mice, *i.e.* increased fasting glucose levels, glucose intolerance, insulin resistance, and hepatic Tregs and Th17 cells, were recapitulated in HFD-fed $CD11c^{\Delta AMPK\alpha1}$ mice (Fig. S7). These data indicate that increased hepatic Th17 responses seen in $CD11c^{\Delta LKB1}$ mice are not strictly dependent on AMPK.

In addition to AMPK, LKB1 phosphorylates several other downstream AMPK-related kinases including MARK1-4, SIK1-3, NUAK1-2, BRSK1-2 and SNRK (23, 24). We therefore investigated which LKB1 target(s) may contribute to altering DC function by analyzing published datasets for their expression in hepatic cDCs, as well as mature GM-CSF-elicited bone-marrow DCs (GMDCs) (30-32). The expression profiles were almost identical between primary hepatic cDCs and GMDCs, showing that all these kinases were expressed to a significant level with the notable exception of *Mark1*, *Brsk2* and *Prkaa2* (encoding AMPKα2), confirming that only the catalytic AMPKα1 isoform is expressed by DCs (29). *Brsk1* and *Nuak1* were solely expressed in hepatic cDCs or GMDCs respectively (Fig. S8A-B). We next determined their role in driving Th17 responses by DCs. To this end, $CD11c^{WT}$ GMDCs were treated with inhibitors of SIK, MARK and NUAK families prior to LPS stimulation, and intracellular levels of Th17-polarizing

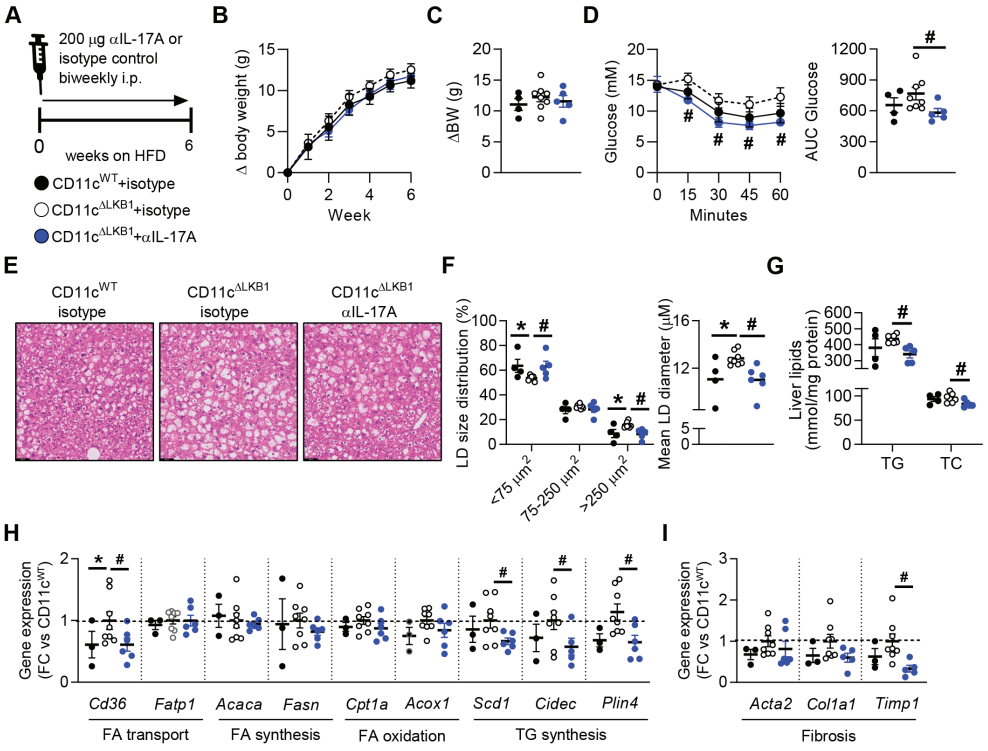

Figure 4. IL-17A neutralization rescued insulin resistance and hepatic steatosis in CD11c$^{\Delta LKB1}$ mice. **A:** CD11c^{WT} (black symbols) and CD11cΔLKB1 mice were fed a HFD for 6 weeks while concomitantly receiving a biweekly intraperitoneal treatment with IL-17A neutralizing antibodies (blue symbols) or isotype control (open symbols). **B-C:** Body weight gain was monitored throughout the experiment. **D:** An i.p. insulin tolerance test was performed during week 6. **E:** At sacrifice, a piece of liver was sectioned and H&E stained. **F:** Lipid droplet size distribution and mean lipid droplet diameter were quantified from H&E-stained slides. **G:** Hepatic TG and TC content were determined. **H-I:** Hepatic gene expression of genes involved in lipid metabolism **(H)** and fibrosis **(I)** was measured by RT-qPCR. Data shown are a pool of two independent experiments. Results are expressed as means ± SEM. Statistical analyses were performed using two-way ANOVA **(B, D, F)** or one-way ANOVA **(C, D-I)** followed by Fisher's post-hoc tests.* P<0.05 vs CD11c^{WT}; # P<0.05 vs CD11c$^{\Delta LKB1}$ + isotype control (n = 4-8 mice per group). The black rectangle at the bottom left of each H&E-stained slides indicates the picture scale (50 μm).

cytokines were assessed by flow cytometry and compared with CD11c$^{\Delta LKB1}$ and CD11c$^{\Delta AMPK\alpha1}$ GMDCs (Fig. 5D, Fig. S8C-D). Largely consistent with liver-derived cDC2s from CD11c$^{\Delta LKB1}$ mice, LKB1-deficient GMDCs displayed upregulated LPS-induced expression of pro-IL-1β, IL-6 and IL-23p19 when compared to wild-type GMDCs, whereas latency-associated peptide (LAP) expression, as a proxy for TGF-β production, was unchanged (Fig. 5E). Strikingly, inhibition of SIKs, but none of the other LKB1 downstream kinases, recapitulated the cytokine profile of LKB1-deficient GMDCs (Fig. 5E), identifying SIKs in DCs as potential regulators of Th17 responses.

To directly demonstrate a role for DC-intrinsic SIK in DC-mediated Th17 priming *in vivo*, we next performed adoptive transfer of LPS- and ovalbumin-pulsed GMDCs into WT recipient mice and assessed T cell cytokine profiles in the draining popliteal lymph nodes after 8 days (Fig. 5F). Transfer of LKB1-deficient GMDCs resulted in an increased Th17 response as indicated by elevated expression of RORγt, the canonical Th17 transcription factor, and IL-17A when compared to both $CD11c^{WT}$ and $CD11c^{\Delta AMPK\alpha1}$ GMDCs (Fig. 5G-H, Fig. S8F). However, adoptive transfer of WT GMDCs after SIK inhibition alone did not increase the Th17 response (Fig. 5G-H, Fig. S8F). This led us to hypothesize that a combination of LKB1 downstream targets, as previously reported in other contexts (33, 34), may be engaged to restrict Th17 responses. Indeed, when SIK inhibition was performed on AMPK-deficient GMDCs these cells fully recapitulated the cytokine profile and the Th17-polarizing capacity of LKB1-deficient GMDCs (Fig. 5E-H, Fig. S8F), suggesting that LKB1 in DCs constrains Th17 responses via a dual regulatory mechanism involving both AMPK and SIK.

Collectively, our data indicate that LKB1 signaling in DCs controls hepatic Th17 differentiation and metabolic homeostasis in obese mice, and we propose a dual role exerted by AMPK and SIK downstream of LKB1 in repressing Th17 responses.

Discussion

The bioenergetic sensor LKB1 was recently shown to be a critical regulator of DC metabolism, activation and T cell priming functions (20-22). Whether LKB1 signaling in DCs links the changing immunometabolic microenvironment during obesity with altered DC function and ultimately whole-body metabolic dysfunctions remained unclear. Here, we report that obesity increased LKB1 phosphorylation in hepatic DCs. Deletion of LKB1 from DCs increased hepatic Th17 cells and aggravated HFD-induced metabolic dysfunctions in obese mice. These immunometabolic defects were restored by neutralizing the Th17 effector cytokine IL-17A. LKB1-deficient DCs displayed a potentiated capacity to promote a Th17 response which was recapitulated by pharmacological/genetic inhibition of both AMPK and SIK in DCs, uncovering a role for an LKB1-AMPK/SIK axis in restraining DC-mediated pathogenic Th17 cell differentiation, thereby controlling whole-body metabolic homeostasis.

Although DCs accumulate in WAT and liver during obesity and contribute to whole-body insulin resistance (5-8), the underlying mechanisms are incompletely understood. Indeed, obese *Flt3l*$^{-/-}$ mice lacking DCs and *Ccr7*$^{-/-}$ mice with impaired DC migration displayed reduced metabolic inflammation and insulin resistance suggesting they have a central role in the development of metabolic dysfunctions (6, 7). Here, we report that DCs from eWAT and liver, but not spleen, of obese mice display increased expression of activation markers, indicating that the obesity-induced changes in the metabolic tissue microenvironment enhance DC activation. Interestingly, both eWAT and liver DCs from obese mice expressed higher levels of CCR7, suggestive of increased migration to draining lymph nodes where they can prime inflammatory T cells. Consistent with an increased pro-inflammatory activation profile of the DCs, we found that obesity altered the CD4 T helper cell pool in eWAT and liver, but not spleen, favoring Th1 cells at the expense of Th2 cells and Tregs in eWAT, and increasing Th1 cells, Th17 cells and Tregs in the liver. Some of these obesity-induced changes in T helper subsets in metabolic tissues have been reported previously (11, 16). Moreover, $XCR1^{+}$ type 1 conventional DCs (cDC1s), efficient at cross-presenting antigens to CD8 T cells, were reported to increase hepatic steatosis and contribute to liver pathology, which was associated

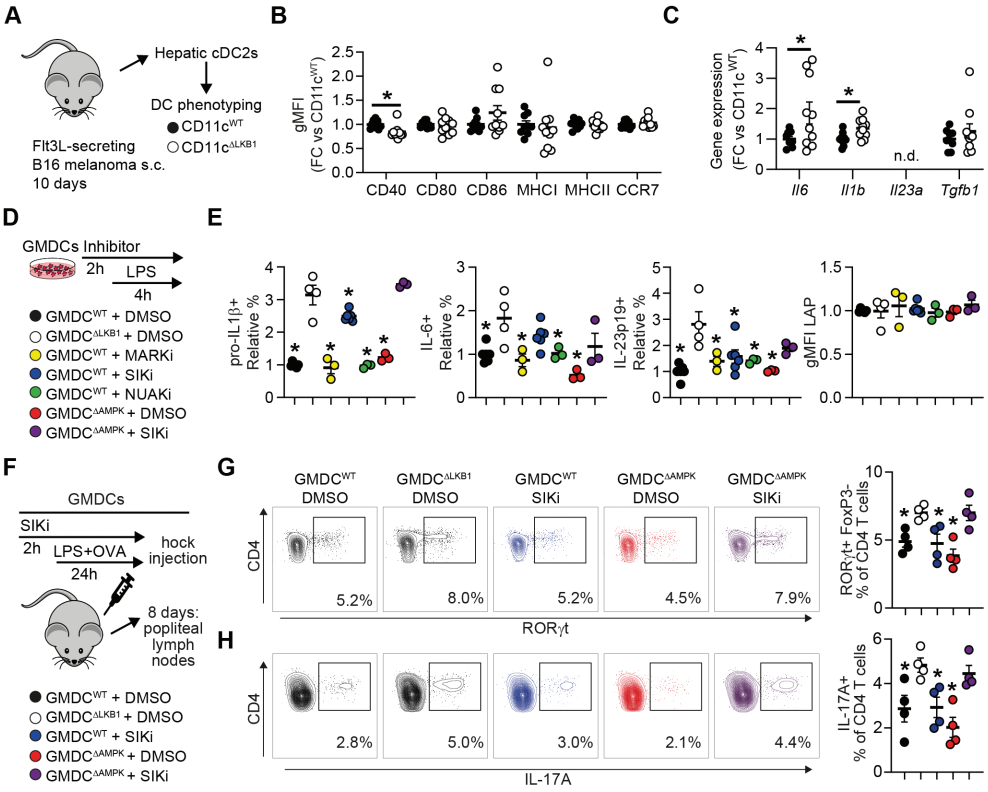

Figure 5. LKB1 deficiency in DCs increases a Th17 response, which is mediated via its downstream targets AMPK and SIK.
A-C: CD11c^{WT} (black symbols) and CD11c$^{\Delta LKB1}$ (open symbols) mice were subcutaneously injected with Flt3L-secreting B16 melanomas to expand the DC pool. After 10 days, hepatic cDC2s were FACS sorted for DC phenotyping **(A)**. Expression of indicated DC markers was measured by flow cytometry **(B)**. Expression of indicated genes was measured by RT-qPCR after ex vivo overnight LPS stimulation **(C)**. **D-E:** GM-CSF cultured bone marrow-derived DCs (GMDCs) from CD11c^{WT} (WT) mice and CD11c$^{\Delta AMPK\alpha1}$ (AMPK KO) mice were treated with inhibitors targeting LKB1 downstream targets or DMSO for 2 h, before LPS stimulation in the presence of Brefeldin A for 4 h and compared with CD11c$^{\Delta LKB1}$ GMDCs (LKB1 KO). Pro-IL-1β, IL-6, IL-23p19 and LAP-expressing GMDCs were quantified by intracellular cytokine staining/ flow cytometry and normalized to WT-DMSO. **F-H:** GMDCs (CD11c^{WT}, CD11c$^{\Delta LKB1}$ or CD11c$^{\Delta AMPK\alpha1}$) were treated with DMSO or SIK-inhibitor for 2 h and stimulated with OVA and LPS for 24 hours, before injected into the hock of WT mice. After 8 days, draining popliteal lymph nodes were harvested and RORγt^{+} and IL-17A^{+} Th17 cells were evaluated by flow cytometry. Results are expressed as means ± SEM. Statistical analyses were performed using unpaired t-tests **(B-C)** or one-way ANOVA followed by Dunnett's post-hoc tests **(E-H)**. *P<0.05 vs LKB1 KO (n = 9-10 mice per group for **A-C**; n = 3-6 biological replicates per group for **E** and n = 4 biological replicates per group for **G-H**).

with inflammatory T cell reprogramming in the liver-draining lymph nodes (8). Congruent with this, we found increased HFD-induced IFNγ^{+} CD8 T cells in the liver, most likely resulting from increased cDC1-mediated priming.

In addition to increased DC activation and altered T cell priming in metabolic tissues, we observed a significant increase of Ser431-LKB1 phosphorylation in hepatic DCs of obese mice. LKB1 is phosphorylated at Ser431 by protein kinase C ζ (PKCζ) (35), p90 ribosomal S6 kinase (p90-RSK) and cAMP-dependent protein kinase A (PKA) (36). Although the exact consequence of phosphorylation at this site remains unclear, the residue corresponding to murine Ser431 is conserved in all organisms, suggesting that its phosphorylation may play a role in modulating LKB1 signaling. Despite a lack of a phenotype and normal AMPK activation in knock-in mice carrying a homozygous Ser431 to alanine mutation in LKB1 (37), it has been suggested that Ser431 phosphorylation could promote nuclear export of LKB1 and phosphorylation of some of its cytoplasmic substrates (35).

Interestingly, Ser431-LKB1 phosphorylation was unchanged in splenic and eWAT DCs, indicating that obesity-induced changes in the hepatic microenvironment may specifically alter LKB1 signaling in liver-associated DCs and change its effector functions. Obesity induces persistent changes in the gut microbiota, and endotoxemia through increased gut permeability (38). As a result, the gut and serum metabolome is altered (39, 40), promoting NAFLD pathogenesis through a gut-liver axis (41). Since LPS injection has been reported to acutely increase Ser431-LKB1 phosphorylation in whole lung and liver lysates, and in immortalized Raw264.7 macrophages (42), one may hypothesize that obesity-induced endotoxemia might contribute to increased pLKB1 levels in hepatic DCs from obese mice. Of note, in Raw264.7 macrophages, LPS-induced Ser431-LKB1 phosphorylation suppressed NF-κB signaling, suggesting that increased pLKB1 in hepatic DCs from obese mice may serve as a feedback mechanism to keep inflammation in check. In addition, butyrate, a short-chain fatty acid produced by commensal bacteria that metabolize indigestible fiber, was recently shown to increase Ser431-LKB1 phosphorylation in HepG2 hepatocytes (43), providing conceptual evidence that gut metabolites may alter LKB1 phosphorylation in liver-resident cells. Yet, how LKB1 phosphorylation and other post-translational modifications such as farnesylation (37) affect LKB1 signaling, and how such modifications may be selectively modulated in hepatic DCs during obesity, remain an interesting future area of research.

Deletion of LKB1 from DCs increased hepatic Tregs and Th17 cells in obese mice. The role of Tregs in the regulation of metabolic homeostasis has become controversial over recent years. Hepatic Tregs were reported to control hepatic inflammation and inhibit NASH development (44), while adipose tissue Tregs have been shown to both protect against (45, 46) and aggravate (47-49) metabolic dysfunctions. However, we clearly demonstrate that neutralizing the Th17 effector cytokine IL-17A rescued the metabolic perturbations in HFD-fed CD11c$^{\Delta LKB1}$ mice, indicating an important role for increased Th17 cells rather than Tregs in explaining the metabolic phenotype of obese CD11c$^{\Delta LKB1}$ mice.

Obesity-induced hepatic Th17 cells and IL-17A signaling have consistently been reported to impair insulin sensitivity and promote hepatic steatosis and fibrosis in both HFD-fed mice and NAFLD/NASH patients (12-16, 50-52). Th17 differentiation is dependent on the cytokines IL-6, TGFβ, IL-1β and IL-23 (53, 54), but different combinations can lead to different degrees of pathogenicity. In the context of experimental autoimmune encephalitis, IL-6 and TGFβ-induced Th17 cells were not pathogenic, whereas IL-6, IL-1β and IL-23 induced Th17 cells were pathogenic (55, 56). Furthermore, development of Th17 cells *in vivo* is dependent on SIRPα/CD172a expression on DCs (28, 57), a marker of cDC2s that efficiently prime CD4 T cells. We previously showed that LKB1-deficient splenic cDC2s produced higher levels of IL-6 (22). In addition, others showed that mRNA expression of *Il6*, *Tgfb2* and *Il23a* tended to

be increased in LKB1-deficient total splenic DCs compared to WT DCs, whereas *Tgfb1* and *Tgfb3* were decreased or similar (21). Moreover, increased Th17 priming by LKB1-deficient splenic DCs was at least partly dependent on IL-6, but not TGFβ (21). Here, we find that LPS-stimulated LKB1-deficient GMDCs express significantly enhanced levels of IL-6, pro-IL-1β and IL-23p19, while TGFβ production was not affected. In addition, LKB1-deficient hepatic cDC2s express increased levels of *Il6* and *Il1b*, whereas *Tgfb1* was unchanged and *Il23a* undetectable. These data indicate that LKB1-deficient hepatic cDC2s display a cytokine profile that favors the development of pathogenic Th17 cells. Recent single cell transcriptomics analysis of hepatic Th17 cells from HFD-fed obese mice identified two subsets, of which one was enriched during obesity. The accumulation of this inflammatory hepatic Th17 (ihTh17) subset was regulated through a CXCL9/10-CXCR3 axis, and these cells were sufficient to exacerbate NAFLD pathogenesis through glycolysis-facilitated production of pro-inflammatory cytokines IL-17A, TNF and IFNγ (16). Moreover, increased IL-6, TGFβ, IL-1β and IL-23 levels in steatotic livers were also reported in this study, suggesting involvement of DCs in generating these ihTh17 cells. Given their role in promoting NAFLD pathogenesis, it is tempting to speculate that LKB1-deficient hepatic DCs promote accrual of these ihTh17 cells.

Upon binding to IL-17RA, IL-17 promotes the polyubiquitination of the TNF receptor associated factor (TRAF) 6 adaptor protein and downstream activation of CCAAT/enhancer-binding protein alpha (C/EBPa), MAPKs and NF-κB pathways (58). Interestingly, TRAF6 ubiquitination has been shown to be increased in HFD-fed mice and to be associated with fatty liver (59), while its inhibition was recently shown to alleviate hepatic steatosis and liver fibrosis (60). Interestingly, C/EBPa is involved in the transcriptional regulation of CD36 through direct binding to the *Cd36* gene promoter (61). CD36 is a multifunctional cell-surface scavenger receptor widely expressed in the liver that through facilitating FA uptake (62) has been shown to be positively associated with hepatic TG content in both obese mice and humans (63-65). CD36 indeed plays a central role in the development of NAFLD, notably by promoting hepatic *de novo* lipogenesis (66), and its hepatocyte-specific deletion attenuates fatty liver in HFD-fed mice (67). Altogether, it is therefore tempting to speculate that the elevated hepatic Th17 response of HFD-fed CD11c$^{\Delta LKB1}$ mice contributes to worsened hepatic steatosis and insulin resistance through TRAF6-C/EBPa-mediated enhanced *Cd36* expression. Further studies are required to elucidate the exact molecular mechanisms linking hepatic Th17 cells to LDs and metabolic dysfunctions.

Deletion of AMPKα1 in DCs did not recapitulate the immunometabolic phenotype of CD11c$^{\Delta LKB1}$ obese mice. Indeed, we and others have recently shown that LKB1 functions independently of AMPK in governing Tregs and Th17 cell differentiation (21, 22), which corresponds with a growing line of research showing AMPK-independent effects of LKB1 in immune cells (33, 42). However, we here show that AMPK in DCs regulates Th17 responses *in vivo* in combination with SIKs. SIK inhibition increased expression of the Th17-polarizing cytokines IL-6 and pro-IL-1β, while AMPK deficiency alone had no effects on Th17-polarizing cytokines in GMDCs. Interestingly, one report suggests that AMPK activation may suppress IL-23 in human monocyte-derived DCs (68). Largely congruent with these data, we find that AMPK-deficiency may boost IL-23 and IL-1β production in SIK inhibited DCs. Apart from possible potentiation effects of loss of AMPK signaling on Th17 polarizing cytokine production, LKB1-AMPK signaling has also been shown to restrain Th17 responses by limiting DC-T cell synapse formation (69). Alternatively, AMPK is well described to promote catabolic metabolism in cells, including DCs (18, 70), while glycolysis and mTOR-mediated

anabolic metabolism were shown to play a role in Th17 polarization by DCs (17). Although the metabolic requirements for Th17 polarization by DCs are likely context-dependent, it is therefore tempting to speculate that AMPK deletion may provide the metabolic requirements of DCs for promoting Th17 polarization, while SIK inhibition provides the required cytokine profile, yet this warrants further study.

The SIK family consists of three isoforms, SIK1-3, and is involved in regulating hepatic gluconeogenesis, lipid metabolism and tumorigenesis (71), although its underlying mechanisms are only beginning to be understood. SIKs control the phosphorylation and nucleocytoplasmic transport of class IIa histone deacetylases (HDACs) and cAMP-regulated transcriptional coactivators (CRTCs), identifying a role for SIKs in transcriptional regulation (72). CRTC is a coactivator of cAMP response element-binding protein (CREB) (73), and the promotors of *Il6*, *Il1b* and *Il23a* all contain CREB binding sites (74-76). One could thus speculate that inhibition of SIKs may promote CRTC nuclear transport, thereby promoting transcription of Th17-polarizing cytokines. In support of this, SIK1 and SIK3 were shown to control IL-6 production in tumor cells (77), and IL-6 and IL-1β production in Raw264.7 macrophages (78). Conversely, pharmacological inhibition of SIKs was also reported to suppress pro-inflammatory cytokines production in DCs and macrophages (79, 80). As SIK family members display functional redundancy in some settings (72), future studies are required to identify which SIK family member(s) control expression of Th17-polarizing cytokines, and what the mechanistic underpinnings are.

Although our data strongly argue in favor of a DC-intrinsic mechanism, we cannot formally rule out that deletion of LKB1 in other CD11c-expressing cells, such as macrophages, contribute to the immunometabolic phenotype. Indeed, LysM^{cre}-driven LKB1 deletion in macrophages has been shown to increase LPS-induced pro-inflammatory cytokine production (42). However, these LysM$^{\Delta LKB1}$ mice have unchanged Treg numbers (20), indicating that LKB1 deletion from macrophages does not alter T cell responses *in vivo*. In addition, congruent with previous work, only partial knockout of *Stk11* was observed in macrophages from CD11c$^{\Delta LKB1}$ mice (21, 26), which is likely attributable to lower CD11c expression by macrophages as compared to DCs. CD11c on macrophages is considered a proinflammatory/metabolic inflammation-associated marker in eWAT and liver of HFD-fed mice. We demonstrate that CD11c expression was downregulated on eWAT and liver macrophages of CD11c$^{\Delta LKB1}$ mice, both suggesting fewer proinflammatory macrophages as well as that efficiency of cre-mediated recombination is further hampered. Furthermore, we found that expression of the pro-inflammatory marker CD86 on both eWAT and liver macrophages was unchanged, as was *ex vivo* LPS-induced TNF and IL-6 production by CD11c^{+} macrophages from CD11c$^{\Delta LKB1}$ mice (data not shown). Together, this makes it unlikely that macrophages play a dominant role in the immunometabolic phenotype of CD11c$^{\Delta LKB1}$ mice. However, the use of zDC^{cre} mice, a model for cDC-specific conditional gene deletion that does not affect macrophages (81), may also be considered for future study.

Altogether, our data reveal a key role for LKB1 signaling in liver-resident DCs in limiting liver-specific and whole-body metabolic dysfunctions in the context of obesity, by constraining hepatic Th17 accrual. We suggest the involvement of an LKB1-AMPK/SIK axis to control Th17-responses by DCs, potentially opening interesting therapeutic options in controlling pathogenic Th17 cell development in metabolic inflammation and other hyperinflammatory disorders.

Methods

Animals, diet and treatment

All experiments were performed in accordance with the Guide for the Care and Use of Laboratory Animals of the Institute for Laboratory Animal Research. *Itgax*^{cre} (CD11c; PMID: 17591855), *Stk11*$^{fl/fl}$ (LKB1; PMID: 12226664), *Prkaa1*$^{fl/fl}$ (AMPKα1; PMID: 21124450) and WT mice, all on C57Bl/6J background, were purchased from The Jackson Laboratory or Envigo and crossed, housed and bred at the LUMC. Mice were housed in a temperature-controlled room with a 12-hour light-dark cycle and *ad libitum* access to food and tap water under specific pathogen free conditions. To reduce variation due to sex hormone cycles on whole-body metabolism, male mice were used for all *in vivo* experiments. An *a priori* power calculation was done. Analysis was performed blinded to the conditions.

8-16 weeks old age-matched WT, *Stk11*$^{fl/fl}$ (CD11c^{WT}), *Itgax*^{cre} *Stk11*$^{fl/fl}$ (CD11c$^{\Delta LKB1}$), *Prkaa1*$^{fl/fl}$ (CD11c^{WT}) and *Itgax*^{cre} *Prkaa1*$^{fl/fl}$ (CD11c$^{\Delta AMPK\alpha1}$) male mice were fed a high fat diet (HFD, 45% energy derived from fat, D12451, Research Diets) for 18-24 weeks as indicated.

For IL-17A neutralization experiments, 12-19 weeks old age-matched CD11c^{WT} and CD11c$^{\Delta LKB1}$ mice were systematically randomized over treatment groups based on body weight and fasting blood glucose levels, and fed a HFD for 6 weeks while concomitant biweekly treatment with 200 µg anti-mouse IL-17A (clone 17F3) or IgG1 κ isotype control (clone MOPC-21; both Bio X Cell). At sacrifice, spleen, visceral white adipose tissue (epididymal; eWAT), brown adipose tissue (intrascapular; BAT) and liver were weighed and collected for further processing.

Body composition and indirect calorimetry

Body composition was measured by MRI using an EchoMRI (Echo Medical Systems). Indirect calorimetry was performed in groups of 7-8 mice using a Comprehensive Laboratory Animal Monitoring System (Columbus Instruments) with free access to food and tap water. Mice were individually housed at room temperature and a standard 12-hour light/dark cycle was maintained throughout the measurements. Mice were acclimated to the cages for a period of 48 hours before the start of 4 days of measurements at 20 minute intervals. Food intake was assessed by real-time feed weight measurements. Oxygen consumption and carbon dioxide production were measured, and based on this respirometry, energy expenditure (EE), and carbohydrate (CHO) and fatty acid (FA) oxidation were calculated as previously described (82).

Isolation of leukocytes from spleen

Spleens were collected in 500 µL RPMI 1640 + Glutamax (Life Technolgies), mechanically disrupted, and digested for 20 min at 37 °C in medium supplemented with 1 mg/mL Collagenase D (Roche) and 2000 U/mL DNase I (Sigma-Aldrich). Digested samples were filtered through 100 µm filters and subjected to erythrocyte lysis buffer (0.15 M NH_4Cl, 1 mM $KHCO_3$, 0.1 mM Na_2EDTA) before counting using a hemocytometer.

Isolation of stromal vascular fraction from adipose tissue

After a 1 minute transcardial perfusion with PBS post sacrifice, eWAT samples were collected and digested as described previously (83, 84). In short, eWAT samples were minced and incubated for 1 hour at 37°C in an incubator under agitation (60 rpm) in HEPES-buffered

Krebs solution, containing 0.5-1 g/L collagenase type I from *Clostridium histolyticum* (Sigma-Aldrich), 2% (w/v) dialyzed bovine serum albumin (BSA, fraction V; Sigma-Aldrich) and 6 mM D-Glucose (Sigma-Aldrich). The samples were passed through a 100 µm filter (Corning Life Sciences) which was washed with PBS supplemented with 2.5 mM EDTA and 5% FCS. After allowing the adipocytes to settle for ~10 min, the infranatant, consisting of immune cells, was collected and pelleted at 350 x g for 10 min at room temperature. The pellet was treated with erythrocyte lysis buffer, washed with PBS/EDTA/FCS, and counted using a hemocytometer.

Isolation of leukocytes from liver

Livers were collected and digested as described previously (83, 84). In short, livers were minced and incubated for 45 min at 37°C in RPMI 1640 + Glutamax containing 1 mg/mL collagenase type IV from *Clostridium histolyticum*, 200 U/mL DNase (both Sigma-Aldrich) and 1 mM $CaCl_2$. The digested tissues were passed through a 100 µm cell strainer (Corning Life Sciences) which was subsequently washed with PBS/EDTA/FCS. After centrifugation (530 x g, 10 min at 4°C), cells were resuspended in 30 mL PBS/EDTA/FCS and spun down at 50 x g for 3 min at 4°C to pellet the hepatocytes. The supernatant was collected, treated with erythrocyte lysis buffer and $CD45^+$ leukocytes were isolated using LS columns and CD45 MicroBeads (35 µL beads per sample, Miltenyi Biotec) according to the manufacturer's protocol. Isolated liver leukocytes were counted using a hemocytometer.

Flow cytometry

For assessing LKB1/ACC phosphorylation state in spleen, eWAT and liver, tissues were collected and immediately minced in 1.85% formaldehyde solution (Sigma-Aldrich) and digested as described above. For confirmation of AMPK deficiency in $CD11c^{\Delta AMPK\alpha1}$ mice, digested splenocytes were incubated for 1 hour at 37°C, before fixation in 1.85% formaldehyde solution. Isolated cell suspensions were permanently permeabilized using 100% methanol for 10 min at -20°C. For other purposes, cells were stained using a Fixable Aqua Dead Cell Stain Kit (Invitrogen) or Zombie UV Fixable Viability Kit (Biolegend) for 20 min at room temperature. Unless sorted or measured alive, cells were fixed for 1 h at 4°C using a FOXP3/Transcription Factor Staining Buffer Set (Invitrogen, for FOXP3 and RORγT detection) or 15 min at room temperature using a 1.85% formaldehyde solution in PBS (Sigma-Aldrich, for everything else). For detection of intracellular cytokines, isolated cells were cultured for 4 h in RPMI 1640 + Glutamax in the presence of 10 µg/mL Brefeldin A (Sigma-Aldrich) and stimulated with either 100 ng/mL phorbol myristate acetate (PMA) and 1 µg/mL ionomycin (both Sigma-Aldrich; T cells), or 100 ng/mL LPS (Ultrapure, Invivogen; GMDCs). After 4 hours, cells were washed with PBS, stained with live/dead marker, and fixed as described above. Cell suspensions were first pre-incubated with 2.4G2 antibody (kindly provided by Louis Boon) for blocking Fc receptors and next stained for surface markers in PBS supplemented with 0.5% BSA (Roche) and 2 mM EDTA (Sigma-Aldrich) and antibodies for 30 min at 4°C. For detection of phosphorylated proteins, transcription factors and intracellular cytokines, cell suspensions were stained in Permeabilization Buffer (eBioscience) instead. Phosphorylated Ser79-ACC and Ser431-LKB1 were stained using unconjugated rabbit-anti-mouse antibodies prior to staining with other antibodies and goat-anti-rabbit-Alexa Fluor 647. Antibody information is provided in Table S1 and gating strategies for tissues shown in Figure S1. Cells were measured on a FACSCanto II, LSR II or a Cytek Aurora 3-laser spectral flow cytometer and analysed using FlowJo (Version 10.6, TreeStar).

Plasma analysis
Blood samples were collected from the tail tip of 4 h-fasted mice using paraoxon-coated glass capillaries. Fasting blood glucose level was determined using a hand-held Glucometer (Accu-Check; Roche Diagnostics) and plasma insulin level was measured using a commercial kit as per manufacturer's instructions (Chrystal Chem).

Insulin- and glucose tolerance tests
Whole-body insulin tolerance test (ipITT) and glucose tolerance test (ipGTT) were performed 1 week before sacrifice, as previously described (83, 84). In short, a bolus of insulin (0.75U/kg body mass, NOVORAPID, Novo Nordisk) was administered intraperitoneally (i.p.) to 4 h-fasted mice, after which blood glucose levels were measured at t=0, 15, 30, 45 and 60 min post insulin administration using a Glucometer. For ipGTT, 6 h-fasted mice were injected i.p. with 2g/kg total body mass of D-Glucose (Sigma-Aldrich) and blood glucose was measured at t=0, 20, 40, 60 and 90 min post glucose injection using a Glucometer.

Histological analysis
Pieces of eWAT and liver (~30 mg) were fixed in 4% formaldehyde solution (Sigma-Aldrich), paraffin-embedded, sectioned at 4 µm and stained with Hematoxilin and Eosin (H&E). Six fields at 20x magnification (total area 1.68 mm^2) were used for the analysis of adipocyte size, crown-like structures or hepatic steatosis.

Hepatic lipid composition
Liver lipids were extracted as previously described (85). Liver triglyceride and total cholesterol concentrations were measured using commercial kits (all from Instruchemie) and expressed as nanomoles per milligram of total protein content using the Bradford protein assay kit (Sigma-Aldrich).

***In vivo* DC expansion, isolation and sorting**
To expand the DC pool *in vivo*, 2 × 10^6 Flt3L-secreting B16 melanoma cells (kind gift from Dr. Edward Pearce) in 100 µL HBSS were injected subcutaneously into the flank of mice. After 10 days, spleen, liver and eWAT were harvested, and digested and processed as described earlier. cDC2s were further enriched from single cell suspensions by positive isolation with CD11c Microbeads (Miltenyi Biotec; per manufacturer's instructions) and FACS sorting ($MHCII^+$ $CD11c^+$ $CD64^-$ $F4/80^-$ $CD172a^+$ $XCR1^-$) on a BD FACSAria using a 100 µm nozzle at 20 PSI. Subsequently, sorted cDC2s were stimulated with 100 ng/mL LPS for 16 h for assessing cytokine expression by RT-qPCR.

BM-derived DC cultures
Bone marrow-derived DCs were cultured as described previously (22). Briefly, bone marrow cells were flushed from femurs and tibias, and 5 × 10^6 cells were plated in tissue culture-treated petri dishes (NUNC) in 10 mL of differentiation medium, consisting of RMPI 1640 Glutamax (Gibco) supplemented with 5% FCS (Gibco), 25 nM β-mercaptoethanol (Sigma-Aldrich), 100 U/mL penicillin, 100 µg/mL streptomycin and 20 ng/mL of murine GM-CSF (PeproTech). Medium was refreshed on day 4 and day 7, after which on day 10 non-adherent GMDCs were harvested. 1 x 10^5 GMDCs were seeded in a round-bottom 96-well plate and rested overnight. The next day, GMDCs were incubated for 2 h at 37°C with 50 µM MARK

inhibitor (MARK/Par-1 Activity Inhibitor, 39621; Calbiochem), 50 nM SIK inhibitor (HG-9-91-01; Cayman Chemical) or 1 μM NUAK inhibitor (WZ 4003; Tocris).

GMDCs adoptive transfer

GMDCs were pretreated for 2 hours with DMSO or SIK inhibitor (HG-9-91-01) and subsequently stimulated for 24 hours with 100 ng/mL LPS and 100 μg/mL OVA (InvivoGen). Cells were harvested, washed and 450,000 GMDCs, suspended in 30 μL HBSS without phenol red (ThermoFisher), were injected into the hock of WT C57Bl/6J mice. After eight days the draining popliteal lymph nodes were harvested and the Th17 response was analyzed by measuring RORγT expression and intracellular IL-17A by flow cytometry. The IL-17A concentration was also measured after a 48 hour OVA-specific restimulation of popliteal lymph node cells using BD cytometric bead array (CBA) flex-set kits (BD Biosciences, according manufactures instructions.

RNA-isolation and RT-qPCR

RNA was extracted from snap-frozen liver samples and LPS-stimulated sorted cDC2s or GMDCs using TriPure RNA Isolation reagent. Total RNA (200-400 ng for sorted cDC2s or GMDCs; *2 mg for liver*) was reverse transcribed using the M-MLV Reverse Transcriptase kit (ThermoFisher). Real-time qPCR runs were performed on a CFX96 Real-time C1000 thermal cycler (Biorad) using the GoTaq qPCR Master Mix kit (Promega). Gene expression was normalized to the housekeeping gene *Rplp0* and expressed as fold change compared to $CD11c^{WT}$ samples. A list of primer sequences can be found in Table S2.

Western Blot

GMDCs were washed in PBS, snap-frozen in liquid nitrogen and lysed in ice-cold buffer containing: 50 mM Hepes (pH 7.6), 50 mM NaF, 50 mM KCl, 5 mM NaPPi, 1 mM EDTA, 1 mM EGTA, 1 mM DTT, 5 mM β-glycerophosphate, 1 mM sodium vanadate, 1% NP40, and protease inhibitors cocktail (Complete, Roche). Proteins were separated by SDS-PAGE and transferred to a PVDF membrane. Membranes were blocked for 1 h at room temperature in TTBS buffer (20 mM Tris–HCl [pH 7.6], 137 mM NaCl, and 0.25% [v/v] Tween 20) containing 5% (w/v) fat free milk. Membranes were incubated with primary antibodies overnight at 4°C, washed in TTBS buffer, incubated with horseradish peroxidase-conjugated secondary antibodies for 2 hours at room temperature, washed again and developed using enhanced chemiluminescence. Primary antibodies: AMPK (Cell Signaling #2532) and HSP90 (Santa Cruz #sc7947).

Statistical analysis

All data are presented as mean ± standard error of the mean (SEM). Statistical analysis was performed using GraphPad Prism version 8 for Windows (GraphPad Software) with unpaired t-test, one-way or two-way analysis of variance (ANOVA) followed by Fisher's or Dunnett's post-hoc tests. Differences between groups were considered statistically significant at $P < 0.05$.

Study approval

Mouse experiments have received approval from the Dutch Central Authority for Scientific Procedures on Animals (CCD; animal license number AVD116002015253).

Author contributions

HJP van der Zande, EC Brombacher, M. Yazdanbakhsh, B. Everts and B. Guigas conceptualized research; HJP van der Zande, EC Brombacher, JM Lambooij, F. Otto and B. Guigas analyzed data; HJP van der Zande, EC Brombacher, JM Lambooij, LR Pelgrom, A. Zawistowska-Deniziak, TA Patente, G. Heieis, F. Otto and A. Ozir-Fazalalikhan performed research; M. Yazdanbakhsh, B. Everts and B. Guigas supervised the study; and HJP van der Zande, EC Brombacher, B. Everts and B. Guigas wrote the manuscript. HJP van der Zande and EC Brombacher contributed equally to this study and should be considered as shared first author; the author order was established based on the chronological contribution to the manuscript. Same reasoning applies to senior authorship, with B Everts and B Guigas having also contributed equally to the study.

Acknowledgements

This study was supported by the Dutch Organization for Scientific Research (NWO) Graduate School Program (022.006.010 to HvdZ) and the LUMC fellowship (to BE). The funders had no role in study design, data collection and analysis, decision to publish, or preparation of the manuscript. The authors thank Ko Willems van Dijk and Patrick Rensen (Leiden University Medical Center) for allowing the use of the LUMC metabolic phenotyping platform (MRI and metabolic cages) and Selah Voorbraak for appreciable technical help during the revision of the manuscript. The authors also acknowledge the LUMC Flow cytometry Core Facility (FCF) for technical support and cell sorting assistance.

Conflict of interest statement

The authors have declared that no conflict of interest exists.

References

1. Gregor MF, Hotamisligil GS. Inflammatory mechanisms in obesity. Annu Rev Immunol. 011;29:415-45.
2. van der Zande HJP, Zawistowska-Deniziak A, Guigas B. Immune Regulation of Metabolic Homeostasis by Helminths and Their Molecules. Trends Parasitol. 2019;35(10):795-808.
3. Hotamisligil GS, Shargill NS, Spiegelman BM. Adipose expression of tumor necrosis factor-alpha: direct role in obesity-linked insulin resistance. Science. 1993;259(5091):87-91.
4. Stienstra R, Joosten LA, Koenen T, van Tits B, van Diepen JA, van den Berg SA, et al. The inflammasome-mediated caspase-1 activation controls adipocyte differentiation and insulin sensitivity. Cell Metab. 2010;12(6):593-605.
5. Bertola A, Ciucci T, Rousseau D, Bourlier V, Duffaut C, Bonnafous S, et al. Identification of adipose tissue dendritic cells correlated with obesity-associated insulin-resistance and inducing Th17 responses in mice and patients. Diabetes. 2012;61(9):2238-47.
6. Stefanovic-Racic M, Yang X, Turner MS, Mantell BS, Stolz DB, Sumpter TL, et al. Dendritic cells promote macrophage infiltration and comprise a substantial proportion of obesity-associated increases in CD11c+ cells in adipose tissue and liver. Diabetes. 2012;61(9):2330-9.
7. Cho KW, Zamarron BF, Muir LA, Singer K, Porsche CE, DelProposto JB, et al. Adipose Tissue Dendritic Cells Are Independent Contributors to Obesity-Induced Inflammation and Insulin Resistance. J Immunol. 2016;197(9):3650-61.
8. Deczkowska A, David E, Ramadori P, Pfister D, Safran M, At The B, et al. XCR1(+) type 1 conventional dendritic cells drive liver pathology in non-alcoholic steatohepatitis. Nat Med. 2021;27(6):1043-54.
9. Wu D, Molofsky AB, Liang HE, Ricardo-Gonzalez RR, Jouihan HA, Bando JK, et al. Eosinophils sustain adipose alternatively activated macrophages associated with glucose homeostasis. Science. 2011;332(6026):243-7.
10. Molofsky AB, Nussbaum JC, Liang HE, Van Dyken SJ, Cheng LE, Mohapatra A, et al. Innate lymphoid type 2 cells sustain visceral adipose tissue eosinophils and alternatively activated macrophages. J Exp Med. 2013;210(3):535-49.
11. Feuerer M, Herrero L, Cipolletta D, Naaz A, Wong J, Nayer A, et al. Lean, but not obese, fat is enriched for a unique population of regulatory T cells that affect metabolic parameters. Nat Med. 2009;15(8):930-9.
12. Tang Y, Bian Z, Zhao L, Liu Y, Liang S, Wang Q, et al. Interleukin-17 exacerbates hepatic steatosis and inflammation in non-alcoholic fatty liver disease. Clin Exp Immunol. 2011;166(2):281-90.
13. Fabbrini E, Cella M, McCartney SA, Fuchs A, Abumrad NA, Pietka TA, et al. Association between specific adipose tissue CD4+ T-cell populations and insulin resistance in obese individuals. Gastroenterology. 2013;145(2):366-74 e1-3.
14. Harley IT, Stankiewicz TE, Giles DA, Softic S, Flick LM, Cappelletti M, et al. IL-17 signaling accelerates the progression of nonalcoholic fatty liver disease in mice. Hepatology. 2014;59(5):1830-9.
15. Gomes AL, Teijeiro A, Buren S, Tummala KS, Yilmaz M, Waisman A, et al. Metabolic Inflammation-Associated IL-17A Causes Non-alcoholic Steatohepatitis and Hepatocellular Carcinoma. Cancer Cell. 2016;30(1):161-75.
16. Moreno-Fernandez ME, Giles DA, Oates JR, Chan CC, Damen M, Doll JR, et al. PKM2-dependent metabolic skewing of hepatic Th17 cells regulates pathogenesis of non-alcoholic fatty liver disease. Cell Metab. 2021;33(6):1187-204 e9.
17. Patente TA, Pelgrom LR, Everts B. Dendritic cells are what they eat: how their metabolism shapes T helper cell polarization. Curr Opin Immunol. 2019;58:16-23.
18. Pearce EJ, Everts B. Dendritic cell metabolism. Nat Rev Immunol. 2015;15(1):18-29.

19. Brombacher EC, Everts B. Shaping of Dendritic Cell Function by the Metabolic Micro-Environment. Front Endocrinol (Lausanne). 2020;11:555.

20. Chen S, Fang L, Guo W, Zhou Y, Yu G, Li W, et al. Control of Treg cell homeostasis and immune equilibrium by Lkb1 in dendritic cells. Nat Commun. 2018;9(1):5298.

21. Wang Y, Du X, Wei J, Long L, Tan H, Guy C, et al. LKB1 orchestrates dendritic cell metabolic quiescence and anti-tumor immunity. Cell Res. 2019;29(5):391-405.

22. Pelgrom LR, Patente TA, Sergushichev A, Esaulova E, Otto F, Ozir-Fazalalikhan A, et al. LKB1 expressed in dendritic cells governs the development and expansion of thymus-derived regulatory T cells. Cell Res. 2019;29(5):406-19.

23. Jaleel M, McBride A, Lizcano JM, Deak M, Toth R, Morrice NA, et al. Identification of the sucrose non-fermenting related kinase SNRK, as a novel LKB1 substrate. FEBS Lett. 2005;579(6):1417-23.

24. Lizcano JM, Goransson O, Toth R, Deak M, Morrice NA, Boudeau J, et al. LKB1 is a master kinase that activates 13 kinases of the AMPK subfamily, including MARK/PAR-1. EMBO J. 2004;23(4):833-43.

25. Shackelford DB, Shaw RJ. The LKB1-AMPK pathway: metabolism and growth control in tumour suppression. Nat Rev Cancer. 2009;9(8):563-75.

26. Caton ML, Smith-Raska MR, Reizis B. Notch-RBP-J signaling controls the homeostasis of CD8- dendritic cells in the spleen. J Exp Med. 2007;204(7):1653-64.

27. Teijeiro A, Garrido A, Ferre A, Perna C, Djouder N. Inhibition of the IL-17A axis in adipocytes suppresses diet-induced obesity and metabolic disorders in mice. Nat Metab. 2021;3(4):496-512.

28. Nishimura T, Saito Y, Washio K, Komori S, Respatika D, Kotani T, et al. SIRPalpha on CD11c(+) cells induces Th17 cell differentiation and subsequent inflammation in the CNS in experimental autoimmune encephalomyelitis. Eur J Immunol. 2020;50(10):1560-70.

29. Nieves W, Hung LY, Oniskey TK, Boon L, Foretz M, Viollet B, et al. Myeloid-Restricted AMP-Kalpha1 Promotes Host Immunity and Protects against IL-12/23p40-Dependent Lung Injury during Hookworm Infection. J Immunol. 2016;196(11):4632-40.

30. Gainullina A, Huang L-H, Todorov H, Kim K, Yng LS, Kent A, et al. Open Source ImmGen: network perspective on metabolic diversity among mononuclear phagocytes. bioRxiv. 2020:2020.07.15.204388.

31. Remmerie A, Martens L, Thone T, Castoldi A, Seurinck R, Pavie B, et al. Osteopontin Expression Identifies a Subset of Recruited Macrophages Distinct from Kupffer Cells in the Fatty Liver. Immunity. 2020;53(3):641-57 e14.

32. Liu Y, Zhang Q, Ding Y, Li X, Zhao D, Zhao K, et al. Histone lysine methyltransferase Ezh1 promotes TLR-triggered inflammatory cytokine production by suppressing Tollip. J Immunol. 2015;194(6):2838-46.

33. He N, Fan W, Henriquez B, Yu RT, Atkins AR, Liddle C, et al. Metabolic control of regulatory T cell (Treg) survival and function by Lkb1. Proc Natl Acad Sci U S A. 2017;114(47):12542-7.

34. Gormand A, Berggreen C, Amar L, Henriksson E, Lund I, Albinsson S, et al. LKB1 signalling attenuates early events of adipogenesis and responds to adipogenic cues. J Mol Endocrinol. 2014;53(1):117-30.

35. Xie Z, Dong Y, Scholz R, Neumann D, Zou MH. Phosphorylation of LKB1 at serine 428 by protein kinase C-zeta is required for metformin-enhanced activation of the AMP-activated protein kinase in endothelial cells. Circulation. 2008;117(7):952-62.

36. Sapkota GP, Kieloch A, Lizcano JM, Lain S, Arthur JS, Williams MR, et al. Phosphorylation of the protein kinase mutated in Peutz-Jeghers cancer syndrome, LKB1/STK11, at Ser431 by p90(RSK) and cAMP-dependent protein kinase, but not its farnesylation at Cys(433), is essential for LKB1 to suppress cell vrowth. J Biol Chem. 2001;276(22):19469-82.

37. Houde Vanessa P, Ritorto Maria S, Gourlay R, Varghese J, Davies P, Shpiro N, et al. Investiga-

tion of LKB1 Ser431 phosphorylation and Cys433 farnesylation using mouse knockin analysis reveals an unexpected role of prenylation in regulating AMPK activity. Biochemical Journal. 2014;458(1):41-56.

38. Nagpal R, Newman TM, Wang S, Jain S, Lovato JF, Yadav H. Obesity-Linked Gut Microbiome Dysbiosis Associated with Derangements in Gut Permeability and Intestinal Cellular Homeostasis Independent of Diet. J Diabetes Res. 2018;2018:3462092.

39. Thaiss CA, Itav S, Rothschild D, Meijer MT, Levy M, Moresi C, et al. Persistent microbiome alterations modulate the rate of post-dieting weight regain. Nature. 2016;540(7634):544-51.

40. Liu R, Hong J, Xu X, Feng Q, Zhang D, Gu Y, et al. Gut microbiome and serum metabolome alterations in obesity and after weight-loss intervention. Nat Med. 2017;23(7):859-68.

41. Martin-Mateos R, Albillos A. The Role of the Gut-Liver Axis in Metabolic Dysfunction-Associated Fatty Liver Disease. Front Immunol. 2021;12:660179.

42. Liu Z, Zhang W, Zhang M, Zhu H, Moriasi C, Zou MH. Liver kinase B1 suppresses lipopolysaccharide-induced nuclear factor kappaB (NF-kappaB) activation in macrophages. J Biol Chem. 2015;290(4):2312-20.

43. Zhao ZH, Wang ZX, Zhou D, Han Y, Ma F, Hu Z, et al. Sodium Butyrate Supplementation Inhibits Hepatic Steatosis by Stimulating Liver Kinase B1 and Insulin-Induced Gene. Cell Mol Gastroenterol Hepatol. 2021.

44. Ma X, Hua J, Mohamood AR, Hamad ARA, Ravi R, Li Z. A high-fat diet and regulatory T cells influence susceptibility to endotoxin-induced liver injury. Hepatology. 2007;46(5):1519-29.

45. Han JM, Wu D, Denroche HC, Yao Y, Verchere CB, Levings MK. IL-33 Reverses an Obesity-Induced Deficit in Visceral Adipose Tissue ST2+ T Regulatory Cells and Ameliorates Adipose Tissue Inflammation and Insulin Resistance. J Immunol. 2015;194(10):4777-83.

46. Wara AK, Wang S, Wu C, Fang F, Haemmig S, Weber BN, et al. KLF10 Deficiency in CD4(+) T Cells Triggers Obesity, Insulin Resistance, and Fatty Liver. Cell Rep. 2020;33(13):108550.

47. Bapat SP, Myoung Suh J, Fang S, Liu S, Zhang Y, Cheng A, et al. Depletion of fat-resident Treg cells prevents age-associated insulin resistance. Nature. 2015;528(7580):137-41.

48. Wu D, Wong CK, Han JM, Orban PC, Huang Q, Gillies J, et al. T reg-specific insulin receptor deletion prevents diet-induced and age-associated metabolic syndrome. J Exp Med. 2020;217(8).

49. Beppu LY, Mooli RGR, Qu X, Marrero GJ, Finley CA, Fooks AN, et al. Tregs facilitate obesity and insulin resistance via a Blimp-1/IL-10 axis. JCI Insight. 2021;6(3).

50. Rau M, Schilling AK, Meertens J, Hering I, Weiss J, Jurowich C, et al. Progression from Nonalcoholic Fatty Liver to Nonalcoholic Steatohepatitis Is Marked by a Higher Frequency of Th17 Cells in the Liver and an Increased Th17/Resting Regulatory T Cell Ratio in Peripheral Blood and in the Liver. J Immunol. 2016;196(1):97-105.

51. Rolla S, Alchera E, Imarisio C, Bardina V, Valente G, Cappello P, et al. The balance between IL-17 and IL-22 produced by liver-infiltrating T-helper cells critically controls NASH development in mice. Clinical Science. 2015;130(3):193-203.

52. Tan Z, Qian X, Jiang R, Liu Q, Wang Y, Chen C, et al. IL-17A Plays a Critical Role in the Pathogenesis of Liver Fibrosis through Hepatic Stellate Cell Activation. The Journal of Immunology. 2013;191(4):1835-44.

53. Volpe E, Servant N, Zollinger R, Bogiatzi SI, Hupe P, Barillot E, et al. A critical function for transforming growth factor-beta, interleukin 23 and proinflammatory cytokines in driving and modulating human T(H)-17 responses. Nat Immunol. 2008;9(6):650-7.

54. Manel N, Unutmaz D, Littman DR. The differentiation of human T(H)-17 cells requires transforming growth factor-beta and induction of the nuclear receptor RORgammat. Nat Immunol. 2008;9(6):641-9.

55. Ghoreschi K, Laurence A, Yang XP, Tato CM, McGeachy MJ, Konkel JE, et al. Generation of pathogenic T(H)17 cells in the absence of TGF-beta signalling. Nature. 2010;467(7318):967-71.

56. Lee Y, Awasthi A, Yosef N, Quintana FJ, Xiao S, Peters A, et al. Induction and molecular signature of pathogenic TH17 cells. Nat Immunol. 2012;13(10):991-9.

57. Scott CL, Tfp ZM, Beckham KS, Douce G, Mowat AM. Signal regulatory protein alpha (SIRPalpha) regulates the homeostasis of CD103(+) CD11b(+) DCs in the intestinal lamina propria. Eur J Immunol. 2014;44(12):3658-68.

58. Dostert C, Grusdat M, Letellier E, Brenner D. The TNF Family of Ligands and Receptors: Communication Modules in the Immune System and Beyond. Physiological Reviews. 2018;99(1):115-60.

59. Zhang Z, Wen H, Peng B, Weng J, Zeng F. HFD-induced TRAF6 upregulation promotes liver cholesterol accumulation and fatty liver development via EZH2-mediated miR-429/PPARα axis. Molecular Therapy - Nucleic Acids. 2021;24:711-27.

60. Zhang JL, Du BB, Zhang DH, Li H, Kong LY, Fan GJ, et al. OTUB1 alleviates NASH through inhibition of the TRAF6-ASK1 signaling pathways. Hepatology. 2022;75(5).

61. Qiao L, Zou C, Shao P, Schaack J, Johnson PF, Shao J. Transcriptional Regulation of Fatty Acid Translocase/CD36 Expression by CCAAT/Enhancer-binding Protein α *. Journal of Biological Chemistry. 2008;283(14):8788-95.

62. Silverstein RL, Febbraio M. CD36, a Scavenger Receptor Involved in Immunity, Metabolism, Angiogenesis, and Behavior. Science Signaling. 2009;2(72):re3-re.

63. Koonen DPY, Jacobs RL, Febbraio M, Young ME, Soltys C-LM, Ong H, et al. Increased Hepatic CD36 Expression Contributes to Dyslipidemia Associated With Diet-Induced Obesity. Diabetes. 2007;56(12):2863-71.

64. Greco D, Kotronen A, Westerbacka J, Puig O, Arkkila P, Kiviluoto T, et al. Gene expression in human NAFLD. American Journal of Physiology-Gastrointestinal and Liver Physiology. 2008;294(5):G1281-G7.

65. Miquilena-Colina ME, Lima-Cabello E, Sánchez-Campos S, García-Mediavilla MV, Fernández-Bermejo M, Lozano-Rodríguez T, et al. Hepatic fatty acid translocase CD36 upregulation is associated with insulin resistance, hyperinsulinaemia and increased steatosis in non-alcoholic steatohepatitis and chronic hepatitis C. Gut. 2011;60(10):1394.

66. Zeng H, Qin H, Liao M, Zheng E, Luo X, Xiao A, et al. CD36 promotes de novo lipogenesis in hepatocytes through INSIG2-dependent SREBP1 processing. Molecular Metabolism. 2022;57:101428.

67. Wilson CG, Tran JL, Erion DM, Vera NB, Febbraio M, Weiss EJ. Hepatocyte-Specific Disruption of CD36 Attenuates Fatty Liver and Improves Insulin Sensitivity in HFD-Fed Mice. Endocrinology. 2016;157(2):570-85.

68. Shi Q, Yin Z, Liu P, Zhao B, Zhang Z, Mao S, et al. Cilostazol Suppresses IL-23 Production in Human Dendritic Cells via an AMPK-Dependent Pathway. Cell Physiol Biochem. 2016;40(3-4):499-508.

69. Wildenberg ME, Vos AC, Wolfkamp SC, Duijvestein M, Verhaar AP, Te Velde AA, et al. Autophagy attenuates the adaptive immune response by destabilizing the immunologic synapse. Gastroenterology. 2012;142(7):1493-503 e6.

70. Krawczyk CM, Holowka T, Sun J, Blagih J, Amiel E, DeBerardinis RJ, et al. Toll-like receptor-induced changes in glycolytic metabolism regulate dendritic cell activation. Blood. 2010;115(23):4742-9.

71. Sun Z, Jiang Q, Li J, Guo J. The potent roles of salt-inducible kinases (SIKs) in metabolic homeostasis and tumorigenesis. Signal Transduct Target Ther. 2020;5(1):150.

72. Wein MN, Foretz M, Fisher DE, Xavier RJ, Kronenberg HM. Salt-Inducible Kinases: Physiology, Regulation by cAMP, and Therapeutic Potential. Trends Endocrinol Metab. 2018;29(10):723-35.

73. Altarejos JY, Montminy M. CREB and the CRTC co-activators: sensors for hormonal and metabolic signals. Nat Rev Mol Cell Biol. 2011;12(3):141-51.

74. Dendorfer U, Oettgen P, Libermann TA. Multiple regulatory elements in the interleukin-6 gene mediate induction by prostaglandins, cyclic AMP, and lipopolysaccharide. Mol Cell Biol. 1994;14(7):4443-54.

75. Chandra G, Cogswell JP, Miller LR, Godlevski MM, Stinnett SW, Noel SL, et al. Cyclic AMP signaling pathways are important in IL-1 beta transcriptional regulation. J Immunol. 1995;155(10):4535-43.

76. Kocieda VP, Adhikary S, Emig F, Yen JH, Toscano MG, Ganea D. Prostaglandin E2-induced IL-23p19 subunit is regulated by cAMP-responsive element-binding protein and C/AATT enhancer-binding protein beta in bone marrow-derived dendritic cells. J Biol Chem. 2012;287(44):36922-35.

77. Hollstein PE, Eichner LJ, Brun SN, Kamireddy A, Svensson RU, Vera LI, et al. The AMPK-Related Kinases SIK1 and SIK3 Mediate Key Tumor-Suppressive Effects of LKB1 in NSCLC. Cancer Discov. 2019;9(11):1606-27.

78. Yong Kim S, Jeong S, Chah KH, Jung E, Baek KH, Kim ST, et al. Salt-inducible kinases 1 and 3 negatively regulate Toll-like receptor 4-mediated signal. Mol Endocrinol. 2013;27(11):1958-68.

79. Lombardi MS, Gillieron C, Dietrich D, Gabay C. SIK inhibition in human myeloid cells modulates TLR and IL-1R signaling and induces an anti-inflammatory phenotype. J Leukoc Biol. 2016;99(5):711-21.

80. Sundberg TB, Choi HG, Song JH, Russell CN, Hussain MM, Graham DB, et al. Small-molecule screening identifies inhibition of salt-inducible kinases as a therapeutic strategy to enhance immunoregulatory functions of dendritic cells. Proc Natl Acad Sci U S A. 2014;111(34):12468-73.

81. Durai V, Murphy KM. Functions of Murine Dendritic Cells. Immunity. 2016;45(4):719-36.

82. van der Zande HJP, Lambooij JM, Chavanelle V, Zawistowska-Deniziak A, Otero Y, Otto F, et al. Effects of a novel polyphenol-rich plant extract on body composition, inflammation, insulin sensitivity, and glucose homeostasis in obese mice. Int J Obes (Lond). 2021.

83. Hussaarts L, Garcia-Tardon N, van Beek L, Heemskerk MM, Haeberlein S, van der Zon GC, et al. Chronic helminth infection and helminth-derived egg antigens promote adipose tissue M2 macrophages and improve insulin sensitivity in obese mice. FASEB J. 2015;29(7):3027-39.

84. van der Zande HJP, Gonzalez MA, de Ruiter K, Wilbers RHP, Garcia-Tardon N, van Huizen M, et al. The helminth glycoprotein omega-1 improves metabolic homeostasis in obese mice through type 2 immunity-independent inhibition of food intake. FASEB J. 2021;35(2):e21331.

85. Thomas A, Belaidi E, Moulin S, Horman S, van der Zon GC, Viollet B, et al. Chronic Intermittent Hypoxia Impairs Insulin Sensitivity but Improves Whole-Body Glucose Tolerance by Activating Skeletal Muscle AMPK. Diabetes. 2017;66(12):2942-51.

Supplementary information

Supplementary table 1: Antibodies and reagents for flow cytometry

Target	Clone	Conjugate	Source	Identifier
B220	RA3-6B2	FITC	eBioscience	11-0452
CD3	17A2	APC-eF780	eBioscience	47-0032
CD3	17A2	BV605	Biolegend	100237
CD3	17A2	FITC	eBioscience	11-0032
CD4	GK1.5	BV650	BD Biosciences	563232
CD4	GK1.5	PE-Cy7	eBioscience	25-0041
CD4	GK1.5	PerCP-eFluor 710	eBioscience	46-0041
CD8a	53-6.7	BV711	Biolegend	100759
CD8a	53-6.7	PE	eBioscience	12-0081
CD11b	M1/70	FITC	eBioscience	11-0112
CD11b	M1/70	PE-Cy7	eBioscience	25-0112
CD11c	N418	BV421	Biolegend	117330
CD11c	HL3	FITC	BD Biosciences	553801
CD11c	HL3	Horizon V450	BD Biosciences	560521
CD11c	N418	PE-Cy7	eBioscience	25-0114
CD19	MB19-1	FITC	eBioscience	11-0191
CD40	HM40-3	FITC	eBioscience	11-0402
CD44	IM7	eFluor 450	eBioscience	48-0441
CD45	30-F11	BV785	Biolegend	103149
CD45.2	104	FITC	Biolegend	109806
CD45.2	104	eFluor 450	eBioscience	48-0454
CD64	X54-5/7.1	PE	Biolegend	139304
CD64	X54-5/7.1	PE/Dazzle 594	Biolegend	139319
CD64	X54-5/7.1	PerCP-Cy5.5	Biolegend	139308
CD80	16-10A1	APC	eBioscience	17-0801
CD86	GL-1	APC/Fire 750	Biolegend	105045
CD86	GL-1	PE	BD Biosciences	553692
CD172a	P84	PE	Biolegend	144011
CD197/CCR7	4B12	PerCP-Cy5.5	Biolegend	120116
F4/80	BM8	APC	eBioscience	17-4801
F4/80	BM8	BV711	Biolegend	123147
FOXP3	FJK-16s	APC	eBioscience	17-5773
Goat-anti-Rabbit	Polyclonal	Alexa Fluor 647	Invitrogen	A21244

Target	Clone	Conjugate	Source	Identifier
GR-1	RB6-8C5	FITC	BD Biosciences	553126
IFNγ	XMG1.2	FITC	eBioscience	11-7311
IL-5	TRFK5	PE	Biolegend	504303
IL-6	MP5-20F3	APC	Biolegend	504507
IL-17A	eBio17B7	PE-Cy7	eBioscience	25-7177
IL-17A	TC11-18H10.1	PerCP-Cy5.5	Biolegend	506919
IL-23p19	fc23cpg	eFluor 660	Invitrogen	50-7023
LAP	TW7-16B4	PerCP-eF710	Invitrogen	46-9821
Ly6C	HK1.4	APC-Cy7	Biolegend	128026
MHCI/H-2Kb	AF6-88.5	Pacific Blue	Biolegend	116514
MHCII	M5/114 15.2	Alexa Fluor 700	Invitrogen	56-5321
MHCII	M5/114 15.2	APC-eFluor 780	eBioscience	47-5321
MHCII	M5/114 15.2	FITC	eBioscience	11-5321
NK1.1	PK136	FITC	eBioscience	11-5941
Phospho-ACC (Ser79)	D7D11	-	Cell Signaling	11818S
Phospho-LKB1 (Ser431)	C67A3	-	Cell Signaling	3482S
Pro-IL-1β	NJTEN3	PE	Invitrogen	12-7114
RORgT	Q31-378	PE	BD Biosciences	562607
Siglec-F	E50-2440	PE	BD Biosciences	552126
XCR1	ZET	BV650	Biolegend	148220

Other reagents	Source	Identifier
LIVE/DEAD™ Fixable Aqua Dead Cell Stain Kit	Invitrogen	L34957
Zombie UV™ Fixable Viability Kit	Biolegend	423107

Supplementary table 2: qPCR primers

Gene	Accession number	Forward primer	Reverse primer
Acaca	NM_133360.2	CAGCTGGTGCAGAGGTACCG	TCTACTCGCAGGTACTGCCG
Acox1	NM_015729	GGGACCCACAAGCCTCTGCCA	GTGCCGTCAGGCTTCACCTGG
Acta2	NM_007392.3	AGCCATCTTTCATTGGGATGG	CCCCTGACAGGACGTTGTTA
Cidec	NM_178373	CCATCAGAACAGCGCAAGAAG	AGAGGGTTGCCTTCACGTTC
Cd36	NM_001159558	GCAAAGAACAGCAGCAAAATC	CAGTGAAGGCTCAAAGATGG
Col1a1	NM_007742.3	GAGAGGTGAACAAGGTCCCG	AAACCTCTCTCGCCTCTTGC
Cpt1a	NM_013495	AGGAGACAAGAACCCCAACA	AAGGAATGCAGGTCCACATC
Fasn	NM_007988	CACAGGCATCAATGTCAACC	TTTGGGAAGTCCTCAGCAAC
Fabp1	NM_017399.4	GCCACCATGAACTTCTCCGGCA	GGTCCTCGGGCAGACCTATTGC
Il1b	NM_008361	GACCCCAAAAGATGAAGGGCT	ATGTGCTGCTGCGAGATTTG
Il6	NM_031168.2	CCTCTCTGCAAGAGACTTCCAT	ACAGGTCTGTTGGGAGTGGT
Il23a	NM_031252.2	GCACCAGCGGGACATATGAA	CAAGCAGAACTGGCTGTTGTC
Plin4	NM_020568.3	TGCCCCCTCATCTAAAGTGTC	AGGCATCTTCACTGCTGGTC
Rplp0	NM_007475	TCTGGAGGGTGTCCGCAACG	GCCAGGACGCGCTTGTACCC
Scd1	NM_009127.4	GCTCTACACCTGCCTCTTCGGGAT	TCCAGAGGCGATGAGCCCCG
Stk11	NM_011492.4	GTGCCAAGCTCATGGGTACT	CACCGAGGTCGGAGATCTTG
Tgfb1	NM_011577	GCTGAACCAAGGAGACGGAA	ATGTCATGGATGGTGCCCAG
Timp1	NM_011593	AGTGCCTGCAGCTTCTTGGT	CAGCCAGCACTATAGGTCTTTGAG

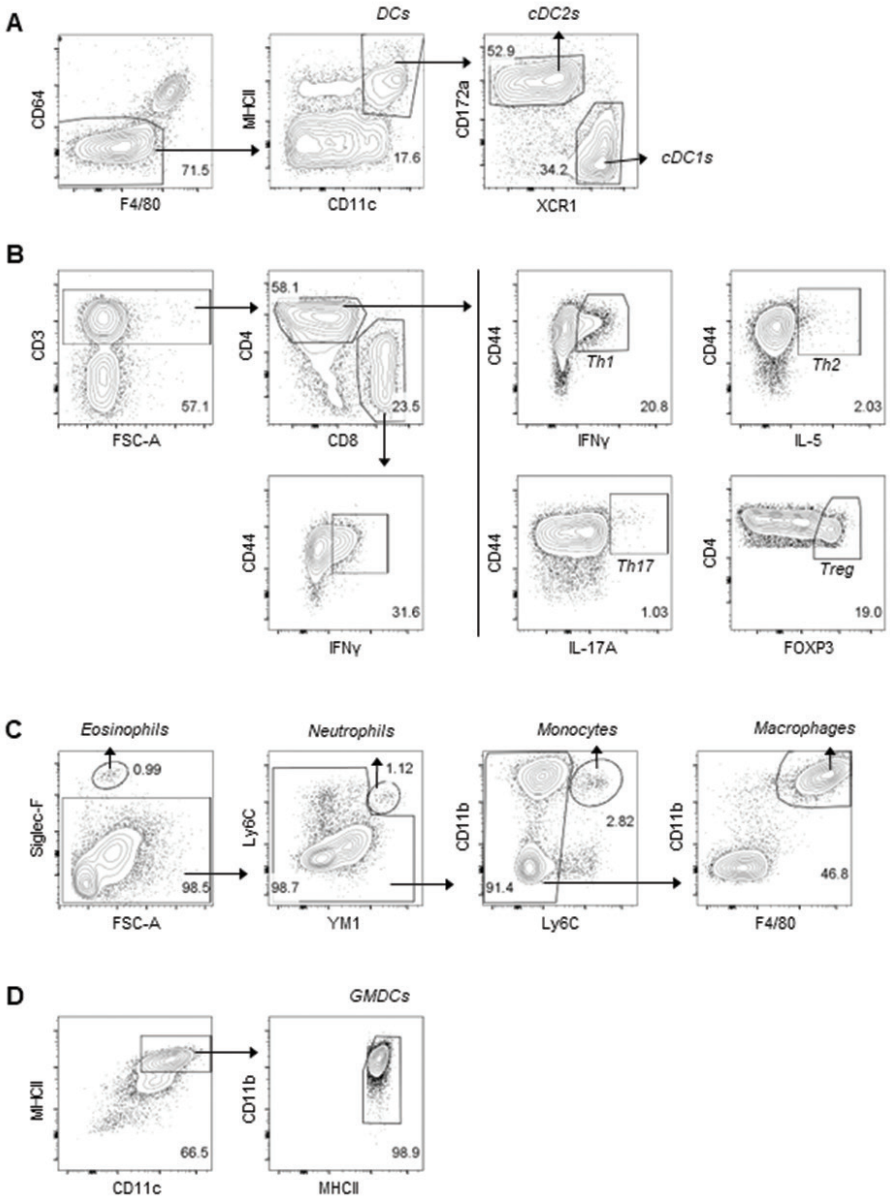

Figure S1. Gating strategies. A: Gating strategy for analysis of DCs and cDC subsets. CD11b and CD8a were used as alternatives for CD172a and XCR1, respectively. **B:** Gating strategy for T (helper) cell subsets is shown. **C:** Gating strategy for identification of myeloid cell subsets. **D:** Gating strategy for identification of GMDCs. Isolated cells were pre-gated on live CD45^{+} single cells. For T (helper) cell subset analysis, cells were additionally pre-gated as lineage-, which included antibodies directed against B220, CD11b, CD11c, GR-1 and NK1.1. Representative sample was chosen from eWAT samples for A-C. Gating strategies were similar for the indicated cell populations in liver and spleen.

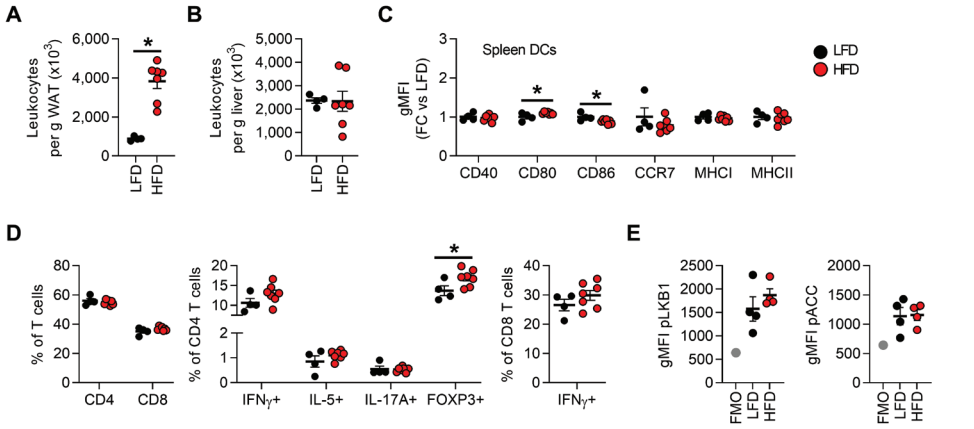

Figure S2. Leukocytes per gram WAT and liver, and splenic DCs and T cells are mostly unaffected by obesity.

Mice were fed a LFD (black symbols) or a HFD (red symbols) for 24 weeks. **A-B:** Absolute numbers of leukocytes per g tissue in eWAT **(A)** and liver **(B)**. **C:** At sacrifice, spleen was collected and immune cells were isolated and analysed by flow cytometry. Relative expression of indicated DC markers by splenic DCs. **D:** Cells were restimulated with PMA/ionomycin in the presence of Brefeldin A for detection of intracellular cytokines, and were analysed by flow cytometry. CD4 and CD8 T cell, Th1, Th2, Th17 and Treg CD4 T cell, and IFNγ$^+$ CD8 T cell percentages in spleen. **E:** Spleens were immediately formaldehyde-fixed after collection and immune cells were isolated. Phosphorylated LKB1 (Ser431) and ACC (Ser79) were measured in DCs from spleen by flow cytometry. Results are expressed as means ± SEM. * P<0.05 vs LFD (n = 4-7 mice per group). Related to figure 1.

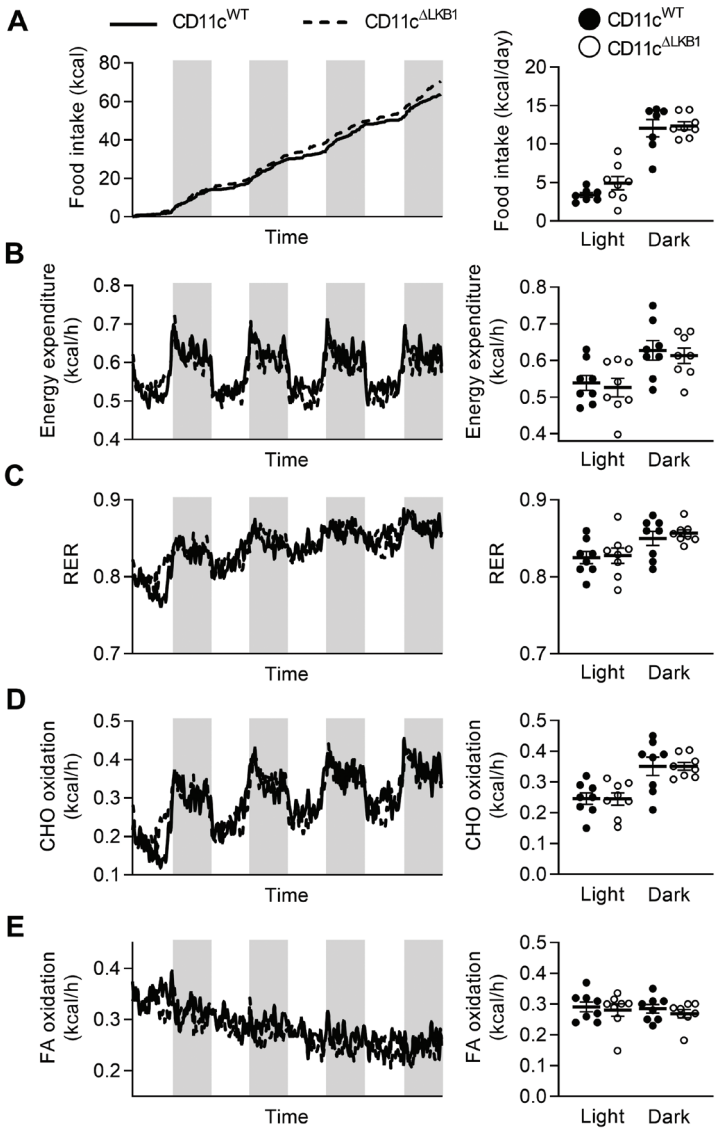

Figure S3. LKB1 deficiency in DCs does not affect food intake and whole-body energy expenditure. CD11c^{WT} (black symbols) and CD11c$^{\Delta LKB1}$ (open symbols) mice were fed a HFD for 18 weeks. At week 15, mice were subjected to individual indirect calorimetric measurements using fully automated metabolic cages with free access to food and water. **A-E:** Cumulative food intake **(A)**, energy expenditure (EE; **B**), respiratory exchange rate (RER; **C**), carbohydrate (CHO; **D**) and fatty acid (FA; **E**) oxidation were measured for 4 consecutive days (white part = light phase; grey part = dark phase). The daily averages for each of the abovementioned parameters were calculated. Results are expressed as means ± SEM. (n = 7-8 mice per group). Related to figure 2.

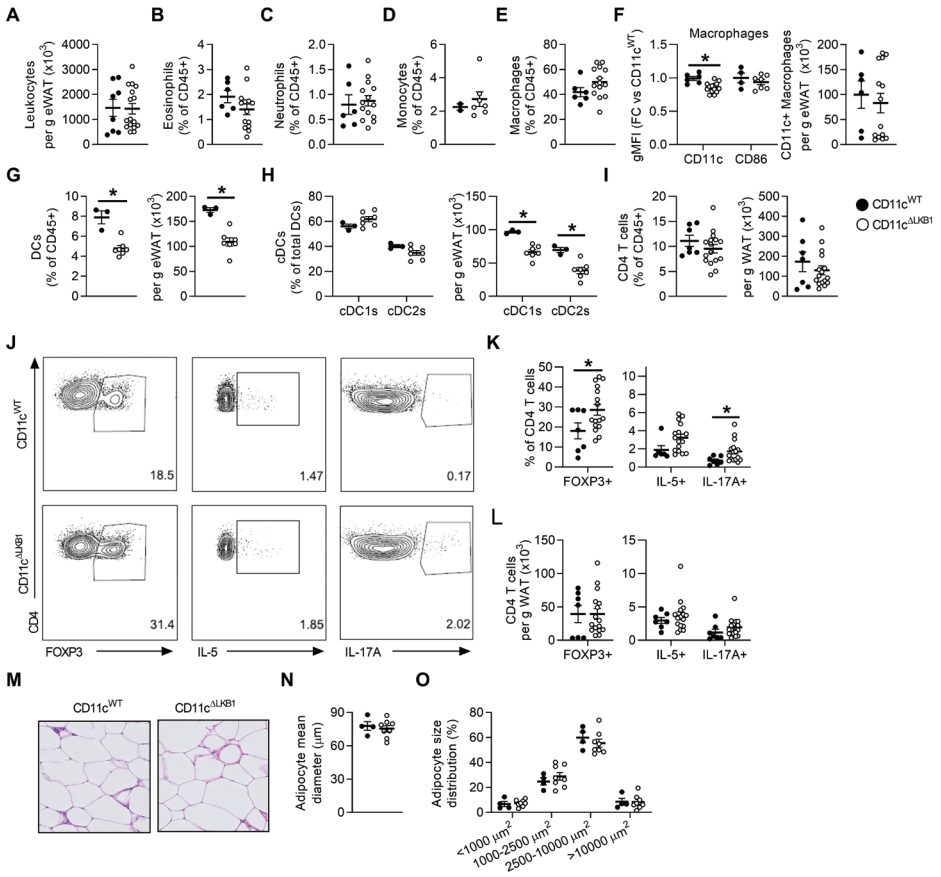

Figure S4. LKB1 deficiency in DCs does not aggravate adipose tissue immunometabolic dysfunctions in obese mice.

CD11c^{WT} (black symbols) and CD11c$^{\Delta LKB1}$ mice (open symbols) were fed a HFD for 18 weeks. **A-I:** At sacrifice, eWAT was collected and immune cells isolated and analysed by flow cytometry. Total leukocytes per gram eWAT were quantified **(A)**. Percentages of eosinophils **(B)**, neutrophils **(C)**, monocytes **(D)** and macrophages **(E)** in eWAT expressed as frequencies of total leukocytes. Expression of CD11c and CD86 on eWAT macrophages relative to CD11c^{WT} mice and total CD11c^{+} macrophages as cells per gram eWAT **(F)**. Abundances of DCs **(G)**, cDC subsets **(H)** and CD4 T cells **(I)**. **J-N:** eWAT immune cells were restimulated with PMA and ionomycin in the presence of Brefeldin A for intracellular cytokine detection. Representative plots **(J)** and percentages of FOXP3^{+} Treg , IL-5^{+} Th2 and IL-17A^{+} Th17 cells were determined as frequencies of CD4 T cells **(K)** and as absolute cell number per gram eWAT **(L)**. **M:** A part of eWAT was sectioned and H&E-stained. **N-O:** Mean adipocyte diameter **(N)** and adipocyte size distribution **(O)** were quantified from H&E stained slides. Data shown are a pool of two independent experiments, except for **D, F-H** and **O-Q**. Results are expressed as means ± SEM. * P<0.05 vs CD11c^{WT} (n = 7-16 mice per group for **A-C, E** and **I-N**; n = 3-8 mice per group for **D, F-H** and **O-Q**).

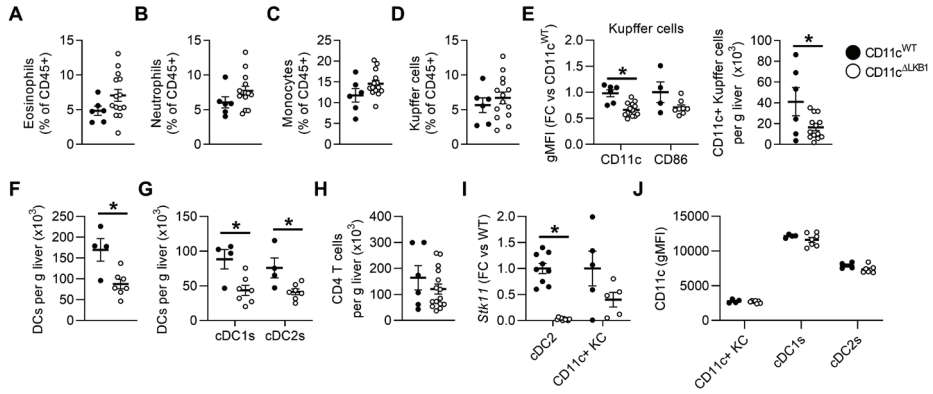

Figure S5. Effects of LKB1 deletion from DCs on myeloid cell subsets in the liver.
CD11c^{WT} (black symbols) and CD11c$^{\Delta LKB1}$ (open symbols) mice were fed a HFD for 18 weeks. At sacrifice, liver was collected and immune cells were isolated and analysed by flow cytometry. **A-D:** Percentages of hepatic eosinophils **(A)**, neutrophils **(B)**, monocytes **(C)** and Kupffer cells **(D)** expressed as frequencies of total leukocytes. **E:** Expression of CD11c and CD86 on Kupffer cells, expressed as fold change vs CD11cWT and total CD11c+ Kupffer cells per gram liver. **F-H:** absolute cell numbers per gram liver for total cDCs **(F)**, cDC subsets **(G)** and CD4 T cells **(H)**. **I:** Expression of *Stk11* as measured by RT-qPCR in cDC2s and CD11c^{+} Kupffer cells (KC) from chow-fed mice. **J:** Expression of CD11c in CD11c^{+} Kupffer cells and dendritic cell subsets. Data shown are a pool of two independent experiments, except for CD86 expression in **E, I** and **J**. Results are expressed as means ± SEM. * P<0.05 vs CD11c^{WT} (n = 4-14 mice per group). Related to figure 3.

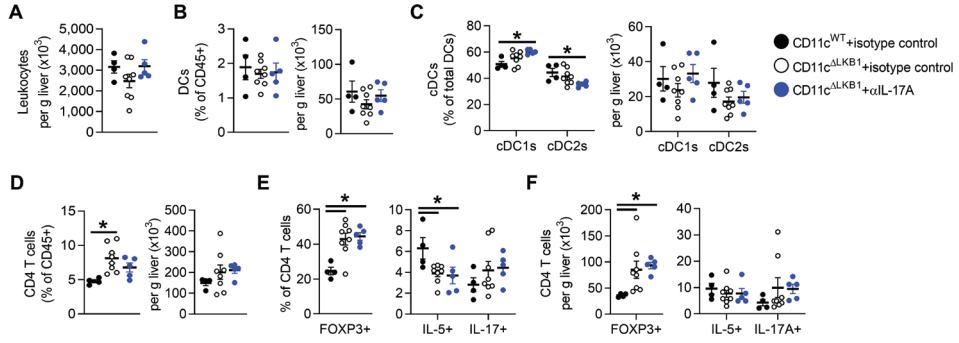

Figure S6. Effects of IL-17A neutralization on hepatic immune cells.
Mice were treated as described in the legend of figure 5. **A-D:** At sacrifice, liver was collected and immune cells were isolated and phenotyped by flow cytometry. Total number of leukocytes per gram liver **(A)**, and abundances of DCs **(B)**, cDC subsets **(C)** and CD4 T cells **(D)** were determined. **E-F:** Hepatic leukocytes were restimulated with PMA/ionomycin in the presence of Brefeldin A for detection of intracellular cytokines. Abundance of FOXP3^{+} Tregs **(E)**, IL-5^{+} Th2 cells and IL-17A^{+} Th17 cells **(F)** were determined as frequencies of CD4 T cells and as absolute cell number per gram liver. Data shown are a pool of two independent experiments. Results are expressed as means ± SEM. * P<0.05 vs CD11c^{WT} (n = 4-8 mice per group). Related to figure 4.

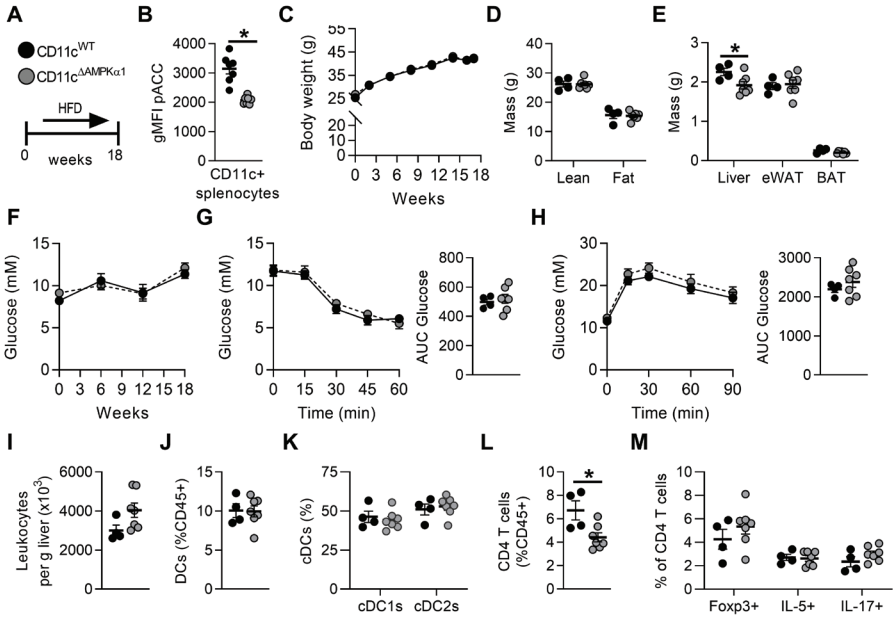

Figure S7. Deletion of AMPKα1 from DCs does not recapitulate the immunometabolic phenotype of CD11c$^{\Delta LKB1}$ mice. A: Staining for the AMPK-specific phosphorylation site Ser79 on ACC in CD11c+ splenocytes. **B:** CD11c^{WT} (black symbols) and CD11c$^{\Delta AMPK\alpha1}$ mice (grey symbols) were fed a HFD for 18 weeks. **C:** Body weight was monitored throughout the experiment. **D-E:** Body composition **(D)** and weights of liver, eWAT and BAT **(E)** were measured at the end of the experiment. **F:** Fasting blood glucose was measured at the indicated weeks. **G:** An i.p. insulin tolerance test was performed 1 week before sacrifice and AUC calculated. **H:** An i.p. glucose tolerance test was performed 1 week before sacrifice and AUC calculated. **I-L:** At sacrifice, liver was collected and immune cells isolated. Total leukocytes per gram liver were quantified **(I)**. Percentages of DCs **(J)**, cDC subsets **(K)** and CD4 T cells **(L)** were determined by flow cytometry. **M:** Liver leukocytes were restimulated with PMA and ionomycin in the presence of Brefeldin A for intracellular cytokine detection. Percentages of FOXP3$^+$ Treg, IL-5$^+$ Th2 and IL-17A$^+$ Th17 cells were determined as frequencies of CD4 T cells. Results are expressed as means ± SEM. Statistical analyses were performed using unpaired t-tests **(B, D+E, G-M)** or two-way ANOVA followed by Fisher's post-hoc tests **(C, F-H)**. * P<0.05 vs CD11c^{WT} (n = 4-7 mice per group).

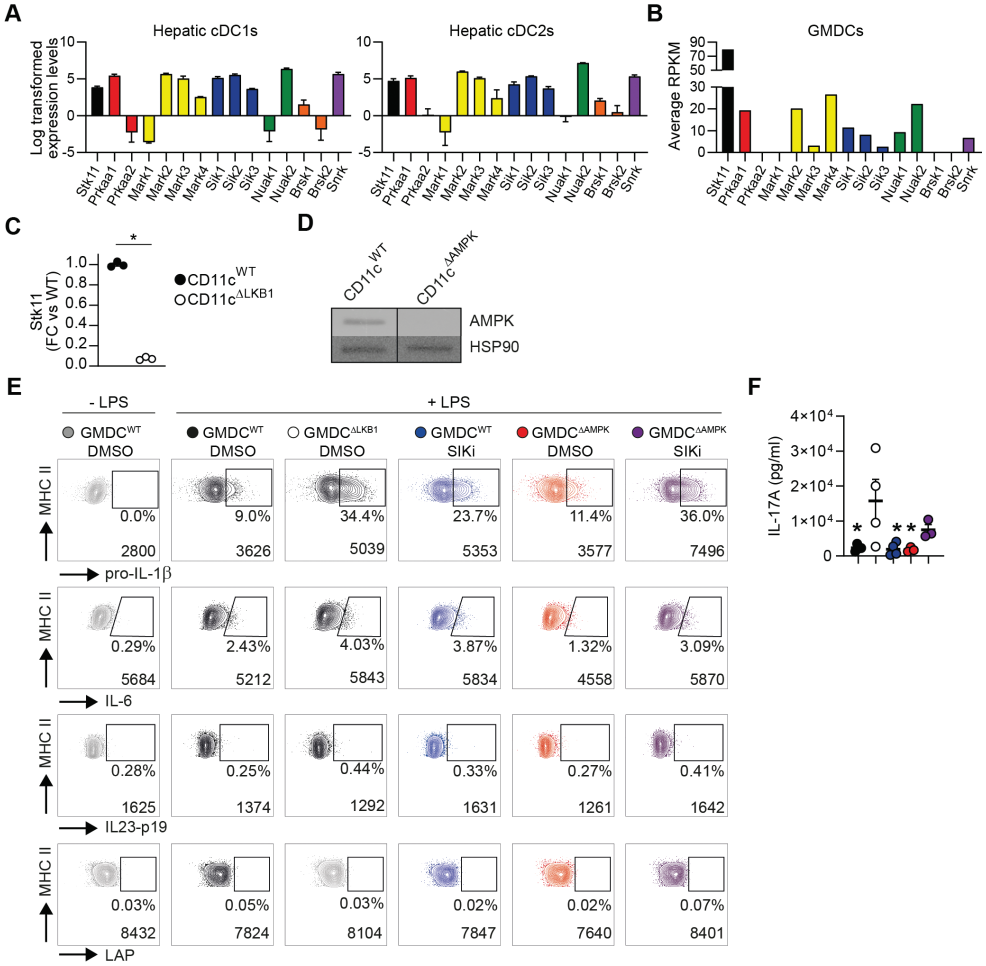

Figure S8. Transcriptional analysis of LKB1 and its substrates in DCs. A-B: Expression of *Stk11* (encoding LKB1) and its downstream targets *Prkaa1-2* (encoding AMPKα1-2), *Mark1-4*, *Sik1-3*, *Nuak1-2*, *Brsk1-2* and *Snrk* in murine hepatic cDC1s and cDC2s (**A**; 30) and mature GM-CSF-elicited bone marrow DCs (GMDCs) (**B**; 32). **C:** *Stk11* expression in GMDCs from CD11c^{WT} (black symbols) and CD11c$^{\Delta LKB1}$ mice (open symbols) at day 10 of culture. **D:** AMPK expression in GMDCs from CD11c^{WT} and CD11c$^{\Delta AMPK}$ at day 10 of culture. Lanes were run on the same gel, but were non-contiguous. Data is representative of 2 biological replicates. **E:** GMDCs were stimulated with or without LPS in the presence of Brefeldin A for intracellular cytokine detection. Representative plots for figure 5E, depicting the frequencies of positive cells and gMFI. **F:** IL-17A detected in supernatant after a 48 hour antigen-specific restimulation of popliteal lymph node cells. Results are expressed as means ± SEM. * P<0.05 vs CD11c^{WT} **(C)** or*P<0.05 vs LKB1 KO **(F)**. Related to figure 5.

Part 3

AMPK as Regulator of Tolerance


AMPK

5

AMPK activation induces RALDH^{high} tolerogenic dendritic cells through rewiring of glucose and lipid metabolism

E. C. Brombacher[1], T. A. Patente[1], A. J. van der Ham[1], T. J. A. Moll[1], F. Otto[1], F. W. M. Verheijen[2], E. A. Zaal[2], A.H. de Ru[3], R. T. N. Tjokrodirijo[3], C. R. Berkers[2], P. A. van Veelen[3], B. Guigas[1], B. Everts[1]

[1]Department of Parasitology, Leiden University Medical Center, Leiden, The Netherlands
[2]Department Biomolecular Health Sciences, Utrecht University, Utrecht, The Netherlands
[3]Center for Proteomics and Metabolomics, Leiden University Medical Center, Leiden, The Netherlands

Manuscript submitted
DOI bioRχiv: 10.1101/2023.07.04.547639

Abstract

It is well known that dendritic cell (DC) activation and function are underpinned by profound changes in cellular metabolism. Several studies indicate that the ability of DCs to promote tolerance is dependent on catabolic metabolism. The AMP-activated kinase (AMPK) is a central nutrient and energy sensor whose activation promotes catabolism while inhibiting ATP-consuming anabolic pathways. Yet the contribution of AMPK activation to DC tolerogenicity remains unknown. Here, we show that AMPK activation renders human monocyte-derived DCs tolerogenic as evidenced by an enhanced ability to drive differentiation of regulatory T cells, a process dependent on increased RALDH activity. This is accompanied by a number of distinct metabolic changes, in particular increased breakdown of glycerophospholipids, enhanced mitochondrial fission-dependent fatty acid oxidation, and upregulated glucose catabolism. This metabolic rewiring is functionally important as we found interference with these metabolic processes to reduce to various degrees AMPK-induced RALDH activity as well as the tolerogenic capacity of moDCs. Altogether, our findings reveal a key role for AMPK signaling in shaping DC tolerogenicity, and suggest that AMPK may serve as new target to direct DC-driven immune responses in therapeutic settings.

Introduction

Dendritic cells (DCs) are specialized antigen-presenting cells with the ability to prime and polarize T cell responses. As such, DCs play a central role in the establishment of protective adaptive immunity following infections and after vaccination. In addition, their ability to prime regulatory T cells (Tregs) and induce anergy to host self-antigens make them critical regulators of tolerance (1). Hence, promoting tolerogenic DCs (tolDCs) could be an interesting therapeutic strategy for inflammatory diseases. Although several clinical studies have already confirmed the safety of tolDC-based therapies, the clinical benefits are currently limited, in part due to impaired long-lasting maintenance of the tolerogenic state (2–4). Novel insights into the processes that drive and shape DC tolerogenicity are therefore instrumental for devising new strategies to increase efficacy of tolDC-based therapies.

DCs can be exposed to a number of different metabolic micro-environments ranging from a nutrient-deprived tumor micro-environment to nutrient-rich tissues in obese individuals. These metabolic cues and nutrient availability are expected to have a major impact on DC function and the subsequent immune response, as they impinge on intracellular metabolic pathway activity that play a central role in shaping DC immunogenicity (5). Acquisition of an immunogenic DC phenotype is commonly associated with anabolic metabolism and underpinned by enhanced glycolysis and fatty acid synthesis (6,7), while tolDCs are functionally supported by catabolism-centered metabolism, characterized by enhanced glycolysis in combination with elevated oxidative phosphorylation and fatty acid oxidation (FAO) (8–10).

Nutrient-sensing pathways connect environmental cues to changes in cellular bioenergetics and are therefore highly important for DC function. For example, DC activation is facilitated by upregulated glycolysis, which is supported by mechanistic target of rapamycin (mTOR) and counteracted by AMP-activated protein kinase (AMPK) (7), two nutrient sensing enzymes that are activated in nutrient-sufficient and -poor conditions, respectively (11,12). While the role of mTOR in DCs has been extensively studied, less is known about the role of AMPK in DC function (12). AMPK is a central regulator of cellular metabolism, well known for its role in regulating energy homeostasis during nutrient stress. Canonical AMPK activation involves a high AMP/ADP ratio that triggers Liver Kinase B1 (LKB1) to activate AMPK via phosphorylation. AMPK activation inhibits fatty acid synthesis while enhancing FAO, by phosphorylation of acetyl-CoA carboxylase (ACC) isoforms ACC1 and ACC2, respectively. Catabolic metabolism is further promoted by induction of autophagy and downregulating of protein synthesis through inhibition of mTORC1. AMPK also plays an important role in mitochondrial homeostasis by regulating the removal of damaged mitochondria through mitophagy and by stimulating mitochondrial biogenesis (11,13).

There is some evidence that suggests a role for AMPK signaling in DCs in dampening an inflammatory immune response. AMPK activation in bone-marrow derived DCs (BMDCs) suppressed IL-12p40 secretion and CD86 expression (7), while AMPK deficiency in BMDCs promotes secretion of pro-inflammatory cytokines and IFN-γ and IL-17 secretion by T cells (14). Additionally, AMPK deficiency in CD11c-expressing cells worsened lung injury following hookworm infection through increased IL-12/23p40 production by pulmonary CD11c^{+} cells (15). Interestingly, we have recently found that the tolerogenic effects of retinoic acid (RA) on DCs are AMPK dependent, suggesting that AMPK may not only dampen DC immunogenicity, but can also actively contribute to the tolerogenic capacity of DCs (16). Yet, whether AMPK

activation itself is sufficient to induce DC tolerogenicity and immune tolerance and what the underlying mechanisms are remains unknown.

In the present study, we find that drug-induced AMPK activation in DCs is sufficient to promote their tolerogenicity, as evidenced by an enhanced ability to prime functional regulatory T cells through induction of retinaldehyde dehydrogenase (RALDH) activity. We further show that, mechanistically, AMPK activation boosts glycerophospholipid degradation, mitochondrial-fission induced FAO, and glucose catabolism. Interference with these metabolic alterations partly negate the tolerogenic effects of AMPK activation. Together this provides support for an important role of AMPK in rendering DCs tolerogenic through rewiring of lipid and glucose metabolism and may identify AMPK as a potential target for improving tolDC-based immunotherapies.

Results

AMPK activation renders DCs tolerogenic through promotion of RALDH activity

To study the effect AMPK activation on DC function, we treated human monocyte-derived DCs (moDCs) with 991, a direct small-molecule AMPK activator (17). AMPK activation was rapidly induced by 991, as assessed by phosphorylation on Ser79 of its downstream target Acetyl-CoA Carboxylase (ACC) (18), and remained stable over time (Supp. Fig. 1A). To investigate the effects of AMPK activation on DC immunogenicity, immature moDCs (iDCs) were treated overnight with 991 before LPS stimulation (Fig. 1A). 24 hours later both iDCs and LPS-treated mature DCs (mDCs) showed increased AMPK activation (Fig. 1B), while simultaneously reducing mTORC1 activity, as assessed by phosphorylation of S6, a downstream target of mTORC1 (Supp. Fig. 1B). Of note, 991 treatment did not affect cell viability (Supp. Fig. 1C). 991 stimulation diminished LPS-induced activation of DCs when compared to DMSO-treated cells, as evidenced by reduction in several activation markers, as well as IL-10 and IL12p40 secretion after co-culture with a CD40L expressing cell line to mimic T cell interactions (Fig. 1C, D and Supp. Fig. 1D,E). Conversely, expression of CD103 was increased (Fig. 1C), a marker also upregulated on RA-induced tolerogenic DCs which are known to promote Treg differentiation through retinaldehyde dehydrogenase (RALDH)-driven RA production (19,20). Interestingly, 991 treatment also promoted RALDH activity in mDCs (Fig. 1E).

Next, the effect of AMPK activation on T cell priming by mDCs was evaluated. A co-culture with allogenic naïve $CD4^+$ T cells showed that the ability of mDCs to promote IFN-γ, IL-4, and IL-10 secretion by T cells was not modulated by 991 (Fig. 1F and Supp. Fig. 1F). However, the capacity of these T cells to reduce proliferation of bystander T cells was enhanced compared to T cells primed with DMSO-treated mDCs (Fig. 1G), indicating that AMPK activation renders DCs tolerogenic as determined by their ability to prime functional regulatory T cells. A similar trend towards induction of Tregs was observed when DCs were treated with AICA riboside (AICAR), another AMPK activator (Supp. Fig. 1G,H). Of note, further phenotypic characterization of Tregs primed by 991-stimulated mDCs did not reveal enrichment of any of the main previously described subsets of induced Tregs, including $CD127^-$ $CD25^+FoxP3^+CTLA4^+$ Tregs (induced Tregs (iTregs)) (21), $ICOS^+$ Tregs (22), $TIGIT^+$ Tregs (23), or $Lag3^+CD49b^+$ Treg1 cells (24) (Supp. Fig. 1I, J), suggesting that AMPK-activated DCs drive induction of a non-canonical Treg population (21–24).

We next questioned whether the tolerogenic effects of AMPK activation were dependent on increased RALDH activity. mDCs were therefore treated with RALDH2 inhibitor bisdiamide

during 991 treatment and subsequent LPS stimulation (Supp. Fig. 1K). RALDH inhibition prevented 991-induced suppression in expression of HLA-DR, CD86, CD83 and CD80 to various degrees (Supp. Fig. 1L). IL-10 and IL-12p40 secretion was further decreased upon RALDH inhibition compared to control groups (Supp. Fig. 1M). The suppressive capacity of T cells primed with 991-treated DCs was not affected when RALDH was inhibited during DC culture alone (Supp. Fig. 1N), but strikingly, when bisdiamide was also added during T cell co-culture, the ability of 991-stimulated mDCs to prime functional Tregs was lost. Since T cells did not show detectable RALDH activity (Supp. Fig. 1K), this indicates that RALDH activity in 991-stimulated mDCs during DC-T cell coculture is required for these DCs to exert their tolerogenic effect (Fig. 1H). Altogether, AMPK activation in DCs induces tolerogenicity and promotes priming of non-canonical functional regulatory T cells through induction of RALDH activity.

AMPK activation drives catabolic glycerophospholipid metabolism

To gain insight into how AMPK activation induces DC tolerogenicity we performed untargeted metabolomics and proteomics on DMSO- and 991-treated iDCs and mDCs. LPS treatment had clear effects on both the metabolome and the proteome of DCs. Strikingly, LPS stimulation did not lead to any of these changes in 991-treated cells (Supp. Fig. 2A,B), supporting our earlier observations that AMPK activation counteracts LPS-induced DC maturation. 991 treatment promoted increases in several proteins and metabolites irrespective of LPS stimulation, while the downregulated hits upon 991 treatment mainly consisted of proteins and metabolites whose accumulation were induced by LPS (Supp. Fig. 2C-E). Pathway enrichment analysis on the proteome revealed that pathways enriched upon 991 stimulation in LPS-treated mDCs were all associated with (catabolic) lipid metabolism (Fig. 2A), in particular glycero(phospho) lipid catabolism. Metabolomic data also indicated enhanced glycerolipid metabolism, as well as upregulation of the pentose phosphate pathway (Fig. 2B). Integration of the proteomic and metabolomic data sets using web-service ‘genes and metabolites’ (GAM) (25), created a metabolic network that additionally highlighted changes in amino acid metabolism and TCA cycle metabolites, and further affirmed significant changes in lipid metabolism, including glycero(phospho)lipid metabolism (Fig. 2C). Additionally, most 991-specific metabolite and protein changes in glycero(phospho)lipid metabolism occurred independently of DC maturation (Fig. 2D,E). The proteomic/metabolic network connected an accumulation of glycerol-3-phosphate and a decrease in membrane-lipid phosphatidylcholine (Fig. 2F) to upregulation of two proteins involved in breakdown of glycerophospholipids, namely Patatin-like phospholipase domain-containing protein 6 (PNPLA6) and Glycerophosphocholine Phosphodiesterase 1 (GPCPD1) (Fig. 2G). PNPLA6, also known as Neuropathy Target Esterase (NTE), is a phospholipase that hydrolyzes phosphatidylcholine (PC), thereby releasing fatty acids and glycerophosphocholine (26). GPCPD1, also known as GDE5, hydrolyzes glycerophosphocholine (GroPCho) to glycerol-3-phosphate (G3P) and choline (27). Phosphatidylethanolamine (PE), another membrane lipid of which the abundance also decreased upon 991 treatment (Fig. 2F), can also be hydrolyzed to G3P and ethanolamine via PNPLA6 and GPCPD1, albeit with a lower affinity (26,27). We aimed to determine whether breakdown of PC and PE via PNPLA6 and GPCPD1 contributes to AMPK-induced tolerogenicity and hence, we silenced expression of both *PNPLA6* and *GPCPD1* in iDCs, before adding 991 and LPS, with siRNA. qPCR analysis revealed that 991 induced *PNPLA6* and *GPCPD1* protein expression was mirrored at the transcriptional level (Fig. 2H). Gene

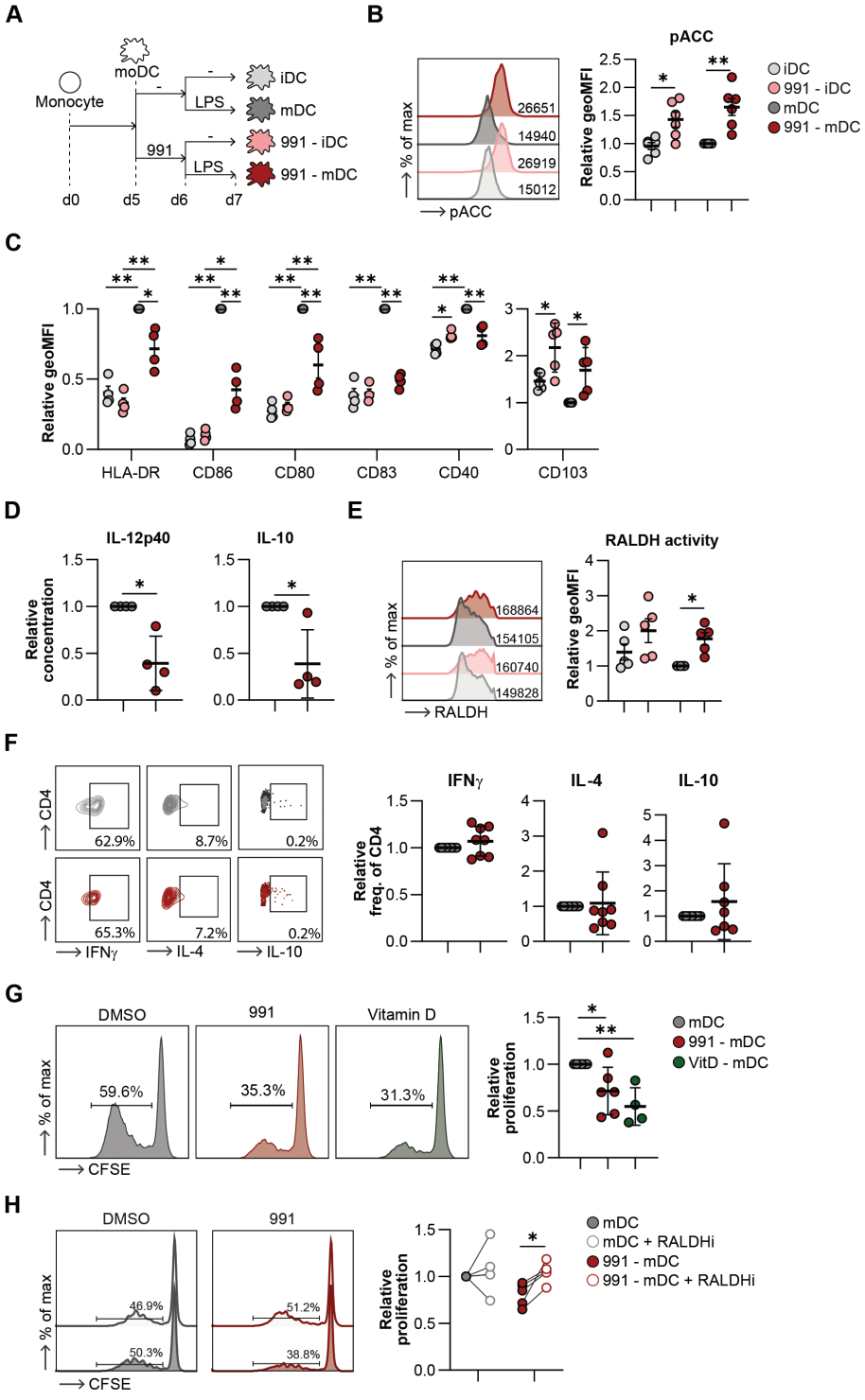
A
Monocyte
moDC
991
LPS
LPS
iDC
mDC
991 - iDC
991 - mDC
d0
d5
d6
d7
B
pACC
% of max
pACC
26651
14940
26919
15012
Relative geoMFI
iDC
991 - iDC
mDC
991 - mDC
C
Relative geoMFI
HLA-DR
CD86
CD80
CD83
CD40
CD103
D
IL-12p40
IL-10
Relative concentration
E
RALDH activity
% of max
RALDH
168864
154105
160740
149828
Relative geoMFI
F
CD4
62.9%
8.7%
0.2%
65.3%
7.2%
0.2%
IFNγ
IL-4
IL-10
Relative freq. of CD4
G
DMSO
991
Vitamin D
% of max
59.6%
35.3%
31.3%
CFSE
Relative proliferation
mDC
991 - mDC
VitD - mDC
H
DMSO
991
% of max
46.9%
50.3%
51.2%
38.8%
CFSE
Relative proliferation
mDC
mDC + RALDHi
991 - mDC
991 - mDC + RALDHi

Figure 1. AMPK activation induces tolerogenic DCs via promotion of RALDH activity. A: Schematic overview of experimental set-up. Monocytes were isolated from PBMCs and differentiated in moDCs in the presence of GM-CSF + IL-4. On day 5 cells were treated with either DMSO or 991. On day 6, 100 ng/mL of LPS was added if indicated and 24 hours later cells were harvested for functional assays. **B:** Representative histogram and normalized quantification of phosphorylation of ACC (Ser79). **C:** Normalized expression of indicated markers by moDCs. **D:** Relative concentration of IL-10 and IL12p40 in the supernatants of mDCs after a 24 hour co-culture with CD40L-expressing J558 cells. **E:** Representative histogram and normalized quantification of RALDH activity. **F:** Representative plots and normalized percentages of $CD4^+$ T cells of intracellular cytokines after restimulation with PMA/ionomycin in the presence of Brefeldin A. **G, H:** Representative histograms and normalized percentage of proliferation of bystander T cells after co-culture with irradiated T cells primed with **(G)** 991/DMSO-treated mDCs and **(H)** in presence or absence of RALDH inhibitor (RALDHi) bisdiamine during both mDC maturation and mDC-T cell co-culture. Results are expressed as means ± SEM. Datapoints represent independent experiments with different donors. Statistical analyses were performed using paired t-tests **(D, F)**, one-way Anova with Sidak post-hoc test **(G)** or two-way Anova with Tukey post-hoc test **(B, C, E, H)**. *p < 0.05, **p < 0.01.

silencing strongly reduced expression of both genes, although this was less pronounced in 991-treated cells (Fig. 2H). Expression of activation markers and IL-12p40 and IL-10 secretion was not affected by silencing of *PNPLA6* and *GPCPD1* (Supp. Fig. 2G), while RALDH activity in silenced 991-stimulated mDCs showed a reduction in most donors (Fig. 2I). Correspondingly, 991-driven induction of functional Tregs by mDCs was partly lost after silencing of *PNPLA6* and *GPCPD1* (Fig. 2J). Altogether these data suggest that AMPK activation in mDCs promotes catabolic lipid metabolism and that breakdown of glycerophospholipids, mediated by PNPLA6 and GPCPD1, are contributing to AMPK-induced tolerogenicity.

Fatty acid oxidation is important for AMPK-induced tolerogenicity

As our data indicate enhanced lipid catabolism upon AMPK activation and given that AMPK is known to promote mitochondrial FAO, we further investigated the effects of 991 treatment on mitochondrial metabolism and FAO. Basal mitochondrial respiration, ATP production, and spare respiratory capacity were not affected by AMPK activation (Fig. 3A,B, Supp. Fig. 3A) and neither were mitochondrial mass or membrane potential (Supp. Fig. 3B). Interestingly, 991 treatment increased the protein expression ratio between complex II and complex I of the electron transport chain. This is a metabolic adaptation commonly associated with increased FAO, as it allows for more efficient oxidation of complex II substrate $FADH_2$ that is generated during FAO. Hence, this AMPK-activation driven change in ratio may reflect increased FAO rates (Fig. 3C). Indeed, [U-^{13}C]-palmitate tracing, revealed a trend towards increased uptake and oxidation of palmitate, marked by higher abundance of labeled Palmitoyl-L-Carnitine and the presence of palmitate-derived carbons in acetyl-CoA, the final product of FAO (Fig. 3D-G). Although the total levels of acetyl-CoA and palmitate-derived acetyl-CoA (M+2) were higher after 991 treatment, the contribution of palmitate to acetyl-CoA was low in these cells, at around 3 percent. AMPK activation did not change carnitine palmitoyltransferase-1A (CPT1A) expression (Supp. Fig. 3C), suggesting that enhanced FAO is driven by higher CPT1A activity and/or by increased free FA availability. In support of the latter, we found that AMPK activation promoted long-chain fatty acid uptake, while lipid droplet accumulation was unaffected (Fig. 3H). Additionally, release of endogenous FAs from phospholipids upon AMPK activation, as shown in Fig. 2, may contribute to increasing intracellular fatty acid levels to fuel enhanced FAO.

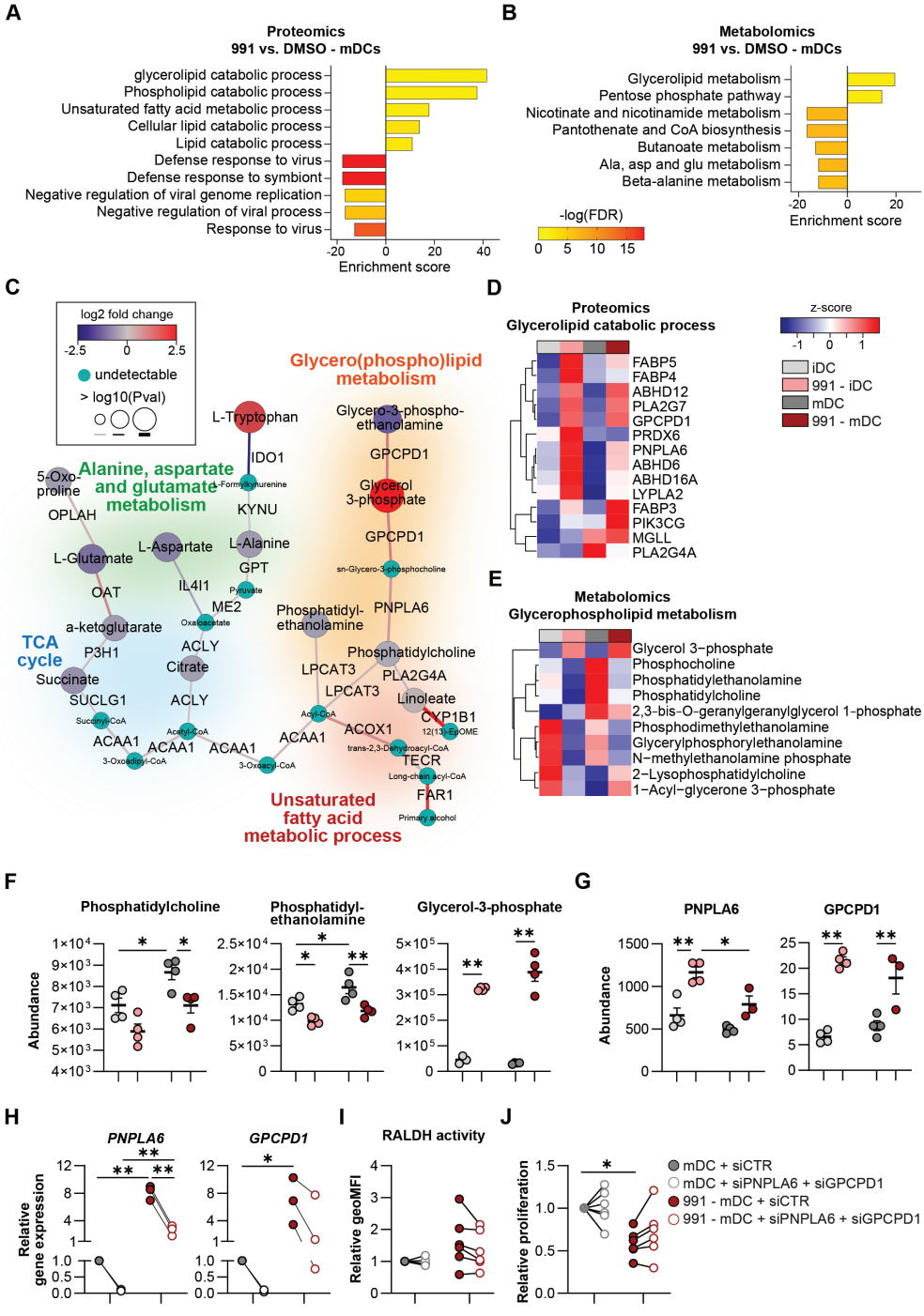
A
Proteomics
991 vs. DMSO - mDCs
glycerolipid catabolic process
Phospholipid catabolic process
Unsaturated fatty acid metabolic process
Cellular lipid catabolic process
Lipid catabolic process
Defense response to virus
Defense response to symbiont
Negative regulation of viral genome replication
Negative regulation of viral process
Response to virus
-20 0 20 40
Enrichment score
B
Metabolomics
991 vs. DMSO - mDCs
Glycerolipid metabolism
Pentose phosphate pathway
Nicotinate and nicotinamide metabolism
Pantothenate and CoA biosynthesis
Butanoate metabolism
Ala, asp and glu metabolism
Beta-alanine metabolism
-20 0 20
Enrichment score
-log(FDR)
0 5 10 15
C
log2 fold change
-2.5 0 2.5
undetectable
> log10(Pval)
Glycero(phospho)lipid metabolism
Alanine, aspartate and glutamate metabolism
TCA cycle
Unsaturated fatty acid metabolic process
L-Tryptophan
IDO1
N-Formyl-L-kynurenine
KYNU
5-Oxo-proline
OPLAH
L-Glutamate
L-Aspartate
L-Alanine
GPT
Pyruvate
IL4I1
OAT
ME2
Oxaloacetate
a-ketoglutarate
P3H1
ACLY
Citrate
Succinate
SUCLG1
Succinyl-CoA
Acetyl-CoA
ACAA1
3-Oxoadipyl-CoA
3-Oxoacyl-CoA
Glycero-3-phospho-ethanolamine
GPCPD1
Glycerol 3-phosphate
sn-Glycero-3-phosphocholine
Phosphatidyl-ethanolamine
PNPLA6
Phosphatidylcholine
LPCAT3
PLA2G4A
Linoleate
Acyl-CoA
ACOX1
CYP1B1
12(13)-EpOME
trans-2,3-Dehydroacyl-CoA
TECR
Long-chain acyl-CoA
FAR1
Primary alcohol
D
Proteomics
Glycerolipid catabolic process
z-score
-1 0 1
iDC
991 - iDC
mDC
991 - mDC
FABP5
FABP4
ABHD12
PLA2G7
GPCPD1
PRDX6
PNPLA6
ABHD6
ABHD16A
LYPLA2
FABP3
PIK3CG
MGLL
PLA2G4A
E
Metabolomics
Glycerophospholipid metabolism
Glycerol 3−phosphate
Phosphocholine
Phosphatidylethanolamine
Phosphatidylcholine
2,3-bis-O-geranylgeranylglycerol 1-phosphate
Phosphodimethylethanolamine
Glycerylphosphorylethanolamine
N−methylethanolamine phosphate
2−Lysophosphatidylcholine
1−Acyl−glycerone 3−phosphate
F
Phosphatidylcholine
Phosphatidyl-ethanolamine
Glycerol-3-phosphate
Abundance
G
PNPLA6
GPCPD1
Abundance
H
PNPLA6
GPCPD1
Relative gene expression
I
RALDH activity
Relative geoMFI
J
Relative proliferation
mDC + siCTR
mDC + siPNPLA6 + siGPCPD1
991 - mDC + siCTR
991 - mDC + siPNPLA6 + siGPCPD1

Figure 2: AMPK activation drives glycerophospholipid breakdown. Proteomics and metabolomics were performed on DMSO/991-treated iDCs and mDCs. **A:** Gene ontology (GO) pathway enrichment of significantly up- and downregulated proteins in AMPK-activated mDCs. **B:** KEGG enrichment analysis of significantly up- and downregulated metabolites in AMPK-activated mDCs. **C:** network analysis of integrated proteomics and metabolomics data from mDCs. **D, E:** Heatmap depicting relative expression of **(D)** proteins and **(E)** metabolites involved in glycerophospholipid metabolism. **F, G:** Dotplots showing the abundance as determined by metabolomics or proteomics of **(F)** metabolites and **(G)** proteins involved in glycerophospholipid metabolism that are strongly affected by AMPK activation. **H:** Relative gene expression of *PNPLA6* and *GPCPD1* 72 hours after electroporation with control siRNA (siCTR), or siRNA targeting *PNPLA6* or *GPCPD1*. **I:** normalized quantification of RALDH activity. **J:** Normalized percentage of proliferation of bystander T cells after a T cell suppression assay. Results are expressed as means ± SEM. Datapoints represent independent experiments with different donors. Statistical analyses were performed using paired t-tests **(H)** or two-way Anova with Tukey post-hoc test **(F, G, I, J)**. *p < 0.05, **p < 0.01.

To study whether FAO is important for the AMPK-induced Treg-priming capacity of mDCs we blocked mitochondrial import of long-chain fatty acids by silencing *CPT1A* (Fig. 3I). *CPT1A* knockdown did not change uptake of Bodipy C16 and neutral lipid accumulation (Bodipy 493/503), nor did it restore the AMPK-induced inhibition of activation markers and IL-12p40 and IL-10 secretion (Supp. Fig. 3D-F). However, silencing *CPT1A* decreased the AMPK-driven increase in RALDH activity in 991-stimulated mDCs, as well as the suppressive capacity of T cells primed by these DCs (Fig. 3I-K). Taken together, these data show that AMPK activation increases FAO, which promotes RALDH activity and thereby the tolerogenic capacities of moDCs.

AMPK activation drives fatty acid oxidation through mitochondrial fission

AMPK-induced FAO has been shown to be supported by changes in the mitochondrial fission/fusion balance (28). We therefore evaluated mitochondrial morphology and questioned whether fission and fusion play a role in the AMPK-driven metabolic and immunological changes. We observed that in both iDCs and mDCs AMPK activation induced fragmentation of mitochondria, indicative of increased fission (Fig. 4A-B). Fusion can be promoted by AMPK through blocking recruitment of DRP1 to the mitochondria via phosphorylation DRP1 (S637) (29), while phosphorylation of mitochondrial fission factor (MFF) (S172), the receptor for DRP1, promotes fission (30). 991 treatment did not induce phosphorylation of DRP1 (S637) and counteracted the LPS-induced increase of DRP1 phosphorylation, while it did promote phosphorylation of MFF (S172/S146) in mDCs (Fig. 4C). Furthermore, expression of *FIS1*, a gene involved in mitochondrial fission, increased upon AMPK activation (Supp. Fig. 4A), together providing further support for induction of mitochondrial fission following AMPK activation in moDCs.

Next, we addressed whether AMPK-driven mitochondrial fission is required for FAO by inhibiting mitochondrial fission using mdivi1, an inhibitor of DRP1 (31). Of note, mdivi1 was also shown to inhibit complex I of the electron transport chain, but at the tested concentration in our model, mdivi1 solely affected mitochondrial morphology and not respiration (Supp. Fig. 4B-D) (32). [U-^{13}C]-palmitate tracing in 991-stimulated mDCs in presence of mdivi1 revealed that inhibition of mitochondrial fission tended to increase C_{16}-labeled palmitoyl-L-carnitine abundance in 991-stimulated mDCs (Fig. 4D, E), while the abundance of palmitate-derived carbon ending up in acetyl-CoA was reduced (Fig. 4F, G). Although the contribution of palmitate

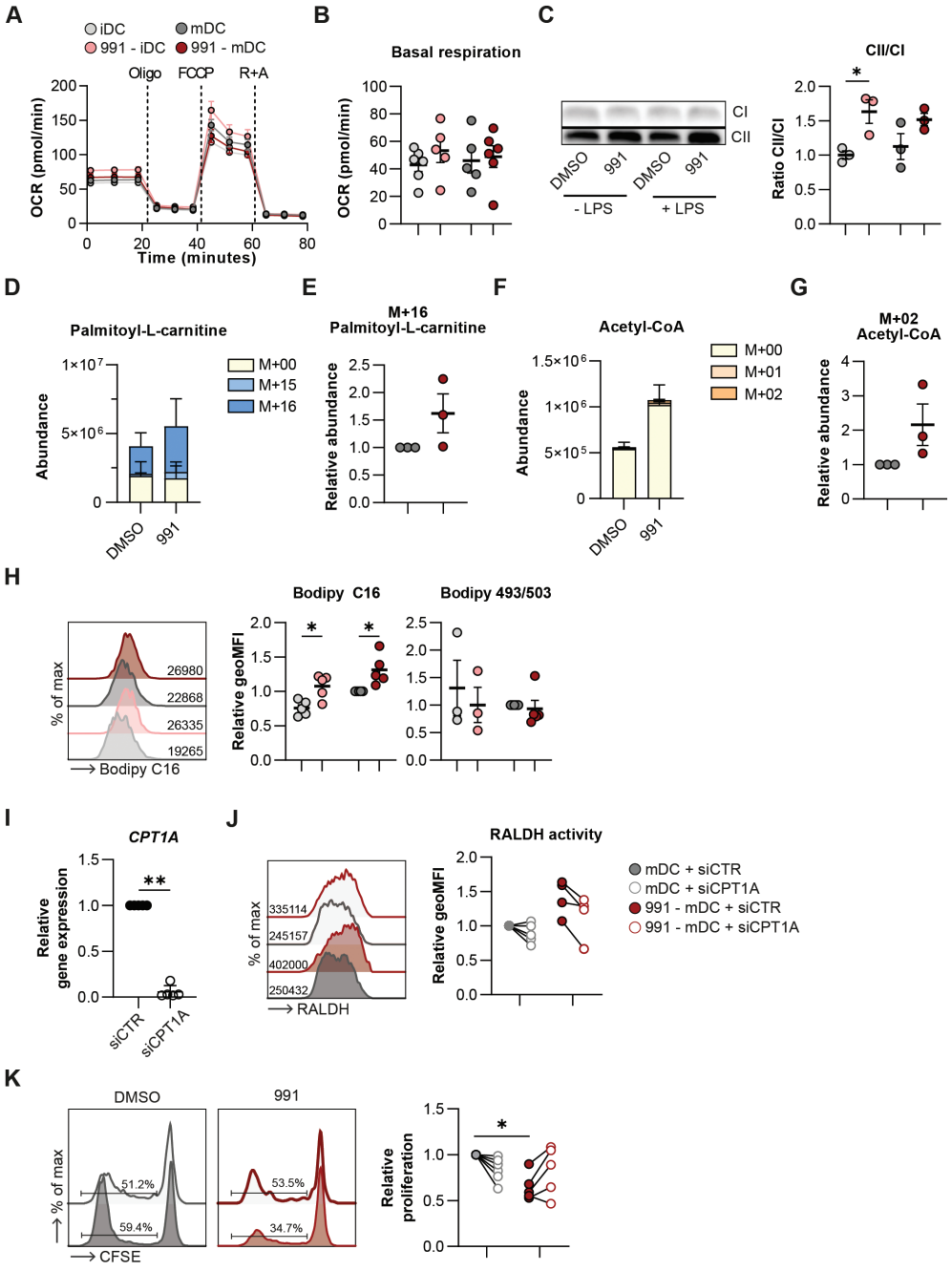

Figure 3: AMPK-induced tolerogenicity is driven by FAO. A, B: Real-time oxygen consumption rate (OCR) as measured by Seahorse extracellular flux analysis and **(B)** quantification of basal respiration rates. **C:** Western Blot of complex I (CI) and complex II (CII) of the electron transport chain and quantification of the ratio between CII and CI. **D-G:** [U-^{13}C]-palmitate tracing was performed in

DMSO/991-treated mDCs. Figures show **(D)** total abundance of palmitoyl-L-carnitine and **(E)** abundance of the labeled M+16 fraction of palmitoyl-L-carnitine normalized per donor and **(F)** total abundance of acetyl-CoA and **(G)** abundance of the labeled M+02 fraction of acetyl-CoA normalized per donor. **H:** representative histogram of Bodipy C16 uptake and normalized quantification of Bodipy C16 and Bodipy 495/503. **I:** Relative gene expression of CPT1A in mDCs 72 hours after electroporation with control siRNA (siCTR) or siRNA targeting CPT1A (siCPT1A). **J:** Representative histogram and normalized quantification of RALDH activity. **K:** Representative histograms and normalized percentage of proliferation of bystander T cells after a T cell suppression assay. Results are expressed as means ± SEM **(B-D, E, G-I)** or means ± SD **(E+G)**. Datapoints represent independent experiments with different donors. Statistical analyses were performed using paired t-tests **(E, G, I)** or two-way Anova with Tukey post-hoc test **(B, C, H, J, K)**. *p < 0.05, **p < 0.01.

to acetyl-CoA is low, the combination of increased palmitoyl-L-carnitine and lower total and labeled acetyl-CoA levels indicates lower palmitate oxidation. Together, this suggests that the AMPK-driven increase in palmitate oxidation is partly dependent on enhanced mitochondrial fission. Inhibition of mitochondrial fission did not affect tolerogenic properties of 991-stimulated mDCs (Supp. Fig. 4E, F), which may indicate that residual FAO following mdivi1 treatment is sufficient to support tolerogenic properties of the AMPK-conditioned DCs. Altogether these data indicate that AMPK activation induces mitochondrial fission to support enhanced FAO in DCs.

Glucose oxidation contributes to AMPK-induced tolerogenicity

The increased accumulation of acetyl-CoA upon AMPK activation could only partly be explained by increased oxidation of palmitate (Fig. 3G). An important alternative carbon source for mitochondrial acetyl-CoA is glucose. To test whether increased glycolysis contributed to elevated levels of acetyl-CoA in 991-stimulated DCs, we performed [U-^{13}C]-glucose tracing experiments. This revealed that AMPK activation induced a significant increase in flux of glucose-derived carbons into glucose-6-phosphate and lactate, resulting in a 3-fold and 2-fold increase in total glucose-6-phosphate and lactate levels, respectively (Fig. 5A and Supp. Fig. 5A,B), suggesting that AMPK activation enhances glycolytic flux. AMPK activation also promoted pyruvate import into the mitochondria, as increased abundance of labeled carbons in acetyl-CoA was observed (Fig. 5B and Supp. Fig. 5C,D), that could account for the increased accumulation of acetyl-CoA in these cells. The increase in glucose-derived carbon flux into acetyl-CoA in response to 991 treatment and the corresponding increase in total acetyl-CoA abundance was still partly observed in (iso)citrate, but not in further downstream TCA cycle metabolites (Fig. 5B and Supp. Fig. 5C,D). Of note, in contrast to the AMPK-induced increase in FAO, glucose oxidation was not dependent on mitochondrial fission (Supp. Fig. 4G,H). To address whether mitochondrial glucose catabolism is required for AMPK-induced tolerogenicity, we blocked mitochondrial pyruvate import using UK5099, an inhibitor for mitochondrial pyruvate carrier 1 (MPC1) (33). While MPC1 inhibition did not restore expression of activation markers or IL-12p40 and IL-10 secretion by 991-stimulated mDCs (Supp. Fig. 5E,F), and had mixed effects on RALDH activity, it prevented the ability of these cells to promote functional Tregs (Fig. 5C,D). Altogether, our data suggest that in addition to FAO, AMPK activation promotes mitochondrial catabolism of glucose which also underpins the tolerogenic capacity of 991-stimulated moDCs.

Discussion

Catabolic metabolism has been a well-described feature of tolDCs (9,10). While AMPK functions as central regulator of catabolic metabolism, little is known about the role of AMPK in driving DC tolerogenicity. Despite several reports showing a role for AMPK in dampening DC activation (7,14,15), only recently a role for AMPK in promoting regulatory T cell responses was described, as it was shown that RA-induced tolDCs require AMPK to prime Tregs (16). On the contrary, AMPK is also activated in vitamin D3 (vitD) induced tolDCs (34), but not required for tolerogenicity in this context (16,35). Here, we show that direct activation of AMPK is sufficient to render DCs tolerogenic. Mechanistically, we demonstrate that this tolerogenic capacity is underpinned by enhanced RALDH activity and dependent on metabolic rewiring involving increased breakdown of glycerophospholipids, mitochondrial fission-dependent FAO, and elevated glucose catabolism.

Well-described mechanisms through which DCs induce Treg responses include IL-10(36) or TGF-β secretion (37), indoleamine 2,3-dioxygenase (IDO) expression (38), and RALDH activity (39). Our data indicate that AMPK-induced tolDCs promote Treg priming through enhanced RALDH activity. RALDH is the rate-limiting enzyme catalyzing the conversion of vitamin A-derivative retinol to RA and its expression in intestinal (19,20) and skin DCs (40) is important to maintain immune tolerance. We observed that inhibition of RALDH activity during moDC-T cell co-culture, but not during moDC culture alone, reduced Treg induction, suggesting that RALDH-produced RA directly acts on T cells for Treg induction.

The tolerogenic effects of AMPK activation in mDCs result in functional Tregs that do not seem to share a phenotype with any canonical Treg subset. The abundance of $FoxP3^+$ $CTLA4^+$ induced Tregs was lower in T cells upon priming with 991-stimulated DCs and so were $ICOS^+$ Tregs, $TIGIT^+$ Tregs and IL-10-secreting $CD49b^+LAG3^+$ Treg1s (21–24). Further studies are warranted to identify the effector mechanism(s) through which Tregs primed with 991-stimulated DCs exert their immunosuppressive effects (41).

Through an integrated proteomics and metabolomics analysis we identified breakdown of glycerophospholipids as one of the main metabolic consequence of AMPK activation in DCs. Importantly, 991-stimulated mDCs in which this process was partly inhibited through downregulation of *PNPLA6* and *GPCPD1*, were functionally less tolerogenic, demonstrating a role for glycerophospholipid breakdown in driving the tolerogenic-capacity of these moDCs. Interestingly, degradation of phospholipids has previously been reported in VitD, dexamethansone (Dex) and VitD+Dex-induced tolDCs (42), although the functional relevance was not explored. We now show a key role for phospholipid breakdown in supporting the tolerogenic properties of DCs. Yet, how this process mechanistically underpins tolDC function remains to be addressed. Since we found the tolerogenic effects to be dependent on FAO as well, it is tempting to speculate that phospholipid catabolism supports tolDC function by means of generating free fatty acids for mitochondrial FAO. In addition, it is conceivable that lipid-mediators derived from AMPK-induced phospholipid degradation, may also exert tolerogenic effects through autocrine or paracrine mechanisms. For instance, phospholipid composition is dynamically regulated in immune cells and has been shown to govern immune cell activation through changes in membrane fluidity and production of soluble lipid mediators that mediate signal transduction and cell-cell communication (43). Moreover, deregulation of phospholipid metabolism in tumor cells leads to accumulation of anti-inflammatory lipid mediators that

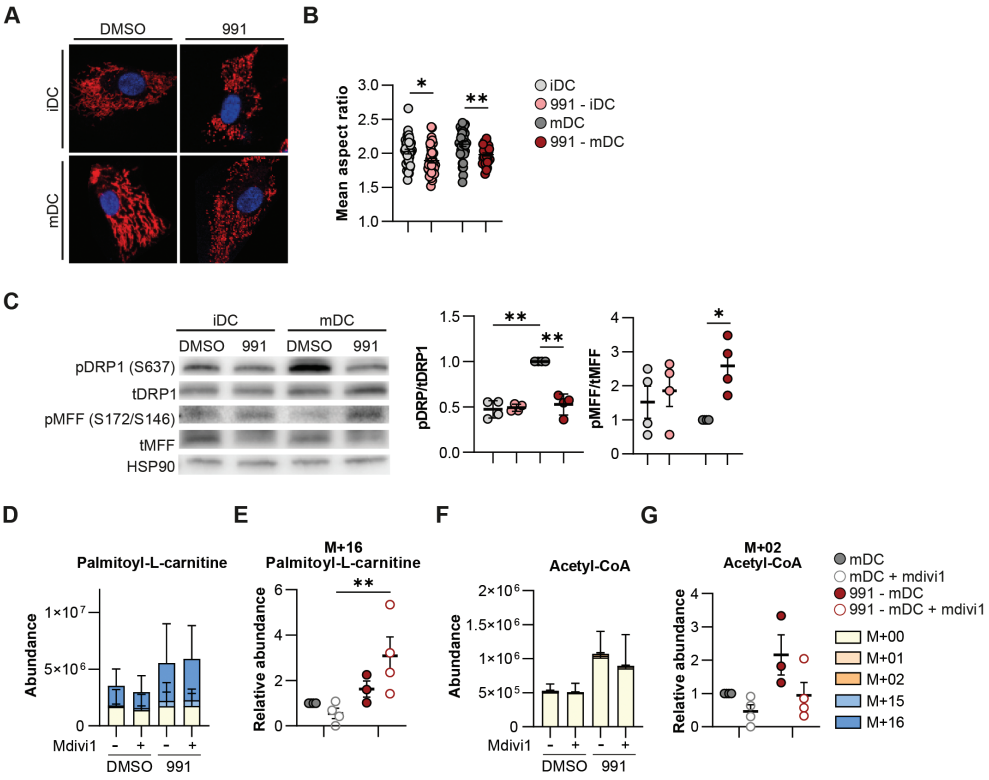

Figure 4: Mitochondrial fission induced by AMPK activation promotes FAO. A: Confocal images of DMSO/991-treated iDCs and mDCs. Blue: nucleus. Red: mitochondria. **B:** Quantification of the average aspect ratio of mitochondria per cell. **C:** Western Blot of phosphorylated DRP1 (pDRP1), total DRP1 (tDRP1), phosphorylated MFF (pMFF), total MFF (tMFF), and HSP90 and the ratio for pDRP1/tDRP1 and pMFF/tMFF, normalized for HSP90 and relative to DMSO-treated mDCs. **D-G:** [U-^{13}C]-palmitate tracing was performed in DMSO/991-treated mDCs, with or without mdivi1. **(D)** Total abundance of palmitoyl-L-carnitine and **(E)** abundance of the labeled M+16 fraction of palmitoyl-L-carnitine normalized per donor and **(F)** total abundance of acetyl-CoA and **(G)** abundance of the labeled M+02 fraction of acetyl-CoA normalized per donor.Results are expressed as means ± SEM **(B, C, E, G)** or means ± SD **(D,F)**. Datapoints represent independent experiments with different donors. Statistical analyses were performed using two-way Anova with Tukey post-hoc **test (B, C, E, G)**. *p < 0.05, **p < 0.01.

suppress the anti-tumor immune response (44). Further studies are warranted to explore whether these mechanisms also play a role in AMPK-activation driven DC tolerogenicity.

In addition to a role for glycerophospholipid catabolism, we show that AMPK activation-induced tolerogenicity is underpinned by increased FAO. We find this increase to be dependent on mitochondrial fission, a functional connection that has been reported previously in HeLa cells and which we here extend to DCs (28). AMPK phosphorylates multiple proteins involved in mitochondrial dynamics and the observed specific increase in AMPK-mediated phosphorylation of MFF-S172/S146 suggests that AMPK activation in moDCs results in phosphorylation of fission-promoting targets, thereby inducing mitochondrial fragmentation

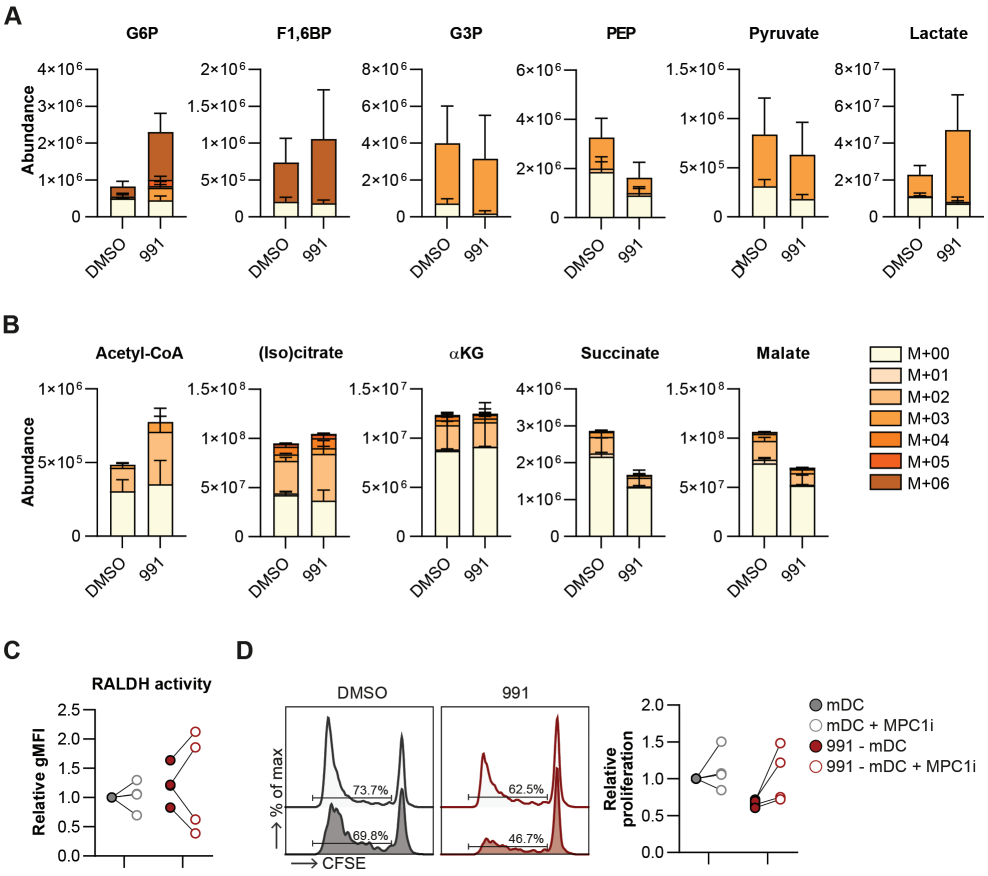

Figure 5: Glucose metabolism promotes AMPK-induced tolerogenicity. A, B: [U-^{13}C]-glucose tracing was performed in DMSO/991-treated mDCs. Figures show total abundance of (labeled) metabolites involved in **(A)** glycolysis and **(B)** TCA cycle. **C:** Normalized quantification of RALDH activity. **D:** Representative histograms and normalized percentage of proliferation of bystander T cells after a T cell suppression assay. Glucose 6-phosphate (G6P), fructose 1,6-biphosphate (F1,6BP), phosphoenolpyruvate (PEP), alpha-ketoglutarate (αKG). Results are expressed as means ± SEM **(C,D)** or means ± SD **(A,B)**. Datapoints represent independent experiments with different donors. Statistical analyses were performed using two-way Anova with Tukey post-hoc test **(C, D)**. *p < 0.05, **p < 0.01.

(13). Despite the observation that blocking FAO through CPT1A silencing compromises AMPK-induced tolerogenicity, we found that lowering FAO to baseline levels through inhibition of mitochondrial fission was not sufficient to prevent Treg induction. This indicates that the remaining levels of FAO, possibly together with elevated glucose catabolism, are sufficient to support the tolerogenic effect induced by AMPK activation. Our findings are largely consistent with earlier work showing that tolDCs induced by a combination of VitD and Dex display increased FAO, which was found to contribute to suppression of early T cell activation (8). Moreover, tumor-associated murine DCs harbor FAO-dependent immunosuppressive

capacities. Tumor-derived Wnt3a induces IDO expression and lowers IL-6 and IL-12 secretion via FAO (45), and BMDCs treated with tumor-derived vesicles showed immune dysfunction in a PPAR-α and FAO dependent manner (46). However, in other DC subsets FAO has also been documented to support pro-inflammatory functions, as plasmacytoid DC activation upon stimulation of endosomal toll-like-receptors was found to rely on FAO (47–49), highlighting that the nature of the role of FAO in supporting DC function is likely DC subset dependent.

While these studies support a role for FAO in DC tolerogenicity, little is known about the mechanisms downstream of FAO that contribute to expression of anti-inflammatory genes and other immune suppressive mediators. Our data indicate that FAO mediates increased RALDH activity upon AMPK activation, although how exactly increased FAO supports RALDH activity remains unexplored. Supplementation of butyrate to moDCs is known to promote RALDH partly through inhibition of histone deacetylases (HDACs) (50). Since AMPK can inhibit HDACs through direct phosphorylation (51), and given that FAO-derived β-hydroxybutyrate, similar to butyrate, can inhibit HDACs (52), it is tempting to speculate that the AMPK-induced increase in FAO together with the direct phosphorylation of the protein may contribute to HDAC inhibition and subsequent promotion of RALDH activity.

Alongside FAO, AMPK activation increased glucose catabolism as revealed by enhanced glucose-derived carbon flux into acetyl-CoA. Blocking mitochondrial pyruvate import prevented the ability of 991-stimulated moDCs to prime functional Tregs, indicating an important role for glucose-derived mitochondrial metabolites in inducing immune suppression. Increased glycolysis was also observed in DCs rendered tolerogenic by VitD alone (35,53), VitD and Dex (34), or by Nuclear Receptor Corepressor 1 (nCoR1) ablation (54). While initial reports suggested that glucose availability and glycolysis, but not glucose oxidation, are essential for VitD-induced tolDCs (35), more recent studies also indicated an essential role for glucose oxidation in VitD-induced tolerogenicity (53). This is different from nCoR1-deficient DCs, in which MPC1 inhibition further increased tolerogenicity (54), indicating that mitochondrial glucose oxidation may serve different roles depending on how DCs are rendered tolerogenic. In our study, we observed reduced tolerogenicity upon MPC1 inhibition, but why this is the case remains to be addressed. The relatively large contribution of glucose-derived carbons to acetyl-CoA compared to downstream TCA cycle intermediates upon AMPK activation, may point towards a role for acetyl-CoA distinct from fueling the TCA cycle in supporting AMPK-activation driven DC tolerogenicity. Acetyl-CoA can also be used for histone acetylation and in other myeloid cells, such as IL-4 polarized macrophages, acetyl-CoA accumulation fueled by glucose-derived carbons was found to be required for gene-specific histone modifications that induce M2-activation (55). Moreover, it was recently found in T cells that glucose-derived pyruvate can be converted into acetyl-CoA in the nucleus by nuclear pyruvate dehydrogenase to alter epigenetic marks (56). As our tracing experiments cannot differentiate between subcellular pools of acetyl-CoA, it would be worth exploring whether this is also occurring in DCs and whether the accumulation of acetyl-CoA, potentially in combination with FAO-driven effects on HDAC activity, impact epigenetic modifications in these tolerogenic DCs and thereby their function.

Overall, based on our data we propose a model in which AMPK activation promotes RALDH activity and rewiring of lipid and glucose metabolism, to render DC tolerogenic. Currently little is known about AMPK activation in DCs *in situ*, but there is some evidence that suggests this pathway is activated and may be functionally relevant in physiological tolerance promoting environments like the intestine (16), or in pathological immunosuppressive

conditions such as the tumor micro-environment (57). Specifically, in the former setting, tolerogenic $CD103^+CD11b^+$ DCs in the murine small intestine have been shown to exhibit high AMPK activity and high RALDH activity, and AMPK deficiency in these $CD11c^+$ cells induced a switch from a tolerogenic towards a more immunogenic phenotype. AMPK activation in tumor-associated DCs has, to our knowledge, not been directly quantified. However, since elevated AMPK levels have been observed in other tumor-infiltrating immune cells (58,59) and phosphorylation of AMPK activator LKB1 has been reported in tumor-infiltrating DCs (60), it is likely that the tumor microenvironment is also a setting with increased AMPK activation in DCs. Further studies are required to determine whether AMPK signaling or downstream pathways are relevant for DC tolerogenicity in these immunosuppressive environments. Finally, unraveling the metabolic underpinnings behind DC tolerogenicity may also provide new insights into how DC-based therapies could be improved. There have been several clinical trials in which the use of *ex vivo* or *in vivo* generated tolDCs has been evaluated for treatment of autoimmune diseases, Crohn's disease, or to prevent transplant rejection (2–4), unfortunately thus far, with variable success rates. Therefore, our work does not only provide new fundamental insights into the metabolic underpinnings of DC-driven tolerogenic responses, but also provides a rationale to explore AMPK as a potential actionable target for the generation of tolDCs for clinical purposes.

Material and methods

Monocyte-derived dendritic cell culture and stimulation

Monocytes were purified from buffy coats of healthy donors (Sanquin, Amsterdam, The Netherlands), through peripheral blood mononuclear cell isolation by Ficoll density gradient centrifugation and magnetic separation using CD14 MicroBeads (130-050-201, Miltenyi Biotec), according to manufacturer's protocol. Monocytes were cultured in complete RPMI (RPMI-1640 (42401-042, Gibco) with 10% FCS (Greiner Bio-one), 100 U/mL penicillin (Eureco-Pharma), 100 µg/mL streptomycin (S9137, Sigma-Aldrich), and 2 mM L-glutamine (G8540, Sigma-Aldrich) supplemented with 10 ng/mL human rGM-CSF (PHC2013, Gibco) and 0.86 ng/mL human rIL4 (204-IL, R&D Systems) to induce moDC differentiation. On day 2/3 medium was refreshed and new cytokines were added. On day 5 moDCs were harvested and replated and if indicated treated with 100µM 991 (129739-36-2, Spirochem), 10 µm Mdivi1 (M0199, Sigma-Aldrich), 10 nM Vitamin D3 (D1530, Sigma-Aldrich), 45 µm Bisdiamine (WIN 18446, 4736/50, Bio-techne), 50 µm UK-5099 (PZ0160, Sigma Aldrich) or DMSO (102931, Merck Millipore). On day 6, moDCs were stimulated with 100 ng/mL ultrapure LPS (E. coli 0111 B4 strain, InvivoGen, San Diego) or left untreated. On day 7 moDCs were harvested and used for further experiments, including analysis of activation markers by flow cytometry and IL-12(p70) and IL-10 secretion by ELISA (555183 and 555157, BD Biosciences). For this, supernatant of moDCs was collected before harvesting moDCs at day 7, or after a 24 hour co-culture with CD40L-expressing J558 cells.

T cell polarization

moDCs were cultured with allogeneic naïve CD4+ T cells in complete RPMI, supplemented with staphylococcal enterotoxin B (10 pg/mL). On days 6 and 8, 10 U/mL human rIL-2 (202-IL, R&D Systems) was added to expand the T cells. On day 11 cells were harvested and replated for cytokine analysis. Intracellular cytokine production was analyzed using flow cytometry after

4 hours of polyclonal restimulation with 100 ng/mL phorbol myristate acetate (PMA, P8139, Sigma-Aldrich) and 1 µg/mL ionomycin (I0634, Sigma Aldrich) in the presence of 10 µg/mL Brefaldin A (B7651, Sigma-Aldrich). IL-10 secretion was determined by ELISA in supernatants harvested after a 24 hour restimulation with anti-CD3 (555336, BD Biosciences) and anti-CD28 (555725, BD Biosciences).

T cell suppression assay

moDCs were cultured with allogenic naïve CD4$^+$ T cells in a 1:10 ratio in complete IMDM (IMDM (BE12-722F, Lonza) with 100 U/mL penicillin, 100 µg/mL streptomycin, 2 mM L-glutamine, and 1 mM pyruvate (P5280, Sigma-Aldrich)). On day 7 T cells (test T cells) were harvested, stained with 1uM Cell Trace Violet (C34557, Thermo Fisher Scientific), irradiated (3000 RAD), and co-cultured with autologous carboxyfluorescein succinimidyl ester (CFSE, C34554, Thermo Fisher Scientific) stained CD4$^+$ memory T cells (bystander T cells) in a 2:1 ratio in the presence of LPS matured moDCs. After 6 days cells were harvested and proliferation of bystander T cells was measured using flow cytometry.

Flow cytometry

In general, cells were stained with a viability dye (Zombie NIR™ Fixable Viability Kit, #423106 BioLegend or LIVE/DEAD™ Fixable Aqua, #L34957, Thermo) for 20 minutes at room temperature before fixation with 1.85% formaldehyde (F1635, Sigma). For assessment of phosphorylated proteins cells were fixed in 4% ultra-pure formaldehyde (#18814-20, Polysciences) for 10 minutes at 37°C directly after cell-culture, and for Treg characterization cells were fixed with FoxP3/Transcription factor staining buffer set (00-5523-00, Invitrogen) for 1 hour at 4°C. Metabolic dyes and T cell proliferation were measured in live cells. Extracellular proteins were stained for 30 minutes at 4°C in FACS buffer (PBS (220/12257974/1110, Braun), supplemented with 0.5% BSA (10735086001, Roche) and 2 mM EDTA (15575-038, Thermo Fisher Scientific). For intracellular protein and cytokine detection, cells were permeabilized for 20 minutes at 4°C in permeabilization buffer (#00-8333-56, Thermo Fisher Scientific), before staining for 30 minutes at 4°C in permeabilization buffer. Prior to staining with antibodies against phosphorylated proteins, cells were also permeabilized in 96% methanol (67-56-1, Fisher chemical) for 20 minutes at -20°C. Cells were stained with metabolic dyes as previously described (61). Briefly, live cells were incubated with, BODIPYTM FL C16 (D3821, Thermo Fisher Scientific), BODIPYTM 493/503 (D3922, Thermo Fisher Scientific), TMRM (T668, Thermo Fisher Scientific) or MitoTracker™ Green FM (M7514, Thermo Fisher Scientific) in PBS for 15 minutes at 37°C before measurement. Aldefluor kit (01700, Stemcell Technologies) was used for assessing RALDH activity, according to manufacturer's protocol. Briefly, cells were stained for 30 minutes at 37°C with 1 µM of Aldefluor reagent dissolved in assay buffer. Cells were kept in assay buffer until measurement. Samples were acquired on FACSCanto II or Cytek Aurora 3-laser spectral flow cytometer and analyzed using FlowJo (Version 10.6, TreeStar). Antibody information is provided in Table 1.

Small interfering RNA (siRNA) transfection

On day 4 of the moDC differentiation, cells were harvested and transfected with 20 nM non-targeting siRNA (D-001206-13-05, Dharmacon), or siRNAs targeting CPT1A (M-009749-02, Dharmacon), PNPLA6 (s21441, Thermo Fisher Scientific), or GPCPD1 (L-013836-01-0005, Dharmacon). Electroporation was performed with the Neon Transfection System (Invitrogen),

using one pulse (1600 V, 20 ms). After electroporation, cells were overnight cultured without antibiotics and polarizing cytokines in RPMI with 10% FCS and 2 mM L-glutamine. The next morning fresh medium containing antibiotics, IL-4, and GM-CSF was added to the cells.

Metabolomics data and analysis

Metabolites were extracted from $5x10^5$ moDCs. Cells were washed with 75 mM ammonium carbonate (A9516, Sigma-Aldrich) in HPLC-grade water (15651400, Honeywell) at 37°C, before metabolite extraction for 3 minutes in 600 µl 70% ethanol at 70°C. Samples were centrifuged at 14000 rpm for 10 min at 4°C and supernatants were shipped to General Metabolics for analysis as previously described (62). Briefly, polar metabolites were analyzed on a non-targeted metabolomics platform in negative ion mode. 886 unique ions were identified of which 632 were annotated according to the human KEGG database. Data filtering based on interquartile range, log transformation, and normalization (mean-centered and divided by the standard deviation) was done using Metaboanalyst (www.metaboanalyst.ca), as was further analysis including pathway enrichment and differential expression analysis.

Proteomics data and analysis

Proteins were extracted from $1x10^6$ moDCs, after cells were washed in PBS and snap-frozen in liquid nitrogen. Cell lysis, digestion and TMT labeling were performed as previously described (63). Cells were lysed using a 5% SDS lysis buffer (100 mM Tris-HCl pH7.6) and were incubated at 95 °C for 4 minutes. Protein determination was performed using Pierce BCA Gold protein assay (Thermo Fisher Scientific). 100 µg protein of each sample was reduced, alkylated and excess iodoacetamide quenched using with 5 mM TCEP, 15 mM iodoacetamide and 10 mM DTT, respectively. Protein was retrieved using chloroform/methanol precipitation and resulting pellets were re-solubilized in 40 mM HEPES pH 8.4. TPCK treated trypsin (1:12.5 enzyme/protein ratio) was added to digest protein overnight at 37 °C. Pierce BCA Gold protein assay was used to determine the peptide concentration. The peptides were labeled with TMTpro Label Reagents (Thermo Fisher Scientific) in a 1:4 ratio by mass (peptides/TMT reagents) for 1 h at RT. 5 µL 6% hydroxylamine was added to quench excess TMT reagent and incubated for 15 min at RT. Samples were pooled and lyophilized. The sample was subsequently fractionated on an Agilent 1200 series HPLC system (Agilent Technologies). 60 µg of the pooled peptide sample was dissolved in solvent A (10 mM NH4HCO3 pH 8.4), injected onto and eluted from an Agilent Eclipse Plus C18 2.1 x 150 mm 3.5 micron column (Agilent Technologies). The gradient was run from 2% to 90% solvent B (10 mM NH4HCO3 pH 8.4 final conc. 20/80 water/acetonitrile v/v) in 30 min at a flowrate of 200 µl/min. 12 fractions were made; every 30 sec a fraction was collected in a vial before going to the next vial. After reaching the last vial collection was continued in the first vial. Afterwards the samples were lyophilized.

Mass spectrometry: The lyophilized fractions were dissolved in water/formic acid (100/0.1 v/v) and subsequently analyzed twice by online C18 nanoHPLC MS/MS with a system consisting of an Easy nLC 1200 gradient HPLC system (Thermo, Bremen, Germany), and a LUMOS mass spectrometer (Thermo). Samples were injected onto a homemade precolumn (100 µm × 15 mm; Reprosil-Pur C18-AQ 3 µm, Dr. Maisch, Ammerbuch, Germany) and eluted via a homemade analytical nano-HPLC column (30 cm × 50 µm; Reprosil-Pur C18-AQ 3 um). The gradient was run from 5% to 30% solvent B (20/80/0.1 water/acetonitrile/formic acid (FA) v/v) in 240 min. The nano-HPLC column was drawn to a tip of ~10 µm and acted

as the electrospray needle of the MS source. The mass spectrometer was operated in data-dependent MS/MS mode (SPS-MS3 method) for a cycle time of 2.5 seconds, with a HCD collision energy at 36 V and recording of the MS2 spectrum in the orbitrap, with a quadrupole isolation width of 0.7 Da. In the master scan (MS1) the resolution was 120,000, the scan range 400-1600, at standard AGC target 'standard'. A lock mass correction on the background ion m/z=445.12 was used. Precursors were dynamically excluded after n=1 with an exclusion duration of 45 s, and with a precursor range of 20 ppm. Charge states 2-6 were included. MS2 (CID) was performed in the ion trap at 35%, with AGC target 'standard' and mass range 'normal'. Synchronous precursor selection in MS3 was 'true' at a HCD collision energy of 55% and detection in the orbitrap at a resolution of 50,000, at an AGC target of 300% with a scan range of m/z 100-500. In a post-analysis process, raw data were first converted to peak lists using Proteome Discoverer version 2.5 (Thermo Electron), and submitted to the Uniprot database (Homo sapiens, 20596 entries), using Mascot v. 2.2.07 (www.matrixscience.com) for protein identification. Mascot searches were with 10 ppm and 0.5 Da deviation for precursor and fragment mass, respectively. Enzyme specificity was set to trypsin. Up to three missed cleavages were allowed. Methionine oxidation and acetyl on protein N-terminus were set as variable modifications. Carbamidomethyl on Cys and TMTpro on Lys and N-terminus were set as fixed modifications. Protein FDR of 1% was set. Normalization was on total peptide amount. 8325 proteins were identified of which 3462 were used for further processing after filtering based on high protein confidence and at least 5 unique peptides per protein. Pathway enrichment was performed using Metascape and enriched gene ontology (GO) pathways were considered significant if FDR ≤ 0.05 (64). Integration of metabolomics and proteomics data was performed using Shiny Gam (https://artyomovlab.wustl.edu/shiny/gam/) (25).

^{13}C-tracer experiments

On day 7, 20 hours after LPS stimulation, moDCs were harvested, counted and 5x10^5 cells were replated in 350 µl in complete glucose-free RPMI (11879020, Thermo Fisher Scientific), supplemented with 100 U/mL penicillin, 100 µg/mL streptomycin, and 25 mM HEPES (9136, Sigma Aldrich). Additionally, 350 µl complete glucose-free RPMI was added, supplemented with either 22 mM [U-^{13}C]-Glucose (CLM-1396-PK, Cambridge Isotope Laboratories) and 0.027 mM ^{12}C-Palmitate (76119, Merck Millipore) or 22 mM ^{12}C-Glucose (15023021, Gibco) and 0.027 mM [U-^{13}C]-Palmitate (CLM-409-PK, Cambridge Isotope Laboraties), to reach an end concentration of 11 mM glucose and 0.014 mM palmitate. Palmitate was in-house conjugated to BSA in a 2:1 ratio. Cells were cultured for 4 hours at 37°C before metabolites were extracted. Cells were washed in ice-cold PBS, before extraction in lysis buffer (40% acetonitrile (34967, Honeywell) and 40% methanol in HPLC-grade water). Samples were vortexed 3 times for 3 seconds and centrifuged at 4°C for 15 minutes at full speed. Supernatant was stored at -80°C. Metabolites were analyzed by liquid chromatography – mass spectrometry (LC-MS)-based metabolomics as previously described (65). Briefly, metabolite identification was based on exact mass (5 ppm range), validated by concordance with retention times of standards and peak areas were in their respective linear range of detection. TraceFinder Software (Thermo Fisher Scientific) was used for quantification. Peak intensities were normalized based on mean peak intensity and isotopomer distributions were corrected for natural abundance.

Quantitative polymerase chain reaction (qPCR)
RNA was extracted from snap-frozen moDCs as previously described ((16)). cDNA synthesis was performed using M-MLV Reverse Transcriptase (28025013, Thermo Fisher Scientific) and qPCR was performed with the Gotaq qPCR master mix (A6001, Promega) and the CFX96 Touch Real-Time PCR Detection System (Biorad). Primers are listed in table 2.

Confocal microscopy
On day 5 of moDC differentiation, cells were plated in glass bottom confocal dishes (627871, Greiner) and coated for 2 hours with Poly-D-Lysine (PDL) at 37°C. Treatments were performed as described earlier and cells were analyzed on day 7. 10 minutes prior to imaging nuclei were stained with 50 ng/mL Hoechst 33342 (H3570, Thermo Fisher Scientific) and mitochondria with 10 nM Cy5-methyl-methyl ($Cy5M_2$) (66). Cells were imaged directly using the 40x objective on a SP8X WLL (white light laser) microscope (Leica Microsystems, Wetzlar, Germany) with climate control at 37°C, 5% CO_2. Mitochondrial quantification was done in ImageJ using the MitoAnalyzer Marco as previously described (67).

Seahorse extracellular flux analysis
Mitochondria oxygen consumption rate (OCR) was analyzed using a XF^e96 extracellular flux analyzer (Seahorse Bioscience). moDCs were plated in seahorse cell culture plates coated with Poly-D-Lysine (PDL) at 37°C for 1 hour, in unbuffered, glucose-free RPMI, supplemented with 5% FCS and 2 mM L-glutamine, and incubated for 1 hour at 37°C in a CO_2 free incubator. OCR was measured in response to 10 mM glucose (G8644, Sigma-Aldrich), 1 µM oligomycin (11342, Cayman Chemical), 3 µM fluoro-carbonyl cyanide phenylhydrazone (FCCP) (C2920-Sigma-Aldrich) and 1 µM rotenone (R8875, Sigma-Aldrich) + 1 µM antimycin A (A8674, Sigma-Aldrich).

Western blot
moDCs were washed in PBS, snap-frozen in liquid nitrogen and lysed with EBSB buffer (8% glycerol (7044, J. T. Baker), 3% SDS (151-21-3, VWR Life Science) and 100 mM Tris–HCl [pH 6.8](1.00317, Supelco; 77-86-1, Thermo Fisher Scientific)) for detection of complexes of the electron transport chain, or lysed with RIPA-like buffer (50 mmol/L HEPES (pH 7.6), 50 mmol/L Natrium fluoride (S7920, Sigma Aldrich), 50 mmol/L Potassium chloride (7447407, Merck Millipore) , 5 mmol/L Sodium pyrophosphate decahydrate (13472-36-1, Sigma Aldrich), 1 mmol/L EDTA (E5134, Sigma Aldrich), 1 mmol/L EGTA (E3889, Sigma Aldrich), 1 mmol/L dithiothreitol (V315A, Promega), 5 mmol/L β-glycerophosphate (G6376, Sigma Aldrich), 1 mmol/L sodium orthovanadate (S6508, Sigma Aldrich), 1% NP40 (74385, Sigma Aldrich), and protease inhibitor cocktail (11697498001; Roche). Lysates were boiled for 5 minutes (except lysates used for detection of electron transport chain complexes) and protein content was determined using a BCA kit (23225, Thermo Fisher Scientific). Proteins were separated by SDS-PAGE and transferred to a 45 µm PVDF membrane. Membranes were blocked for 1 hour at room temperature in TTBS buffer (20 mM Tris-HCl [pH 7.6], 137 mM NaCl (1.06404.1000, Merck Millipore), and 0.25% Tween (8.22184.0500, Merck Millipore)) containing 5% fat free milk (Campina). Membranes were incubated with primary antibodies overnight at 4°C, washed in TTBS buffer, incubated with horseradish peroxidase-conjugated secondary antibodies for 2 hours at room temperature, washed again and developed using enhanced chemiluminescence. Primary antibodies: HSP90 (Santa Cruz #sc7947), DRP1

(5391T, Cell Signaling), Phospho-DRP1 (Ser637) (4867S, Cell Signaling), MFF (84580T, Cell Signaling), Phospho-MFF (Ser172, Ser146) (PA5-104614, Thermo Fisher Scientific), total Oxphos antibody cocktail (ab110413, Abcam).
Western blots were quantified using ImageJ software (NIH, Bethesda, MD, USA) and phosphorylation status was normalized to the total abundance of the target protein and a housekeeping protein.

Statistical analysis
Results are expressed as mean ± standard error mean (SEM) except where stated otherwise. Data were analyzed using GraphPad Prism (La Jolla, CA, USA). Comparisons between two or more independent data groups were made by Student's T test or analysis of variance test (ANOVA),respectively. $P<0.05$ was considered statistically significant.

Tables

Table 1: antibodies flow cytometry

Target	Clone	Conjugate	Source	Identifier
CD103	Ber-ACT8	PE-Cy7	BioLegend	350211
CD127	HIL-7R-M21	APC-R700	BD Biosciences	565185
CD14	M5E2	BV510	Biolegend	301842
CD1a	HI149	BV421	BioLegend	300128
CD25	M-A251	APC-Cy7	BD Pharmingen	557753
CD3	UCHT1	AF700	Biolegend	300423
CD4	SK3	PerCP-ef710	Invitrogen	46-0047-42
CD40	5C3	APC	BD Pharmingen	555591
CD49b	P1E6-Cd5	PE-Cy7	BioLegend	359313
CD80	2D10	PE-Cy5	Biolegend	305209
CD83	HB15e	PE	eBioscience	12-0839-42
CD86	2331 (FUN-1)	FITC	BD Pharmingen	555657
CTLA4	BNI3	PE-Cy5	BD Pharmingen	555854
FoxP3	PCH101	APC	Invitorgen	17-4776-42
Goat anti-Rabbit	polyclonal	AF647	Invitrogen	A21244
HLA-DR	L243	APC-Cy7	Biolegend	307618
ICOS	C398.4A	FITC	BioLegend	313505
IDO	eyedio	PE	Invitrogen	12-9477-41
IFNγ	B27	V450	BD Biosciences	560371
IL-10	JES3-19F1	APC	BioLegend	506807
IL-4	8D4-8	PE-Cy7	eBioscience	25-7049-82
ILT3	ZM3.8	BV480	BD Optibuild	746718
LAG-3	11C3C65	BV605	BioLegend	369323

PD-L1	MIH3	PE-Cy7	Biolegend	374506
PD-L2	MIH18	FITC	Milteny Biotec	130-098-528
Phopho-S6 (S240)	N4-41	-	BD Biosciences	560430
Phospho-ACC (ser79)	D7D11	-	Cell signaling	11818S
TIGIT	A15153G	BV711	BioLegend	372741

Table 2: primers

Target	Forward	Reverse
PNPLA6	TGACCCGCCTTATCCACCTA	CCAGAGCCTGCTGGGAAG
GPCPD	ACAAAGGCTGCACCATGACT	CCATCGAGGTGCAGGAAACT
CPT1A	GCGCACTACAAGGACATGGGCA	CACCATGGCCCGCACGAAGT
MFN1	AGCGGCTTTCCAAGCCTAAT	CTGTCTGCGTACGTCTTCCA
DRP1	AAACTTCGGAGCTATGCGGT	AGGACGAGGACCAGTAGCAT
FIS1	AGGCCTTAAAGTACGTCCGC	TGCCCACGAGTCCATCTTTC

Acknowledgements

This work was supported by an LUMC fellowship awarded to BE.

Author Contributions

ECB and BE designed and analyzed the experiments. ECB, TAP, AJH, TJAM, and FO performed the experiments. FWMV, EAZ, and CRB aided with the ^{13}C-tracer experiments. AHR, RTNT, and PAV aided with the proteomics experiments. BG helped in the discussion and reviewed the manuscript. BE conceived and supervised the study and wrote the manuscript together with ECB.

Competing Interests

The authors declare no competing interests.

References

1. Kapsenberg ML. Dendritic-cell control of pathogen-driven T-cell polarization. Nat Rev Immunol. 2003;3(12):984–93.
2. Mohammadi B, Saghafi M, Abdulsattar Faraj T, Kamal Kheder R, Sajid Abdulabbas H, Esmaeili SA. The role of tolerogenic dendritic cells in systematic lupus erythematosus progression and remission. Int Immunopharmacol. 2023;115.
3. Ness S, Lin S, Gordon JR. Regulatory Dendritic Cells, T Cell Tolerance, and Dendritic Cell Therapy for Immunologic Disease. Front Immunol. 2021;12.
4. Passeri L, Marta F, Bassi V, Gregori S. Tolerogenic dendritic cell-based approaches in autoimmunity. Int J Mol Sci. 2021;22(16).
5. Brombacher EC, Everts B. Shaping of Dendritic Cell Function by the Metabolic Micro-Environment. Front Endocrinol. 2020;11.
6. Everts B, Amiel E, Huang SCC, Smith AM, Chang CH, Lam WY, et al. TLR-driven early glycolytic reprogramming via the kinases TBK1-IKKε supports the anabolic demands of dendritic cell activation. Nat Immunol. 2014;15(4):323–32.
7. Krawczyk CM, Holowka T, Sun J, Blagih J, Amiel E, DeBerardinis RJ, et al. Toll-like receptor-induced changes in glycolytic metabolism regulate dendritic cell activation. Blood. 2010;115(23):4742–9.
8. Malinarich F, Duan K, Hamid RA, Bijin A, Lin WX, Poidinger M, et al. High Mitochondrial Respiration and Glycolytic Capacity Represent a Metabolic Phenotype of Human Tolerogenic Dendritic Cells. The Journal of Immunology. 2015;194(11):5174–86.
9. Patente TA, Pelgrom LR, Everts B. Dendritic cells are what they eat: how their metabolism shapes T helper cell polarization. Curr Opin Immunol. 2019;58:16–23.
10. Møller SH, Wang L, Ho PC. Metabolic programming in dendritic cells tailors immune responses and homeostasis. Cell Mol Immunol. 2022;19(3):370–83.
11. Steinberg GR, Hardie DG. New insights into activation and function of the AMPK. Nat Rev Mol Cell Biol. 2022;24:255–72.
12. Snyder JP, Amiel E. Regulation of dendritic cell immune function and metabolism by cellular nutrient sensor mammalian target of rapamycin (mTOR). Front Immunol. 2019;10.
13. Trefts E, Shaw RJ. AMPK: restoring metabolic homeostasis over space and time. Mol Cell. 2021;81(18):3677–90.
14. Carroll KC, Viollet B, Suttles J. AMPKα1 deficiency amplifies proinflammatory myeloid APC activity and CD40 signaling. J Leukoc Biol. 2013;94(6):1113–21.
15. Nieves W, Hung LY, Oniskey TK, Boon L, Foretz M, Viollet B, et al. Myeloid-Restricted AMPKα1 Promotes Host Immunity and Protects against IL-12/23p40–Dependent Lung Injury during Hookworm Infection. The Journal of Immunology. 2016;196(11):4632–40.
16. Patente TA, Brombacher EC, Heieis GA, Pelgrom LR, Zawistowska-Deniziak A, Otto F, et al. Metabolic sensor AMPK licenses CD103+ dendritic cells to induce Treg responses. bioRxiv. 2023;
17. Bultot L, Jensen TE, Lai YC, B Madsen AL, Collodet C, Kviklyte S, et al. Benzimidazole derivative small-molecule 991 enhances AMPK activityand glucose uptake induced by AICAR or contraction in skeletal muscle. Am J Physiol Endocrinol Metab. 2016;311:706–19.
18. Hardie DG, Ross FA, Hawley SA. AMPK: A nutrient and energy sensor that maintains energy homeostasis. Nat Rev Mol Cell Biol. 2012;13(4):251–62.
19. Sun CM, Hall JA, Blank RB, Bouladoux N, Oukka M, Mora JR, et al. Small intestine lamina propria dendritic cells promote de novo generation of Foxp3 T reg cells via retinoic acid. Journal of Experimental Medicine. 2007;204(8):1775–85.

20. Coombes JL, Siddiqui KRR, Arancibia-Cárcamo C V., Hall J, Sun CM, Belkaid Y, et al. A functionally specialized population of mucosal CD103+ DCs induces Foxp3+ regulatory T cells via a TGF-β -and retinoic acid-dependent mechanism. Journal of Experimental Medicine. 2007;204(8):1757–64.

21. Boonpiyathad T, Sözener ZC, Akdis M, Akdis CA. The role of treg cell subsets in allergic disease. Asian Pac J Allergy Immunol. 2020;38(3):139–49.

22. Zheng J, Chan PL, Liu Y, Qin G, Xiang Z, Lam KT, et al. ICOS regulates the generation and function of human CD4+ Treg in a CTLA-4 dependent manner. PLoS One. 2013;8(12).

23. Joller N, Lozano E, Burkett PR, Patel B, Xiao S, Zhu C, et al. Treg cells expressing the coinhibitory molecule TIGIT selectively inhibit proinflammatory Th1 and Th17 cell responses. Immunity. 2014;40(4):569–81.

24. Gagliani N, Magnani CF, Huber S, Gianolini ME, Pala M, Licona-Limon P, et al. Coexpression of CD49b and LAG-3 identifies human and mouse T regulatory type 1 cells. Nat Med. 2013;19(6):739–46.

25. Sergushichev AA, Loboda AA, Jha AK, Vincent EE, Driggers EM, Jones RG, et al. GAM: a web-service for integrated transcriptional and metabolic network analysis. Nucleic Acids Res. 2016;44(1):194–200.

26. Van Tienhoven M, Atkins J, Li Y, Glynn P. Human neuropathy target esterase catalyzes hydrolysis of membrane lipids. Journal of Biological Chemistry. 2002;277(23):20942–8.

27. Okazaki Y, Ohshima N, Yoshizawa I, Kamei Y, Mariggiò S, Okamoto K, et al. A novel glycerophosphodiester phosphodiesterase, GDE5, controls skeletal muscle development via a non-enzymatic mechanism. Journal of Biological Chemistry. 2010;285(36):27652–63.

28. Song JE, Alves TC, Stutz B, Šestan-Peša M, Kilian N, Jin S, et al. Mitochondrial fission governed by drp1 regulates exogenous fatty acid usage and storage in hela cells. Metabolites. 2021;11(5).

29. Li J, Wang Y, Wang Y, Wen X, Ma XN, Chen W, et al. Pharmacological activation of AMPK prevents Drp1-mediated mitochondrial fission and alleviates endoplasmic reticulum stress-associated endothelial dysfunction. J Mol Cell Cardiol. 2015;86:62–74.

30. Toyama EQ, Herzig S, Courchet J, Lewis TL, Losón OC, Hellberg K, et al. Metabolism: AMP-activated protein kinase mediates mitochondrial fission in response to energy stress. Science. 2016;351(6270):275–81.

31. Cassidy-Stone A, Chipuk JE, Ingerman E, Song C, Yoo C, Kuwana T, et al. Chemical Inhibition of the Mitochondrial Division Dynamin Reveals Its Role in Bax/Bak-Dependent Mitochondrial Outer Membrane Permeabilization. Dev Cell. 2008;14(2):193–204.

32. Bordt EA, Clerc P, Roelofs BA, Saladino AJ, Tretter L, Adam-Vizi V, et al. The Putative Drp1 Inhibitor mdivi-1 Is a Reversible Mitochondrial Complex I Inhibitor that Modulates Reactive Oxygen Species. Dev Cell. 2017;40(6):583–94.

33. Halestrap AP. The Mitochondrial Pyruvate Carrier. Kinetics and specificity for substrated and inhibitors. Vol. 148, Biochem. J. 1975.

34. Adamik J, Munson P V., Hartmann FJ, Combes AJ, Pierre P, Krummel MF, et al. Distinct metabolic states guide maturation of inflammatory and tolerogenic dendritic cells. Nat Commun. 2022;13(1):1–19.

35. Ferreira GB, Vanherwegen AS, Eelen G, Gutiérrez ACF, VanLommel L, Marchal K, et al. Vitamin D3 induces tolerance in human dendritic cells by activation of intracellular metabolic pathways. Cell Rep. 2015;10(5):711–25.

36. Boks MA, Kager-Groenland JR, Haasjes MSP, Zwaginga JJ, van Ham SM, ten Brinke A. IL-10-generated tolerogenic dendritic cells are optimal for functional regulatory T cell induction - A comparative study of human clinical-applicable DC. Clinical Immunology. 2012;142(3):332–42.

37. Awasthi A, Carrier Y, Peron JPS, Bettelli E, Kamanaka M, Flavell RA, et al. A dominant function for interleukin 27 in generating interleukin 10-producing anti-inflammatory T cells. Nat Immunol. 2007;8(12):1380–9.

38. Rodrigues CP, Ferreira ACF, Pinho MP, De Moraes CJ, Bergami-Santos PC, Barbuto JAM. Tolerogenic IDO+ dendritic cells are induced by pd-1-expressing mast cells. Front Immunol. 2016;7(9).

39. Mucida Daniel, Park Yunji, Kim Gisen, Turovskaya Olga, Scott Lain, Kronenberg Mitchell, et al. Reciprocal TH17 and RegulatoryT Cell Differentiation Mediated by Retinoic Acid. Science (1979). 2007;317(5835):256–60.

40. Weckel A, Dhariwala MO, Ly K, Tran VM, Ojewumi OT, Riggs JB, et al. Long-term tolerance to skin commensals is established neonatally through a specialized dendritic cell subgroup. Immunity. 2023;56.

41. Chung DJ, Rossi M, Romano E, Ghith J, Yuan J, Munn DH, et al. Indoleamine 2,3-dioxygenase-expressing mature human monocyte-derived dendritic cells expand potent autologous regulatory T cells. Blood. 2009;114:555–63.

42. Ferreira GB, Kleijwegt FS, Waelkens E, Lage K, Nikolic T, Hansen DA, et al. Differential protein pathways in 1,25-dihydroxyvitamin D 3 and dexamethasone modulated tolerogenic human dendritic cells. J Proteome Res. 2012;11(2):941–71.

43. O'Donnell VB, Rossjohn J, Wakelam MJO. Phospholipid signaling in innate immune cells. Journal of Clinical Investigation. 2018;128(7):2670–9.

44. Saito R de F, Andrade LN de S, Bustos SO, Chammas R. Phosphatidylcholine-Derived Lipid Mediators: The Crosstalk Between Cancer Cells and Immune Cells. Front Immunol. 2022;13.

45. Zhao F, Xiao C, Evans KS, Theivanthiran T, DeVito N, Holtzhausen A, et al. Paracrine Wnt5a-β-Catenin Signaling Triggers a Metabolic Program that Drives Dendritic Cell Tolerization. Immunity. 2018;48(1):147–60.

46. Yin X, Zeng W, Wu B, Wang L, Wang Z, Tian H, et al. PPARα Inhibition Overcomes Tumor-Derived Exosomal Lipid-Induced Dendritic Cell Dysfunction. Cell Rep. 2020;33(3).

47. Qiu CC, Atencio AE, Gallucci S. Inhibition of fatty acid metabolism by etomoxir or TOFA suppresses murine dendritic cell activation without affecting viability. Immunopharmacol Immunotoxicol. 2019;41(3):361–9.

48. Wu D, Sanin DE, Everts B, Chen Q, Qiu J, Buck MD, et al. Type 1 Interferons Induce Changes in Core Metabolism that Are Critical for Immune Function. Immunity. 2016;44(6):1325–36.

49. Basit F, de Vries IJM. Dendritic Cells Require PINK1-Mediated Phosphorylation of BCKDE1α to Promote Fatty Acid Oxidation for Immune Function. Front Immunol. 2019;10.

50. Kaisar MMM, Pelgrom LR, van der Ham AJ, Yazdanbakhsh M, Everts B. Butyrate conditions human dendritic cells to prime type 1 regulatory T cells via both histone deacetylase inhibition and G protein-coupled receptor 109A signaling. Front Immunol. 2017;8.

51. Mihaylova MM, Vasquez DS, Ravnskjaer K, Denechaud PD, Yu RT, Alvarez JG, et al. Class IIa histone deacetylases are hormone-activated regulators of FOXO and mammalian glucose homeostasis. Cell. 2011;145(4):607–21.

52. Shimazu T, Hirschey MD, Newman J, He W, Shirakawa K, Le Moan N, et al. Suppression of oxidative stress by β-hydroxybutyrate, an endogenous histone deacetylase inhibitor. Science (1979). 2013;339(6116):211–4.

53. Vanherwegen AS, Eelen G, Ferreira GB, Ghesquière B, Cook DP, Nikolic T, et al. Vitamin D controls the capacity of human dendritic cells to induce functional regulatory T cells by regulation of glucose metabolism. Journal of Steroid Biochemistry and Molecular Biology. 2019;187:134–45.

54. Sen K, Pati R, Jha A, Mishra GP, Prusty S, Chaudhary S, et al. NCoR1 controls immune tolerance in conventional dendritic cells by fine-tuning glycolysis and fatty acid oxidation. Redox Biol. 2023;59.

55. Covarrubias AJ, Aksoylar HI, Yu J, Snyder NW, Worth AJ, Iyer SS, et al. Akt-mTORC1 signaling regulates Acly to integrate metabolic input to control of macrophage activation. 2016;5(11612).

56. Mocholi E, Russo L, Gopal K, Ramstead AG, Hochrein SM, Vos HR, et al. Pyruvate metabolism controls chromatin remodeling during CD4+ T cell activation. Cell Rep. 2023;42(6).

57. Arner EN, Rathmell JC. Metabolic programming and immune suppression in the tumor microenvironment. Cancer Cell. 2023;41(3):421–33.

58. Trillo-Tinoco J, Sierra RA, Mohamed E, Cao Y, de Mingo-Pulido A, Gilvary DL, et al. AMPK alpha-1 intrinsically regulates the function and differentiation of tumor myeloid-derived suppressor cells. Cancer Res. 2019;79(19):5034–47.

59. An J, Ding Y, Yu C, Li J, You S, Liu Z, et al. AMP-activated protein kinase alpha1 promotes tumor development via FOXP3 elevation in tumor-infiltrating Treg cells. iScience. 2022;25(1).

60. Wang Y, Du X, Wei J, Long L, Tan H, Guy C, et al. LKB1 orchestrates dendritic cell metabolic quiescence and anti-tumor immunity. Cell Res. 2019;29(5):391–405.

61. Brombacher EC, Patente TA, Quik M, Everts B. Characterization of Dendritic Cell Metabolism by Flow Cytometry. In: Sisirak V, editor. Dendritic Cells Methods in Molecular Biology. Humana Press; 2023. p. 219–37.

62. Fuhrer T, Heer D, Begemann B, Zamboni N. High-throughput, accurate mass metabolome profiling of cellular extracts by flow injection-time-of-flight mass spectrometry. Anal Chem. 2011;83(18):7074–80.

63. Paulo JA, Gygi SP. Nicotine-induced protein expression profiling reveals mutually altered proteins across four human cell lines. Proteomics. 2017;17(1–2).

64. Zhou Y, Zhou B, Pache L, Chang M, Khodabakhshi AH, Tanaseichuk O, et al. Metascape provides a biologist-oriented resource for the analysis of systems-level datasets. Nat Commun. 2019;10(1).

65. Zaal EA, Wu W, Jansen G, Zweegman S, Cloos J, Berkers CR. Bortezomib resistance in multiple myeloma is associated with increased serine synthesis. Cancer Metab. 2017;5(1).

66. Winkel BMF, de Korne CM, van Oosterom MN, Staphorst D, Bunschoten A, Langenberg MCC, et al. A tracer-based method enables tracking of plasmodium falciparum malaria parasites during human skin infection. Theranostics. 2019;9(10):2768–78.

67. Chaudhry A, Shi R, Luciani DS. A pipeline for multidimensional confocal analysis of mitochondrial morphology, function, and dynamics in pancreatic b-cells. Am J Physiol Endocrinol Metab. 2020;318:87–101.

Supplementary figures

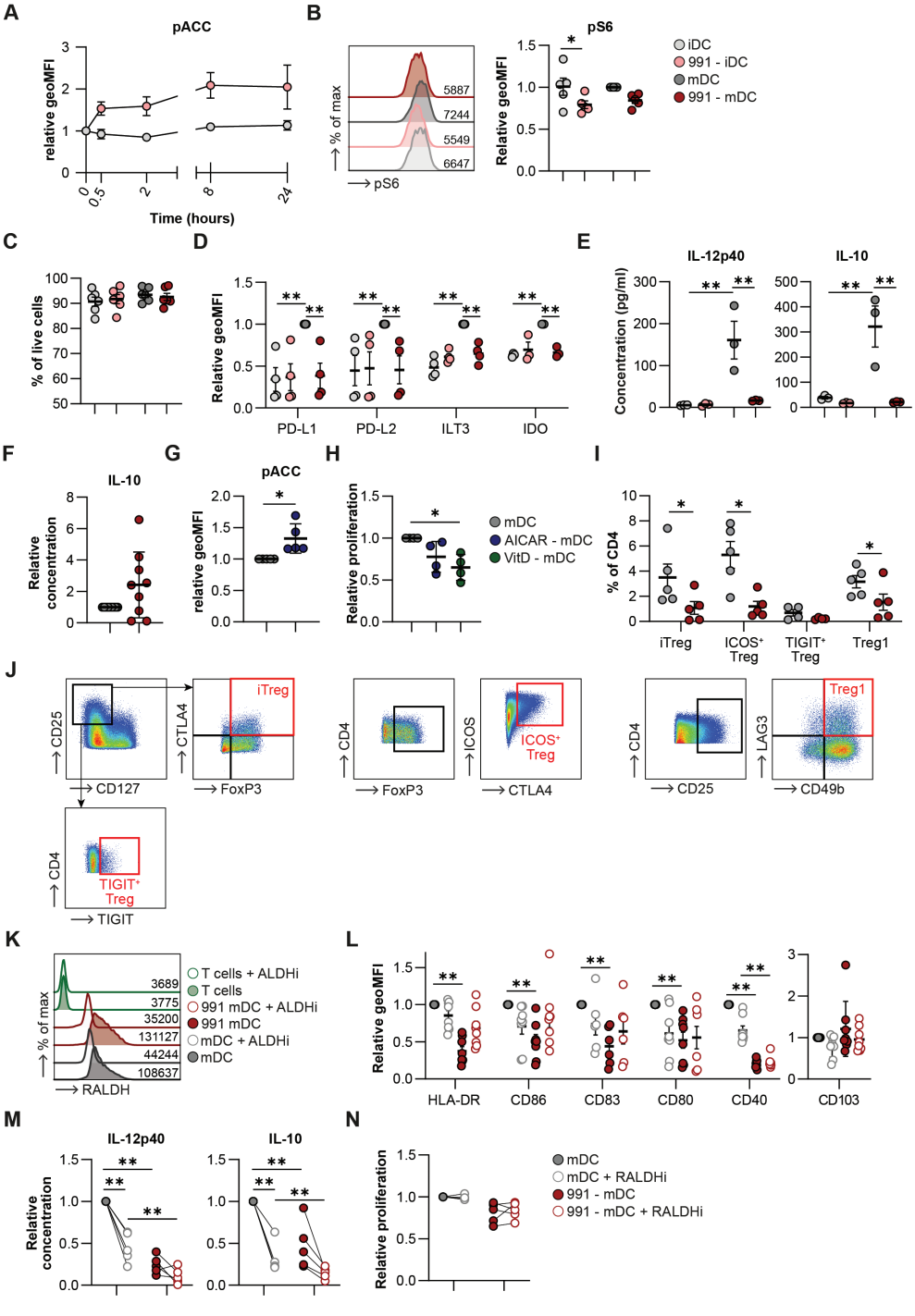

Supplementary figure 1. Effects of 991 and RALDH inhibition on moDCs and T cell priming. A: Phosphorylation of ACC (Ser79) at different time points as determined by flow cytometry. **B:** Representative histogram and normalized quantification of phosphorylation of S6 (Ser240). **C:** Percentage of live cells as % of total moDCs. **D:** Normalized expression of indicated markers on moDCs. **E:** Concentration of IL-12p40 and IL-10 in the supernatants of moDCs. **F:** Relative concentration of IL-10 in the supernatants of T cells primed with 991/DMSO-treated mDCs after a 24 hour restimulation with αCD3/αCD28 antibodies. **G:** Normalized quantification of phosphorylation of ACC (Ser79) after treatment with H^2O/AICAR. **H:** Normalized percentage of proliferation of bystander T cells after a T cell suppression assay. **I:** Abundance of $CD25^+FoxP3^+CTLA4^+$ induced Tregs (iTregs), $CD25^+FoxP3^+ICOS^+$ Tregs ($ICOS^+$ Treg), $CD25^+TIGIT^+$ Treg ($TIGIT^+$ Treg) and $CD25^+CD49b^+LAG3^+$ Tregs (Treg1) in total $CD4^+$ T cells after priming with DMSO/991-treated mDCs. **J:** Gating strategy of T cell subsets as described in I. **K:** representative histograms of RALDH activity after treatment with RALDH inhibitor bisdiamine (RALDHi). Representative of 4 independent experiments. **L:** Normalized expression of indicated markers. **M:** Normalized concentration of IL-12p40 and IL-10 after a 24hour co-culture with with CD40L-expressing J558 cells. **N:** Normalized quantification of bystander T cell proliferation after co-culture with irradiated T cells primed with 991/DMSO-treated mDC cultured in presence or absence of RALDH inhibitor bisdiamine (RALDHi). Results are expressed as means ± SEM. Datapoints represent independent experiments with different donors. Statistical analyses were performed using paired t-tests **(F, G, I)**, one-way Anova with Sidak post-hoc test **(H)** or two-way Anova with Tukey post-hoc test **(A-E, L-N)**. *$p < 0.05$, **$p < 0.01$.

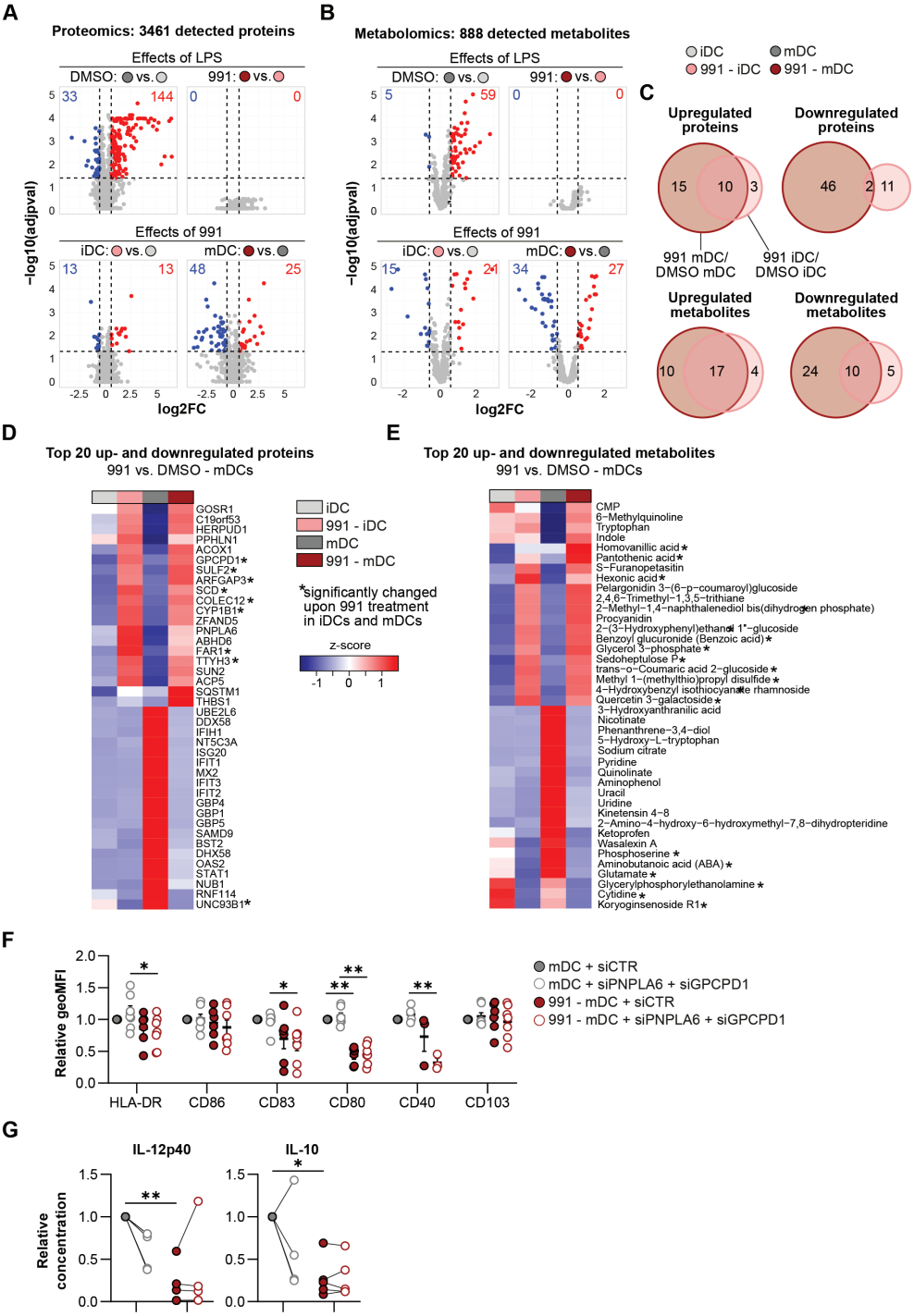
A
Proteomics: 3461 detected proteins
Effects of LPS
DMSO: vs.
991: vs.
33
144
0
0
Effects of 991
iDC: vs.
mDC: vs.
13
13
48
25
−log10(adjpval)
log2FC
B
Metabolomics: 888 detected metabolites
Effects of LPS
DMSO: vs.
991: vs.
5
59
0
0
Effects of 991
iDC: vs.
mDC: vs.
15
24
34
27
−log10(adjpval)
log2FC
C
iDC
mDC
991 - iDC
991 - mDC
Upregulated proteins
Downregulated proteins
15
10
3
46
2
11
991 mDC/ DMSO mDC
991 iDC/ DMSO iDC
Upregulated metabolites
Downregulated metabolites
10
17
4
24
10
5
D
Top 20 up- and downregulated proteins
991 vs. DMSO - mDCs
GOSR1
C19orf53
HERPUD1
PPHLN1
ACOX1
GPCPD1*
SULF2*
ARFGAP3*
SCD*
COLEC12*
CYP1B1*
ZFAND5
PNPLA6
ABHD6
FAR1*
TTYH3*
SUN2
ACP5
SQSTM1
THBS1
UBE2L6
DDX58
IFIH1
NT5C3A
ISG20
IFIT1
MX2
IFIT3
IFIT2
GBP4
GBP1
GBP5
SAMD9
BST2
DHX58
OAS2
STAT1
NUB1
RNF114
UNC93B1*
iDC
991 - iDC
mDC
991 - mDC
*significantly changed upon 991 treatment in iDCs and mDCs
z-score
-1
0
1
E
Top 20 up- and downregulated metabolites
991 vs. DMSO - mDCs
CMP
6-Methylquinoline
Tryptophan
Indole
Homovanillic acid*
Pantothenic acid*
S-Furanopetasitin
Hexonic acid*
Pelargonidin 3-(6-p-coumaroyl)glucoside
2,4,6-Trimethyl-1,3,5-trithiane
2-Methyl-1,4-naphthalenediol bis(dihydrogen phosphate)
Procyanidin
2-(3-Hydroxyphenyl)ethanol 1*-glucoside
Benzoyl glucuronide (Benzoic acid)*
Glycerol 3-phosphate*
Sedoheptulose P*
trans-o-Coumaric acid 2-glucoside*
Methyl 1-(methylthio)propyl disulfide*
4-Hydroxybenzyl isothiocyanate rhamnoside
Quercetin 3-galactoside*
3-Hydroxyanthranilic acid
Nicotinate
Phenanthrene-3,4-diol
5-Hydroxy-L-tryptophan
Sodium citrate
Pyridine
Quinolinate
Aminophenol
Uracil
Uridine
Kinetensin 4-8
2-Amino-4-hydroxy-6-hydroxymethyl-7,8-dihydropteridine
Ketoprofen
Wasalexin A
Phosphoserine*
Aminobutanoic acid (ABA)*
Glutamate*
Glycerylphosphorylethanolamine*
Cytidine*
Koryoginsenoside R1*
F
Relative geoMFI
HLA-DR
CD86
CD83
CD80
CD40
CD103
mDC + siCTR
mDC + siPNPLA6 + siGPCPD1
991 - mDC + siCTR
991 - mDC + siPNPLA6 + siGPCPD1
G
IL-12p40
IL-10
Relative concentration

Supplementary figure 2: Effects of AMPK activation on proteome and metabolome of moDCs. A, B: Volcano plots depicting all identified **(A)** proteins and **(B)** metabolites. Blue and red dots denote the significantly down- and upregulated proteins/metabolites, respectively. **C:** Venn diagrams showing the overlap between up- and down-regulated proteins and metabolites upon AMPK activation in mDCs and iDCs. **D, E:** Heatmaps depicting the relative expression of the 20 most up- and downregulated **(D)** proteins and **(E)** metabolites upon AMPK activation in mDCs, ranked by log2 fold change and filtered by adjusted p-value <0.05. **F:** Normalized expression of indicated markers. **G:** relative concentration of IL-12p40 and IL-10 in the supernatants of mDCs after co-culture with CD40L-expressing J558 cells. Results are expressed as means ± SEM. Datapoints represent independent experiments with different donors. Statistical analyses were performed two-way Anova with Tukey post-hoc test **(F, G)**. *p < 0.05, **p < 0.01.

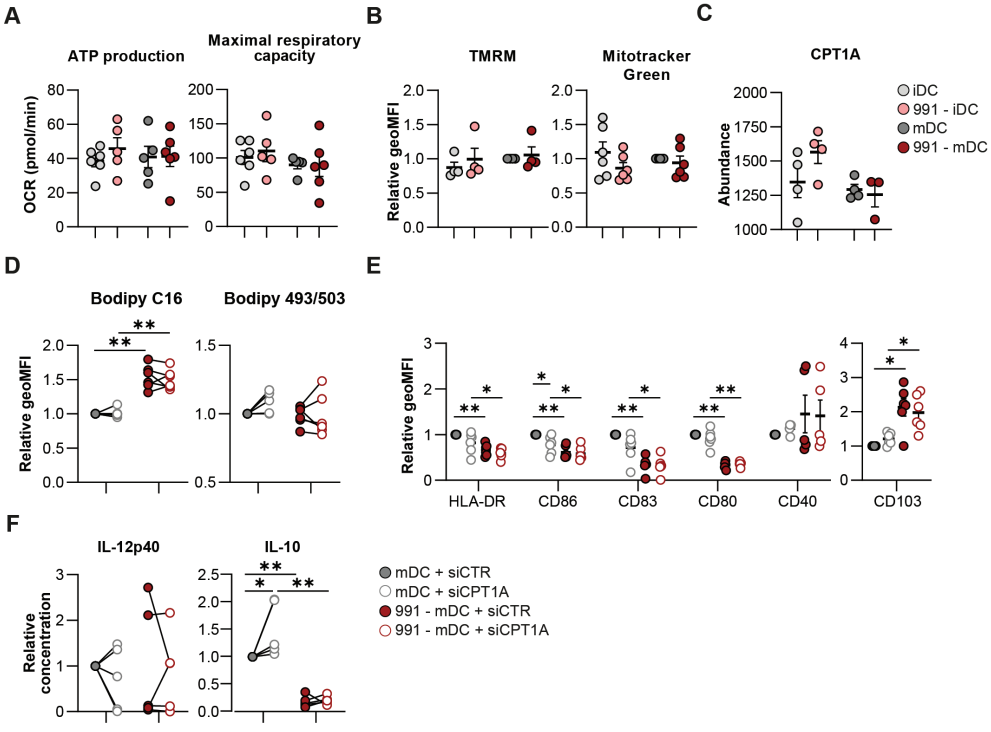

Supplementary figure 3: effects of AMPK activation on mitochondrial metabolism. A: Quantification of ATP production and maximal respiratory capacity of oxygen consumption rate (OCR) derived from Figure 3A. **B:** Normalized quantification of mitochondrial membrane potential (TMRM) and mitochondrial mass (mitotracker green). **C:** Expression of CPT1A derived from the proteomics data. **D:** Normalized quantification of Bodipy C16 and Bodipy 493/503 staining. **E:** Normalized expression of indicated markers. **F:** Normalized concentration of IL-12p40 and IL-10 after a 24hour co-culture with with CD40L-expressing J558 cells. Results are expressed as means ± SEM. Datapoints represent independent experiments with different donors. Statistical analyses were performed using two-way Anova with Tukey post-hoc test **(A-F)**. *p < 0.05, **p < 0.01.

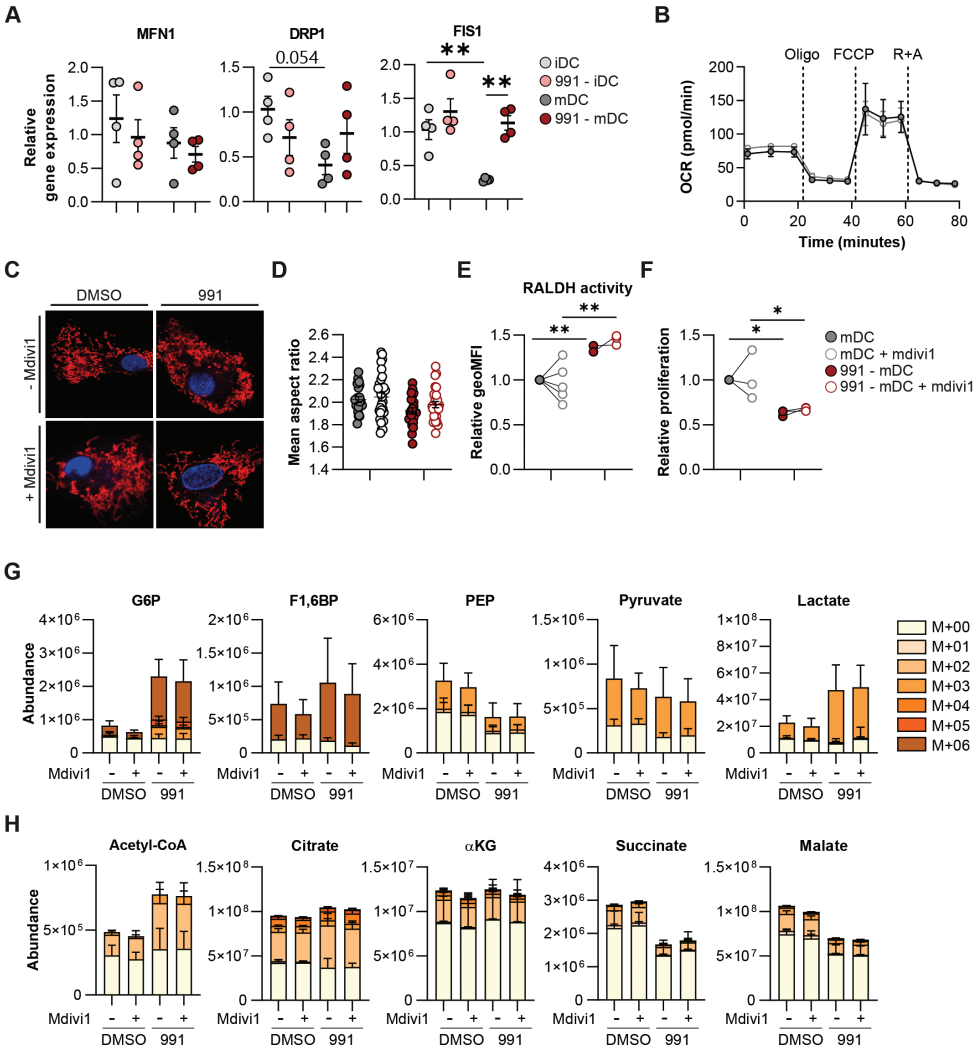

Supplementary figure 4: effects of AMPK activation on mitochondrial fission. A: Relative gene expression of genes regulating mitochondrial dynamics. **B:** Real-time oxygen consumption rate (OCR) as measured by Seahorse extracellular flux analysis. **C:** Confocal images of DMSO/991-treated mDCs with or without mdivi1 treatment. Blue: nucleus. Red: mitochondria. **D:** Quantification of the average aspect ratio of mitochondria per cell. **E: N**ormalized quantification of RALDH activity and **(F)** normalized percentage of proliferation of bystander T cells after a T cell suppression assay. **G, H:** [U-^{13}C]-glucose tracing was performed in DMSO/991-treated mDCs, with or without mdivi1. Figures show total abundance of (labeled) metabolites involved in **(G)** glycolysis and **(H)** TCA cycle. Glucose 6-phosphate (G6P), fructose 1,6-biphosphate (F1,6BP), glycerol 3-phosphate (G3P), phosphoenolpyruvate (PEP), alpha-ketoglutarate (αKG). Results are expressed as means ± SEM **(A, D,E)** or means ± SD **(F,G)**. Datapoints represent independent experiments with different donors. Statistical analyses were performed using two-way Anova with Tukey post-hoc test **(A, D-F)**. *p < 0.05, **p < 0.01.

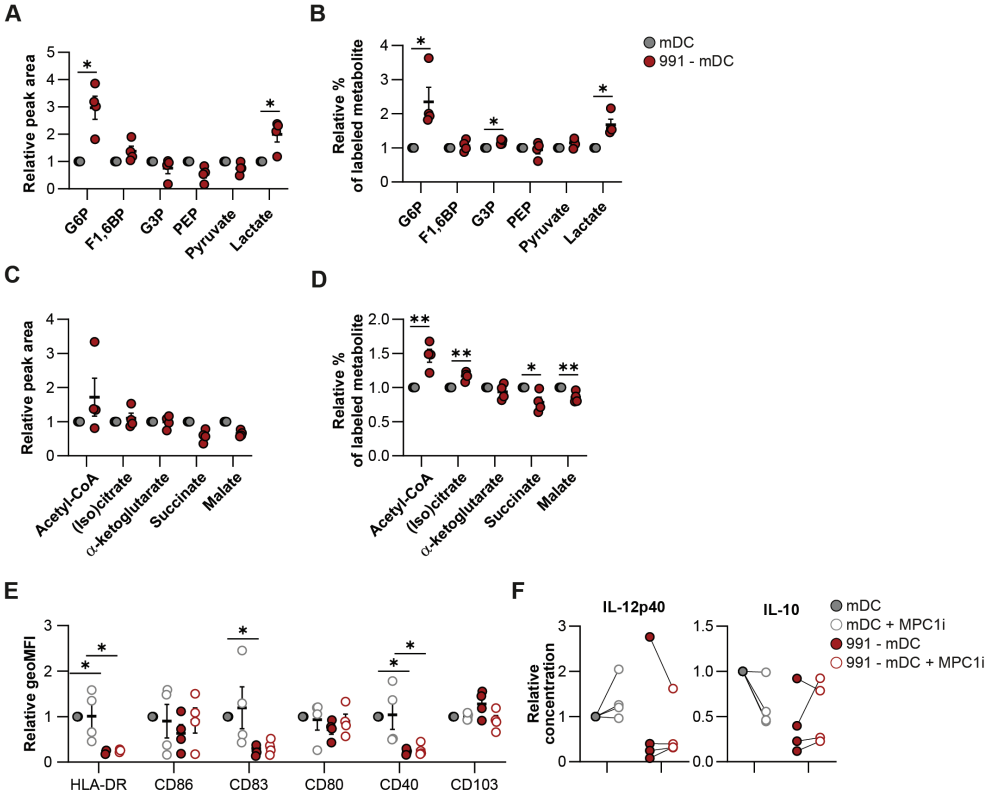

Supplementary figure 5: effects of AMPK activation on glucose metabolism. A-D: Normalized abundance and normalized quantification of relative C13-glucose-labeled fraction of metabolites involved in **(A, B)** glycolysis and **(C, D)** TCA cycle, derived from figure 5A and B. **E:** Normalized expression of indicated markers. **F:** Normalized concentration of IL-12p40 and IL-10 after a 24hour co-culture with with CD40L-expressing J558 cells. Glucose 6-phosphate (G6P), fructose 1,6-biphosphate (F1,6BP), glycerol 3-phosphate (G3P), phosphoenolpyruvate (PEP). Results are expressed as means ± SEM. Datapoints represent independent experiments with different donors. Statistical analyses were performed using paired t-tests **(A-D)** or two-way Anova with Tukey post-hoc test **(E, F)**. *p < 0.05, **p < 0.01.


AMPK

6

AMPK activation in tumor-associated dendritic cells promotes tumor growth

E. C. Brombacher[1], T. A. Patente[1], F. Otto[1], M. Quik[1], G. A. Heieis[1], L. P. Almeida[1], J. M. Lambooij[1], R. Arens[2], B. Everts[1]

[1]Department of Parasitology, Leiden University Medical Center, Leiden, The Netherlands
[2]Department of Immunology, Leiden University Medical Center, Leiden, The Netherlands

Manuscript in preparation

Abstract

Dendritic cells (DCs) in tumors are often less immunogenic and are commonly exposed to a nutrient poor tumor microenvironment (TME). Several studies indicate that tolerogenicity of DCs is dependent on engagement of catabolic metabolism. An important upstream metabolic sensor that promotes catabolic metabolism under nutrient-deprived conditions is AMP-activated kinase (AMPK). Yet whether or how AMPK activation controls tolerogenicity of tumor-associated (TA)-DCs in the TME is still not known. Here we found that TA-DCs displayed enhanced AMPK activity in a murine melanoma model. Mice with a selective deficiency of AMPKα1 in DCs were better capable of controlling melanoma tumor growth than their wild-type littermates. AMPKα1-deficiency in TA-cDC1s induced accumulation of GLUT1^{+} cDC1s and promoted CD86 expression, suggesting that loss of AMPKα1, may render DCs more immunogenic. Correspondingly, tumor-infiltrating CD8^{+} T cells expressed higher levels of TNF in CD11c$^{\Delta AMPK\alpha1}$ mice when compared to CD11c^{WT} mice. Metabolically, loss of AMPKα1 particularly boosted expression of acetyl-CoA carboxylase-1 (ACC1), a key enzyme in fatty acid synthesis, in TA-DCs. Functionally, inhibition of ACC activity did not affect CD8^{+} T cell priming by TA-DCs, but instead it potentiated their ability to induce regulatory T cells *ex vivo*, suggesting that this pathway may control tolerogenicity in TA-DCs. While the exact immunological effector mechanisms that drive tumor progression downstream of AMPK signaling in DCs remain to be explored, our findings reveal a key role for AMPK-signaling in shaping DC immunogenicity with possible implication for the treatment of malignancies.

Introduction

Tumor cells require significant amounts of energy and nutrients for growth and proliferation. Oncogenic signals induce metabolic rewiring to meet the bioenergetic and biosynthetic needs of malignant cells, which leads to metabolic stress for other cells residing in the same tumor microenvironment (TME), including immune cells. Cancer cells induce an immunosuppressive environment by shaping a metabolically heterogenous TME with hypoxic regions, low nutrient availability, and accumulation of metabolic waste products (1,2). A major sensor of such metabolic stress is AMP-activated protein kinase (AMPK), which maintains energy homeostasis in nutrient-stressful conditions (3). Interestingly, AMPK activation is also known to have anti-inflammatory effects (4) and could therefore provide a link between a nutrient restricted micro-environment and suppression of tumor-infiltrating immune cells.

Dendritic cells (DCs), in particular type 1 conventional DCs (cDC1s) (5), are critical for the anti-tumor immune response and hence there is significant interest in targeting DCs for antitumor immunotherapies (6). This includes targeted delivery of antigens and adjuvants to DCs as well as *ex vivo* loading of tumor-derived DCs or monocyte-derived DCs with tumor antigens (6,7). However, DCs residing in the TME are often compromised in function due to immunosuppressive tumor-derived factors and this has yet to be overcome (8). Thus far little is known about the role of AMPK in driving immune suppression in tumor-associated DCs (TA-DCs). AMPK activation was previously shown to suppress LPS-induced DC activation (9,10) and we recently observed that AMPK signaling can induce tolerogenic DCs that promote priming of regulatory T cells (Chapter 5). Interestingly, increased expression of canonical AMPK activator liver kinase B1 (LKB1) in TA-DCs (11), may point towards increased signaling of the LKB1-AMPK axis in these cells. If AMPK activation is indeed enhanced in TA-DCs and whether this compromises DC immunogenicity remains to be explored.

In other TA-immune cells this has been studied in more detail. For instance, myeloid-derived suppressor cells (MDSCs) (12) and regulatory T cells (Tregs) (13) in various murine tumors show increased AMPK activation and total protein abundance, respectively, when compared to their splenic counterparts. AMPKα1-deficiency in MDSCs improves anti-tumor cytotoxicity and reduces tumor development (12), as does Treg-specific AMPKα1-deficiency (13). On the contrary, a decrease in total AMPK accumulation is also observed for Tregs in B16F10 melanoma compared to peripheral Tregs in tumor-free mice (14) and AMPK loss in the total T cell pool supports tumor growth, due to enhanced T cell death and a reduction in $CD8^+$ T cell activation (15). This highlights an important role for AMPK signaling in shaping the biology of various immune cells in the TME.

Here, we investigated whether this also applies to TA-DCs by assessing if the TME alters AMPK activity and thereby their functional properties. We show that TA-DCs from murine melanomas display increased AMPK activity compared to splenic DCs. Mice deficient for AMPK in CD11c-expressing cells showed reduced tumor growth, suggesting heightened AMPK activation in TA-DCs contributes to impaired anti-tumor immune responses.

Results

AMPK activation in TA-DCs promotes tumor growth

To investigate whether AMPK activity is induced in immune cells residing in an immunosuppressive, nutrient-limited TME, we inoculated mice subcutaneously with highly

glycolytic B16F10 OVA-expressing melanoma cells (16) and analyzed the phosphorylation of AMPK-specific phosphorylation site S79 on ACC (pACC) using flow cytometry (17). Interestingly, tumor-infiltrating immune cells (gating strategy provided in Supp. Fig. 1A-D), including TA-cDC1s, showed increased levels of pACC compared to their spleen-derived counterparts (Fig. 1A). Similarly, immune cells in the tumor draining lymph node (TDLN) exhibited higher pACC signal compared to their counterparts in the contralateral non-draining lymph node (NDLN) (Fig. 1B), altogether indicating increased AMPK activation in tumor-associated immune cells. To study whether this increased AMPK signaling specifically in DCs affects the anti-tumor immune response, we compared tumor growth in mice with a Cre-induced deletion of AMPKα1 in CD11c-expressing cells ($CD11c^{\Delta AMPK\alpha1}$) to Cre-negative AMPK sufficient littermates ($CD11c^{WT}$). We confirmed the specificity of the model by showing there was a DC-specific decrease in AMPK signaling in splenocytes from $CD11c^{\Delta AMPK\alpha1}$ mice (Fig. 1C). Of note, the decrease in pACC signal in $CD11c^{\Delta AMPK\alpha1}$ DCs differed between tissues and was less pronounced in TA-cDC2s and NDLN-cDC2s (Supp. Fig. 2A). Although there was a trend towards reduced kinetics in tumor growth in $CD11c^{\Delta AMPK\alpha1}$ mice this did not reach statistical significance (Fig. 1D), However, there was significant lower tumor weight in $CD11c^{\Delta AMPK\alpha1}$ mice at the time of sacrifice, 3 weeks after inoculation (Fig. 1E, F). Together this suggests that heightened AMPK signaling in TA-DCs compromises control of tumor growth.

CD86 expression by cDC1s is suppressed by AMPK activation

To explore potential mechanisms underlying the reduced tumor growth in $CD11c^{\Delta AMPK\alpha1}$ mice, we next determined how AMPK activation affects DC abundance and phenotype within the tumor and TDLNs. Tumor-infiltrating leukocyte numbers (Fig. 2A) and the frequency of total cDCs or DC subsets within the tumor (Fig. 2B,C) or TDLN (Supp. Fig. 2B,C) were not affected by loss of AMPKα1 in DCs. Abundance of other myeloid populations within the tumor were also not different between $CD11c^{WT}$ and $CD11c^{\Delta AMPK\alpha1}$ mice (Supp. Fig. 2D). AMPKα1-deficiency induced an increase in CD86 expression in TA- and TDLN cDC1s (Fig. 2D, Supp. Fig. 2E), while activation status of cDC2s remained unchanged (Fig. 2E and Supp. Fig. 2F). Regulatory markers PD-L1, indoleamine-pyrrool 2,3-dioxygenase (IDO) (8), and TIM3 (18) (Fig. 2D, E), and immunosuppressive retinaldehyde dehydrogenase (RALDH) activity (19) (Fig. 2F,G) did not change upon AMPKα1-deficiency in neither cDC1s nor cDC2s and expression levels of cytokines were also not affected after *ex vivo* stimulation with LPS and CpG in the presence of Brefeldin A in neither tumor (Fig. 2H,I) nor TDLN DCs (Supp. Fig. 2G,H). Of note, a subset of macrophages also expresses CD11c (Supp. Fig. 3A), and consistent with no differences in pACC levels in total splenic macrophages (Fig. 1C), AMPK signaling did not differ in tumor-associated macrophages of $CD11c^{\Delta AMPK\alpha1}$ mice compared to $CD11c^{WT}$ mice (Supp. Fig. 3B). Furthermore, there was no change in abundance, activation and polarization markers, or cytokine expression in both $MHCII^{high}$ or $MHCII^{low}$ macrophages as result of loss of AMPKα1 in CD11c-expressing cells (Supp. Fig. 3C-G). Thus, at population level AMPK signaling only appears to selectively limit CD86 expression by cDC1s in both tumor and TDLNs.

AMPK activation suppresses ACC1 expression and limits accumulation of $GLUT1^{+}$ TA-cDC1s

Given the known role for AMPK in driving metabolic changes (3) and the importance for metabolism in shaping DC immunogenicity (9) and tolerogenicity (20,21), we hypothesized that AMPKα1-deficiency might affect intracellular metabolism, thereby affecting immunogenicity

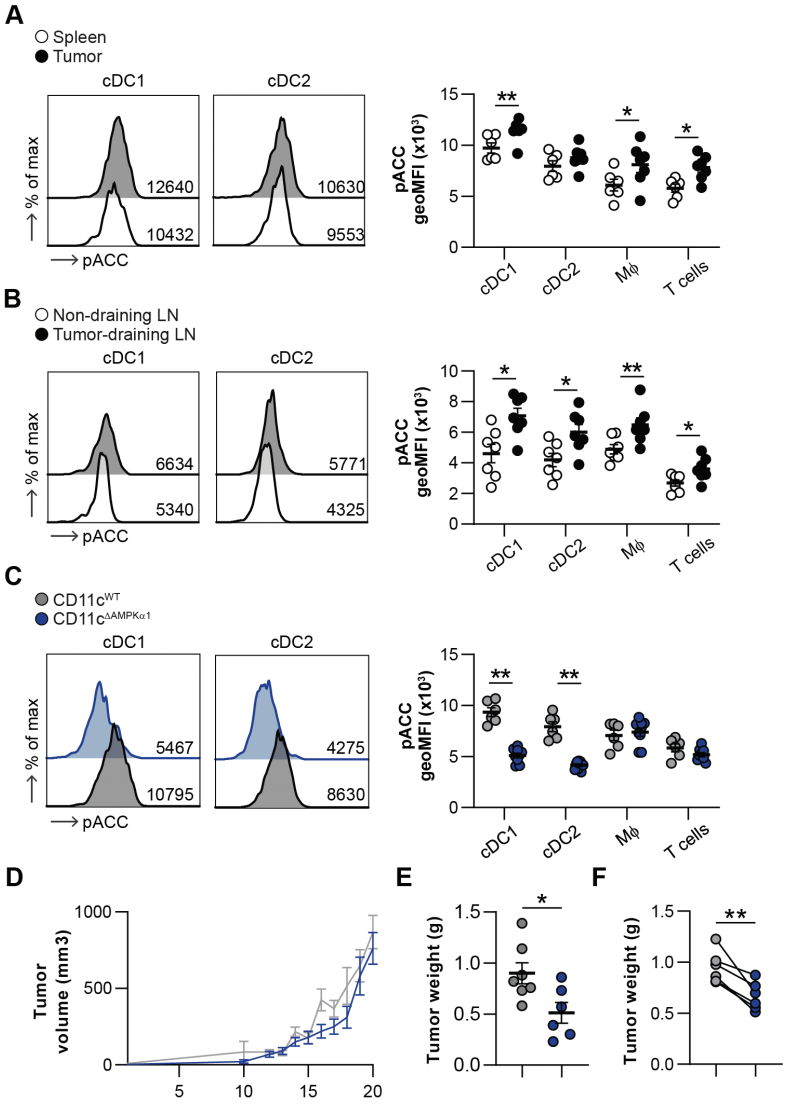

Figure 1: AMPK signaling in TA-DCs promotes tumor growth. A,B: Representative histogram and normalized quantification of phosphorylation levels of ACC (Ser79) (pACC) in cDC1s, cDC2s, macrophages (mφ), and T cells derived from (A) spleen and tumor, (B) non-draining inguinal lymph node and tumor-draining inguinal lymph node. **C:** Representative histogram and normalized quantification of pACC levels in splenic immune cells derived from CD11c^{WT} and CD11c$^{\Delta AMPK\alpha1}$ mice. **D:** B16F10-OVA melanoma growth kinetics in CD11c^{WT} and CD11c$^{\Delta AMPK\alpha1}$ mice. n = 43-46. **E,F:** Mice were sacrificed after approximately 20 days and tumors were weighed. Tumor weight of **(E)** one representative experiment and **(F)** the average tumor weight of individual experiments. Results are expressed as means ± SEM. Statistical analyses were performed using unpaired or paired t-tests, *p < 0.05, **p < 0.01.

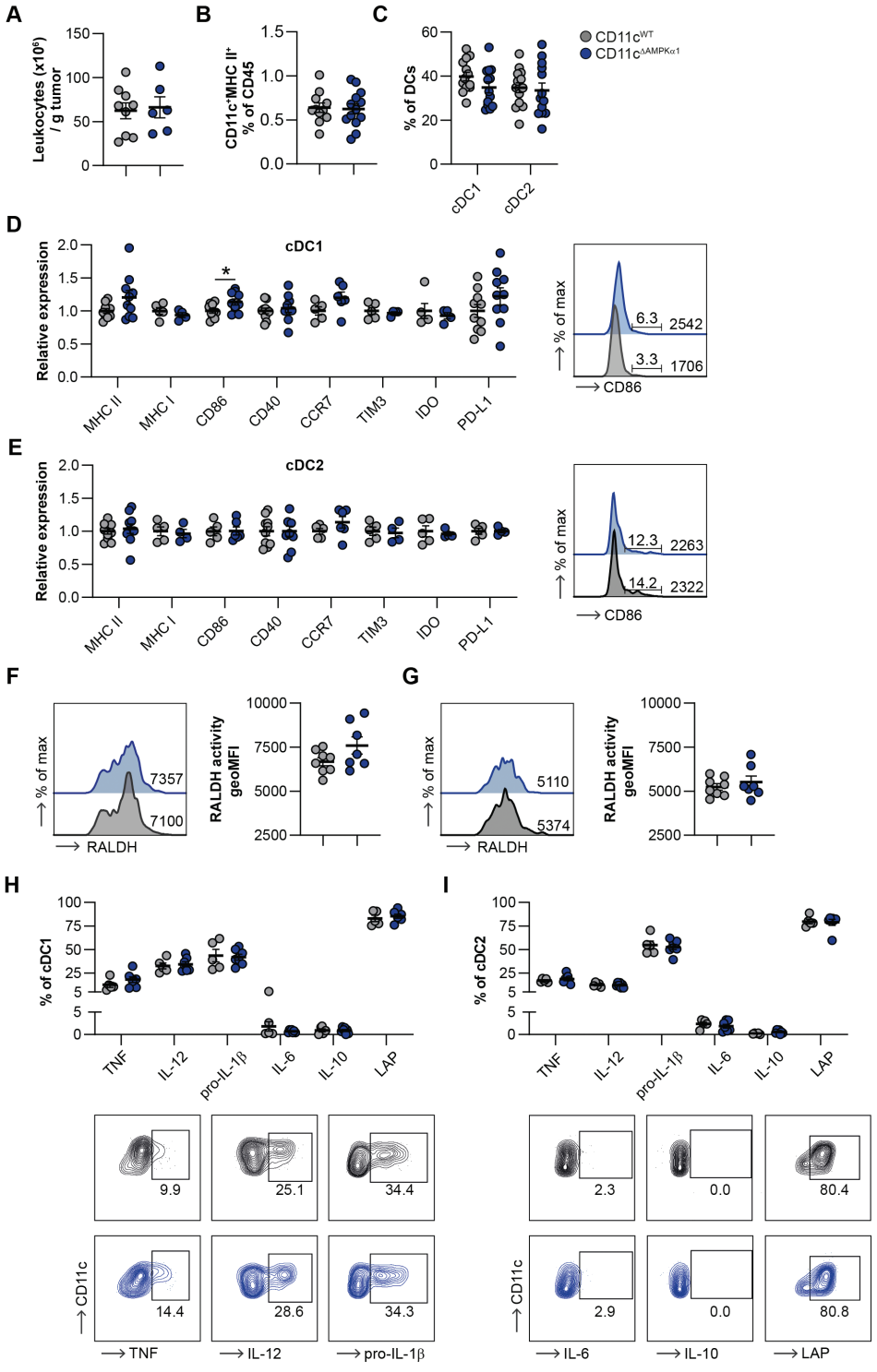
A
Leukocytes (x10⁶) / g tumor
B
CD11c+MHC II+ % of CD45
C
% of DCs
cDC1
cDC2
CD11c^WT
CD11c^ΔAMPKα1
D
cDC1
Relative expression
MHC II
MHC I
CD86
CD40
CCR7
TIM3
IDO
PD-L1
% of max
6.3
2542
3.3
1706
CD86
E
cDC2
12.3
2263
14.2
2322
F
RALDH
7357
7100
RALDH activity geoMFI
G
5110
5374
H
% of cDC1
TNF
IL-12
pro-IL-1β
IL-6
IL-10
LAP
9.9
25.1
34.4
14.4
28.6
34.3
CD11c
I
% of cDC2
2.3
0.0
80.4
2.9
0.0
80.8

Figure 2: Effects of AMPK signaling on TA-DC activation. A: Absolute number of total leukocytes in tumor samples. **B,C:** Frequencies of **(B)** total $CD11c^{+}MHCII^{+}$ DCs and **(C)** of cDC1s and cDC2s. **D,E:** Relative expression of activation markers on tumor-derived **(D)** cDC1s and **(E)** cDC2s and representative histogram of CD86 levels. **F,G:** Representative histogram and quantification of RALDH activity in **(F)** TA-cDC1s and **(G)** TA-cDC2s. **H,I:** Tumor digests were stimulated with LPS and CpG in the presence of Brefeldin A for intracellular cytokine detection. Representative plots and percentages of cytokine expression within **(H)** cDC1s and **(I)** cDC2s. Results are expressed as means ± SEM. Statistical analyses were performed using unpaired t-tests, *$p < 0.05$.

and anti-tumor immunity. Hence, we addressed metabolic rewiring in $CD11c^{\Delta AMPK\alpha1}$ mice and $CD11c^{WT}$ mice using various metabolic dyes (22). No changes in glucose uptake (2-NBDG), long chain fatty acid uptake (Bodipy C16), lipid droplets (LipidTOX), or mitochondrial mass (Mitotracker Deep Red (MDR)) were observed in AMPKα1-deficient TA-DCs and TDLN DCs, but AMPKα1-deficient TDLN cDC1s showed a decrease in mitochondrial membrane potential (TMRM) (Supp. Fig. 4A-D).

To further explore the metabolic consequence of AMPKα1-deficiency in TA-DCs, we analyzed the expression of key metabolic enzymes (Supp. Fig. 4E), as a proxy for activity of core metabolic pathways (23,24). Interestingly, both TA-cDC1s and cDC2s from $CD11c^{\Delta AMPK\alpha1}$ mice showed an increase in acetyl-CoA carboxylase-1 (ACC1) expression, a rate-limiting enzyme in fatty acid synthesis, and a small decrease for glucose-6-phosphate dehydrogenase (G6PD), a key enzyme in the pentose phosphate pathway. AMPKα1-deficient TA-cDC2s additionally had reduced expression of glucose transporter 1 (GLUT1) and enhanced expression of succinate dehydrogenase A (SDHA), a TCA cycle/electron transport chain enzyme (Fig. 3A,B).

As the tumors of $CD11c^{\Delta AMPK\alpha1}$ mice are smaller compared to those of $CD11c^{WT}$ mice, the metabolic changes between $CD11c^{WT}$ and $CD11c^{\Delta AMPK\alpha1}$ TA-DCs can be a consequence of changes in the metabolic tumor micro-environment, instead of, or in addition to, being a result of cell-intrinsic altered AMPK signaling. Hence, we addressed whether $CD11c^{neg}$ cells (Supp. Fig. 4H) (T cells, B cells, monocytes, and neutrophils), that should not be affected by intrinsic AMPKα1-deficiency, also showed differences in expression of metabolic markers when comparing $CD11c^{\Delta AMPK\alpha1}$ mice to $CD11c^{WT}$ mice. Interestingly, most changes observed in TA-DCs, also occurred in tumor-infiltrating T cells, B cells, and monocytes. Neutrophils also showed metabolic differences between $CD11c^{WT}$ and $CD11c^{\Delta AMPK\alpha1}$ mice, but distinct from the other immune cell subsets (Fig. 3C). The metabolic differences observed in tumor-infiltrating $CD11c^{neg}$ leukocytes were absent or reduced in leukocytes derived from lymph nodes or spleen, while most metabolic changes observed in TA-DCs were still present, or even stronger in TDLN and/or NDLN (Fig. 3D-F). Furthermore, a consistent increase in ACC1 for AMPKα1-deficient DCs was observed within all tissues, suggesting that AMPK signaling suppresses expression of metabolic markers, and in particular ACC1, independent of the TME. Downregulation of G6PD and GLUT1 in AMPKα1-deficient TA-DCs, on the other hand, is likely to be a consequence of changes in tumor specific signals between $CD11c^{WT}$ and $CD11c^{\Delta AMPK\alpha1}$ mice, as this was not observed in other tissues, but was visible in TA-$CD11c^{neg}$ immune cells. This indicates that the effect of loss of AMPKα1 on TA-DC metabolism is not only cell intrinsic, but may also be secondary to difference in tumor size as evidenced by overlapping metabolic changes with other TA-immune cells.

To better map potential heterogeneity in metabolic and immunological profiles within TA-DC subsets as a consequence of loss of AMPKα1, we performed an unsupervised clustering

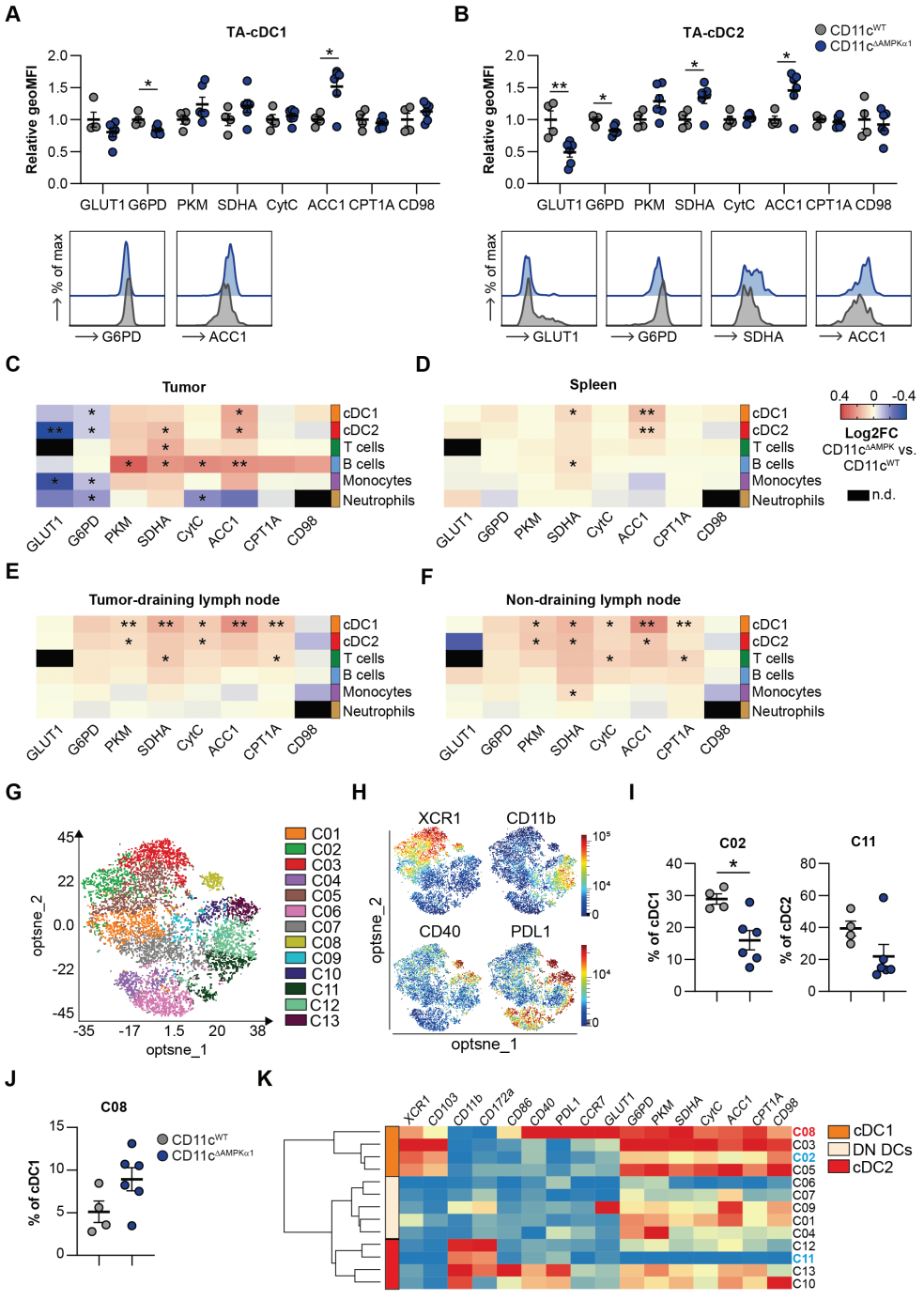
A
TA-cDC1
Relative geoMFI
GLUT1 G6PD PKM SDHA CytC ACC1 CPT1A CD98
% of max
G6PD
ACC1
B
TA-cDC2
CD11c^WT
CD11c^ΔAMPKα1
GLUT1
SDHA
C
Tumor
D
Spleen
Log2FC
CD11c^ΔAMPK vs. CD11c^WT
n.d.
cDC1
cDC2
T cells
B cells
Monocytes
Neutrophils
E
Tumor-draining lymph node
F
Non-draining lymph node
G
optsne_1
optsne_2
C01 C02 C03 C04 C05 C06 C07 C08 C09 C10 C11 C12 C13
H
XCR1
CD11b
CD40
PDL1
I
C02
C11
% of cDC1
% of cDC2
J
C08
K
XCR1 CD103 CD11b CD172a CD86 CD40 PDL1 CCR7 GLUT1 G6PD PKM SDHA CytC ACC1 CPT1A CD98
DN DCs

Figure 3: AMPK signaling induces metabolic changes in TA-DCs. A,B: Relative expression of metabolic markers and representative histograms of tumor-derived **(A)** cDC1s and **(B)** cDC2s. **C-F:** Heatmaps showing relative expression levels of metabolic markers in immune cells isolated from **(C)** tumor, **(D)** spleen, **(E)** TDLN, and **(F)** NDLN, depicted as log2 fold chain (L2FC) from CD11c$^{\Delta AMPK\alpha1}$ when compared to CD11c^{WT} mice. **G:** Clusters derived from FlowSOM clustering performed on tumor-derived CD11c^{+}MHCII^{+} DCs using activation, lineage and metabolic markers. **H:** Expression intensity of XCR1, CD11b, CD40 and PD-L1 on FlowSOM clusters. **I,J:** Most **(I)** downregulated and **(J)** upregulated clusters from CD11c$^{\Delta AMPK\alpha1}$ mice compared to CD11c^{WT} mice depicted as frequencies of parent DC subset. **K:** Heatmap showing mean expression levels in FlowSOM clusters. Double negative DCs (DN DCs). Results are expressed as means ± SEM. Statistical analyses were performed using unpaired t-tests, *p < 0.05, **p < 0.01. n.d. = not detectable.

analysis on CD11c^{+}MHCII^{+} TA-DCs based on lineage, activation, and metabolic markers. This revealed 13 clusters that separated cDC1s, cDC2s, and a DC subset negative for both cDC1 and cDC2 markers (double negative DCs) (Fig. 3G,H). Differential cluster abundance analysis between CD11c^{WT} and CD11c$^{\Delta AMPK\alpha1}$ TA-DCs highlighted changes in frequencies of clusters C08, C02, and C11 (Supp Fig. 4F and Fig. 3I,J). Interestingly, C02 and C11 are subsets of cDC1s and cDC2s respectively, whose abundance decreased in CD11c$^{\Delta AMPK\alpha1}$ mice (Fig. 3I), and are characterized by low expression of metabolic enzymes (Fig. 3K), suggesting that AMPK activation suppresses metabolic activity in particular TA-DC subsets. Furthermore, the abundance of C08 was higher in CD11c$^{\Delta AMPK\alpha1}$ mice and represents a subset of cDC1s with high expression of activation and metabolic markers, in particular GLUT1 (Fig. 3J,K and Supp. Fig. 4G).

Taken together, these data suggest that AMPK signaling in TA-DCs suppresses expression of key metabolic enzymes, in particular ACC1, drives accumulation of cDC1s and cDC2s with low metabolic activity, and prevents accumulation of a GLUT1^{+} cDC1 subset with a high activation status.

ACC activity in CD11c^{+} cells suppresses Treg induction *ex vivo*

The observed increase in ACC1 expression in DCs from CD11c$^{\Delta AMPK\alpha1}$ mice could reflect enhanced fatty acid synthesis (FAS), a metabolic feature linked to increased DC immunogenicity (25). Hence, we hypothesized that AMPK signaling in TA-DCs may limit CD4^{+} and CD8^{+} T cell priming by restricting ACC expression/activity. To test this, we co-cultured tumor-derived OVA-stimulated CD11c^{+} cells from CD11c^{WT} and CD11c$^{\Delta AMPK\alpha1}$ (Supp. Fig. 5A) with naïve CD4^{+} OT-II cells, or naïve CD8^{+} OT-I cells (Fig. 5A). To evaluate the effects of ACC expression in TA-DCs on T cell priming and polarization, we cultured CD11c^{+} cells prior to T cell co-culture in presence or absence of ACC inhibitor CP 640,186 (ACCi), which inhibits both ACC1 and ACC2, thereby inhibiting FAS and promoting FAO, respectively. AMPKα1-deficiency in TA-CD11c^{+} cells did not affect CD4^{+} T cell activation or Treg induction *ex vivo*, as no differences in CD44^{+}, FoxP3^{+}, CTLA-4^{+}, PD-1^{+}, or CD25^{+} populations could be found after 3 days of culturing (Fig. 4B). TNF, IFN-γ, IL-10, and LAP (as a proxy for TGF-β) expression following polyclonal restimulation after 8 days of co-culture were also unaffected by loss of AMPKα1 in TA-CD11c^{+} cells (Supp. Fig. 5B,C). Interestingly, irrespective of the genetic background ACC inhibition in TA-CD11c^{+} cells resulted in decreased CD44, CTLA-4, and PD-1 expression (Fig. 4B,C), and promoted TNF expression by co-cultured CD4^{+} T cells (Supp. Fig. 5A). LAP and Foxp3 expression additionally increased upon ACC inhibition selectively in WT-CD11c^{+}

cells. AMPKα1-deficiency in TA-CD11c$^+$ cells did also not affect CD8$^+$ T cell priming *ex vivo*, indicated by similar proliferation rates, CD44 and PD-1 expression, and no differences in TNF, IFN-γ, and IL-10 expression (Fig. 4D and Supp. Fig. 5D). ACC inhibition in TA-CD11c$^+$ DCs from both CD11c^{WT} and CD11c$^{\Delta AMPK\alpha1}$ mice lowered PD1 expression, while CD44 expression, proliferation rates, and cytokine expression were unaffected (Fig. 4D and Supp. Fig. 5D). Together, these results indicate that ACC expression favors immunogenic CD4$^+$ T cell priming by TA-CD11c$^+$ cells *ex vivo*, irrespective of AMPK signaling.

As AMPK is activated upon nutrient-stress, we hypothesized that the absence of differences in T cell priming capacity between TA-DCs from CD11c^{WT} and CD11c$^{\Delta AMPK\alpha1}$ mice *ex vivo* might be a consequence of exposure to nutrient-rich culture media, a context in which AMPK signaling would be minimal. Therefore, we sorted splenic cDC2s from CD11c^{WT} and CD11c$^{\Delta AMPK\alpha1}$ mice and cultured cells in B16-conditioned medium (B16 CM) or control IMDM, in presence of OVA, after pre-incubation with DMSO or ACCi. After overnight incubation we washed the cells and started a co-culture with naïve CD4$^+$ T cells (Fig. 4F). Of note, a similar protocol was applied for cDC1s, but they did not survive. However, also this experimental setup did not reveal differences in CD4$^+$ T cell priming between TA-cDC2s isolated from CD11c^{WT} and CD11c$^{\Delta AMPK\alpha1}$ mice (Fig. 4G,H and Supp. Fig. 5E). Similar to our previous results, ACC inhibition promoted FoxP3 and dampened CD44, CTLA-4, and PD-1 expression (Fig. 4G,H and Supp. Fig. 5E). Additionally, a decrease in CD25 expression upon ACC inhibition was found (Supp. Fig. 5E). Summarized, *ex vivo* co-culture experiments could not discern a difference in T cell priming potential between AMPKα1-deficient and sufficient TA-DCs, although they do indicate that increased ACC1 expression in AMPKα1-deficient TA-DCs may reduce their ability to prime FoxP3$^+$ Tregs.

AMPK activation in TA-DCs has a limited effect on intra-tumoral T cells

We next aimed to assess to what extent these *ex vivo* T cell priming data by AMPKα1-deficient TA-DCs would be mirrored *in vivo* and whether there are differences in the intra-tumoral T cell compartment that can explain the decrease in tumor growth observed in CD11c$^{\Delta AMPK\alpha1}$ mice when compared to CD11c^{WT} mice. Total T cell abundance and CD4$^+$ or CD8$^+$ frequencies were similar in tumors from CD11c^{WT} and CD11c$^{\Delta AMPK\alpha1}$ mice (Fig. 5A,B). Further assessment of the CD4$^+$ T cell compartment did not reveal differences in the abundance of CD44$^+$CD62L$^-$ effector T cells or FoxP3$^+$ Tregs (Fig. 5C,D). Within the Treg compartment, CTLA-4, PD-1 or KLRG1 expression did not differ between CD11c^{WT} and CD11c$^{\Delta AMPK\alpha1}$ mice (Fig. 5E) and polyclonal restimulation did not show differences in TNF or IFN-γ expression by CD4$^+$ T cells, although an increase in IL-10 expression was observed as a consequence of loss of AMPKα1 in CD11c-expressing cells (Fig. 5F). Likewise, abundance of activated CD44$^+$ CD8$^+$ T cells, PD-1$^+$ or KLRG1$^+$ CD8$^+$ T cells was similar between tumors from CD11c^{WT} and CD11c$^{\Delta AMPK\alpha1}$ mice and also no differences in frequency of OVA-specific CD8$^+$ T cells could be detected (Fig. 5G-I). OVA-specific restimulation and polyclonal restimulation using PMA/ionomycin were used to asses cytokine expression in CD8$^+$ T cells and although IFN-γ and IL-10 levels were similar between both genotypes, expression of TNF was increased upon polyclonal restimulation (Fig. 5J,K). We also investigated expression of LAMP-1 on the membrane, as marker for recent degranulation, as well as the expression of cytotoxic mediators granzyme B (GZB) and perforin, and observed that these were similar between TA-CD8$^+$ T cells from CD11c^{WT} and CD11c$^{\Delta AMPK\alpha1}$ mice (Fig. 5L). Finally, abundance of other major immune cell subsets found in the TME, including B cells and NK cells (Supp. Fig. 6A), as well as activation

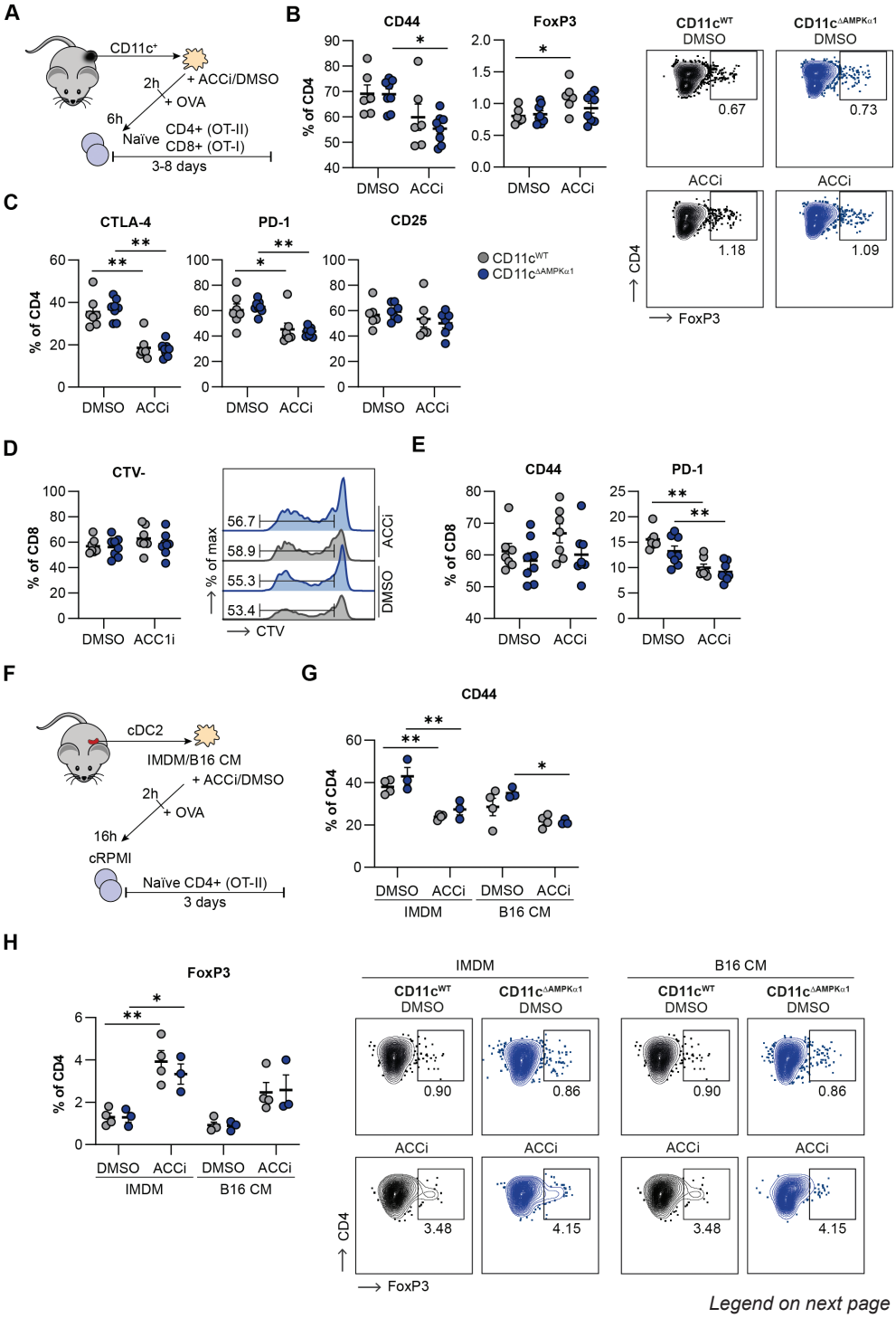

Legend on next page

Figure 4: ACC expression, but not AMPK activation in DCs affects *ex vivo* T cell priming. A: CD11c$^+$ cells were isolated from tumors and cultured in the presence of ACCi or DMSO for 2 hours, before OVA was added. After an additional 4 hours cells were washed and co-cultured with naïve CD4$^+$ OT-II or naïve CD8$^+$ OT-I cells. After 3 days cells were fixed for T cell characterization and proliferation rates, after 8 days cells were used for cytokine analyses. **B,C:** Characterization of CD4$^+$ T cells. (**B**) Frequency of CD44- and FoxP3-expressing cells within total CD4$^+$ T cells and representative plots for FoxP3. (**C**) Frequency of CTLA-4, PD-1, and CD25 expressing cells within total CD4$^+$ T cells. **D,E:** Characterization of CD8$^+$ T cells. (**D**) Proliferation rates and representative histograms and (**E**) percentage of CD44+ and PD-1+ cells within total CD8$^+$ T cells. **F:** cDC2s were sorted from spleens and cultured in IMDM or B16 conditioned medium in the presence of ACCi or DMSO for 2 hours, before OVA was added. After overnight culture cells were washed and co-cultured with naïve CD4$^+$ OT-II T cells. After 3 days cells were fixed for T cell characterization. **G,H:** (**G**) CD44 and (**H**) FoxP3 expression by CD4$^+$ T cells and representative plots for FoxP3 staining. Results are expressed as means ± SEM. Statistical analyses were performed using two-way Anova with Tukey post-hoc test. *$p < 0.05$, **$p < 0.01$.

phenotype of the latter (Supp. Fig. 6B-D), were similar between tumors in both mouse strains. These data suggest that AMPKα1-deficiency in TA-DCs has little impact on CD4$^+$, CD8$^+$, and NK-cell responses in the TME, although we did find AMPK signaling in DCs to suppress TNF secretion by TA-CD8$^+$ T cells.

Discussion

AMPK is a major regulator of cellular metabolism that is activated upon metabolic stress (26) and has anti-inflammatory effects (9,27). This let us to hypothesize that AMPK may serve as a link between nutrient stress and immunosuppression in the TME. Here, we show that AMPK activity is increased in TA-DCs compared to splenic DCs, and similarly TDLN-DCs exhibit higher AMPK signaling compared to NDLN-DCs. Loss of AMPKα1 in DCs leads to a reduction in tumor growth, thereby suggesting that AMPK may limit the capacity of DCs to induce a sufficient anti-tumor immune response. Although it was previously shown that AMPK was required for priming of Tregs by DCs (27), no differences could be found in the Treg-inducing capacity of TA-DCs from CD11c^{WT} and CD11c$^{\Delta AMPK\alpha1}$ mice. However, AMPKα1-deficient cDC1s had increased CD86 expression and tumor-infiltrating CD8$^+$ T cells expressed higher levels of TNF, which might contribute to lower tumor growth in CD11c$^{\Delta AMPK}$ mice. Furthermore, we show that AMPK signaling in DCs induces several metabolic changes, including suppression of ACC1 expression, which can affect the T cell priming capacity of DCs.

Although a consistent smaller tumor size was observed 3 weeks after tumor challenge in CD11c$^{\Delta AMPK\alpha1}$ compared to CD11c^{WT} mice, tumor growth kinetics during those 3 weeks did not significantly differ. Possibly, differences in tumor size between CD11c$^{\Delta AMPK\alpha1}$ and CD11c^{WT} mice may only become apparent during the later stages of tumor growth, because it is only in these settings that intra-tumoral metabolic stress level are sufficiently high to trigger AMPK activation in DCs, to subsequently dampen their immunostimulatory potential.

The TME contains various metabolic cues that could potentially activate AMPK (1,2), including low glucose levels (28), hypoxia (17), lactate (29), and metabolically activated long-chain fatty-acids (30). Canonical AMPK activation is induced by a high AMP/ATP ratio and requires LKB1 (26), which was observed to be increased in TA-DCs (11). This could suggest LKB1-induced canonical AMPK activation in TA-DCs. A recent study showed that in

multiple murine cancer models, myeloid cells, particularly macrophages, are well capable of consuming intra-tumoral glucose and can even outcompete tumor cells for glucose uptake (31), indicating that glucose exposure in the TME is not low enough to serve as trigger for AMPK activation in TA-myeloid cells. However, whether this also holds true for DCs remains to be determined. Moreover, most of their work was performed in MC38 cells, which are less glycolytic than B16F10 melanoma tumor cells used in our studies, making it possible that in our model glucose levels may be actually sufficiently low to contribute to induction of AMPK signaling in DCs (16). To address this, direct genetic modification of key enzymes in glycolysis, analogous to what has been done in a model for sarcoma (32), would be a promising approach to selectively assess the consequences of increased or decreased glucose levels in the TME on AMPK activation in tumor-infiltrating leukocytes.

The observation that AMPK signaling is augmented in both TA-DCs and DCs from the TDLN, could indicate that the enhanced AMPK activation is maintained when DCs migrate from tumor to TDLN. Another possibility is that both the TME and the TDLN contain AMPK-inducing factors. For instance, TDLNs can receive lymphatic drainage from tumors and it has been shown that lactic acid from B16F10 melanomas can transfer to TDLN through tumor-associated lymphatic vessels, thereby lowering the pH in TDLN (33). It is possible that other soluble factors from the TME also drain to the TDLN, thereby affecting AMPK signaling and immune cell activation. Further studies are required to discover the tumor-derived factors that promote AMPK activation in tumor as well as TDLN.

Although we cannot exclude a role for other CD11c-expressing cells in contributing to reduced tumor growth in CD11c$^{\Delta AMPK\alpha1}$ mice, the observations that we did not find any changes in frequency or phenotype of other immune cells that expressed some levels of CD11c, would argue for a key role for DCs in driving the phenotype. Indeed, we found effects of AMPK signaling on activation markers of TA-DCs and TDLN-DCs, in particular suppression of CD86 expression on cDC1s, as well as trends for reduced MHC II, CCR7, and PD-L1 levels on cDC1s CD11c^{WT} compared to CD11c$^{\Delta AMPK\alpha1}$ mice. We also assessed expression of markers associated with tolerogenic DCs, including TIM3 (18), IDO (34), and RALDH activity (19), but did not observe AMPK-dependent regulation. Recently, several studies have highlighted existence of regulatory DC populations that are unique in driving tumor progression (35,36). Whether function or abundance of these mregDCs (mature DCs enriched in immunoregulatory molecules) are affected by AMPK signaling remains to be explored.

Metabolically, there were more profound changes as a result of AMPKα1 loss in TA-DCs. Pyruvate kinase M (PKM), a rate-limiting enzyme of glycolysis, SDHA, and ACC1 were all upregulated in AMPKα1-deficient cDC1s and cDC2s in at least two tissues, indicating that AMPK signaling may limit glycolysis and fatty acid synthesis. Furthermore, cytochrome C (CytC), a protein that transfers electrons between complex III and complex IV of the electron transport chain, and carnitine palmitoyltransferase IA (CPT1A), a mitochondrial fatty acid transporter, were significantly upregulated in cDC1s in both TDLN and NDLN and CytC was also significantly increased in TDLN of CD11c$^{\Delta AMPK\alpha1}$ mice. While AMPK is known to promote catabolic metabolism, these data may suggest that in our model AMPK activation limits overall metabolic activity (26). Moreover, within the tumor, loss of AMPKα1 increased the abundance of a GLUT1-expressing cDC1 subpopulation additionally characterized by high expression of activation markers. As glucose metabolism is highly important for DC activation (9,25), it is tempting to speculate this subset of GLUT1^{+} cDC1s play a critical role in enhancing anti-tumor immunity in CD11c$^{\Delta AMPK\alpha1}$ mice. Furthermore, ACC1 expression increased upon AMPK

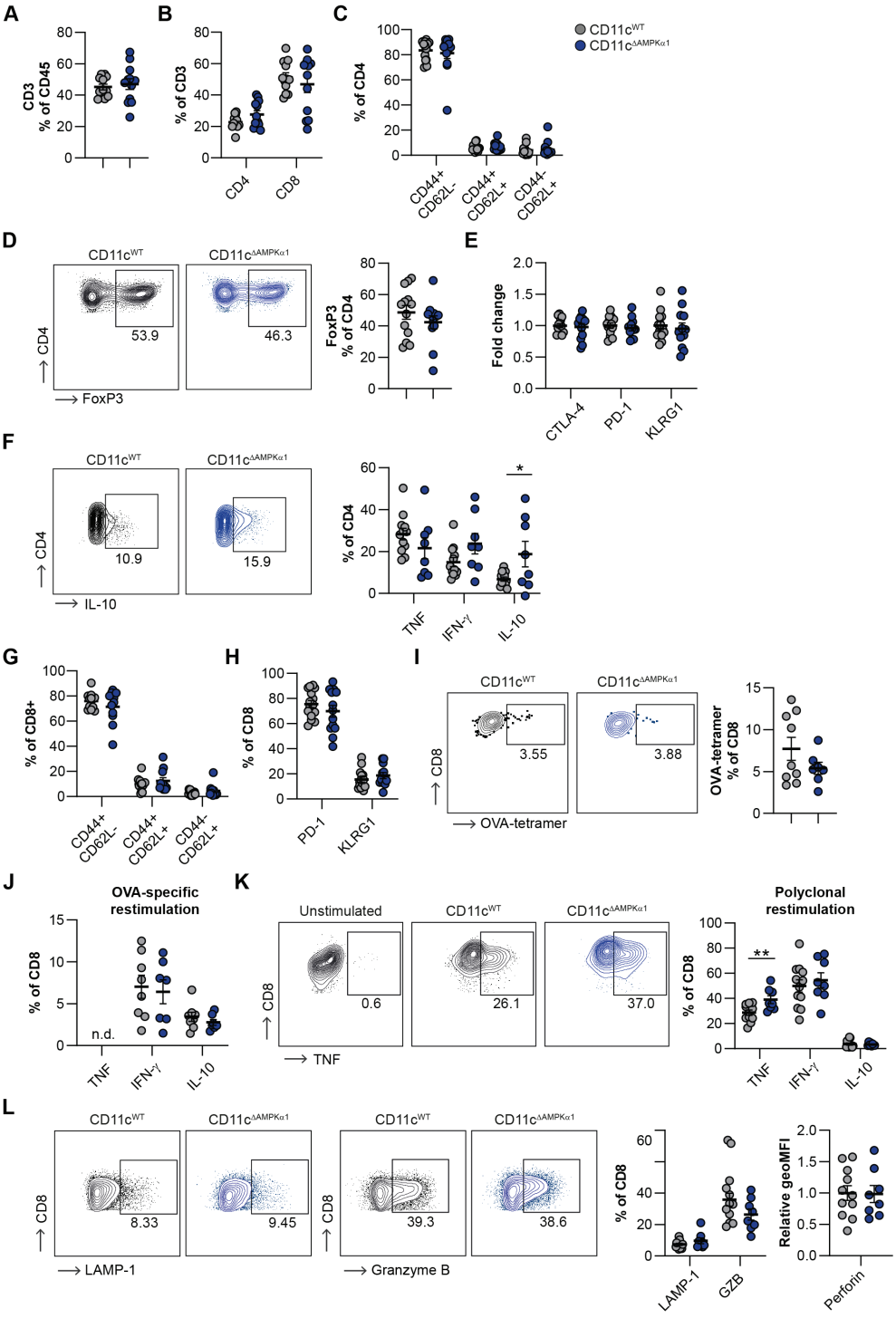
A
B
C
CD3 % of CD45
% of CD3
% of CD4
CD4
CD8
CD44+ CD62L-
CD44+ CD62L+
CD44- CD62L+
CD11c^WT
CD11c^ΔAMPKα1
D
E
F
CD4
FoxP3
53.9
46.3
FoxP3 % of CD4
Fold change
CTLA-4
PD-1
KLRG1
IL-10
10.9
15.9
TNF
IFN-γ
G
H
I
% of CD8+
% of CD8
CD8
OVA-tetramer
3.55
3.88
OVA-tetramer % of CD8
J
K
L
OVA-specific restimulation
Unstimulated
Polyclonal restimulation
n.d.
0.6
26.1
37.0
LAMP-1
Granzyme B
8.33
9.45
39.3
38.6
GZB
Perforin
Relative geoMFI

Figure 5: AMPK signaling DCs limits tumor-infiltrating CD8⁺ T cell activation. A,B: Frequencies of **(A)** total T cells and **(B)** CD4⁺ and CD8⁺ T cells. **C-E:** CD4⁺ T cell characterization. **(C)** Effector vs. naïve T cells frequencies, **(D)** FoxP3⁺ CD4 T cell frequencies and representative plot, and **(E)** expression of levels of CTLA-4, PD-1, and KLRG1 by FoxP3⁺ CD4⁺ T cells. **F:** Cytokine levels after restimulation with PMA and ionomycin in the presence of Brefeldin A and representative plot of IL-10. **G-I:** CD8⁺ T cell characterization. **(G)** Activated and naïve CD8⁺ T cell frequencies, **(H)** expression of PD-1 and KLRG1 on CD8⁺ T cells, and **(I)** representative plots and frequencies of OVA-specific CD8⁺ T cells. **J,K:** Intracellular cytokine staining after **(J)** OVA-specific restimulation and **(K)** PMA and ionomycin restimulation in the presence of Brefeldin A. A representative plot for TNF is shown. **L:** Expression levels and representative plots for cytotoxicity markers. LAMP-1 was added during restimulation with PMA/ionomycin in presence of Brefeldin A and granzyme B and perforin were stained intracellularly. Results are expressed as means ± SEM. Statistical analyses were performed using unpaired t-test. *p < 0.05, **p < 0.01. n.d. = not detectable.

loss in both TA-cDC1s and TA-cDC2s as well as in those DCs from other assessed tissues. It was previously reported that AMPK can transcriptionally repress ACC levels through sterol response element-binding protein 1c (SREBP1c) and hence AMPK activation in TA-DCs may not only inhibit ACC1 activity through phosphorylation (26), but may also limit ACC1 transcription through SREBP1c phosphorylation (37). ACC1 expression is a key enzyme in FAS and it could suggest that AMPK activation suppresses FAS, a metabolic feature known to be important for immunogenic DC activation (25).

Since we previously showed that Treg accumulation during schistosomiasis is reduced in $CD11c^{\Delta AMPK\alpha1}$ compared to $CD11c^{WT}$ mice (27), we hypothesized that the reduced tumor growth could be a consequence of impaired Treg accumulation in the tumors from the KO mice. Furthermore, ACC1 levels increased in AMPKα1-deficient TA-DCs and *ex vivo* data suggest that ACC1 expression in DCs reduces their ability to prime FoxP3⁺ Tregs. However, we did not observe differences in tumor-infiltrating Tregs, nor changes in expression of regulatory markers, between $CD11c^{WT}$ and $CD11c^{\Delta AMPK\alpha1}$ mice. The lack of intra-tumoral Treg differences between $CD11c^{\Delta AMPK}$ and $CD11c^{WT}$ was mirrored by *ex vivo* T cell priming studies with naïve CD4⁺ T cells with tumor-derived CD11c-expressing cells even when *ex vivo* co-cultures with cDC2s activated with OVA in B16 conditioned medium were performed to better mimic the TME *ex vivo*. Hence, TA-DCs do not appear to depend on AMPK activation for Treg priming

On the other hand, we did observe an increase in TNF secretion by CD8⁺ T cells. TNF can have both pro- (38) and anti-tumorigenic (39) functions in B16 melanoma and therefore it remains to be determined whether the increased TNF expression by CD8⁺ T cells contributes to the reduction in tumor growth in $CD11c^{\Delta AMPK\alpha1}$ mice. This enhanced CD8 T cell activation would be largely consistent with our findings that TA-cDC1s from $CD11c^{\Delta AMPK\alpha1}$ displayed a higher activation status . However, *Ex vivo* priming of naïve CD8⁺ T cells did not differ between $CD11c^{\Delta AMPK}$ and $CD11c^{WT}$ cells. This could be related to nutrient-rich culture conditions, or indicate that AMPK signaling in TA-DCs affects their ability to reactivate tumor infiltrating CD8⁺ T cells, rather than CD8⁺ T cell priming itself. In addition to cross-presentation and CD8⁺ T cell activation, TA-cDC1s can also activate and stimulate NK cells (40), but our data did not indicate changes in NK cell function. It is noteworthy that the current study does not include functional T cell assays. *Ex vivo* cytotoxicity assays with tumor-derived CD8⁺ T cells and NK cells, or suppression assays with CD4⁺ T cells may provide new insights into the anti-tumor immune response induced by AMPKα1-deficient TA-DCs.

In summary, in addition to studies in T cells (13) and MDSCs (12), we now show that AMPK signaling in TA-DCs compromises tumor control. Targeting AMPK in TA-DCs could therefore have therapeutic potential. In this context it is important to note that the effect of AMPK blockade in immune cells is not always beneficial for anti-tumor immunity (14) and neither is AMPK inhibition in cancer cells. AMPK can function as a tumor-suppressor by limiting cell growth and proliferation, but also as oncogene by providing protection against metabolic stress caused by poor vascularization (41). Hence, devising strategies for targeted manipulation of AMPK signaling selectively in DCs would be crucial to increase chances of therapeutic success. In addition, it will be interesting to study whether AMPKα1-deficiency in TA-DCs could promote the efficacy of other immunotherapies. For instance, various types of DC vaccines improve PD-L1, CTLA-4 (42) and/or PD-1 blockade (43) in B16F10 melanoma.

Our data indicate that AMPK signaling in TA-DCs and TDLN-DCs promotes tumor growth and inhibits anti-tumor immunity. Although further studies are needed to delineate the exact mechanism that drives tumor progression, AMPK-induced metabolic changes are likely to contribute to altered T cell priming and activation by TA-DCs. Based on our results we propose a role for limited $CD8^+$ T cell activity due to AMPK signaling in DCs, with potentially additional contributions from other T cell populations, that gain immunosuppressive features by AMPK-activated DCs. The recent developments in the field of immunometabolism and the growing interest in targeting metabolism in the TME as therapeutic strategy, make AMPK signaling in TA-DCs a highly relevant topic that warrants further investigations.

Material and methods

Mice

Itgax^{cre} (CD11c) (44), *Prkaa1*$^{fl/fl}$ (AMPKα1) (45) mice, OVA-specific $CD4^+$ T cell receptor transgenic mice (OT-II), and OVA-specific $CD8^+$ T cell receptor transgenic mice (OT-I), all on C57Bl/6J background, were crossed, housed and bred at the LUMC, in a temperature-controlled room with a 12-hour light-dark cycle and *ad libitum* access to food and tap water under specific pathogen free conditions. Experiments were performed in accordance with the Guide for the Care and Use of Laboratory Animals of the Institute for Laboratory Animal Research and have received approval from the Dutch Central Authority for Scientific Procedures on Animals (CCD; animal license numbers AVD116002015253 and AVD1160020186804).

B16F10 culture

B16F10-OVA-expressing melanoma cells were cultured in IMDM (BE12-722F, Lonza), supplemented with 10% heat-inactivated FCS (S-FBS-EU-015, Serana), 100 U/mL penicillin (16128286, Eureco-pharma), 100 µg/mL streptomycin (S9137, Sigma-Aldrich), 1 mg/mL Active Geneticin/G148 (2448984, Gibco), 2 mM L-glutamine (G8540, Sigma-Aldrich), and 1 mM pyruvate (P5280, Sigma-Aldrich). Cells were split two to three times per week.

Tumor challenge

Mice were inoculated subcutaneously with 3×10^5 B16F10-OVA-expressing melanoma cells in 100 µl HBSS without phenol red (14175095, ThermoFisher). Tumor growth was measured three times a week using a caliper and tumor volume was calculated using the ellipsoid volume

formula (1/2 x length x width x height). Mice were euthanized through cervical dislocation after 18-20 days, or when tumor size reached >1500 mm^3 in volume.

Isolation of leukocytes from spleen, inguinal lymph nodes, and tumor

Spleens were collected in 500 µL RPMI 1640 + Glutamax (61870036, Life Technolgies), mechanically disrupted, and digested for 20 min at 37°C in medium supplemented with 1 mg/mL Collagenase D (11088866001, Roche) and 30 U/mL DNase I (D4263, Sigma-Aldrich). Digested samples were filtered through 100 µm filters and subjected to erythrocyte lysis buffer (0.15 M NH_4Cl, 1 mM $KHCO_3$, 0.1 mM Na_2EDTA (15575-038, ThermoFisher) before counting in complete RPMI (cRPMI, RPMI 1640 + Glutamax, supplemented with 10% heat-inactivated FCS, 25 nM β-mercaptoethanol (M6250, Sigma-Aldrich), 100 U/mL penicillin, and 100 µg/mL streptomycin).

Tumors were collected, mechanically disrupted and digested in cRPMI supplemented with 1 mg/mL collagenase type IV from Clostridium histolyticum (C5138, Sigma-Aldrich) and 50 U/mL DNase at 200 rpm for 45 minutes at 37°C. Digested samples were filtered through 100 µm filters and subjected to erythrocyte lysis buffer before counting in cRPMI.

For assessment of *in situ* pACC status of immune cells by flow cytometry (see below), organs were collected and fixed prior to tissue processing in 500 µL of 2% formaldehyde/PBS (220/12257974/1110, Braun), as previously described (22), followed by digestion as described above.

Intracellular cytokine detection

Intracellular cytokine production was analyzed using flow cytometry. For polyclonal restimulation of T cells, tumor-infiltrating leukocytes were restimulated for 4 hours at 37°C in cRPMI with 100ng/mL phorbol myristate acetate (PMA, P8139, Sigma-Aldrich) and 1 ug/mL ionomycin (I0634, Sigma Aldrich) in the presence of 10 µg/mL Brefeldin A (B7651, Sigma-Aldrich) and an anti-CD107a antibody. For OVA-specific restimulation of T cells, tumor-infiltrating leukocytes were co-cultured in cRPMI for 5 hours at 37°C with D1 dendritic cells (46), pre-loaded with 1 µg/mL SIINFEKL, in the presence of Brefeldin A. For *ex vivo* DC and macrophage stimulation, tumor-infiltrating leukocytes were stimulated for 4 hours at 37°C in cRPMI supplemented with 100 ng/mL LPS (0111:B4, InvivoGen) and 5 µg/mL CpG (ODN 1826, InvivoGen) in the presence of Brefeldin A.

Flow cytometry

In general, cells were stained with a viability dye (Zombie NIR™ Fixable Viability Kit, 423106 BioLegend) for 20 minutes at room temperature before fixation with 1.85% formaldehyde (F1635, Sigma) or for 1 hour at 4°C with FoxP3/Transcription factor staining buffer set (00-5523-00, Invitrogen). Metabolic dyes, RALDH activity, tetramer, and T cell proliferation were measured in live cells. Surface proteins were stained for 30 minutes at 4°C in FACS buffer (PBS supplemented with 0.5% BSA (10735086001, Roche) and 2mM EDTA (15575-038, ThermoFisher). For intracellular stainings cells were permeabilized for 20 minutes at 4°C in permeabilization buffer (#00-8333-56 – ThermoFisher), before staining for 30 minutes at 4°C in permeabilization buffer. Prior to staining with phospho-ACC, cells were also permeabilized in 96% methanol (67-56-1, Fisher chemical) for 20 minutes at -20°C. Cells were stained with metabolic dyes as previously described (22). Briefly, cells were cultured at 37°C in PBS, supplemented with 2-NBDG (N13195, ThermoFisher), BODIPY™ FL C16

(D3821, ThermoFisher), LipidTOX (H34476, ThermoFisher), TMRM (T668, ThermoFisher) or MitoTracker™ Deep Red FM (M22426, ThermoFisher) prior to measurement. Aldefluor kit (01700, Stemcell Technologies) was used for assessing RALDH activity, according to manufacturer's protocol. Briefly, cells were stained for 30 minutes at 37°C with 1 µM of Aldefluor reagent dissolved in assay buffer. Cells were kept in assay buffer until measurement. Samples were acquired on Cytek Aurora 3-laser of Cytek Aurora 5-laser spectral flow cytometer and analyzed using FlowJo (Version 10.6, TreeStar). Antibody information is provided in Table 1.

***Ex vivo* T cell co-culture assays**

$CD11c^+$ cells were isolated from digested spleens and tumors using LS columns and CD11c MicroBeads (130-125-835, Miltenyi Biotec) according to the manufacturer's protocol. CD11c+ cells were cultured at 37°C in cRPMI and treated with 60 µM ACC inhibitor CP 640,186 (17691-5, Sanbio) or DMSO (102931, Merck Millipore) for 2 hours, before stimulation with 100 µg/mL OVA (vac-pova-100, InvivoGen). After 4 hours cells were washed and co-cultured with naïve $CD4^+$ or $CD8^+$ T cells.

cDC2s were sorted from splenic $CD11c^+$ cells, isolated as described above, and FACS sorted ($MHCII^+$ $CD11c^+$ $CD64^-$ $F4/80^-$ $CD172a^+$ $XCR1^-$) on a BD FACSAria using a 100 µm nozzle at 20 PSI. cDC2s were cultured in B16-conditioned medium (supernatant derived from a one week B16F10 melanoma culture) or control IMDM medium and treated with 60 µM DMSO or ACCi for 2 hours, before stimulation with 100 µg/mL OVA. The next day cells were washed and cultured with naïve $CD4^+$ T cells. Naïve $CD4^+$ T cells and naïve $CD8^+$ T cells were negatively isolated using mojosort mouse CD4/CD8 naïve T cell isolation kits (480040, 480044, BioLegend) from OT-II and OT-I mice, respectively, according to the manufacturer's protocol. $CD8^+$ T cells were stained with Cell Trace Violet (C34557, ThermoFisher) prior to co-culture. 7000 $CD11c^+$ cells were co-cultured with 70,000 T cells and after 3 days half of the cells were harvested to measure proliferation and FoxP3 expression. Remaining cells were supplemented with IL-2 (202-IL, R&D Systems) and used for polyclonal T cell restimulation on day 8.

OMIQ analysis

$CD45^+CD3^-CD19^-SiglecH^-SiglecF^-Ly6C^-Ly6G^-F4/80^-CD64^-CD326^-CD11c^+MHCII^+$ TA-DCs were gated in FlowJo, exported, and uploaded into OMIQ. Samples were subsampled using a maximum equal distribution. After sub-sampling, opt-SNE was performed using activation (CD86, CD80, CD40, CCR7), lineage (XCR1, CD103, CD11b, CD172a), and metabolic markers (GLUT1, G6PD, PKM, SDHA, CytC, ACC1, CPT1A, CD36) using the default settings, followed by FlowSOM clustering using the default settings. EdgeR was used to determine significantly different clusters and the heatmap was generated with Euclidean clustering.

Statistical analysis

Results are expressed as mean ± standard error mean (SEM) except stated otherwise. Data was analyzed using GraphPad Prism (La Jolla, CA, USA). Comparisons between two or more independent data groups were made by Student's T test (parametric data)/ Wilcoxon test (nonparametric data) or analysis of variance test (ANOVA), respectively. $P<0.05$ was considered statistically significant.

Table 1: Antibodies for flow cytometry

Target	Fluorophore	Clone	company	identifier
ACC1	-	EPR23235-147	Abcam	ab269273
B220	BV510	RA3-6B2	BioLegend	103248
CCR7/ CD197	BV786	4B12	BD Bioscience	564355
CD103	BUV661	M290	BD Bioscience	741504
CD107a	BV421	1D4B	Biolegend	121617
CD11b	BUV563	M1/70	BD Bioscience	741242
CD11c	BUV496	HL3	BD Bioscience	750483
CD172a	BUV805	P84	BD Bioscience	741997
CD19	ef450	eBio1D3	eBioscience	48-0193-82
CD206	BV785	C068C2	BioLegend	141729
CD25	PEcy5	PC61.5	BioLegend	102010
CD27	BV605	LG.3A10	BioLegend	124249
CD3	ef450	17A2	eBioscience	48-0032-82
CD3	BV750	17A2	BioLegend	100249
CD326	BV605	G8.8	Biolegend	118227
CD4	PE	RM4-5	eBioscience	12-0042-83
CD4	BV650	GK1.5	BD Bioscience	563232
CD40	BV510	3/23	BD Bioscience	745041
CD44	BUV737	IM7	BD Bioscience	612799
CD44	PEcy7	IM7	eBioscience	25-0441-81
CD45	APC/Fire 810	30-F11	BioLegend	103173
CD45	BUV805	30-F11	BD Bioscience	748370
CD62L	APC/Fire 810	30-F11	BioLegend	103173
CD64	PEdazzle594	X54-5/7.1	BioLegend	139320
CD8	BV711	53-6.7	Biolegend	100759
CD86	AF700	GL-1	BD Bioscience	560581
CD98	BUV615	H202-141	BD Bioscience	752360
CLTA4	BV421	UC10-4B9	BioLegend	106312
F4/80	BV711	BM8	Biolegend	123147
FoxP3	APC	FJK-16s	Invitrogen/ eBioscience	12-5773-82
Goat anti-Rabbit	AF647	-	Invitrogen	A21244
Granzyme B	PE	NGZB	eBio	12-8898-80

IDO	PE	eyedio	eBioscience	12-9477-41
IL-10	AF488	JESS-16E3	Invitrogen	53-7101-82
IL-12	APC	C15.6	BD	554480
IL-6	ef450	MP5-20F3	eBioscience	48-7061-82
KLRG1	Pedazzle	MAFA	Biolegend	138423
LAP	PerCPef710	Tw7-16B4	Invitrogen/ eBioscience	46-9821-82
Ly6C	PerCP-Cy5.5	HK1.4	BioLegend	128011
Ly6G	SB550	1A8	BioLegend	127663
MHC I	PEcy7	AF6-88.5	BioLegend	116519
MHC II	BUV395	2G9	BD Bioscience	743876
NK1.1	PerCP-Cy5.5	PK136	Biolegend	108727
PD-1	BV785	29f.1a12	Biolegend	135225
PD-L1	BUV737	M1H5	BD Bioscience	568825
Perforin	FITC	eBioOMAK-D	eBio	11-9392-80
Phospho-ACC (ser79)	-	D7D11	Cell signaling	11818S
pro-IL1b	PE	NJTEN3	eBioscience	12-7114
Siglec F	BV480	E50-24440	BD Bioscience	
Siglec H	BV750	511	BioLegend	129611
TIM3	FITC	RMT3-23	eBioscience	11-5870-82
TNFa	PE/Cy7	MP6-XT22	BioLegend	506324
XCR1	BV650	ZET	BioLegend	148220
G6PD	-	EPR20668	Abcam	ab210702
CPT1A	-	EPR21843-71-2F	Abcam	ab234111
CytC	-	7H8.2C12	Abcam	ab13575
GLUT1	-	EPR3915	Abcam	ab115730
SDHA	-	EPR9043(B)	Abcam	ab137040
PKM	-	EPR10138(B)	Abcam	ab150377

Acknowledgements

D1 dendritic cells were kindly provided by Marcel Camps and Ferry Ossendorp (LUMC). A special thanks to Marion König and Roos van Schuijlenburg for their help during experiments. This work was supported by an LUMC fellowship awarded to B.E.

References

1. Chang CH, Qiu J, O'Sullivan D, Buck MD, Noguchi T, Curtis JD, et al. Metabolic Competition in the Tumor Microenvironment Is a Driver of Cancer Progression. Cell. 2015;162(6):1229–41.
2. Arner EN, Rathmell JC. Metabolic programming and immune suppression in the tumor microenvironment. Cancer Cell. 2023;41(3):421–33.
3. Hardie DG, Ross FA, Hawley SA. AMPK: A nutrient and energy sensor that maintains energy homeostasis. Nat Rev Mol Cell Biol. 2012;13(4):251–62.
4. Salminen A, Hyttinen JMT, Kaarniranta K. AMP-activated protein kinase inhibits NF-κB signaling and inflammation: Impact on healthspan and lifespan. J Mol Med. 2011;89(7):667–76.
5. Böttcher JP, Reis e Sousa C. The Role of Type 1 Conventional Dendritic Cells in Cancer Immunity. Trends Cancer. 2018;4(11):784–92.
6. Wculek SK, Cueto FJ, Mujal AM, Melero I, Krummel MF, Sancho D. Dendritic cells in cancer immunology and immunotherapy. Nat Rev Immunol. 2020;20(1):7–24.
7. Filin IY, Kitaeva K V., Rutland CS, Rizvanov AA, Solovyeva V V. Recent Advances in Experimental Dendritic Cell Vaccines for Cancer. Front Oncol. 2021;11.
8. Kvedaraite E, Ginhoux F. Human dendritic cells in cancer. Sci Immunol. 2022;7:9409.
9. Krawczyk CM, Holowka T, Sun J, Blagih J, Amiel E, DeBerardinis RJ, et al. Toll-like receptor-induced changes in glycolytic metabolism regulate dendritic cell activation. Blood. 2010;115(23):4742–9.
10. Carroll KC, Viollet B, Suttles J. AMPKα1 deficiency amplifies proinflammatory myeloid APC activity and CD40 signaling. J Leukoc Biol. 2013;94(6):1113–21.
11. Wang Y, Du X, Wei J, Long L, Tan H, Guy C, et al. LKB1 orchestrates dendritic cell metabolic quiescence and anti-tumor immunity. Cell Res. 2019;29(5):391–405.
12. Trillo-Tinoco J, Sierra RA, Mohamed E, Cao Y, de Mingo-Pulido A, Gilvary DL, et al. AMPK alpha-1 intrinsically regulates the function and differentiation of tumor myeloid-derived suppressor cells. Cancer Res. 2019;79(19):5034–47.
13. An J, Ding Y, Yu C, Li J, You S, Liu Z, et al. AMP-activated protein kinase alpha1 promotes tumor development via FOXP3 elevation in tumor-infiltrating Treg cells. iScience. 2022;25(1).
14. Pokhrel RH, Acharya S, Ahn JH, Gu Y, Pandit M, Kim JO, et al. AMPK promotes antitumor immunity by downregulating PD-1 in regulatory T cells via the HMGCR/p38 signaling pathway. Mol Cancer. 2021;20(1).
15. Rao E, Zhang Y, Zhu G, Hao J, Persson XMT, Egilmez NK, et al. Deficiency of AMPK in CD8 + T cells suppresses their anti-tumor function by inducing protein phosphatase-mediated cell death. Oncotarget. 2015;6(10):7944–58.
16. Bohn T, Rapp S, Luther N, Klein M, Bruehl TJ, Kojima N, et al. Tumor immunoevasion via acidosis-dependent induction of regulatory tumor-associated macrophages. Nat Immunol. 2018;19(12):1319–29.
17. Steinberg GR, Hardie DG. New insights into activation and function of the AMPK. Nat Rev Mol Cell Biol. 2022;24:255–72.
18. Dixon KO, Tabaka M, Schramm MA, Xiao S, Tang R, Dionne D, et al. TIM-3 restrains anti-tumour immunity by regulating inflammasome activation. Nature. 2021;595(7865):101–6.
19. Coombes JL, Siddiqui KRR, Arancibia-Cárcamo C V., Hall J, Sun CM, Belkaid Y, et al. A functionally specialized population of mucosal CD103+ DCs induces Foxp3+ regulatory T cells via a TGF-β -and retinoic acid-dependent mechanism. Journal of Experimental Medicine. 2007;204(8):1757–64.
20. Malinarich F, Duan K, Hamid RA, Bijin A, Lin WX, Poidinger M, et al. High Mitochondrial Respiration and Glycolytic Capacity Represent a Metabolic Phenotype of Human Tolerogenic Dendritic Cells. The Journal of Immunology. 2015;194(11):5174–86.

21. Ferreira GB, Vanherwegen AS, Eelen G, Gutiérrez ACF, VanLommel L, Marchal K, et al. Vitamin D3 induces tolerance in human dendritic cells by activation of intracellular metabolic pathways. Cell Rep. 2015;10(5):711–25.
22. Brombacher EC, Patente TA, Quik M, Everts B. Characterization of Dendritic Cell Metabolism by Flow Cytometry. In: Sisirak V, editor. Dendritic Cells Methods in Molecular Biology. 2023. p. 219–37.
23. Pelgrom LR, Patente TA, Otto F, Nouwen L V., Ozir-Fazalalikhan A, van der Ham AJ, et al. mTORC1 signaling in antigen-presenting cells of the skin restrains CD8+ T cell priming. Cell Rep. 2022;40(1):1–17.
24. Heieis GA, Patente TA, Tak T, Almeida L, Everts B. Spectral flow cytometry reveals metabolic heterogeneity in tissue macrophages. BioRxiv. 2022;
25. Everts B, Amiel E, Huang SCC, Smith AM, Chang CH, Lam WY, et al. TLR-driven early glycolytic reprogramming via the kinases TBK1-IKKε supports the anabolic demands of dendritic cell activation. Nat Immunol. 2014;15(4):323–32.
26. Hardie DG, Schaffer BE, Brunet A. AMPK: An Energy-Sensing Pathway with Multiple Inputs and Outputs. Vol. 26, Trends in Cell Biology. 2016. p. 190–201.
27. Patente TA, Brombacher EC, Heieis GA, Pelgrom LR, Zawistowska-Deniziak A, Otto F, et al. Metabolic sensor AMPK licenses CD103+ dendritic cells to induce Treg responses. bioRxiv. 2023;
28. Zhang CS, Hawley SA, Zong Y, Li M, Wang Z, Gray A, et al. Fructose-1,6-bisphosphate and aldolase mediate glucose sensing by AMPK. Nature. 2017;548(7665):112–6.
29. Zhou Y, Liu X, Huang C, Lin D. Lactate Activates AMPK Remodeling of the Cellular Metabolic Profile and Promotes the Proliferation and Differentiation of C2C12 Myoblasts. Int J Mol Sci. 2022;23(22):1–16.
30. Pinkosky SL, Scott JW, Desjardins EM, Smith BK, Day EA, Ford RJ, et al. Long-chain fatty acyl-CoA esters regulate metabolism via allosteric control of AMPK β1 isoforms. Nat Metab. 2020;2(9):873–81.
31. Reinfeld BI, Madden MZ, Wolf MM, Chytil A, Bader JE, Patterson AR, et al. Cell-programmed nutrient partitioning in the tumour microenvironment. Nature. 2021;593(7858):282–8.
32. Chang CH, Qiu J, O'Sullivan D, Buck MD, Noguchi T, Curtis JD, et al. Metabolic Competition in the Tumor Microenvironment Is a Driver of Cancer Progression. Cell. 2015;162(6):1229–41.
33. Riedel A, Helal M, Pedro L, Swietlik JJ, Shorthouse D, Schmitz W, et al. Tumor-Derived Lactic Acid Modulates Activation and Metabolic Status of Draining Lymph Node Stroma. Cancer Immunol Res. 2022;10(4):482–97.
34. Zhao F, Xiao C, Evans KS, Theivanthiran T, DeVito N, Holtzhausen A, et al. Paracrine Wnt5a-β-Catenin Signaling Triggers a Metabolic Program that Drives Dendritic Cell Tolerization. Immunity. 2018;48(1):147–60.
35. Maier B, Leader AM, Chen ST, Tung N, Chang C, LeBerichel J, et al. A conserved dendritic-cell regulatory program limits antitumour immunity. Nature. 2020;580(7802):257–62.
36. Zhang Q, He Y, Luo N, Patel SJ, Han Y, Gao R, et al. Landscape and Dynamics of Single Immune Cells in Hepatocellular Carcinoma. Cell. 2019;179(4):829–45.
37. Li Y, Xu S, Mihaylova MM, Zheng B, Hou X, Jiang B, et al. AMPK phosphorylates and inhibits SREBP activity to attenuate hepatic steatosis and atherosclerosis in diet-induced insulin-resistant mice. Cell Metab. 2011;13(4):376–88.
38. Rodriguez YI, Campos LE, Castro MG, Bannoud N, Blidner AG, Filippa VP, et al. Tumor Necrosis Factor Receptor-1 (p55) Deficiency Attenuates Tumor Growth and Intratumoral Angiogenesis and Stimulates CD8+ T Cell Function in Melanoma. Cells. 2020;9(11).
39. Dondossola E, Dobroff AS, Marchiò S, Cardó-Vila M, Hosoya H, Libutti SK, et al. Self-targeting of TNF-releasing cancer cells in preclinical models of primary and metastatic tumors. Proc Natl Acad Sci U S A. 2016;113(8):2223–8.

40. Bödder J, Zahan T, van Slooten R, Schreibelt G, de Vries IJM, Flórez-Grau G. Harnessing the cDC1-NK Cross-Talk in the Tumor Microenvironment to Battle Cancer. Front Immunol. 2021;11.

41. Vara-Ciruelos D, Russell FM, Grahame Hardie D. The strange case of AMPK and cancer: Dr Jekyll or Mr Hyde? Open Biol. 2019;9(7).

42. Zheng F, Dang J, Zhang H, Xu F, Ba D, Zhang B, et al. Cancer Stem Cell Vaccination With PD-L1 and CTLA-4 Blockades Enhances the Eradication of Melanoma Stem Cells in a Mouse Tumor Model. Journal of Immunotherapy. 2018;41(8):361–8.

43. Yazdani M, Gholizadeh Z, Nikpoor AR, Mohamadian Roshan N, Jaafari MR, Badiee A. Ex vivo dendritic cell-based (DC) vaccine pulsed with a low dose of liposomal antigen and CpG-ODN improved PD-1 blockade immunotherapy. Sci Rep. 2021;11(1).

44. Caton ML, Smith-Raska MR, Reizis B. Notch-RBP-J signaling controls the homeostasis of CD8- dendritic cells in the spleen. Journal of Experimental Medicine. 2007;204(7):1653–64.

45. Nakada D, Saunders TL, Morrison SJ. Lkb1 regulates cell cycle and energy metabolism in haematopoietic stem cells. Nature. 2010;468(7324):653–8.

46. Winzler C, Rovere P, Rescigno M, Granucci F, Penna G, Adorini L, et al. Maturation Stages of Mouse Dendritic Cells in Growth Factor-dependent Long-Term Cultures. Vol. 185, J. Exp. Med. 1997.

Supplementary figures

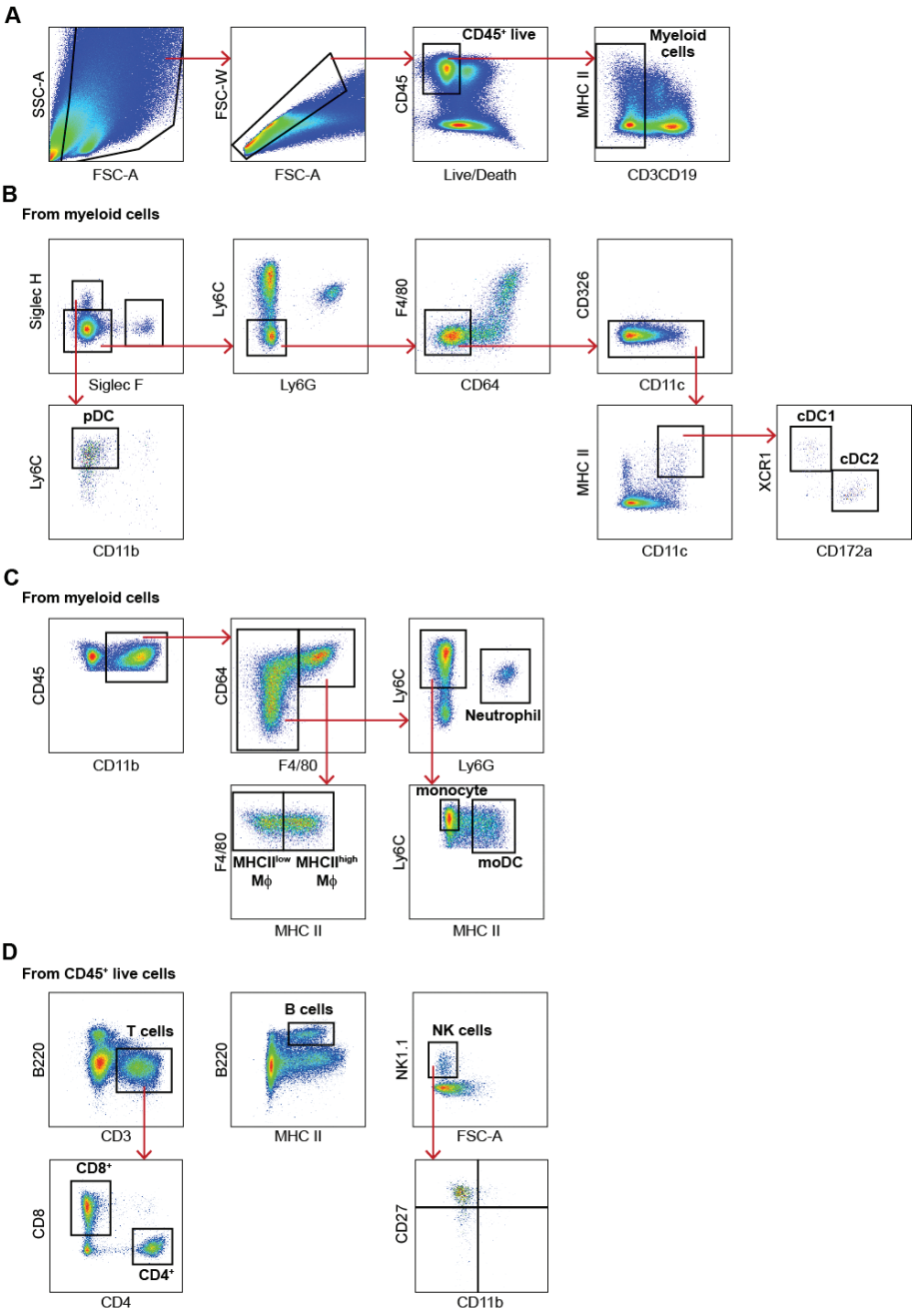

Supplementary figure 1: Gating strategy. A-D: Gating strategy of (A) total myeloid cells from digested tumor samples, **(B)** plasmacytoid DCs (pDCs), cDC1s, and cDC2s, **(C)** neutrophils, macrophages, monocytes, and monocyte-derived DCs (moDCs), and **(D)** T cells, B cells, and NK cells.

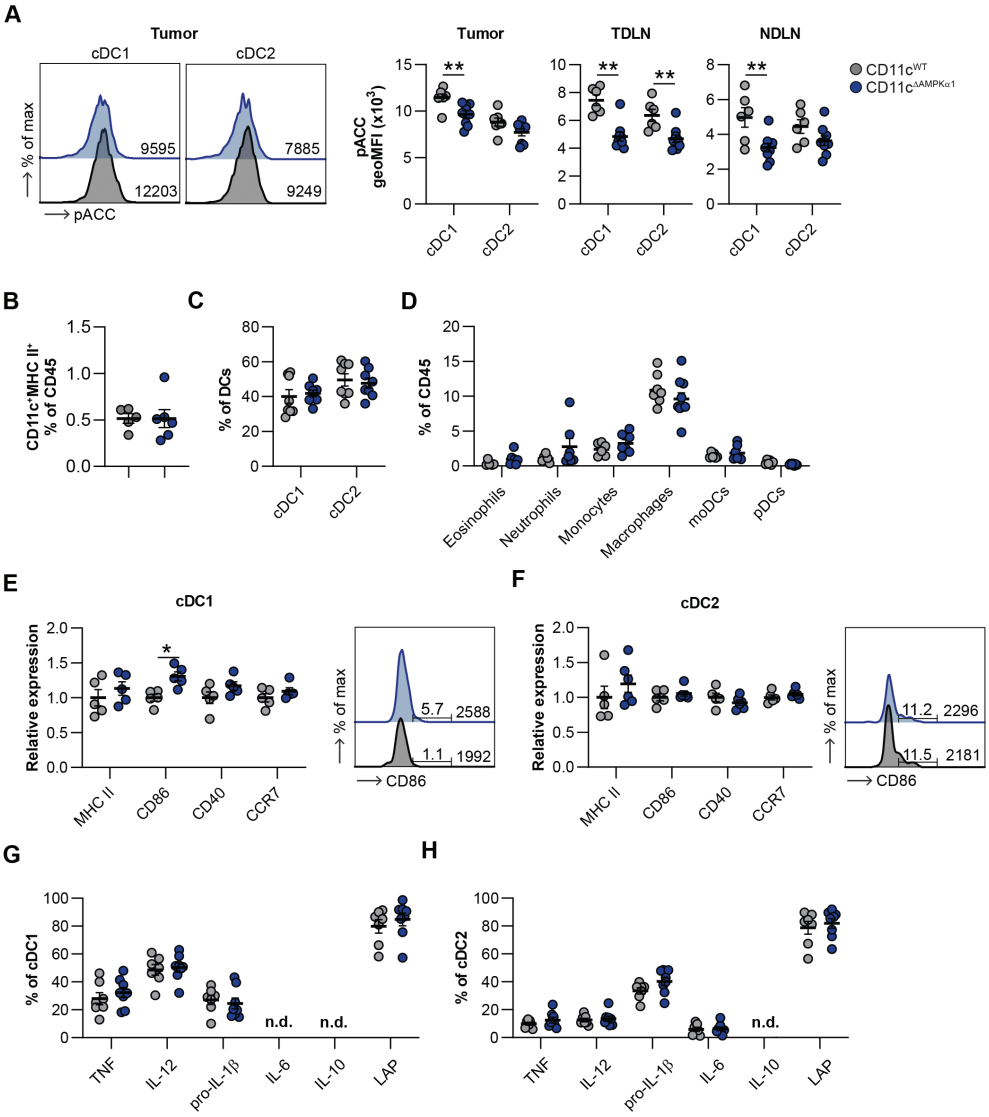

Supplementary figure 2: Effects of AMPK signaling on TDLN-DC activation. A: Representative histogram and normalized quantification pACC levels in cDC1s and cDC2s from tumor, TDLN and NDLN. **B,C:** Frequencies of **(B)** total CD11c⁺MHCII⁺ DCs and **(C)** of cDC1s and cDC2s from TDLN. **D:** Frequencies of myeloid cells in total CD45⁺ live cells derived from tumor samples. **E,F:** Relative expression of activation markers on TDLN-derived **(E)** cDC1s and **(F)** cDC2s and representative histogram of CD86 levels. **G,H:** TDLN digests were stimulated with LPS and CpG in the presence of Brefeldin A for intracellular cytokine detection. Frequencies of cytokine expression within **(G)** cDC1s and **(H)** cDC2s. Results are expressed as means ± SEM. Statistical analyses were performed using unpaired t-tests, *p < 0.05, **p < 0.01. n.d. = not detectable.

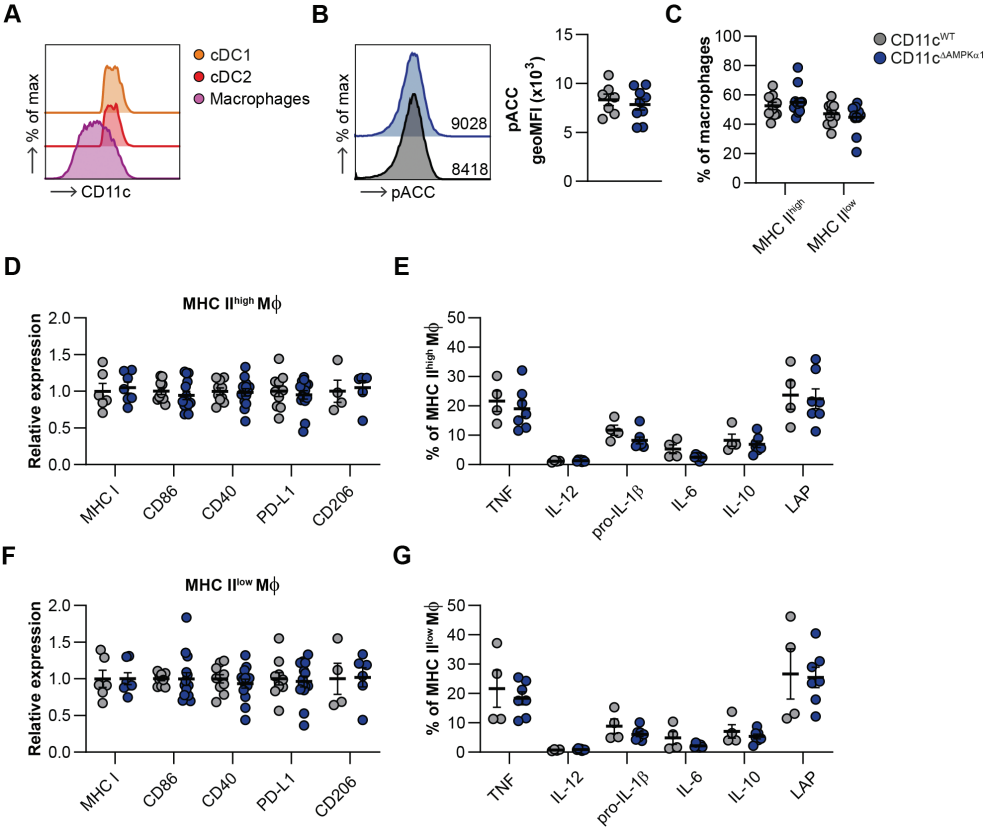

Supplementary figure 3: Macrophage characterization in tumors from CD11c^{WT} and CD11c$^{\Delta AMPK\alpha1}$ mice. A: Representative histogram of CD11c levels in tumor-derived cDC1s, cDC2s, and macrophages **B:** Representative histogram and normalized quantification pACC in macrophages. **C:** Frequencies of MHCII^{low} and MHCII^{high} macrophages. **D-G:** Relative expression of activation markers after tumor digestion, and cytokine levels after LPS + CpG stimulation in presence of Brefeldin A in **(D,E)** MHCII^{high} macrophages and **(F,G)** MHCII^{low} macrophages. Results are expressed as means ± SEM. Statistical analyses were performed using unpaired t-tests, *p < 0.05, **p < 0.01. n.d. = not detectable.

Supplementary figure 4: AMPKα1-deficiency affects metabolism of DCs. A-D: Relative expression and representative histograms of metabolic dyes in tumor-derived **(A)** cDC1s and **(B)** cDC2s, and TDLN-derived **(C)** cDC1s and **(D)** cDC2s. **E:** Illustration indicating metabolic targets and associated metabolic pathways that were assessed using flow cytometry. GLUT1 = Glucose transporter 1. G6PD = Glucose-6-phosphate dehydrogenase, PKM = Pyruvate kinase M, SDHA = Succinate Dehydrogenase A, CytC = Cytochrome C, ACC1 = Acetyl-CoA carboxylase 1, CPT1a = Carnitine Palmitoyltransferase 1A. **F:** Volcano plot of differential expression analysis between flowsom clusters from TA-DCs from CD11c^{WT} and CD11c$^{\Delta AMPK\alpha1}$ mice. **G:** Manual gating confirms high GLUT1 expression in CD86^{+}CD40^{+} cDC1s. **H:** Representative histogram of CD11c expression in tumor-derived immune cells. Results are expressed as means ± SEM. Statistical analyses were performed using unpaired t-tests (**A-D**), *p < 0.05.

Figure on next page

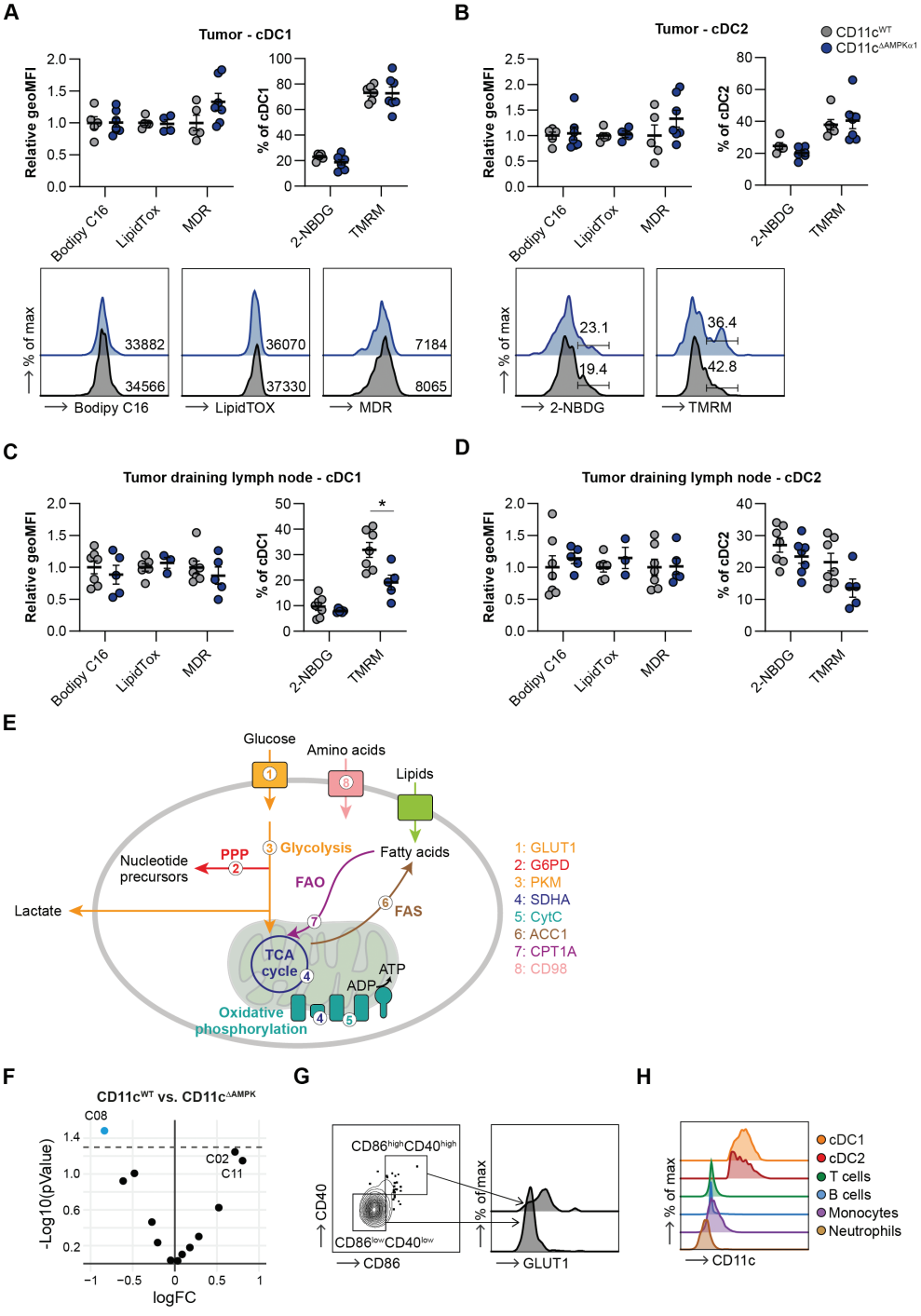
A
Tumor - cDC1
Relative geoMFI
% of cDC1
Bodipy C16
LipidTox
MDR
2-NBDG
TMRM
% of max
33882
34566
36070
37330
7184
8065
B
Tumor - cDC2
CD11c^WT
CD11c^ΔAMPKα1
% of cDC2
23.1
19.4
36.4
42.8
C
Tumor draining lymph node - cDC1
D
Tumor draining lymph node - cDC2
E
Glucose
Amino acids
Lipids
Nucleotide precursors
PPP
Glycolysis
Fatty acids
FAO
FAS
Lactate
TCA cycle
ATP
ADP
Oxidative phosphorylation
1: GLUT1
2: G6PD
3: PKM
4: SDHA
5: CytC
6: ACC1
7: CPT1A
8: CD98
F
CD11c^WT vs. CD11c^ΔAMPK
-Log10(pValue)
logFC
C08
C02
C11
G
CD86^high CD40^high
CD86^low CD40^low
CD40
CD86
GLUT1
H
cDC1
cDC2
T cells
B cells
Monocytes
Neutrophils
CD11c

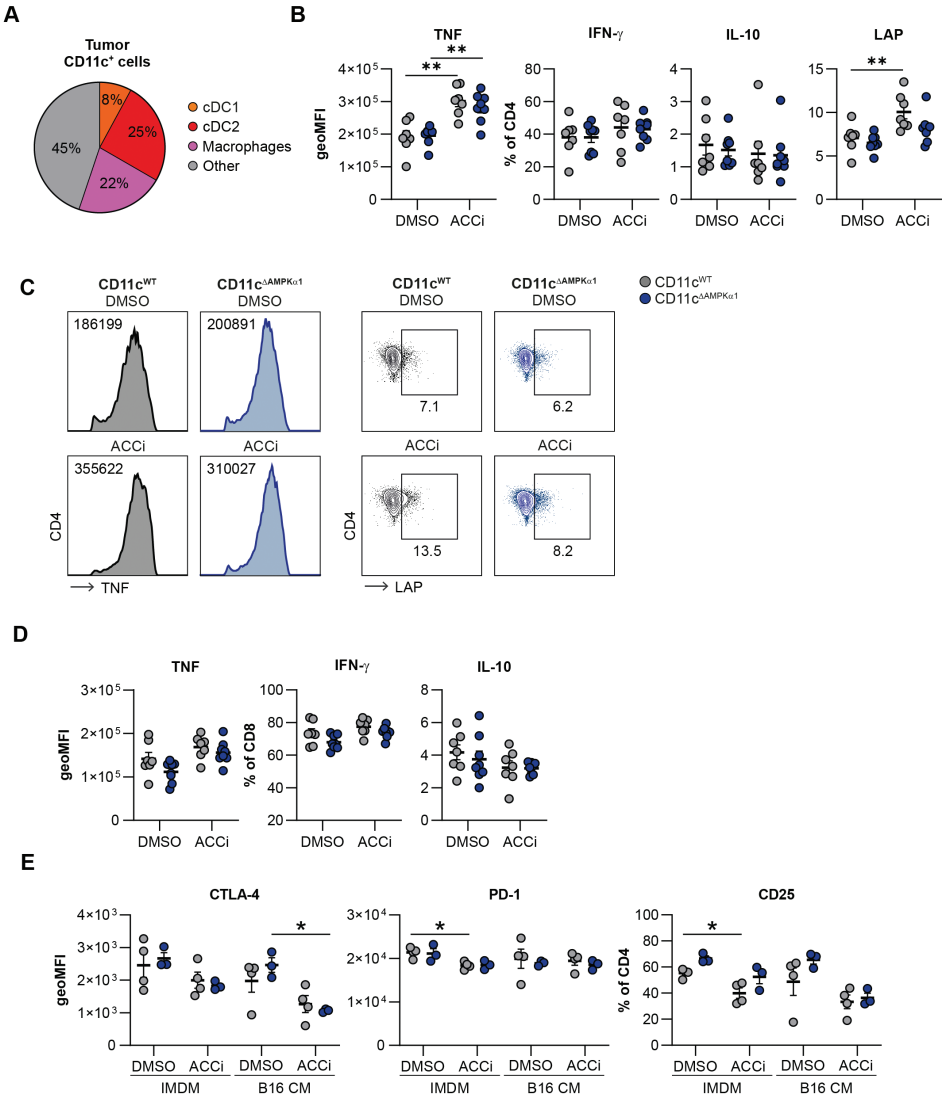

Supplementary figure 5: ACC expression in DCs suppresses TNF and LAP levels in CD4⁺ T cells after *ex vivo* priming. A: Cell distribution within CD11c⁺ cells. **B-D:** After 8 days of DC-T cell co-culture, cells were restimulated with PMA and ionomycin in presence of Brefeldin A. Cytokine levels and representative lots of TNF and LAP expression by (**B,C**) CD4⁺ OT-II T cells and (**D**) CD8⁺ OT-I T cells. **E:** Expression levels of CTLA-4, PD-1, and CD25 by CD4⁺ T cells after 3 day co-culture with sorted cDC2s. Results are expressed as means ± SEM. Statistical analyses were performed using two-way Anova with Tukey post-hoc test. *p < 0.05, **p < 0.01.

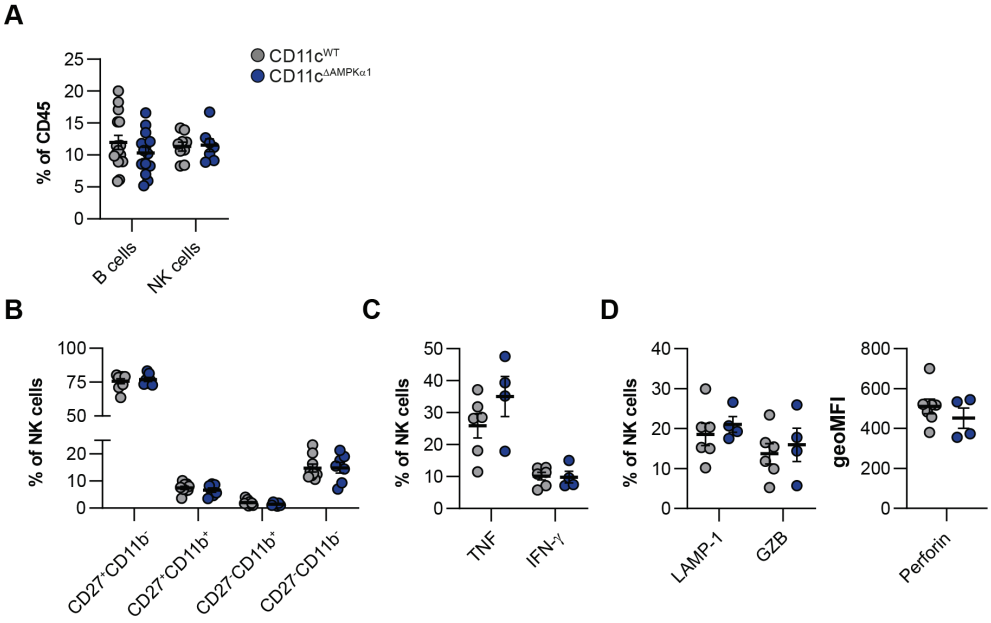

Supplementary figure 6: No differences in intra-tumoral NK cells between CD11c^{WT} and CD11c$^{\Delta AMPK\alpha1}$ mice. A: Frequencies of total B cells and NK cells. **B:** Frequencies of different NK cell subsets based on CD27 and CD11b expression. **C:** cytokine levels after PMA and ionomycin restimulation in the presence of Brefeldin A. **D:** Expression levels of cytotoxicity markers. LAMP-1 was added during restimulation with PMA/ionomycin in presence of Brefeldin A and granzyme B and perforin were stained intracellularly. Results are expressed as means ± SEM. Statistical analyses were performed using unpaired t-test. *p < 0.05, **p < 0.01.


AMPK

7

Metabolic sensor AMPK licenses CD103^{+} dendritic cells to induce Treg responses

Thiago A. Patente[1], Eline C. Brombacher[1], Graham A. Heieis[1], Leonard R. Pelgrom[1], Anna Zawistowska-Deniziak[1,2], Frank Otto[1], Arifa Ozir-Fazalalikhan[1], Alwin J. van der Ham[1], Bruno A. Guigas[1], José A. M. Barbuto[3], Bart Everts[1]

[1]Department of Parasitology, Leiden University Medical Center, Leiden, The Netherlands
[2]Department of Parasitology, Institute of Functional Biology and Ecology Faculty of Biology, University of Warsaw, Poland
[3]Laboratory of Tumor Immunology, Department of Immunology, Institute of Biomedical Sciences, University of São Paulo, Brazil

Manuscript under revision
DOI bioRχiv: 10.1101/2023.02.21.528293

Abstract

Dendritic cells (DCs) play a crucial role in promoting tolerance through priming of regulatory T cells (Treg). Several studies indicate DC tolerogenicity is dependent on catabolic metabolism. However, the role of AMP-activated Kinase (AMPK), a key energy and nutrient sensor driving catabolic metabolism, in this process is unclear. We found that human retinoic acid-induced tolerogenic $CD103^+$ DCs (RA-DCs) display increased AMPK signaling. Interestingly, RA-DCs, but not vitamin-D3- or dexamethasone-induced tolerogenic DCs, required AMPK for Treg induction. Mechanistically, AMPK underpinned RA-driven tolerogenicity by promoting RALDH activity in a FoxO3-dependent manner. Correspondingly, mice deficient for AMPK in DCs ($CD11c^{\Delta AMPK\alpha1}$) harbored reduced frequencies of intestinal $CD103^+CD11b^+$ DCs with impaired RALDH activity. Importantly, upon infection with parasitic worm *Schistosoma mansoni*, that elicits strong Th2 and Treg responses, $CD11c^{\Delta AMPK\alpha1}$ mice showed a defect in Treg accumulation and concomitantly, displayed an impaired ability to control Type 2 immunity-driven granulomatous inflammation against the parasite eggs. Together, our findings identify AMPK as a key regulator of tolerance by $CD103^+$ DCs.

Introduction

Dendritic cells (DCs) are professional antigen-presenting cells that regulate the priming and maintenance of $CD4^+$ and $CD8^+$ T cell responses and thus play an important role in the development of adaptive immune responses (1). DCs are also key players in maintaining immune tolerance by preventing T cell proliferation and promoting the development of regulatory T cells (Tregs) (2,3). DC populations with tolerogenic properties (tolDCs) commonly express CD103 and can be found in most peripheral tissues, where they play a crucial role in orchestrating peripheral Treg (pTreg) responses and in maintaining tissue-specific tolerance and homeostasis. Most insights in the biology of these tolDCs have been gained from studies on $CD103^+$DCs residing in the lamina propria of the gut. Here, acquisition of tolerogenic properties by intestinal DCs is largely driven by dietary Vitamin A, which through its active metabolite RA (4,5), induces DCs to become $CD103^+$ and express retinaldehyde dehydrogenase (RALDH)2 that allows them to produce RA themselves. This RA, in conjunction with TGF-β licenses $CD103^+$DCs to prime pTregs (Coombes, 2007; Mucida, 2007). The biology of tolDCs has also been extensively studied in *in vitro* models in which DCs can be rendered tolerogenic following exposure to immunesuppressive or modulatory compounds, including RA, as a model for $CD103^+$DCs (6), dexamethasone (7–9) and the active metabolite of vitamin D3 (10–12) Depending on the type of tolerogenic stimulus, different mechanisms have been proposed to control the differentiation of Tregs by these tolDCs. In addition to increased RALDH activity (13), this includes low costimulatory signal strength (14), increased expression of surface bound Immunoglobulin-like transcript members, soluble factors such as IL-10, TGF-β, (15), and/or of indoleamine 2,3-dioxygenase (IDO) (16,17).

Recently, it has become clear that immune cell activation and function, including that of DCs, are closely linked to changes in cellular metabolism (18–20). While the metabolic requirements for the acquisition of an immunogenic phenotype by myeloid DCs are fairly well characterized (21–23), the metabolic pathways involved in the development and function of tolDCs, are less well defined (2,24). There is some evidence that tolDCs rely on oxidative phosphoryalation (OXPHOS) for their tolerogenic functions (2,24) and it has been shown that inhibiting anabolic metabolism in DCs promotes the development of a tolerogenic phenotype (25), indicating a role for catabolic/oxidative metabolism in Treg induction by DCs. However, currently, how exogenous tolerogenic signals are integrated to promote this catabolic profile in tolDCs are still largely unknown.

AMP-activated protein kinase (AMPK) is a key sensor of cellular energy status, restoring energy homeostasis upon nutrient deprivation by inhibiting anabolic pathways and promoting catabolic pathways (26,27). There is some data to suggest a role for AMPK in shaping the immunogenic properties of DCs. For instance, human DCs treated with VitD3 displayed increased AMPK activation, which was associated with increased mitochondrial activity (11) and elevated mitochondrial glucose oxidation (Vanherwegen et al., 2018), suggesting a possible role for AMPK signaling in tolDCs differentiation via metabolic alterations. In addition, AMPK deficiency in CD11c-expressing cells was shown to hamper host defense against hookworm infection in mice, a feature associated with increased IL-12/23p40 secretion and poor induction of a type 2 immune response (28). Concomitantly, murine bone marrow-derived DCs (BMDCs) from AMPK knockout mice displayed an increased inflammatory phenotype characterized by an enhanced ability to induce IFN-γ– and IL-17-secreting T cells (29). While these studies suggest that AMPK signaling in DCs is involved in dampening immune

responses, the exact role played by this kinase in tolDC induction, metabolism and function remains an open question.

Here, we set out to characterize the metabolic properties of differently generated tolDCs and to define the role of AMPK signaling in their differentiation and ability to induce Tregs. We show that specifically human retinoic acid-induced tolerogenic CD103$^+$ DCs (RA-DCs) are characterized by increased AMPK signaling and that this AMPK signaling is required for the induction of functional Tregs. We found AMPK to mediate this via increasing RALDH activity, through FoxO3-signaling, independently from metabolic rewiring. Similarly, murine intestinal tolerogenic RALDH$^+$CD103$^+$ DCs displayed high AMPK activation and their RALDH activity was abrogated upon loss of AMPK signaling. Furthermore, we link the loss of AMPK in DCs to impaired Treg induction and exacerbated pathology during infection with the parasitic helminth *Schistosoma mansoni*. Taken together, these data identify a key role for AMPK signaling in RA-driven development of tolDCs, that mitigate tissue pathology during inflammation.

Results

Differently generated human tolDCs display distinct metabolic profiles.

To characterize and compare the metabolic properties of different tolDCs, we generated moDCs from peripheral blood CD14$^+$ monocytes with GM-CSF and IL-4, followed by LPS stimulation in the absence (mDC) or presence of three well-known tolerogenic compounds: retinoic acid (RA-DCs) (6), dexamethasone (Dex-DCs) (7–9) and the active metabolite of vitamin D3 (VitD3-DCs) (10–12). In accordance with previous studies (30,31), all tolerogenic compounds reduced moDC differentiation, as indicated by reduced CD1a expression and increased CD14 expression in the case of VitD3 (Figure S1A). Furthermore, in line with literature (32–34) VitD3, but not Dex, significantly increased the expression of PD-L1 and ILT3, two co-inhibitory molecules involved in controlling the inflammatory response (35), while RA treatment increased the expression of the gut homing integrin, CD103 (Figure 1A and Figure S1B) as well as RALDH activity (Figure 1B). The LPS-induced costimulatory molecule expression by DCs was overall inhibited when cells were treated with VitD3, RA and Dex (Figure 1A), but only VitD3 and Dex reduced the secretion of IL-12p70 and increased the secretion of IL-10 by DCs (Figure 1C). Importantly, irrespective of these phenotypic differences, all tolDCs induced stable and functional Tregs capable of suppressing bystander T cell proliferation (Figure 1D) and that are characterized either by increased CTLA-4 (by all tolDCs; Figure S1C) Foxp3 (by RA-DCs; Figure 1E) or IL-10 expression (by Dex- and RA-DCs; Figure 1F).

Following validation of their tolerogenic phenotype and function we next investigated the metabolic profile of the differently generated tolDCs. VitD3 induced the most pronounced core metabolic alterations, as evidenced by increased rates in glycolysis and OXPHOS (Figure 1G). On the other hand, Dex did not induce any core metabolic changes, while RA only reduced the spare respiratory capacity (SRC) of DCs (Figure 1G). In contrast to control DCs, all tolDCs showed increased levels of OXPHOS upon LPS stimulation (Figure S2), which is indicative of increased mitochondrial glucose oxidation and catabolic metabolism. Flow cytometry-based analysis of expression of rate-limiting metabolic enzymes in key metabolic pathways (36,37), corroborated these findings, by revealing that amongst the different tolDCs, VitD3-DCs displayed the most pronounced changes in metabolic enzyme expression (Figure 1I, S1D). Although principal component analysis of the metabolic enzyme expression data

showed co-clustering of VitD3-DCs with RA-DCs, but not Dex-DCs (Figure 1H), modulation of several metabolic enzymes by RA was distinct from VitD3, including reduction in Acetyl-CoA Carboxylase (ACC)1 and glucose transporter (Glut)1 expression, potentially indicating a more catabolic metabolic profile (Figure 1I).

Finally, we assessed activation status of AMP-activated protein kinase (AMPK) as one of the central energy sensors controlling catabolic metabolism. Interestingly increased phosphorylation of AMPK at Thr172 (Figure 1J), as well as of its direct substrate, ACC at Ser79 (Figure S1E), was observed in both VitD3- and RA-DCs, but not Dex-DCs. Together these data reveal that different tolDCs with distinct tolerogenic immune features also display divergent metabolic programs as well as levels in AMPK signaling.

RA-DCs depend on AMPK signaling for induction of regulatory T cells

In light of the known link between tolDC function and catabolic metabolism, we next aimed to explore the functional relevance of high AMPK signaling in the differently generated tolDCs. To this end, we silenced AMPKα1, the primary isoform expressed by DCs (38), prior to treatment with the tolerogenic compounds (Figure S3A) and evaluated whether the lack of AMPKα1 signaling would impair phenotype and function of the differently stimulated tolDCs. We found that the metabolic alterations induced by in VitD3 and RA compounds were reversed in the absence of AMPKα1 but not in Dex-DCs (Figure 2A, 2B and S3B). Next, we investigated the effects of AMPKα1 signaling on the ability of tolDCs to induce the differentiation of bona-fide Tregs and found that AMPKα1 silencing did not impair Dex-induced tolerogenicity (Figure 2C). Surprisingly, despite the reversal of metabolic alterations induced by VitD3 following AMPKα1 silencing, AMPKα1 signaling was dispensable for the induction of functional Tregs by VitD-DCs (Figure 2C). Importantly, on the other hand, lack of AMPKα1 significantly compromised the ability of RA-DCs to drive IL-10 production in T cells and to promote their differentiation into functional Tregs (Figure 2C, 2D). To further substantiate these findings, we generated murine RA-BMDCs from mice with a specific deletion of AMPKα1 in CD11c$^+$ positive cells (CD11c$^{\Delta AMPK\alpha1}$) (Figure S3C) and assessed their ability to promote differentiation of FoxP3$^+$ Tregs and to suppress OT-II T cell proliferation. In line with the human DC data, AMPKα1-deficient RA-BMDCs failed to upregulate Foxp3 in cocultured CD4$^+$ T cells and to suppress T cell proliferation, in contrast to their WT counterparts (Figure 2E, 2F). Together, the data show that VitD3 and RA increase AMPKα1 signaling in DCs and that, while AMPKα1 is important for the metabolic alterations observed by both tolerogenic compounds, only RA-DCs rely on AMPKα1 for their tolerogenic functions.

AMPK licenses RA-DCs to promote Tregs through induction of RALDH activity

In the light of these results, we next aimed to address through which mechanisms AMPKα1 signaling renders RA-DCs tolerogenic. To this end, we assessed the consequences of AMPKα1 silencing on the immunological phenotype of RA-DCs. We found AMPKα1 signaling to be important for the reduction of CD80 and for the increase in both CD103 expression and RALDH activity induced by RA (Figure 3A, 3B and Figure S4A). RA-induced RALDH activity in DCs has been shown to be important for the induction of IL-10-secreting T cells and promotion of functional Tregs (6,13,39). Indeed, following treatment with RALDH inhibitor diethylaminobenzaldehyde (DEAB), prior to RA treatment, the ability of human RA-DCs to promote functional Tregs, (Figure 3C) or of murine RA-DCs to suppress proliferation of OT II

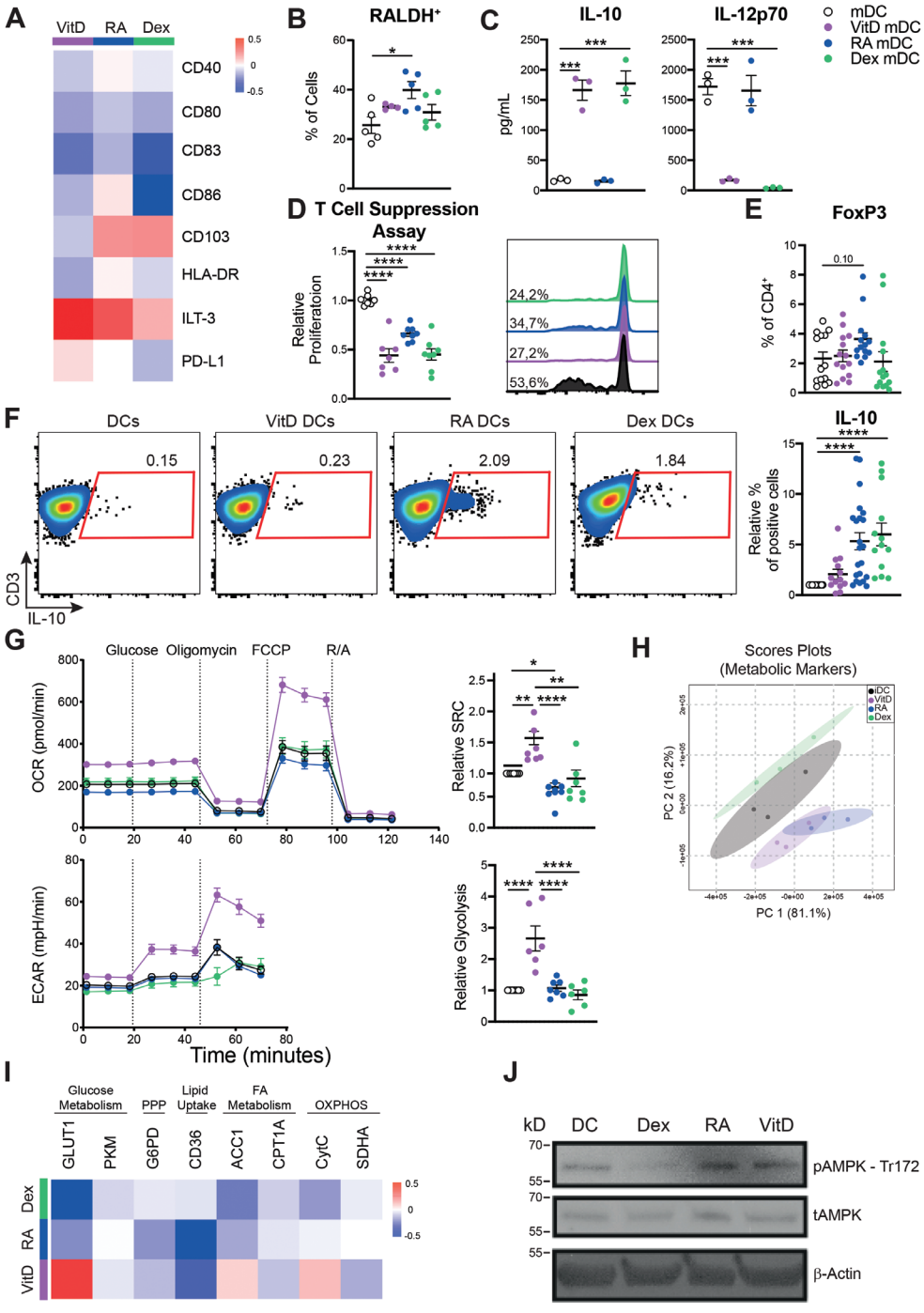
A
VitD
RA
Dex
CD40
CD80
CD83
CD86
CD103
HLA-DR
ILT-3
PD-L1
B
RALDH+
% of Cells
C
IL-10
IL-12p70
pg/mL
mDC
VitD mDC
RA mDC
Dex mDC
D
T Cell Suppression Assay
Relative Proliferatoion
24,2%
34,7%
27,2%
53,6%
E
FoxP3
% of CD4+
0.10
F
DCs
VitD DCs
RA DCs
Dex DCs
0.15
0.23
2.09
1.84
CD3
IL-10
IL-10
Relative % of positive cells
G
Glucose
Oligomycin
FCCP
R/A
OCR (pmol/min)
ECAR (mpH/min)
Time (minutes)
Relative SRC
Relative Glycolysis
H
Scores Plots (Metabolic Markers)
iDC
VitD
RA
Dex
PC 2 (16.2%)
PC 1 (81.1%)
I
Glucose Metabolism
PPP
Lipid Uptake
FA Metabolism
OXPHOS
GLUT1
PKM
G6PD
CD36
ACC1
CPT1A
CytC
SDHA
Dex
RA
VitD
J
kD
DC
Dex
RA
VitD
pAMPK - Tr172
tAMPK
β-Actin

Figure 1: Differently generated human tolerogenic DCs display distinct metabolic profiles. Monocytes were isolated from PBMCs with CD14+ magnetic beads and differentiated in moDCs in the presence of GM-CSF + IL-4. On day 5 cells were treated with either VitD3, RA or Dex. On the 6th day, 100 ng/mL of LPS were added and 24 hours later cells were harvested for functional assays. **(A)** Heatmap of the log2 fold change in geometric mean fluorescence intensity (GeoMFI) of surface markers of tolDCs measured by flow cytometry relative to control-stimulated DCs (mDC) (set to 0). **(B)** frequency of RALDH+ cells in tolDCs measured by flow cytometry. **(C)** tolDCs were co-cultured with CD40L-expressing cell line (J558) for 24 hours, supernatants were collected, and cytokines were measured by ELISA. **(D)** A T cell suppression assay was performed by co-culturing irradiated TolDC primed naïve Th cells with CFSE-labelled memory Th cells from the same donor. On the 6th day CFSE dilution was measured by flow cytometry. **(E-F)** tolDCs were co-cultured with allogeneic naïve T cells and intracellular **(E)** FoxP3 staining and **(F)** levels of IL-10 were measured by flow cytometry. **(G)** Seahorse extracellular flux analysis. Real-time oxygen consumption rate (OCR) (upper left) and extracellular acidification rate (ECAR) (bottom left) in tolDCs. Spare respiratory capacity (SRC) (upper right) and glycolysis (bottom right) were quantified and are displayed as fold change compared to control-stimulated DCs (mDC). **(H)** Principal component analysis (PCA) of tolDCs determined by the expression pattern of metabolic proteins. **(I)** Heatmap of the normalized geoMFI values of intracellular staining for metabolic proteins as determined by flow cytometry relative to mDCs. **(J)** Representative immunoblot of the expression of phosphorylated AMPK, total AMPK and b-actin in DC either left alone or treated with Dex, RA or VitD3 for 48 hours. Data are pooled from 15-22 donors **(A, E, F)**, 5-7 donors **(B, D, G)** or 3 donors **(H,I)**, or are representative of 1 out of 3 independent experiments **(C)**, or 2 independent experiments **(J)**. Mean ± SEM are indicated in the graphs. One-way Anova with Tukey HSD post-test was used to assess statistically significant differences; *p < 0.05, **p < 0.01, ***p < 0.001, ****p<0.0001.

T cells was lost (Figure S4B). This suggests that AMPKα1 signaling underpins the tolerogenic function of RA-DCs through induction of RALDH activity.

To understand how RA stimulates AMPKα1 signaling in moDCs, we first evaluated whether RA treatment could affect cellular energy status by measuring the intracellular levels of AMP, ADP and ATP, as increased ratios in AMP/ATP and ADP/ATP promote AMPKα1 activation (26,27). However, RA neither alter ATP/ADP nor AMP/ATP ratios, suggesting RA does not increase AMPKα1 activity through changes in bioenergetic status (Figure 3D). We next explored whether RA may affect AMPKα1 signaling through binding with its nuclear receptor, retinoic acid receptor (RAR). While preincubation with pan RAR inhibitor AGN 194310 prevented RA-induced changes in expression of CD103 and ILT3 (Figure 3E), it did not affect the increase in AMPKα1 signaling induced by RA treatment (Figure 3F). Together, these data suggest that RA in DCs, independently from changes in bioenergetics or RAR signaling, promotes AMPKα1 activation which is required for increased RALDH activity and thereby induction of Tregs by RA-DCs.

AMPKα1 signals via PGC1α to control CD103 expression and via FoxO3 to control RALDH activity

We next set out to investigate the mechanism through which AMPKα1 drives RALDH activity in DCs. PGC1α is a substrate of AMPK (40) that can act as a co-activator for the nuclear receptor PPARγ (41). As it has been proposed that PGC1α controls RALDH activity in murine CD103+CD11b- DCs (42), we wondered whether AMPKα1-driven RALDH activity in RA-DCs is dependent on PPARγ-PGC1α signaling. We found mRNA expression of both PPARγ and PGC1α to be significantly upregulated in response to RA treatment in DCs (Figure 4A). However, although pharmacological inhibition of PGC1α did prevent RA-induced expression

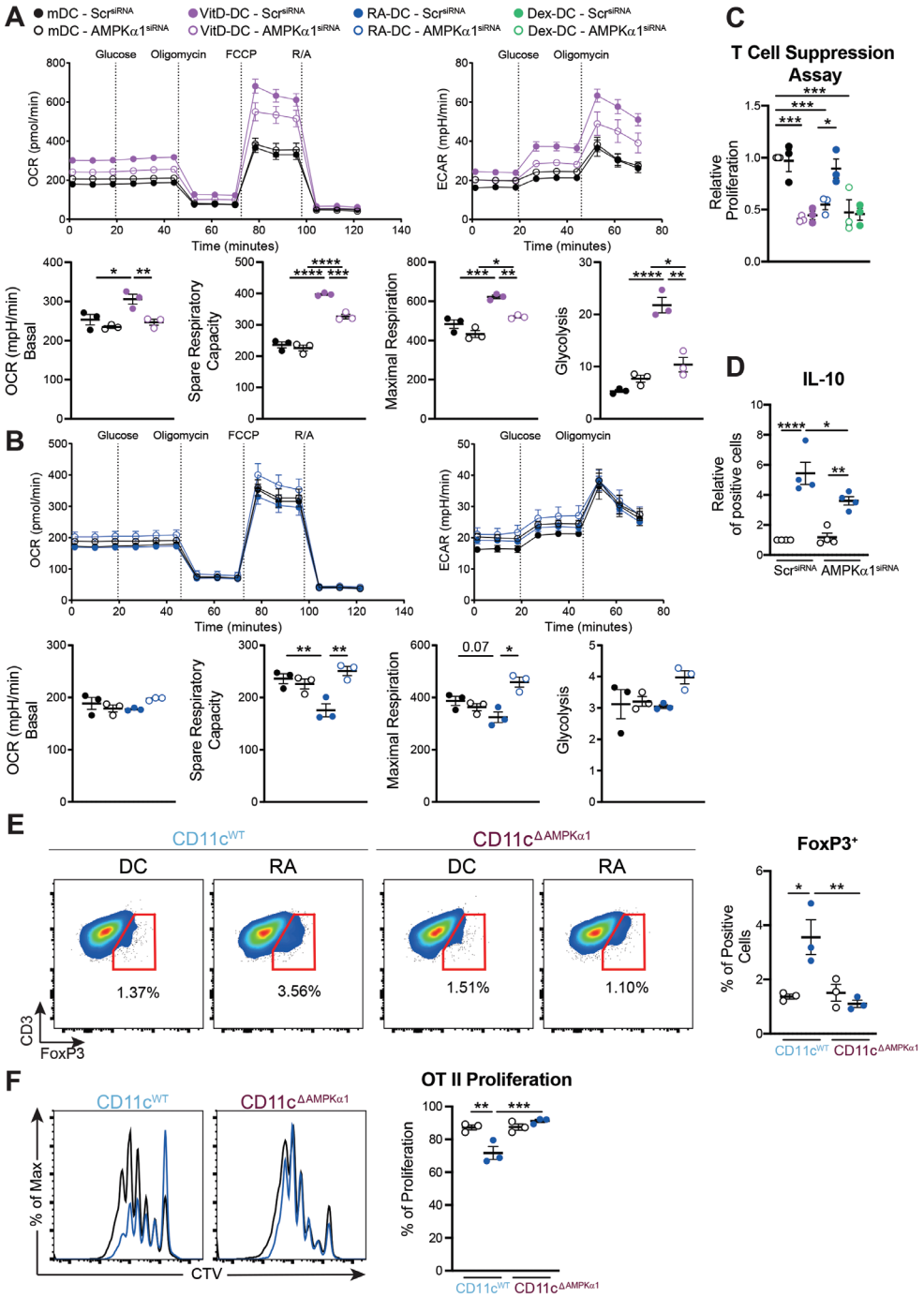
A
mDC - Scr siRNA
mDC - AMPKα1 siRNA
VitD-DC - Scr siRNA
VitD-DC - AMPKα1 siRNA
RA-DC - Scr siRNA
RA-DC - AMPKα1 siRNA
Dex-DC - Scr siRNA
Dex-DC - AMPKα1 siRNA
Glucose
Oligomycin
FCCP
R/A
OCR (pmol/min)
ECAR (mpH/min)
Time (minutes)
OCR (mpH/min) Basal
Spare Respiratory Capacity
Maximal Respiration
Glycolysis
B
C
T Cell Suppression Assay
Relative Proliferation
D
IL-10
Relative of positive cells
Scr siRNA
AMPKα1 siRNA
E
CD11c WT
CD11c ΔAMPKα1
DC
RA
1.37%
3.56%
1.51%
1.10%
CD3
FoxP3
FoxP3+
% of Positive Cells
F
% of Max
CTV
OT II Proliferation
% of Proliferation

Figure 2: RA-DCs depend on AMPK signaling for induction of regulatory T cells. moDCs were silenced for AMPKα1 or non-targeting scramble RNA before treatment with VitD3 or RA. Subsequently, metabolic profile for VitD- **(A)** and RA-treated DCs **(B)** was analyzed using Seahorse extracellular flux analysis and suppressive capacity (C) and IL-10 secretion (D) of T cells primed by tolDCs were assessed. **(E-F)** GM-CSF-derived bone marrow dendritic cells (GMDCs) were differentiated from $CD11c^{WT}$ or $CD11c^{\Delta AMPK\alpha1}$ mice and co-cultured with OT II naïve T cells to evaluate their ability to induce **(E)** FoxP3+ Tregs or **(F)** their ability to induce OT II T cell proliferation. Data are representative of 1 out of 4 donors **(A-B)**, represent 3-4 donors **(C-D)**, or 3 independent experiments **(E-F)**. Mean ± SEM are indicated in the graphs. Two-Way Anova with Sidák's post-test was used to assess statistically significant differences.; *p < 0.05, **p < 0.01, ***p < 0.001, ****p<0.0001.

of CD103 (Figure 4B), neither inhibition of PGC1α nor PPARγ did affect the ability of RA to increase RALDH activity (Figure 4C) nor of RA-DCs to prime Tregs (Figure S4C), suggesting that AMPKα1 does not signal through the PPARγ-PGC1α to induce RALDH activity and tolerogenicity in RA-DCs. Another transcription factor downstream of AMPK is FoxO3, which belongs to the forkhead-box family of transcription factors and plays a role in a variety of processes including longevity, cell differentiation and energy homeostasis (43). in silico analysis revealed that the top phosphorylated site by AMPK in FoxO3 is S413, which has been shown to promote its transcriptional activity (44) (Figure 4D). Congruently, we found that upon RA treatment, DCs displayed increased phosphorylation at S413, (Figure 4E). In addition, phosphorylation of FoxO3 at S253 which is known to prevent its translocation to the nucleus (Brunet et al., 1999), was inhibited (Figure 4E). Importantly, silencing AMPKα1 in moDCs abolished the RA-induced phosphorylation of FoxO3 at S413 (Figure 4F). In addition, while silencing of FoxO3 in moDCs did not affect expression of surface markers modulated by RA, including CD103 (Figure 4G, S4D), the ability of RA to induce RALDH activity and promote tolerogenic DC function was lost (Figure 4H-I). Taken together, these data show that RA triggers AMPKα1 signaling to promote RALDH activity in a FoxO3-dependent manner that is required for subsequent Treg induction.

AMPKα1 signaling governs maintenance and RALDH activity of intestinal CD103+CD11b+ DCs

Next, we explored the functional relevance of these findings in an *in vivo* setting. Naturally occurring tolerogenic RALDH+CD103+ DCs have been identified in various organs, including lung and intestine (45,46). We initially focused on the role of AMPK signalling in the biology of RALDH+CD103+ DCs in the latter organ, since here DCs are thought to be exposed to particularly high levels of RA readily generated by epithelial cells from dietary vitamin A (4,5,47,48). In the intestine, three main conventional DC subsets can be identified, based on differential expression of CD103 and CD11b (Figure S5A) of which particularly CD103+ DCs populations are associated with the induction of Tregs (49). We observed that in naïve WT mice small intestinal lamina propria (siLP) CD103+ DCs (especially CD103+CD11b+) displayed higher levels of pACC compared to CD11b+ DCs, CD64+ macrophages (Mph), T cells or B cells from the same tissues (Figure 5A) as well as compared to DCs from other tissues including lung, liver, spleen and msLN (Figure S6A, S6B). Interestingly, AMPK signaling levels were positively correlated with RALDH activity in these DCs (Figure 5A). Largely in line with our *in vitro* data, we found that mice with a specific deletion of AMPKα1 in CD11c+ cells ($CD11c^{\Delta AMPK\alpha1}$) (Figure S6C), showed a selective reduction in cell frequency of CD103+CD11b+ DCs from

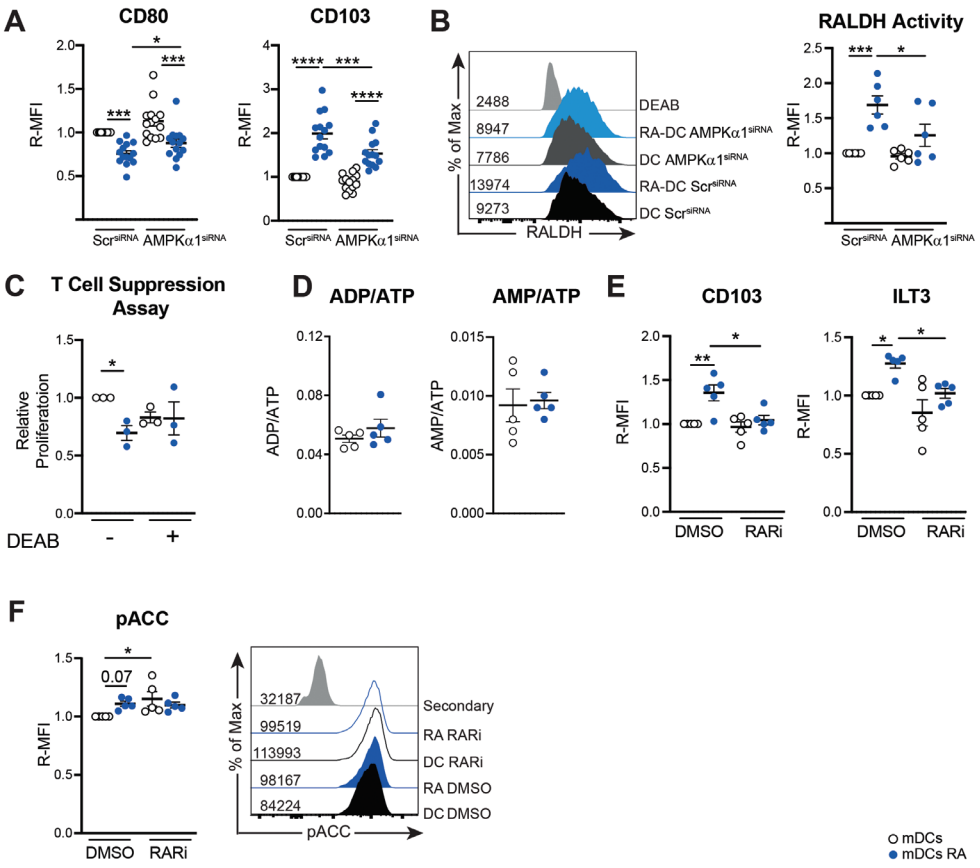

Figure 3: AMPK licenses RA-DCs to promote Tregs through induction of RALDH activity.(A) Relative geoMFI (R-MFI) for the expression of CD80 and of CD103 and from AMPKα1-silenced or scramble-silenced RA-DCs measured by flow cytometry. **(B)** Representative histogram staining for RALDH activity (left) and quantification of R-MFI in RA-DCs silenced for AMPKα1. **(C)** moDCs were pre-treated with either vehicle or DEAB for 30 min before being treated with RA followed by LPS stimulation and T cell suppression assay was performed as described in Figure 1D. **(D)** Intracellular levels of AMP, ADP and ATP in moDCs were measured by HPLC and the ratio of ADP/ATP and AMP/ATP were quantified. **(E-F)** moDCs were pre-treated with either vehicle or retinoic acid receptor inhibitor (RARi) for 1 hour before being treated with RA and **(E)** relative geoMFI (R-MFI) for the expression of CD103 and ILT-3 were evaluated. **(F)** Intracellular levels of phospho acetyl carboxylase (serine 79 - pACC) levels were evaluated in moDCs pre-treated with RARi followed by 4 h of RA treatment (left); representative histogram of the pACC staining on moDCs (right). Data are based on a pool of 14 **(A)**; 6 **(B)**, or 5 donors **(D-F)**. Mean ± SEM are indicated in the graphs. Two-Way Anova with Sidák's post-test **(B-C;E-F)** or student's T test **(D)** were used to assess statistically significant differences.; *p < 0.05, **p < 0.01, ***p < 0.001.

siLP (Figure 5B) as well as a lower RALDH activity in this DC subset (Figure 5C). Reduced frequencies of $CD103^{+}CD11b^{+}$ DCs in $CD11c^{\Delta AMPK\alpha1}$ mice were mirrored in the draining mesenteric (mes)LNs (Figure S6F), although RALDH activity was not affected in these DCs by loss of AMPKα1 (Figure S6G). To further characterize the consequences of loss of AMPKα1

on siLP DC populations, we performed an unbiased analysis of the intestinal DC compartment, through dimensional reduction and unsupervised analysis based on a flow cytometry panel encompassing activation and lineage markers. This resulted in the identification of several different phenotypic clusters within the three subsets of intestinal DCs (Figure 5D, 5E and S6D). Amongst those, cluster PG_04, a $CD103^{+}CD11b^{+}$ population characterized by high RALDH activity and low CD86 and CCR7 expression, was significantly reduced in frequency in $CD11c^{\Delta AMPK\alpha1}$ mice, while the opposite was true for a $RALDH^{lo}CD86^{hi}CCR7^{hi}$ $CD103^{+}$ DC population (PG_09) (Figure 5F, 5H and S6E), indicative of a switch from a tolerogenic to a more immunogenic intestinal DCs phenotype in $CD11c^{\Delta AMPK\alpha1}$ mice.

We also analyzed the lung as another mucosal site with regulatory characteristics where $RALDH^{+}CD103^{+}$ DCs have been identified (45). We did not observe any significant changes in frequencies and RALDH activity at the population level in $CD11b^{+}$ or $CD103^{+}$ DC subsets in the lungs of $CD11c^{\Delta AMPK\alpha1}$ compared to $CD11c^{WT}$ mice (Figure S7A-C). However, when analyzing the lung DC compartment in an unbiased manner, we identified several phenotypic clusters within the $CD103^{+}$ and $CD11b^{+}$ DC subsets with different abundance between $CD11c^{WT}$ and $CD11c^{\Delta AMPK\alpha1}$ mice (Figure S7D, S7E, and S7F). Similar to our findings in the gut, we observed a shift from a tolerogenic to an immunogenic DC phenotype in $CD11c^{\Delta AMPK\alpha1}$ mice, as illustrated by, on the one hand, a reduced frequency of a $CD103^{+}$ DC cluster, with high RALDH activity and low expression of CD80 and CD86 (PG_04), and, on the other hand, an accumulation of a $RALDH^{lo}CD86^{hi}CD80^{hi}$ $CD103^{+}$ DC population (PG_07) (Figure S7G-S7J).

Despite the differences observed in the $CD103^{+}$ DC compartment in the absence of DC-intrinsic AMPK, neither the frequency nor the activation state of Tregs was significantly affected in lung or intestine of naïve $CD11c^{\Delta AMPK\alpha1}$ mice (Figure 5I-K, S6H, I, S7K). Analysis of the Treg populations further revealed no differences in the frequency of Tregs from either thymic (tTreg; $Helios^{+}ROR\gamma t^{-}$) or peripheral origin (pTreg – $Helios^{-}ROR\gamma t^{+}$) (Figure 5J, S6H). Taken together these data suggest that AMPKα1 signaling controls $CD103^{+}$ DCs tolerogenic phenotype by governing RALDH activity, but that this does not grossly affect mucosal Treg populations at steady state.

AMPK signaling in CD11c-expressing cells is important for Treg induction and prevention of immunopathology during *S. mansoni* infection

Although the Treg compartment of $CD11c^{\Delta AMPK\alpha1}$ mice appeared unaffected during steady state, we next wondered whether the altered phenotype of $CD103^{+}$ DCs may affect Treg responses in the context of inflammation. Exposure to house dust mite (HDM) to drive allergic asthma, promoted accumulation of Tregs in the medLNs in WT mice. Interestingly, this was significantly compromised in of $CD11c^{\Delta AMPK\alpha1}$ mice (Figure S7L). However, no differences in cellular infiltrate or eosinophilia in bronchioalveolar lavage (Figure S7M) or lungs (Figure S7N) were observed, suggesting that the defect in Treg accumulation in the lung, as a consequence of allergen challenge, did not significantly impact the inflammatory response and outcome of disease in of $CD11c^{\Delta AMPK\alpha1}$ mice.

We next aimed to investigate whether CD11c-specific AMPKα1 loss affected Treg responses and pathology during infection with parasitic helminth *Schistosoma mansoni*. During schistosomiasis major drivers of pathology are the parasitic eggs released by mature worms residing in the mesenteric vasculature that, as a consequence of egg-induced Type 2 inflammation, lead to granulomatous tissue lesions in the intestine but particularly the liver.

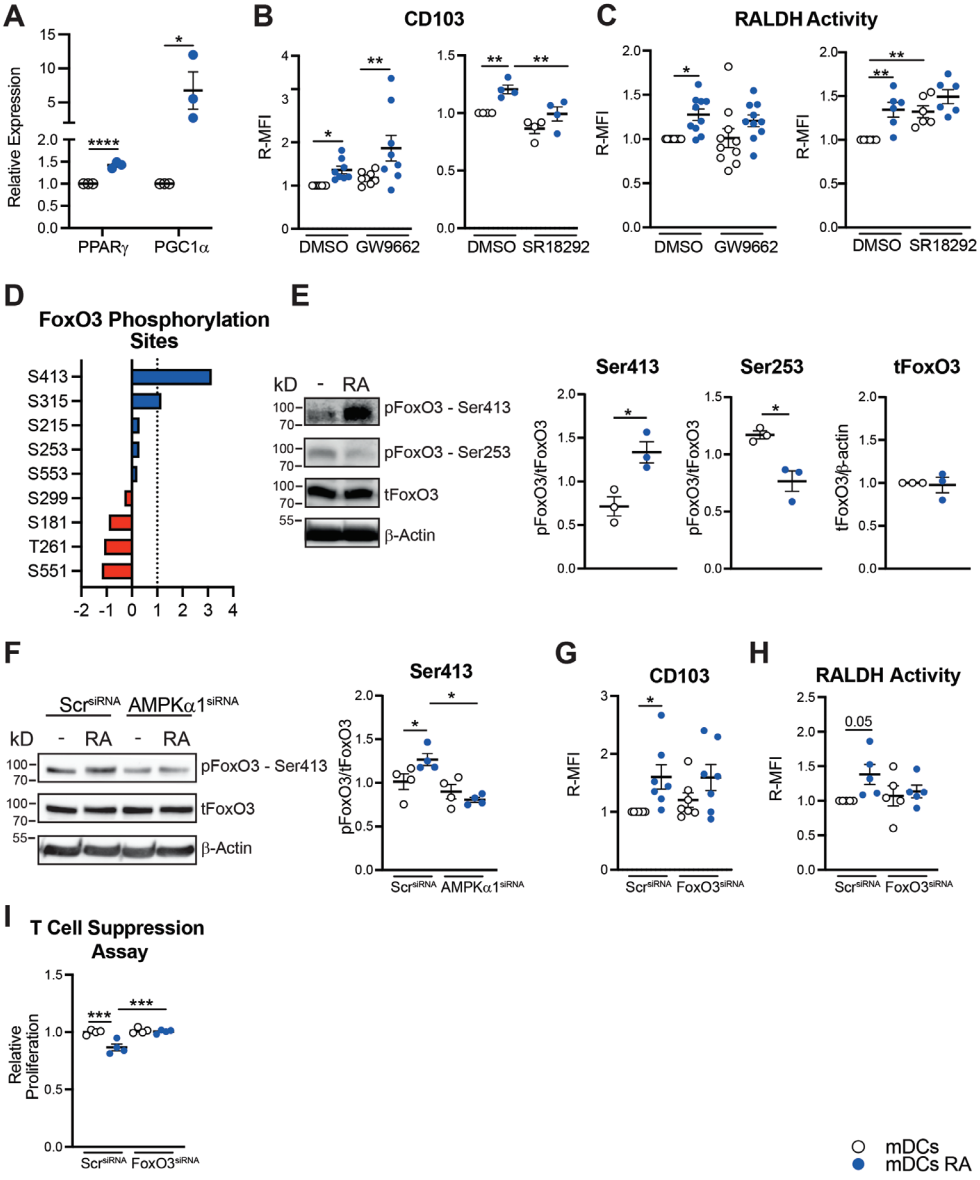

Figure 4: AMPK signals via PGC1α to control CD103 expression and via FoxO3 to control RALDH activity. (A) Gene expression of PPARγ and PGC1α in RA-treated and control moDCs. On day 5 of culture moDCs were treated either with RA or left untreated for 48 hours and mRNA expression levels were determined by RT-qPCR. GAPDH was used as housekeeping gene **(B-C)**. On day 5, moDCs were pre-treated with either DMSO, PPARγ (GW9662) or PGC1α (SR18292) inhibitors for 30 minutes prior to RA treatment, followed by LPS stimulation and **(B)** CD103 expression and **(C)** RALDH activity were quantified by flow cytometry. **(D)** In silico analysis displaying the top predicted AMPK- phosphorylation sites in FoxO3. Dashed line represents the threshold level of AMPK-FoxO3 interaction. **(E)** Representative immunoblot (left) and quantification (right) of the expression levels of FoxO3 Ser413, FoxO3 Ser253, total FoxO3 and b-actin in RA-DCs. **(F)** Representative immunoblot (left) and quantification (right) of

the expression levels of FoxO3 Ser413, total FoxO3 and b -actin in RA-DCs silenced for AMPKα1 as described in Figure 2. **(G)** Expression levels of CD103 and **(H)** RALDH activity in RA-DCs silenced for FoxO3 as described in Figure 2. **(I)** moDCs were silenced for FoxO3 as described in Figure 2 and T cell suppression assay was performed as described in Figure 1D. Data are a pool of 3 **(A)**; 4-8 **(B-C)**, 3-4 **(E-F)**, or 4-7 donors **(G-H)** or are representative for 1 out of 3 independent experiments (I). Statistics are student's T-test **(A;E)** and Two-Way Anova with Sidák's posttest **(B-C;F-I)**, were used to assess statistically significant differences. Mean ± SEM are indicated in the graphs; *p < 0.05, **p < 0.01, ***p < 0.001, ****p<0.0001.Two-Way Anova with Sidák's post-test was used to assess statistically significant differences.; *p < 0.05, **p < 0.01, ***p < 0.001, ****p<0.0001.

During this infection induction of pTregs are crucial for preventing overzealous Th2 responses and uncontrolled granuloma formation especially during the chronic stages of infection. We observed the appearance of a $CD103^+CD11b^+$ DC subset in the liver of both acutely (8 week) and chronically (16 week) infected mice (Figure 6A and S7O) displaying increased AMPK signaling, as determined by ACC phosphorylation levels (Figure 6B and S7P), as well as increased RALDH activity (Figure 6C and S7Q). Importantly, in contrast to the WT littermates, infected of $CD11c^{\Delta AMPK\alpha1}$ mice failed to increase Treg frequencies in their livers at both 8 (Figure 6D, E) and 16 weeks post infection (Figure 6F). At both timepoints, this was associated with an increase in both Th1 and Th2 cytokine secretion in the hepatic lymph nodes (hpLN) (Figure 6G, H) and msLN (Figure 6I) of $CD11c^{\Delta AMPK\alpha1}$ mice. Consistent with an uncontrolled type 2 immune response, we found a higher frequency of alternatively activated $CD11c^-RELM\alpha^+$ macrophages (Figure 6J) as well as an increased liver egg granuloma size in chronically, infected of $CD11c^{\Delta AMPK\alpha1}$ mice compared to infected WT littermates (Figure 6K), indicative of enhanced immunopathology, which was not yet evident during acute stages of infection (Figure S7R). Taken together, the data suggest that AMPKα1 signaling in DCs is important to induce the differentiation and or expansion of $FoxP3^+$ Tregs, to keep effector Th cell responses overzealous egg-induced granulomatous responses in check during *S. mansoni* infection.

Discussion

Despite the well-established function for AMPK signaling in promoting catabolic metabolism (50,51) and the growing appreciation for catabolic metabolism as central component for the tolerogenic functions of DCs (2,24), the importance of AMPK for tolDCs functions has not yet been addressed. Here, we provide evidence that AMPKα1 signaling is crucial for the induction of a tolerogenic phenotype in DCs exposed to RA. Independently from acting on metabolism, AMPKα1 does so by promoting RALDH activity in a FoxO3-dependent manner which is important for the induction of Tregs. In addition, we demonstrate that *in vivo* AMPKα1 signaling in CD11c-expressing cells is important for induction of Tregs during different inflammatory settings.

Characterization of the metabolic properties of the differently generated tolDCs revealed highly divergent profiles, presumably reflecting the differences in molecular targets of Dex, VitD3 and RA through which they modulate DC biology. Most studies interrogating the metabolic properties of human tolDCs have been focused on moDCs treated with VitD3 alone or in conjunction with Dex. Consistent with these earlier reports (11,12,24,52), we find VitD3-DCs to display strong metabolic reprogramming with both features of anabolism and catabolism, whereas Dex-DCs showed relatively modest metabolic changes. On the other

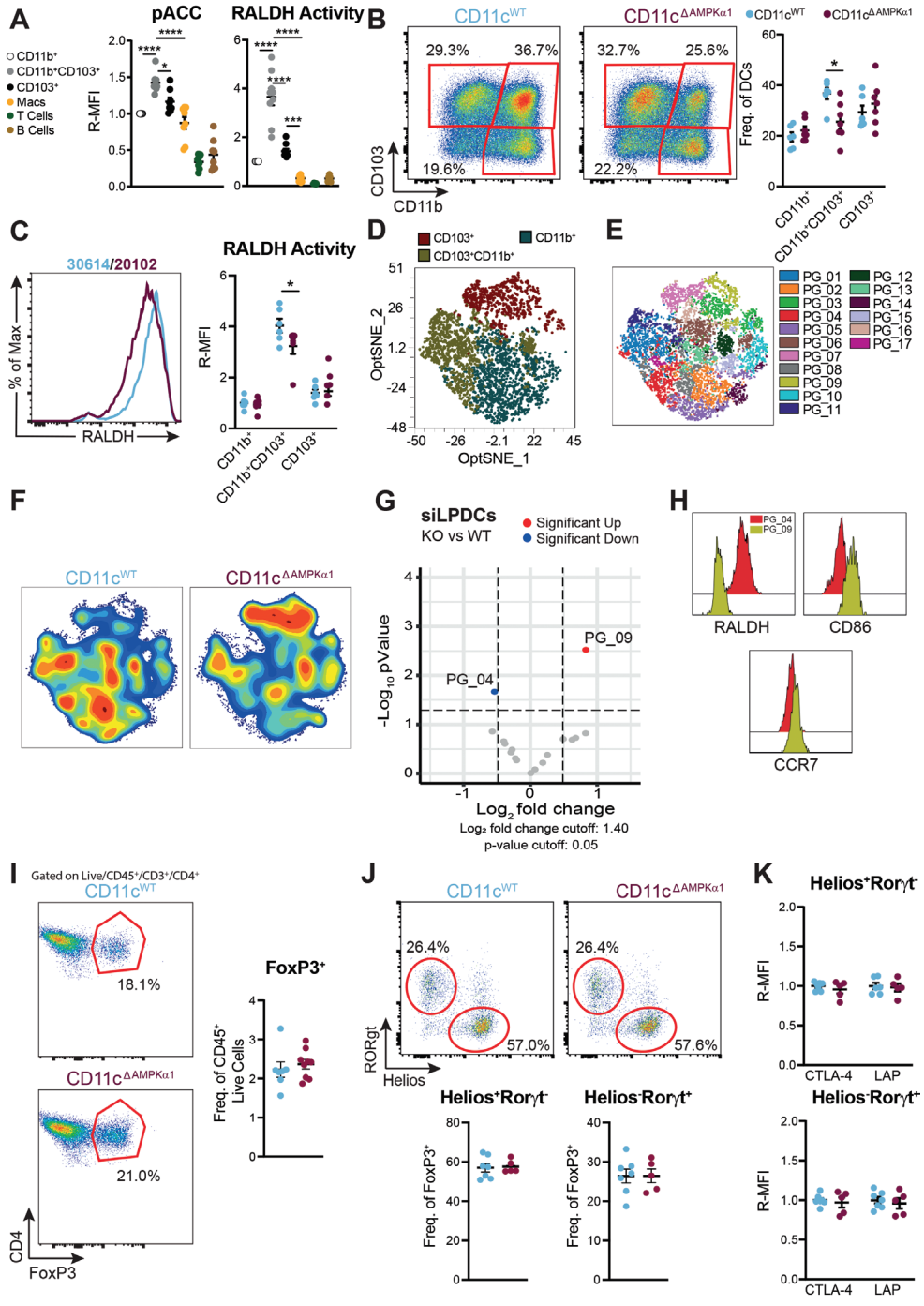
A
pACC
RALDH Activity
CD11b+
CD11b+CD103+
CD103+
Macs
T Cells
B Cells
R-MFI
B
CD11cWT
CD11cΔAMPKα1
29.3%
36.7%
19.6%
32.7%
25.6%
22.2%
CD103
CD11b
Freq. of DCs
C
30614/20102
% of Max
RALDH
RALDH Activity
R-MFI
D
CD103+
CD11b+
CD103+CD11b+
OptSNE_2
OptSNE_1
E
PG_01
PG_02
PG_03
PG_04
PG_05
PG_06
PG_07
PG_08
PG_09
PG_10
PG_11
PG_12
PG_13
PG_14
PG_15
PG_16
PG_17
F
CD11cWT
CD11cΔAMPKα1
G
siLPDCs
KO vs WT
Significant Up
Significant Down
-Log10 pValue
Log2 fold change
Log2 fold change cutoff: 1.40
p-value cutoff: 0.05
PG_04
PG_09
H
PG_04
PG_09
RALDH
CD86
CCR7
I
Gated on Live/CD45+/CD3+/CD4+
CD11cWT
CD11cΔAMPKα1
18.1%
21.0%
CD4
FoxP3
FoxP3+
Freq. of CD45+ Live Cells
J
CD11cWT
CD11cΔAMPKα1
26.4%
57.0%
26.4%
57.6%
RORgt
Helios
Helios+Rorγt-
Helios-Rorγt+
Freq. of FoxP3+
K
Helios+Rorγt-
Helios-Rorγt+
R-MFI
CTLA-4
LAP

Figure 5: AMPK signaling governs maintenance of, and RALDH activity in intestinal CD103$^+$CD11b$^+$ DCs. (A) Relative geometric MFI (R-MFI) of phosphorylation level of acetyl-coA carboxylase - Ser79 (pACC - left) and retinaldehyde dehydrogenase (RALDH) activity in different immune cells in the small intestine lamina propria (siLP) of naïve WT mice. Data were normalized by the expression levels of CD11b$^+$ DCs. **(B)** Representative dot plot (left) and frequency of siLP DC subsets within CD45$^+$ live cells (right) in CD11c^{WT} (salem blue) and CD11c$^{\Delta AMPK\alpha1}$ (purple-red). **(C)** Representative histogram (left) and relative geometric MFI (R-MFI) of RALDH activity in siLP DC subsets. **(D)** Unbiased opt-SNE analysis of siLP DC populations in which CD103$^+$, CD103$^+$CD11b$^+$ and CD11b$^+$ are indicated. **(E)** Phenograph clustering performed on siLP DCs using RALDH, activation and lineage markers. **(F)** Contour plots overlaid on opt-SNE analysis as shown in **(D)** displaying distribution of cells for CD11c^{WT} and CD11c$^{\Delta AMPK\alpha1}$ mice. **(G)** Volcano plot displaying the clusters as displayed in **(E)** with significant differences in frequency between CD11c^{WT} and CD11c$^{\Delta AMPK\alpha1}$ mice. **(H)** Histograms displaying the expression levels of RALDH, CD86 and CCR7 in PG_04 (red) and PG_09 (ochre). **(I)** Representative dot plot for the FoxP3$^+$ regulatory T cells (Tregs) in the siLP of CD11c^{WT} and CD11c$^{\Delta AMPK\alpha1}$ mice (left) and frequency of Tregs within CD45$^+$ live immune cells (right). **(J)** Representative dot plot for the thymic (Helios$^+$RORgt$^-$ - tTregs) and peripheral (Helios$^-$RORgt$^+$ - pTregs)) Tregs in the siLP of CD11c^{WT} and CD11c$^{\Delta AMPK\alpha1}$ mice (top) and frequency of tTregs and pTregs within total Treg population (bottom). **(K)** Quantification of CTLA-4 and latency-associated peptide (LAP) as proxy of TGF-b secretion by tTregs and pTregs in CD11c^{WT} and CD11c$^{\Delta AMPK\alpha1}$ mice. Data are representative of 1 out of 3 (left) or a pool of 3 independent experiments **(A)**; represent a pool of 2 to 3 independent experiments with 3-4 mice per experiment **(A-C;I-K)**; representative of 1 out of 2 independent experiments **(D-H)**. One-Way Anova with Tukey HSD post-test **(A)** or student's T-test **(B-C-K)** were used to assess statistically significant differences. Mean ± SEM are indicated in the graphs; *p < 0.05, ***p < 0.001, ****p<0.0001.

hand, there have been no detailed investigations into the metabolic properties of RA-DCs. We show here that RA promotes metabolic changes that are distinct from those induced by VitD3 and Dex, such as reduction in ACC1 and Glut1 expression, which may point towards a more catabolic metabolism than the other tolDCs (Vanherwegen et al., 2018). As each of these different tolDCs depend on distinct effector mechanisms to exert their tolerogenic effect, our findings may inform future studies to uncover new functional links between specific metabolic programs/sensors and particular tolerogenic traits of DCs.

The differences in metabolic profiles were also reflected at the level of the key cellular nutrient/energy sensor AMPK, with a potent activation observed in VitD-DCs and RA-DCs, but not in Dex-DCs. This observation would be largely in agreement with earlier reports showing that VitD3, but not Dex treatment, increases mitochondrial biogenesis and OXPHOS (53), a well-known consequence of increased AMPK signaling (50,51). Indeed, we found that the increase in both OXPHOS and glycolytic rates observed in VitD3-DCs were dependent on AMPK signaling. Surprisingly, however, we found that the AMPK-dependent metabolic reprogramming was dissociated from the tolerogenic functions of VitD3-DCs. Nonetheless, some level of glycolysis and OXPHOS are required for VitD3-DCs to exert their tolerogenic effects, because earlier work has shown that direct inhibition of any of these processes compromises their tolerogenic properties (11,12).

Interestingly, in contrast to VitD3-DCs, RA-DCs were highly dependent on AMPKα1 signaling to become tolerogenic, both in human and murine *in vitro* models. We found this to be directly linked to the key role that AMPK signaling plays in supporting induction of RALDH activity, a well-known effector mechanism through which RA licenses DCs to promote Treg responses (6). In addition to RALDH, CD103 expression, another well-established marker induced by RA, was also dependent on AMPK signaling. Interestingly, while AMPK-driven

CD103 expression was dependent on PGC1α, we provide evidence for a central role for FoxO3 in mediating AMPK-driven RALDH activity following stimulation with RA. We observed increased phosphorylation levels of AMPK-target site Ser413, (Fasano et al., 2019) which has been shown to increase its transcriptional activity (44). While we provide direct support for RA-induced FoxO3 phosphorylation by AMPK at Ser413 in DCs, it is currently still unclear in this context how FoxO3 gets dephosphorylated at Ser253 following RA treatment. mTOR target Akt is known to mediate phosphorylation of FoxO3 at three conserved residues, including Ser253. Because RA has been shown to inhibit mTOR activation (54)can hypothesize that RA treatment of DCs induces AMPK activation leading to an inhibition of Akt-mTOR axis. This would in turn, result in dephosphorylation of FoxO3 at Ser253, increasing its translocation to the nucleus where AMPK-induced phosphorylation of FoxO3 at Ser413 would increase its transcriptional activity. This two-step activation mechanism of FoxO3 by AMPK has been already demonstrated in neurons undergoing excitotoxic apoptosis (55) and could also be the mechanism underlying RA signaling in DCs.

How RA triggers AMPK activation, remains to be addressed. Canonically, AMPK gets activated upon cellular bioenergetic stress, reflected by increased ratios of AMP/ATP or ADP/ATP. However, we found no changes in these ratios following RA treatment. Also, inhibition of RAR, the main nuclear receptor through which RA mediates its effects on cells, had no effect on AMPK activity, despite reversing most of RA-induced phenotypic changes in DCs. Interestingly, a recent study revealed that RA may potentially directly interact with AMPK to promote its activity (56) and it is tempting to speculate in the light of our negative findings that this may in fact be the key mode of action through which RA controls AMPK activity in DCs.

We found siLP DCs to have the highest baseline AMPK activation levels amongst DCs from different tissues. Since the intestine is one of the primary sites of RA production, this points towards an important role for RA in promoting AMPK activation in DCs *in vivo*, analogous to our *in vitro* studies. Nonetheless a role for other gut-derived factors in promoting AMPK activation in DCs cannot be excluded. For instance, gut microbiota-derived products such as the short chain fatty acids (SCFA) butyrate, acetate and propionate have been shown to induce AMPK activation in other cell types (57)(58,59). Further studies will be needed to define the relative contribution of these local cues to AMPK activation.

The observation that in the siLP AMPK activation status correlated with RALDH activity in DCs and that loss of AMPKα1 resulted in reduced RALDH activity in intestinal $CD103^{+}CD11b^{+}$ DCs, as well as in lung $CD103^{+}$DCs, provides direct *in vivo* evidence for an important role of AMPKα1 signaling in underpinning RALDH activity in DCs. While RALDH activity in intestinal and lung $CD103^{+}$ DCs is well known to be linked to the ability of these cells to induce Treg responses (49,60–62), of $CD11c^{\Delta AMPK\alpha1}$ mice did not show clear defects in the intestinal or lung Treg pool under steady state conditions. This may suggest that the reduction in RALDH activity as a consequence of AMPKα1 loss in the DC compartment is not sufficient to affect homeostatic Treg differentiation by these cells. Additionally or alternatively, recent reports suggest that pTreg differentiation at steady state in the gut is mainly controlled by a novel subset of APCs, independently from intestinal conventional DCs (63–65). However, of note, these cells are reported to express CD11c, and should therefore also be AMPKα1 deficient in $CD11c^{\Delta AMPK\alpha1}$ mice. However, whether that would alter their function remains to be elucidated.

Although we did not find significant changes in Treg populations as a consequence of AMPKα1 deficiency in DCs at steady state, these mice did show a clear defect in Treg

accumulation in the context of *S. mansoni* infection as well as HDM-induced allergic asthma. This suggests that AMPKα1 signaling in DCs is required for differentiation and/or expansion during an immunological challenge. In the case of *S. mansoni* infection, this reduction in Treg accumulation was associated with an increased type 2 cytokine response during both acute and chronic stages of the infection and an increase in liver egg-derived granuloma size during the chronic phase of infection. It is well established that during *S. mansoni* infection, Foxp3+ Tregs accumulate and that these cells play a crucial role in dampening type 2 immune responses and in keeping the granulomatous response in the liver and gut towards the eggs in check (66). Our data would be in line with this concept and suggest that the stronger type 2 immune response and larger granuloma size in infected of CD11c$^{\Delta AMPK\alpha1}$ are secondary to an impaired Treg response. We should note that, at this point, we cannot formally rule out the possibility that the enhanced type 2 immune response is a direct consequence of loss of AMPKα1 signaling in DCs, for instance by enhancing their capacity to prime Th2 responses. However, this scenario seems unlikely as during HDM challenge, of CD11c$^{\Delta AMPK\alpha1}$ mice showed a selective defect in the Treg response, without apparent changes in the Type 2 immune response, as determined by eosinophilia. Moreover, others have found that these mice have in fact a compromised type 2 immune response during lung-stage hookworm infection (28). In this infection model we primarily focused on immune responses in the liver. Due to the inherent technical difficulties of reliably obtaining viable single cell suspensions from the gut from infected mice, we were unable to characterize the Treg response in the intestine of these mice but based on the reported similarities in hepatic and intestinal Treg and Type 2 immune responses during this infection (66), this is likely to mirror the hepatic immune phenotypes. The appearance of a hepatic CD103+CD11b+ DC population during *S. mansoni* infection with similarly high AMPK signaling and RALDH activity as their intestinal counterparts would support this. Since hepatic stellate cells in the liver are known to play a central role in RA metabolism and storage and have been shown to release RA upon inflammatory cues (67), it is tempting to speculate that during *S. mansoni* infection, this is a direct consequence of increased local exposure of hepatic DCs to RA.

In conclusion, our work has revealed AMPK signaling as a crucial pathway in controlling an RA-induced tolerogenic profile in human CD103+ DCs by inducing RALDH activity in a FoxO3-dependent manner, which showed to be functionally important for the induction of Tregs. In addition, we demonstrated that AMPK signaling is key for homeostasis of murine tolerogenic CD103+ DCs in the gut and for induction of Treg responses during immunological challenge. Taken together, these data point towards a key role for AMPK signaling in RA-driven development of tolerogenic DCs which may help with the rational design of new therapeutic approaches that target this signaling axis in DCs to control inflammatory responses.

Methods

Mice

Itgax-cre Prkaa1-fl/fl (AMPKα1), OVA-specific CD4+ T cell receptor transgenic mice (OT-II) and wild type (WT) mice, both male and female and all on a C57BL/6J background, were bred under SPF conditions at the Leiden University Medical Center (LUMC), Leiden, The Netherlands. Mice were culled through cervical dislocation. Anesthesia with ketamine with either dexdomitor or xylazine was used for *S. mansoni* infection. Animal experiments were performed when the mice were between 8-16 weeks old. Animal experiments were

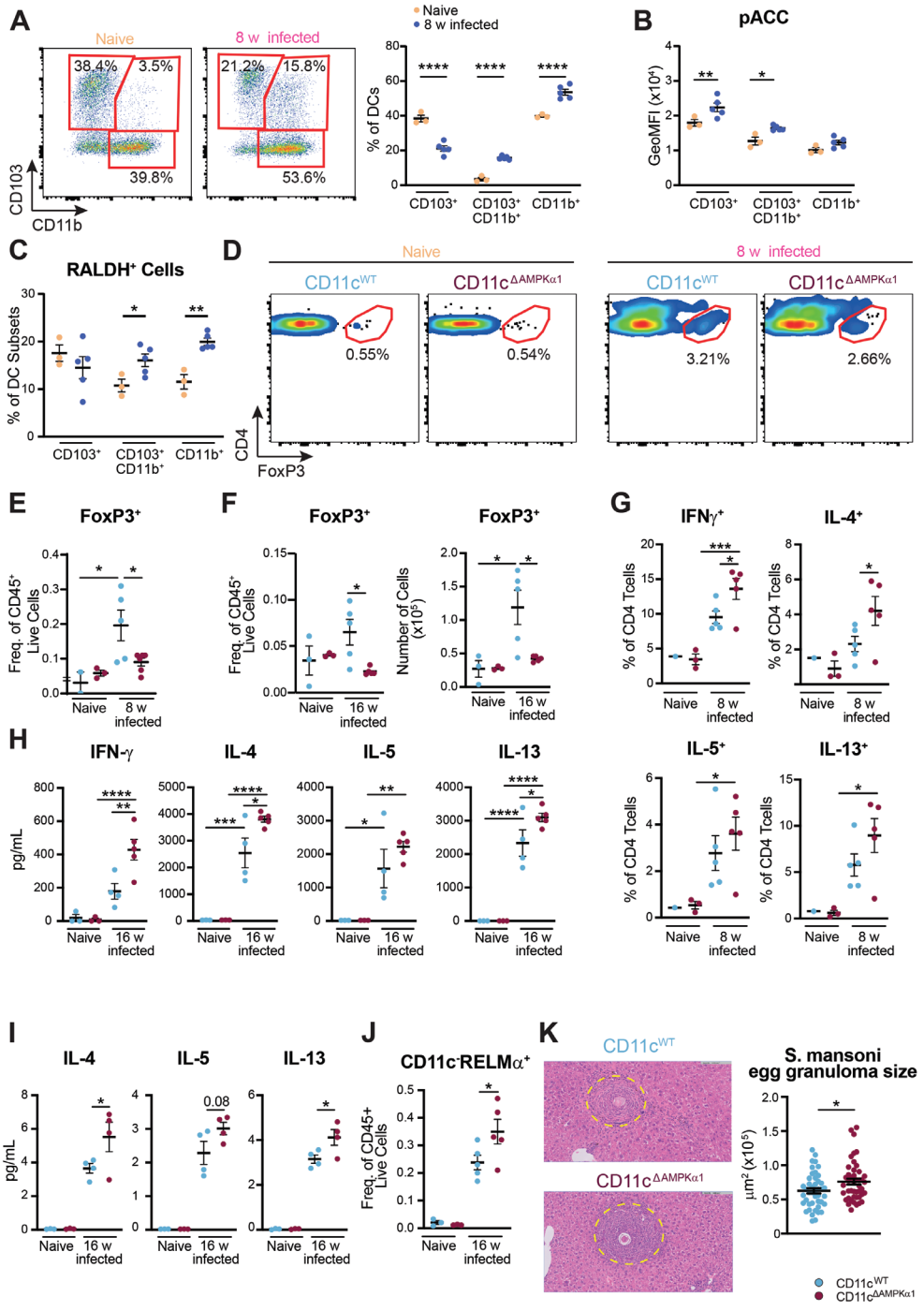
A
Naive
8 w infected
38.4%
3.5%
39.8%
21.2%
15.8%
53.6%
CD103
CD11b
Naive
8 w infected
% of DCs
****
****
****
CD103+
CD103+ CD11b+
CD11b+
B
pACC
GeoMFI (x10⁴)
**
*
CD103+
CD103+ CD11b+
CD11b+
C
RALDH+ Cells
% of DC Subsets
*
**
CD103+
CD103+ CD11b+
CD11b+
D
Naive
8 w infected
CD11cWT
CD11cΔAMPKα1
0.55%
0.54%
3.21%
2.66%
CD4
FoxP3
E
FoxP3+
Freq. of CD45+ Live Cells
Naive
8 w infected
F
FoxP3+
FoxP3+
Freq. of CD45+ Live Cells
Number of Cells (x10⁵)
Naive
16 w infected
G
IFNγ+
IL-4+
% of CD4 Tcells
Naive
8 w infected
H
IFN-γ
IL-4
IL-5
IL-13
pg/mL
Naive
16 w infected
IL-5+
IL-13+
% of CD4 Tcells
Naive
8 w infected
I
IL-4
IL-5
IL-13
pg/mL
0.08
Naive
16 w infected
J
CD11c-RELMα+
Freq. of CD45+ Live Cells
Naive
16 w infected
K
CD11cWT
CD11cΔAMPKα1
S. mansoni egg granuloma size
μm² (x10⁵)
CD11cWT
CD11cΔAMPKα1

Figure 6: AMPK signaling in CD11c-expressing cells is important for Treg induction and to keep the effector T cell and the granulomatous response in check during *S. mansoni* infection. Mice were infected with *S. mansoni* by percutaneous exposure to cercariae and immune cell responses were evaluated in livers and draining hepatic and mesenteric lymph nodes 8 or 16 weeks later. **(A)** Representative dot plot (left) and frequency of DCs (right) in the liver of naive (yellow) and 8 week-infected WT mice (blue). **(B)** GeoMFI of phosphorylation level of acetyl-coA carboxylase-Ser79 (pACC) and **(C)** frequency of retinaldehyde dehydrogenase (RALDH) positive hepatic DC subsets from naïve (yellow) and 8 week-infected WT mice (blue). **(D)** Representative dot plot staining of FoxP3+ Tregs in the liver of $CD11c^{WT}$ and $CD11c^{\Delta AMPK\alpha1}$ mice and FoxP3+ Tregs as frequency of CD4+ T cells. FoxP3+ Treg frequencies within CD45+ live cells in **(E)** 8 and **(F)** 16 week-infected mice or numbers **(F – right)** in 16 week-infected mice. **(G)** Draining hepatic lymph nodes cells from 8 week-infected mice were restimulated with PMA/Ionomycin in the presence of Brefeldin A and CD4 T cells were analyzed for production of indicated cytokines. **(H)** Draining hepatic and **(I)** mesenteric lymph nodes cells were stimulated with 10mg/mL of soluble egg antigen (SEA) and analyzed for production of indicated cytokines by cytometric bead assay (CBA). **(J)** Frequency of $CD11c^{-}RELMa^{+}$ macrophages in the liver of $CD11c^{WT}$ and $CD11c^{\Delta AMPK\alpha1}$ mice**. (K)** Representative H&E staining of liver sections (left) and quantification of size of individual egg granuloma (right) from 16 week-infected $CD11c^{W}T$ and CD11cΔAMPKα1 mice. Dashed line marks border of granuloma around the eggs. Bar, 50 μm. Data are from 1 experiment using 3-4 mice per group **(A-C)** or 3-5 mice per group **(D-K)**. Student's T-test **(K)** or Two-Way Anova with Sidák's post-test **(D-J)** were used to assess statistically significant differences. Mean ± SEM are indicated in the graph.; *p < 0.05, **p < 0.01, ***p < 0.001, ****p<0.0001.

performed in accordance with local government regulations, EU Directive 2010/63EU and Recommendation 2007/526/EC regarding the protection of animals used for experimental and other scientific purposes, as well as approved by the Dutch Central Authority for Scientific Procedures on Animals (CCD). Animal license number AVD116002015253.

Differentiation of monocyte-derived dendritic cells (moDCs)

moDCs were differentiated from monocytes that were isolated from buffy coats from healthy volunteers that donated blood to the national bloodbank Sanquin (Amsterdam, Netherlands) with informed consent. In brief, blood was diluted 1:2 in Hanks' Balanced Salt Solution (HBSS) and placed on 12 mL of Ficoll to obtain mononuclear cells. The solution was centrifuged at 600 x g for 30 minutes at 18 ° C, without braking. Subsequently, the formed mononuclear cell layer was removed, placed in a new tube containing HBSS, for further centrifugation at 1000 rpm for 20 min. The cells were washed 2 more times at 1000 rpm for 20 min and monocytes were isolated using CD14 MACS beads (Miltenyi) according to the manufacturer's recommendations, routinely resulting in a monocyte purity of >95%. Subsequently, $2x10^6$/well of monocytes were cultured in 6 well plate in RPMI medium supplemented with 10% FCS, 100 U/mL of penicillin, 100 μg/mL streptomycin, 2 mM of glutamine, 10 ng/mL human rGM-CSF (Invitrogen) and 0.86ng/mL of human rIL4 (R&D Systems) to differentiate them into moDCs. On day 2/3 of the differentiation process, media was refreshed, and the same concentration of cytokines was added to the cells. On day 5, immature DCs were either treated with 10^{-8} of VitD3 (VitD DCs), 1 μM of retinoic acid (RA DCs), 1 μM of dexamethasone (Dex DCs) or left untreated (mDCs). On day 6, immature DCs were stimulated with 100 ng/mL ultrapure LPS (E. coli 0111 B4 strain, InvivoGen, San Diego). In some experiments, at day 5, moDCs were treated with 10 μM RALDH inhibitor diethylaminobenzaldehyde (DEAB) (Stem Cell Technologies), 10 μM of PPARγ inhibitor (GW9662), 20 μM of PGC1α inhibitor (SR18292) or 1 μM of pan RAR inhibitor (AGN194310) for 30 minutes to 1 hour before treatment with RA.

Extracellular Flux Analysis

The metabolic characteristics of moDCs were analyzed using a Seahorse XFe96 Extracellular Flux Analyzer (Seahorse Bioscience). In brief, $5x10^4$ moDCs were plated in unbuffered, glucose-free RPMI supplemented with 5% FCS and left to rest 1 hour at 37 °C before the assay in an CO_2 free incubator. Subsequently extracellular acidification rate (ECAR) and oxygen consumption rate (OCR) were analyzed in response to glucose (10 mM; port A), oligomycin (1 μM; port B), fluoro-carbonyl cyanide phenylhydrazone (FCCP) (3 μM; port C), and rotenone/antimycin A (1/1 μM; port D) (all Sigma-Aldrich). In some experiments, LPS was added in port B after glucose injection.

RALDH Activity

RALDH activity assay was performed with Aldefluor kit (Stemcell Technologies) according to manufacturer's protocol. Briefly, cells were harvested, transferred to a V bottom 96 well plate, washed in PBS, stained with Fixable Aqua Dead Cell Stain Kit (Invitrogen) for 15 min at RT and then resuspended in 200 μL of assay buffer. 3 μL (end concentration of 45 μM) of RALDH inhibitor diethylaminobenzaldehyde (DEAB) was added to an empty well. Next, 1 μL (1.83 μM) of Aldefluor reagent was added to the well with the cells and immediately homogenized and transferred to the well containing DEAB. Samples were incubated for 30 min at 37° C and kept in assay buffer until the measurement in a BD FACS Canto. For the *in vivo* experiments, samples were stained with 146 nM of Aldefluor followed by staining with mix of antibodies diluted in assay buffer. Cells were kept in assay buffer until the measurement in a 5 laser Cytek Aurora.

Human T-cell culture and analysis of T-cell polarization

For analysis of T-cell polarization, moDCs were cultured with allogenic naive $CD4^+$ T cells for 7 days in the presence of staphylococcal enterotoxin B (10 pg/mL). On day 7, cells were harvested and transferred to a 24 well plate and cultured in the presence of rhuIL-2 (10 U/mL, R&D System) to expand the T cells. Two days later, 2x concentrated rhuIL-2 was added to the well and cells were divided into 2 wells. Then, 2/3 days later, intracellular cytokine production was analyzed after restimulation with 100 ng/mL phorbol myristate acetate (PMA) and 1μg/mL ionomycin (both Sigma) for a total 6h; 10 μg/mL brefeldin A (Sigma) was added during the last 4 h. Subsequently, the cells were stained with Fixable Aqua Dead Cell Stain Kit (Invitrogen) for 15 min at RT, fixed with 1.9% formaldehyde (Sigma-Aldrich), permeabilized with permeabilization buffer (eBioscience) and stained with anti-IL-4, anti-IL-13, anti-IL-10, anti-IL-17A, anti-IFN-γ for 20 min at 4 °C.

T-cell suppression assay

For analysis of suppression of proliferation of bystander T cells by test T cells, $5x10^4$ moDCs were cocultured with $5x10^5$ human naive $CD4^+$ T cells for 6 days. These T cells (test T cells) were harvested, washed, counted, stained with the cell cycle tracking dye 1 μM Cell Trace Violet (Thermo Fisher Scientific) and irradiated (3000 RAD) to prevent expansion. Bystander target T cells (responder T cells), which were allogeneic memory T cells from the same donor as the test T cells, were labeled with 0.5 μM cell tracking dye 5,6-carboxy fluorescein diacetate succinimidyl ester (CFSE). Subsequently, $5x10^4$ test T cells, $2.5x10^4$ responder T cells, and $1x10^3$ allogeneic LPS-stimulated DCs were cocultured for additional 6 days. Proliferation was

determined by flow cytometry, by co-staining with CD3, CD4 and CD25 APC. To some cultures, where indicated, 1 μM pan RAR (AGN194310), was added during the DC-T cell coculture.

Generation of bone marrow-derived GMDCs

BM cells were flushed from mouse femurs and tibia and plated in 'Nunc™ Cell-Culture Treated 6-well plate' wells (#140675, Thermo) at a seeding density of $2x10^6$ cells in a volume of 3 mL of complete RPMI (RPMI-1640 supplemented with GlutaMAX™ and 5% FCS, 25 nM β-mercaptoethanol, 100 U/mL penicillin and 100 μg/mL streptomycin) to which 20 ng/mL of recombinant GM-CSF (#315-03, PeproTech, Hamburg, Germany) was added. Cells were differentiated for 8 days with media refreshment on day 4. At day 6, GMDCs were either treated with 1 μM of RA (Sigma) or left untreated. At day 7, GMDCs were either left untreated or activated with 100 ng/mL of LPS (ultrapure, InvivoGen) and after 24 hours semi-adherent cells were harvested for various assays

***In vitro* murine T cell priming assay**

OT-II cells were negatively isolated with a $CD4^+$ T cell Isolation Kit (Miltenyi). $1x10^4$ GMDCs were settled in a round bottom 96-well plate, pulsed with 100 μg/mL of OVA (InvivoGen) in combination with LPS for 5 h, and washed before adding $1x10^5$ CTV-labeled OT-II cells in 200 μL of medium. After 4 days, cells were harvested and analyzed for proliferation by assessing CTV dilution. For cytokine production, cells were left for 6 days and then 100 μL of media was removed and replaced with 100 μL of media containing PMA/Ionomycin (both from Sigma) in the presence of Brefeldin A (Sigma) for 4 hours. Then, cells were stained with Fixable Aqua Dead Cell Stain Kit (Invitrogen) for 15 min at RT, fixed with FoxP3/Transcription Factor Staining Buffer Set (Invitrogen, for FoxP3 detection) for 1 hour at 4 °C, permeabilized with permeabilization buffer (eBioscience) and stained for anti-CD3, anti-CD4, anti-IFN-γ, anti-IL-10, anti-IL-17A, anti-FoxP3 and anti-CD25.

Flow cytometry

In general, single cell suspensions underwent viability staining for 20 minutes at room temperature (RT) using the LIVE/DEAD™ Fixable Aqua Dead Cell Stain Kit (#L34957, Thermo; 1:400 in PBS [from LUMC pharmacy; Braun, Zeist, The Netherlands) or LIVE/DEAD™ Fixable Blue Cells Stain Kit (#L34957, Thermo; 1:1000 in PBS) and fixation for 15 minutes at RT using 1.85% formaldehyde (F1635, Sigma) in PBS solution before surface staining with antibodies in PBS supplemented with 0.5% BSA [fraction V, #10735086001, Roche, Woerden, The Netherlands] and 2 mM EDTA) for 30 minutes at 4 °C. For detection of metabolic proteins cells were permeabilized with eBioscience permeabilization buffer (#00-8333-56 – Thermo) followed by intracellular staining with a cocktail of antibodies against the metabolic proteins. Antibodies were purchased from AbCam and conjugated in house with AbCam Lightening-Link Conjugation kit. See supplementary table 1 for further information on metabolic antibodies and fluorochrome conjugation. For polyclonal restimulation, single cell suspensions were stimulated with both 0.1 μg/mL of PMA (#P-8139, Sigma) and 1 μg/mL of ionomycin (#I-0634, Sigma) in the presence of 10 μg/mL BrefeldinA (all Sigma Aldrich) for 4 hrs. These single cell suspensions underwent intracellular cytokine staining (ICS) with antibodies in 1x eBioscience™ Permeabilization Buffer (ebioscience - # 00-8333-56).

For detection of phosphorylated ACC on Ser79, cells were pre stained with LIVE/DEAD™ Blue Dead Cell Stain Kit for 20 min at RT and, after washing, single cell suspension

was returned to a cell incubator (37°C & 5% CO2) for 1 hour in cRPMI and fixed with 4% ultra-pure formaldehyde (#18814-20, Polysciences, Hirschberg an der Bergstraße, Germany) for 15 minutes at RT. Single cell suspensions were first stained with anti-phosphorylated ACC in 1x Permeabilization Buffer (#00-8333-56, Thermo) for 1 hour at room before staining with cocktail antibodies in 1x Permeabilization Buffer for 30 minutes at 4°C.

High dimensional spectral flow cytometry analysis

Samples were imported in OMIQ software and parameters were scaled using a conversion factors ranging from 6000-20000. Samples were subsequently gated on live moDCs or $CD64^{-}$ $CD11c^{+}MHCII^{+}$ intestinal DCs and subsampled using a maximum equal distribution across groups. After sub-sampling, UMAP analysis was performed using the metabolic proteins (in case of moDCs) or lineage markers and activation markers (in case of intestinal DCs) as parameters. Next, phenograph clustering (k=100) was performed using the same parameters used for the UMAP. Data was further analyzed with EdgeR to determine significant differences in the clusters among different genotypes and heatmaps and volcano plots were generated in R, using OMIQ-exported data for each cluster.

Quantitative real-time PCR

RNA was extracted from snap-frozen moDCs. The isolation of mRNA was performed using Tripure method. Briefly, 500 µL of Tripure reagent (Sigma) and 1 µL of RNAse-free glycogen (Invitrogen) were added to the pellet of samples. Samples were then vortexed and incubated at RT for 5 min. After this step, 100 µL of RNAse-free chlorophorm was added and samples were inverted vigorously for 30 seconds. Samples were then centrifuged for 12000 x g for 15 min at 4 °C and the upper aqueous phase was transferred to a new RNAse-free 1.5 mL tube. Then, 250 µL of 2-isopropanol was added to each tube and after 5 min of incubation samples were centrifuged for 12000 x g for 15 min at 4 °C. Next, 500 µL of 75% ethanol was added, tubes were vortexed and centrifuged for 12000 x g for 15 min at 4 °C. As much as possible of ethanol was removed and 30 µL of RNAse-free milliQ water was added to the tubes that were incubated for 10 minutes at 55 °C. After this, RNA samples were quantified with NanoDrop (Invitrogen). cDNA was synthesized with reverse transcriptase kit (Promega) using the same amount of RNA for all the samples (settled by the sample with the lowest concentration of RNA). PCR amplification was performed by the SYBR Green method using CFX (Biorad). GAPDH mRNA levels was used as internal control. Specific primers for detected genes are listed in the supplementary Table 2. Relative expression was determined using the $2^{\Delta\Delta Ct}$ method.

Small interfering RNA (siRNA) electroporation

On day 4 of the DC culture, the cells were harvested and transfected with either 20 nM non-target control siRNA or 20 nM AMPKα1 (both Dharmacon) or FoxO3 (Invitrogen) siRNA using Neon Transfection System (Invitrogen) with the following setting: 1.600 V, 20 ms width, one pulse. Following electroporation, $1.2x10^{6}$ cells were seeded per well in to a 6-well plate containing RPMI media without antibiotics. After 24 h, culture medium (RPMI) supplemented with 10% FCS, rIL-4 (0.86 ng/mL, R&D system) and rGM-CSF (10 ng/mL, Invitrogen) was added. AMPKα1 and FoxO3 silencing efficiency was determined by qPCR and the transfection efficiency was greater than 90%.

Western blotting

A minimum of one million GMDCs or moDCs were washed twice with PBS before being lysed in 150 µL of EBSB buffer (8% [w/v] glycerol, 3% [w/v] SDS and 100 mM Tris–HCl [pH 6.8]). Lysates were immediately boiled for 5 min and their protein content was determined using a BCA kit. Ten µg of protein per lain was separated by SDS-PAGE followed by transfer to a PVDF membrane. Membranes were blocked for 1 h at room temperature in TTBS buffer (20 mM Tris–HCl [pH 7.6], 137 mM NaCl, and 0.25% [v/v] Tween 20) containing 5% (w/v) fat free milk and incubated overnight with primary antibodies. The primary antibodies used were AMPK (Cell Signaling #2532), pAMPK Ser79 (Cell Signaling #2535S), FoxO3 (Cell Signaling #2497S), pFoxO3 Ser413 (Cell Signaling #8174S), pFoxO3 Ser 253 (Cell Signaling #9466), HSP90 (Santa Cruz #sc7947) and beta-actin (Sigma #A5441). The membranes were then washed in TTBS buffer and incubated with horseradish peroxidase-conjugated secondary antibodies for 2 hours at RT. After washing, blots were developed using enhanced chemiluminescence.

Digestion of mouse tissues

Lymphoid organs were collected in 500 µL of no additives media (naRPMI = RPMI-1640 supplemented with GlutaMAX™ [#61870-010 or alternatively 61870036, Gibco, Bleiswijk, The Netherlands], in a plate and mechanically disrupted using the back-end of a syringe before addition of 50 µL of a digestion media (dRPMI = naRPMI supplemented with 11x collagenase D (#11088866001, Roche, Woerden, The Netherlands; end concentration of 1 mg/mL) and 11x DNase I (#D4263, Sigma, Zwijndrecht, The Netherlands; end concentration of 2000 U/mL) for 20 minutes at 37°C and 5% CO2. Single cell suspensions were filtered after digestion with a 100 µm sterile filter (#352360, BD Biosciences, Vianen, The Netherlands) before counting in complete RMPI (cRPMI = naRPMI supplemented with 10% heat-inactivated FCS [#S-FBS-EU-015, Serana, Pessin, Germany], 25 nM β-mercaptoethanol [#M6250, Sigma], 100 U/mL penicillin [#16128286, Eureco-pharma, Ridderkerk, The Netherlands; purchased inside the LUMC] and 100 µg/mL streptomycin [#S9137, Sigma]). Spleens were subjected to red blood cell lysis (inhouse; 0.15 M NH4Cl, 1 mM KHCO3, 0.1 mM EDTA [#15575-038, Thermo, Waltham, Massachusetts, United States] in ddH20) for 2 minutes at room temperature before counting.

Small intestine lamina propria isolation

Intestinal LP cells were isolated, as previously described(68). Briefly, intestine was collected, and fat tissues and payer's patch were manually removed. Small intestine was open longitudinally and feces and mucus were removed using PBS and tissues were cut in small pieces of approximately 2 cm and transfer to a 50 mL tube with HBSS no Ca^{2+} or Mg^{2+} (Gibco) supplemented with 10% FCS and 2 mM EDTA. The pieces of intestine were manually shook for 30 seconds, poured into a nitex nylon mesh, and washed again with plain 10 mL of HBSS no Ca^{2+} or Mg^{2+} (Gibco). Tissues were then transferred back to 50 mL tubes, now containing 10 mL of pre warmed HBSS no Ca^{2+} or Mg^{2+} (Gibco) + 2 mM EDTA and placed in an orbital shaker at 200 rpm for 20 min at 37 °C. This procedure was repeated three more times and after the third washing, guts were transferred to a new 50 mL tubes containing 1x digestion mix (RPMI GlutaMAX™ containing 2% FCS, 1mg/mL of Colagenase VIII [Sigma] and 40 u/mL of DNAse I [Sigma]) and incubated for 20 min at 37 °C sin an orbital shaker at 200 rpm. After digestion, 35 mL of PBS containing 2% FCS and 2 mM EDTA was added to the samples and

placed in a 100 µm cell strainer on top of a new 50 mL tube. Samples were centrifuged at 450 x g for 5 min, resuspended in 10 mL of PBS containing 2% FCS and 2 mM EDTA, place in a 40 µm cell strainer and centrifuged at 450 x g for 5 minutes.

***Schistosoma mansoni* acute and chronic infection**

Mice were infected with *S. mansoni* (Puerto Rican strain; Naval Medical Research Institute) by 30 minutes of percutaneous exposure to 35 cercariae on shaved abdomen. Mice were culled 8 weeks later. Cercariae were kept at 30 cercariae per mL of store bought Barleduc water, which was kept very carefully at 31 degrees Celsius. Female mice were anesthetized by intraperitoneal (i.p) injection with 300 µL of 50 mg/kg bodyweight ketamine + 0.5 mg/kg bodyweight dexdomitor, while male mice were anesthetized with 50 mg/kg bodyweight ketamine + 10 mg/kg bodyweight xylazine. Female mice were assisted in waking up by i.p. injection with 150 µL of 0.4 mg/kg bodyweight. All injections were done using PBS and a 25G needle. All anesthetics were purchased at the LUMC pharmacy. Livers were processed like spleens except that single cell suspensions were centrifuged twice at 20 g for 10 minutes in PBS to remove hepatocytes before red blood cell lysis.

House dust mite-induced allergic asthma model

Allergic airway inflammation was induced by sensitizing mice via intranasal administration of 1 µg HDM (Greer, London, United Kingdom) in 50 µL of PBS. One week later, these mice were challenged for 5 consecutive days via intranasal administration of 10 µg HDM in 50 µL of PBS. On day 15, bronchoalveolar lavage (BAL) fluid, lung, and lung draining mediastinal LNs (med LNs) were obtained to determine inflammatory cell recruitment. BAL was performed by instilling the lungs with 3 × 1mL aliquots of sterile PBS (Braun, Oss, The Netherlands). For single-cell suspensions of whole lung tissue, lungs were perfused with sterile PBS via the right ventricle to clear leukocytes and erythrocytes from the pulmonary circulation. Lung and medLN homogenization were performed as described above. Eosinophilia was assessed in BAL and lungs by flow cytometry as a readout for allergic inflammation.

Cytometric bead array

Cell culture supernatants were analyzed for IFN-γ, IL-4, IL-5, IL-10 and IL-13 secretion using a cytokine bead array (#I558296, #558298, #558302, #558300 and #558349 respectively and all BD Biosciences) on a flow cytometer as recommended by the manufacturer, but with both the beads and antibodies diluted 1:10 relative to the original recommendation.

Adenine nucleotides concentration

The intracellular concentration of adenosine mono, di or triphosphate (AMP, ADP, ATP, respectively) were evaluated as previously described (69). Briefly, cells were harvested, transferred to a 1.5 mL tube and washed in ice-cold PBS. After centrifugation cells were rinsed with 250 µl of perchloric acid/EDTA [10% (v/v) HClO4, 25 mM EDTA] and, vortexed and kept on ice for 30 minutes. Then, cell extracts were spun down at 8000 x g for 2 minutes at 4 °C and 200 µl of the supernatant fraction was transferred into a new 1.5mL tube (on ice), where cells lysate was neutralized by adjusting the pH to 6.5-7 with approximately 130 µl of KOH/-MOPS [2 N KOH/0.3 M 3-(N-morpholino)propanesulfonic acid (MOPS)]. Lysate was centrifuged at 8000 x g for 2 minutes at 4 °C and 200 µl of the neutralized fraction was transferred to a new 1.5 mL tube and stored in -80 °C until measurement of AMP, ADP and ATP at ultraviolet (UV)-

based high-performance liquid chromatography (HPLC - DIONEX UltiMate 3000, Thermo Scientific).

Statistical analysis

Results are expressed as mean ± standard error mean (SEM) except stated otherwise. Continuous variables were log-transformed for the analyses when the normality of the distribution was rejected by the Shapiro-Wilk W test and in case of a new normality test failure, the nonparametric alternative was used for the analysis. Differences between groups were analyzed by two-way ANOVA or Kruskall-Wallis (non-parametric analysis) with Tukey HSD or Sidak's multiple comparison post-test as described in figure legends. If there were only two groups, unpaired Student's t-test or Mann-Whitney test (non-parametric analysis) were used. p values < 0.05 were considered significant (*p < 0.05, **p < 0.01, ***p < 0.001) and statistical analyzes were performed using GraphPad Prism v.9.2.

Online supplemental material

Figure S1 shows the metabolic and phenotype characterization of tolerogenic human moDCs. Figure S2 shows the ECAR and OCR from Seahorse extracellular flux analysis of immunogenic and tolerogenic DCs after real-time LPS restimulation. Figure S3 shows the characterization of AMPKα1 deletion in both human and murine DCs and the metabolic characterization of Dex-DCs silenced for AMPKα1. Figure S4 shows the phenotypic characterization of RA-DCs silenced for either AMPKα1 or FoxO3 and the T cells priming capacity of both GMDCs treated with RALDH inhibitor (DEAB) and moDCs treated with either PPARγ (GW9662) or PGC1α (SR18292) inhibitors. Figure S5 shows the gating strategy to identify different murine DC subset sand macrophages within tissues. Figure S6 shows AMPK signaling in different DC subsets within tissues and the characterization of migratory DCs and regulatory T cells in the msLN of $CD11c^{WT}$ and of $CD11c^{\Delta AMPK\alpha1}$ mice. Figure S7 shows the characterization of lungs from $CD11c^{WT}$ and of $CD11c^{\Delta AMPK\alpha1}$ mice under steady state condition or after house dust mite challenge.

Acknowledgements

This work was supported by an LUMC fellowship and NWO ENW grant (OCENW.M.21.057) awarded to BE. The authors want to acknowledge the São Paulo Foundation Research for a fellowship awarded to TAP (# 2018/00719-9 and #2014/26437-9).

Author Contribution

TAP and BE designed the experiments, interpreted data. TAP, ECB, GH, LP, AZD, FO, AOF, AJvH and BG performed the experiments. JAMB helped in the discussion and reviewed the manuscript. BE conceived and supervised the study and wrote the manuscript together with TAP.

Declaration of Interests

The authors declare no competing interests.

References

1. Steinman RM, Witmer MD. Lymphoid dendritic cells are potent stimulators of the primary mixed leukocyte reaction in mice. PNAS. 1978;75(10):5132–6.
2. Zhao F, Xiao C, Evans KS, Theivanthiran T, DeVito N, Holtzhausen A, et al. Paracrine Wnt5a-β-Catenin Signaling Triggers a Metabolic Program that Drives Dendritic Cell Tolerization. Immunity. 2018;48(1):147-160.e7.
3. Steinman RM, Turley S, Mellman I, Inaba K. The induction of tolerance by dendritic cells that have captured apoptotic cells. Journal of Experimental Medicine. 2000;191(3):411–6.
4. Iliev ID, Spadoni I, Mileti E, Matteoli G, Sonzogni A, Sampietro GM, et al. Human intestinal epithelial cells promote the differentiation of tolerogenic dendritic cells. Gut. 2009;58(11):1481.
5. Iliev ID, Mileti E, Matteoli G, Chieppa M, Rescigno M. Intestinal epithelial cells promote colitis-protective regulatory T-cell differentiation through dendritic cell conditioning. Mucosal Immunol. 2009;2(4):340–50.
6. Bakdash G, Vogelpoel LTC, Capel TMM van, Kapsenberg ML, Jong EC de. Retinoic acid primes human dendritic cells to induce gut-homing, IL-10-producing regulatory T cells. Mucosal Immunology. 2015;8(2):265–78.
7. Maggi J, Schinnerling K, Pesce B, Hilkens CM, Catalán D, Aguillón JC. Dexamethasone and Monophosphoryl Lipid A-Modulated Dendritic Cells Promote Antigen-Specific Tolerogenic Properties on Naive and Memory CD4+ T Cells. Frontiers in immunology. 2016;7(8):1473–12.
8. Navarro-Barriuso J, Mansilla MJ, Naranjo-Gómez M, Sánchez-Pla A, Quirant-Sánchez B, Teniente-Serra A, et al. Comparative transcriptomic profile of tolerogenic dendritic cells differentiated with vitamin D3, dexamethasone and rapamycin. Scientific Reports. 2018;8(1):14985.
9. Jauregui-Amezaga A, Cabezón R, Ramírez-Morros A, España C, Rimola J, Bru C, et al. Intraperitoneal Administration of Autologous Tolerogenic Dendritic Cells for Refractory Crohn's Disease: A Phase I Study. Journal of Crohn's & colitis. 2015;9(12):1071–8.
10. Ferreira GB, Gysemans CA, Demengeot J, Cunha JPMCM da, Vanherwegen AS, Overbergh L, et al. 1,25-Dihydroxyvitamin D3 Promotes Tolerogenic Dendritic Cells with Functional Migratory Properties in NOD Mice. Journal of immunology. 2014;192(9):4210–20.
11. Ferreira GB, Vanherwegen AS, Eelen G, Gutiérrez ACF, Van Lommel L, Marchal K, et al. Vitamin D3 Induces Tolerance in Human Dendritic Cells by Activation of Intracellular Metabolic Pathways. Cell Reports. 2015;10(5):711–25.
12. Vanherwegen AS, Eelen G, Ferreira GB, Ghesquière B, Cook DP, Nikolic T, et al. Vitamin D controls the capacity of human dendritic cells to induce functional regulatory T cells by regulation of glucose metabolism. The Journal of steroid biochemistry and molecular biology. 2018;187:134–45.
13. Kaisar MMM, Pelgrom LR, Ham AJ van der, Yazdanbakhsh M, Everts B. Butyrate Conditions Human Dendritic Cells to Prime Type 1 Regulatory T Cells via both Histone Deacetylase Inhibition and G Protein-Coupled Receptor 109A Signaling. Frontiers in immunology. 2017;8:13–4
14. Lan YY, Wang Z, Raimondi G, Wu W, Colvin BL, Creus AD, et al. "Alternatively Activated" Dendritic Cells Preferentially Secrete IL-10, Expand Foxp3+CD4+ T Cells, and Induce Long-Term Organ Allograft Survival in Combination with CTLA4-Ig. Journal of immunology. 2006;177(9):5868–77.
15. Torres-Aguilar H, Sánchez-Torres C, Jara LJ, Blank M, Shoenfeld Y. IL-10/TGF-beta-treated dendritic cells, pulsed with insulin, specifically reduce the response to insulin of CD4+ effector/memory T cells from type 1 diabetic individuals. Journal of Clinical Immunology. 2010;30(5):659–68.
16. Rodrigues CP, Ferreira ACF, Pinho MP, Moraes CJ de, Bergami-Santos PC, Barbuto JAM. Tolerogenic IDO+ Dendritic Cells Are Induced by PD-1-Expressing Mast Cells. Frontiers in

immunology. 2016;7:111–7.

17. Holtzhausen A, Zhao F, Evans KS, Tsutsui M, Orabona C, Tyler DS, et al. Melanoma-Derived Wnt5a Promotes Local Dendritic-Cell Expression of IDO and Immunotolerance: Opportunities for Pharmacologic Enhancement of Immunotherapy. Cancer immunology research. 2015;3(9):1082–95.
18. Buck MD, O'Sullivan D, Pearce EL. T cell metabolism drives immunity. Journal of Experimental Medicine. 2015;212(9):1345–60.
19. Pearce EJ, Everts B. Dendritic cell metabolism. Nature Reviews Immunology. 2015;15(1):18–29.
20. Patente TA, Pelgrom LR, Everts B. Dendritic cells are what they eat: how their metabolism shapes T helper cell polarization. Curr Opin Immunol. 2019;58:16–23.
21. Everts B, Amiel E, Huang SCC, Smith AM, Chang CH, Lam WY, et al. TLR-driven early glycolytic reprogramming via the kinases TBK1-IKKε supports the anabolic demands of dendritic cell activation. Nature immunology. 2014;15(4):323–32.
22. Everts B, Amiel E, Windt GJW van der, Freitas TC, Chott R, Yarasheski KE, et al. Commitment to glycolysis sustains survival of NO-producing inflammatory dendritic cells. Blood. 2012;120(7):1422–31.
23. Guak H, Habyan SA, Ma EH, Aldossary H, Al-Masri M, Won SY, et al. Glycolytic metabolism is essential for CCR7 oligomerization and dendritic cell migration. Nature communications. 2018;9(1):1–12.
24. Malinarich F, Duan K, Hamid RA, Bijin A, Lin WX, Poidinger M, et al. High mitochondrial respiration and glycolytic capacity represent a metabolic phenotype of human tolerogenic dendritic cells. The Journal of Immunology. 2015;194(11):5174–86.
25. Fischer R, Turnquist HR, Taner T, Thomson AW. Use of rapamycin in the induction of tolerogenic dendritic cells. Handbook of experimental pharmacology. 2009;188(188):215–32.
26. González A, Hall MN, Lin SC, Hardie DG. AMPK and TOR: The Yin and Yang of Cellular Nutrient Sensing and Growth Control. Cell Metab. 2020;31(3):472–92.
27. Steinberg GR, Hardie DG. New insights into activation and function of the AMPK. Nat Rev Mol Cell Bio. 2022;1–18.
28. Nieves W, Hung LY, Oniskey TK, Boon L, Foretz M, Viollet B, et al. Myeloid-Restricted AMPKα1 Promotes Host Immunity and Protects against IL-12/23p40–Dependent Lung Injury during Hookworm Infection. Journal of immunology. 2016;196(11):4632–40.
29. Carroll KC, Viollet B, Suttles J. AMPKα1 deficiency amplifies proinflammatory myeloid APC activity and CD40 signaling. J Leukocyte Biol. 2013;94(6):1113–21.
30. Ferreira GB, Overbergh L, Verstuyf A, Mathieu C. 1α,25-Dihydroxyvitamin D3 and its analogs as modulators of human dendritic cells: A comparison dose-titration study. J Steroid Biochem Mol Biology. 2013;136:160–5.
31. Does AM, Kenne E, Koppelaar E, Agerberth B, Lindbom L. Vitamin D3 and phenylbutyrate promote development of a human dendritic cell subset displaying enhanced antimicrobial properties. J Leukocyte Biol. 2014;95(6):883–91.
32. Unger WWJ, Laban S, Kleijwegt FS, Slik AR van der, Roep BO. Induction of Treg by monocyte-derived DC modulated by vitamin D3 or dexamethasone: Differential role for PD-L1. Eur J Immunol. 2009;39(11):3147–59.
33. Penna G, Roncari A, Amuchastegui S, Daniel KC, Berti E, Colonna M, et al. Expression of the inhibitory receptor ILT3 on dendritic cells is dispensable for induction of CD4+Foxp3+ regulatory T cells by 1,25-dihydroxyvitamin D3. Blood. 2005;106(10):3490–7.
34. Manavalan JS, Rossi PC, Vlad G, Piazza F, Yarilina A, Cortesini R, et al. High expression of ILT3 and ILT4 is a general feature of tolerogenic dendritic cells. Transpl Immunol. 2003;11(3–4):245–58.
35. Chang CC, Liu Z, Vlad G, Qin H, Qiao X, Mancini DM, et al. Ig-Like Transcript 3 Regulates

Expression of Proinflammatory Cytokines and Migration of Activated T Cells. J Immunol. 2009;182(9):5208–16.

36. Heieis GA, Patente TA, Tak T, Almeida L, Everts B. Spectral flow cytometry reveals metabolic heterogeneity in tissue macrophages. Biorxiv. 2022;2022.05.26.493548.

37. Pelgrom LR, Patente TA, Otto F, Nouwen LV, Ozir-Fazalalikhan A, Ham AJ van der, et al. mTORC1 signaling in antigen-presenting cells of the skin restrains CD8+ T cell priming. Cell Reports. 2022;40(1):111032.

38. Nurbaeva MK, Schmid E, Szteyn K, Yang W, Viollet B, Shumilina E, et al. Enhanced Ca2+ entry and Na+/Ca2+ exchanger activity in dendritic cells from AMP-activated protein kinase-deficient mice. Faseb J. 2012;26(7):3049–58.

39. Feng T, Cong Y, Qin H, Benveniste EN, Elson CO. Generation of Mucosal Dendritic Cells from Bone Marrow Reveals a Critical Role of Retinoic Acid. Journal of immunology. 2010;185(10):5915–25.

40. Jäger S, Handschin C, St.-Pierre J, Spiegelman BM. AMP-activated protein kinase (AMPK) action in skeletal muscle via direct phosphorylation of PGC-1α. Proc National Acad Sci. 2007;104(29):12017–22.

41. Liang H, Ward WF. PGC-1α: a key regulator of energy metabolism. Adv Physiol Educ. 2006;30(4):145–51.

42. Jin J, Jung IH, Moon SH, Jeon S, Jeong SJ, Sonn SK, et al. CD137 Signaling Regulates Acute Colitis via RALDH2-Expressing CD11b-CD103+ DCs. Cell reports. 2020;30(12):4124-4136.e5.

43. Fasano C, Disciglio V, Bertora S, Signorile ML, Simone C. FOXO3a from the Nucleus to the Mitochondria: A Round Trip in Cellular Stress Response. Cells. 2019;8(9):1110.

44. Greer EL, Oskoui PR, Banko MR, Maniar JM, Gygi MP, Gygi SP, et al. The Energy Sensor AMP-activated Protein Kinase Directly Regulates the Mammalian FOXO3 Transcription Factor. The Journal of biological chemistry. 2007;282(41):30107–19.

45. Guilliams M, Crozat K, Henri S, Tamoutounour S, Grenot P, Devilard E, et al. Skin-draining lymph nodes contain dermis-derived CD103− dendritic cells that constitutively produce retinoic acid and induce Foxp3+ regulatory T cells. Blood. 2010;115(10):1958–68.

46. Ruane D, Brane L, Reis BS, Cheong C, Poles J, Do Y, et al. Lung dendritic cells induce migration of protective T cells to the gastrointestinal tract. J Exp Med. 2013;210(9):1871–88.

47. Mucida D, Park Y, Kim G, Turovskaya O, Scott I, Kronenberg M, et al. Reciprocal TH17 and Regulatory T Cell Differentiation Mediated by Retinoic Acid. Science. 2007;317(5835):256–60.

48. Coombes JL, Siddiqui KRR, Arancibia-Cárcamo CV, Hall J, Sun CM, Belkaid Y, et al. A functionally specialized population of mucosal CD103+ DCs induces Foxp3+ regulatory T cells via a TGF-beta and retinoic acid-dependent mechanism. Journal of Experimental Medicine. 2007;204(8):1757–64.

49. Esterházy D, Canesso MCC, Mesin L, Muller PA, Castro TBR de, Lockhart A, et al. Compartmentalized gut lymph node drainage dictates adaptive immune responses. Nature. 2019;569(7754):126–30.

50. Herzig S, Shaw RJ. AMPK: guardian of metabolism and mitochondrial homeostasis. Nature reviews Molecular cell biology. 2017;19(2):1–15.

51. Garcia D, Shaw RJ. AMPK: Mechanisms of Cellular Energy Sensing and Restoration of Metabolic Balance. Molecular Cell. 2017;66(6):789–800.

52. Adamik J, Munson PV, Hartmann FJ, Combes AJ, Pierre P, Krummel MF, et al. Distinct metabolic states guide maturation of inflammatory and tolerogenic dendritic cells. Nat Commun. 2022;13(1):5184.

53. Ferreira GB, Kleijwegt FS, Waelkens E, Lage K, Nikolic T, Hansen DA, et al. Differential protein pathways in 1,25-dihydroxyvitamin d(3) and dexamethasone modulated tolerogenic human dendritic cells. Journal of proteome research. 2012;11(2):941–71.

54. Guo Y, Zhang H, Chen X, Liu Y. All-trans retinoic acid reduces mammalian target of rapamycin

via a Sirtuin1-dependent mechanism in neurons. Neuroreport. 2021;32(12):975–82.

55. Davila D, Connolly NMC, Bonner H, aacute PW, Dussmann H, Concannon CG, et al. Two-step activation of FOXO3 by AMPK generates a coherent feed-forward loop determining excitotoxic cell fate. Cell Death & Differentiation. 2019;19(10):1–12.

56. Zhang J, Deng B, Jiang X, Cai M, Liu N, Zhang S, et al. All-Trans-Retinoic Acid Suppresses Neointimal Hyperplasia and Inhibits Vascular Smooth Muscle Cell Proliferation and Migration via Activation of AMPK Signaling Pathway. Frontiers in pharmacology. 2019;10:485.

57. Elamin EE, Masclee AA, Dekker J, Pieters HJ, Jonkers DM. Short-Chain Fatty Acids Activate AMP-Activated Protein Kinase and Ameliorate Ethanol-Induced Intestinal Barrier Dysfunction in Caco-2 Cell Monolayers. J Nutrition. 2013;143(12):1872–81.

58. Kawaguchi T, Osatomi K, Yamashita H, Kabashima T, Uyeda K. Mechanism for Fatty Acid "Sparing" Effect on Glucose-induced Transcription. Regulation of carbohydrate-responsive element-binding protein by AMP-activated protein kinase. J Biol Chem. 2002;277(6):3829–35.

59. Sakakibara S, Yamauchi T, Oshima Y, Tsukamoto Y, Kadowaki T. Acetic acid activates hepatic AMPK and reduces hyperglycemia in diabetic KK-A(y) mice. Biochem Bioph Res Co. 2006;344(2):597–604.

60. Molenaar R, Knippenberg M, Goverse G, Olivier BJ, Vos AF de, O'Toole T, et al. Expression of Retinaldehyde Dehydrogenase Enzymes in Mucosal Dendritic Cells and Gut-Draining Lymph Node Stromal Cells Is Controlled by Dietary Vitamin A. J Immunol. 2011;186(4):1934–42.

61. Esterházy D, Loschko J, London M, Jove V, Oliveira TY, Mucida D. Classical dendritic cells are required for dietary antigen-mediated induction of peripheral Treg cells and tolerance. Nature immunology. 2016;17(5):545–55.

62. Denning TL, Norris BA, Medina-Contreras O, Manicassamy S, Geem D, Madan R, et al. Functional Specializations of Intestinal Dendritic Cell and Macrophage Subsets That Control Th17 and Regulatory T Cell Responses Are Dependent on the T Cell/APC Ratio, Source of Mouse Strain, and Regional Localization. J Immunol. 2011;187(2):733–47.

63. Lyu M, Suzuki H, Kang L, Gaspal F, Zhou W, Goc J, et al. ILC3s select microbiota-specific regulatory T cells to establish tolerance in the gut. Nature. 2022;610(7933):744–51.

64. Kedmi R, Najar TA, Mesa KR, Grayson A, Kroehling L, Hao Y, et al. A RORγt+ cell instructs gut microbiota-specific Treg cell differentiation. Nature. 2022;610(7933):737–43.

65. Akagbosu B, Tayyebi Z, Shibu G, Iza YAP, Deep D, Parisotto YF, et al. Novel antigen presenting cell imparts Treg-dependent tolerance to gut microbiota. Nature. 2022;1–3.

66. Turner JD, Jenkins GR, Hogg KG, Aynsley SA, Paveley RA, Cook PC, et al. CD4+CD25+ Regulatory Cells Contribute to the Regulation of Colonic Th2 Granulomatous Pathology Caused by Schistosome Infection. Plos Neglect Trop D. 2011;5(8):e1269.

67. Lee Y, Jeong W. Retinoic acids and hepatic stellate cells in liver disease. J Gastroen Hepatol. 2012;27:75–9.

68. Scott CL, Wright PB, Milling SWF, Mowat AM. Dendritic Cell Protocols - Isolation and Identification of Conventional Dendritic Cell Subsets from the Intestine of Mice and Men. Methods Mol Biology. 2016;1423:101–18.

69. García-Tardón N, Guigas B. AMPK, Methods and Protocols. Methods Mol Biology. 2018;1732:229–37.

Supplementary information

Table 1: Antibody list

Antibodies	Source	Identifier
Anti-mouse CD11b (Clone M1/70)	Invitrogen/eBioscience	25-0112-82
Anti-mouse CD11c (Clone N418)	BioLegend	117330
Anti-mouse CD172a (Clone P84)	BioLegend	144011
Anti-mouse CD103 (Clone 2E7)	BD Biosciences	750718
Anti-mouse CD103 (Clone 2E7)	Invitrogen/eBioscience	13-1031-85
Anti-mouse CD3 (Clone 17A2)	Invitrogen/eBioscience	11-0032-82
Anti-mouse B220 (Clone RA3-6B2)	BioLegend	103248
Anti-mouse B220 (Clone RA3-6B2)	BD Bioscience	553091
Anti-mouse CD3 (Clone 17A2)	Invitrogen/eBioscience	48-0032-82
Anti-mouse CD3 (Clone 17A2)	BioLegend	100237
Anti-mouse CD4 (Clone GK1.5)	Invitrogen/eBioscience	25-0041-81
Anti-mouse CD4 (Clone GK1.5)	Invitrogen/eBioscience	46-0041-82
Anti-mouse CD4 (Clone GK1.5)	BD Biosciences	563232
Anti-mouse CD8a (Clone 53-6.7)	Tonbo Biosciences	20-0081-U025
Anti-mouse CD8a (Clone 53-6.7)	BioLegend	100714
Anti-mouse CD25 (Clone PC61.5)	BD Bioscience	551071
Anti-mouse CD25 (Clone PC61.5)	BioLegend	102010
Anti-mouse CD40 (Clone HM40-3)	Invitrogen/eBioscience	11-0402-82
Anti-mouse CD44 (Clone IM7)	Invitrogen/eBioscience	48-0441-82
Anti-mouse CD44 (Clone IM7)	Invitrogen/eBioscience	25-0441-81
Anti-mouse CD45 (Clone 30-F11)	BD Bioscience	748370
Anti-mouse CD45 (Clone 30-F11)	BD Bioscience	564225
Anti-mouse CD45 (Clone 30-F11)	BioLegend	103173
Anti-mouse CD62L (Clone MEL-14)	Invitrogen/eBioscience	47-0621-82
Anti-mouse CD8a (Clone 53-6.7)	BioLegend	100747
Anti-mouse CD64 (Clone X54-5/7.1)	BioLegend	139304
Anti-mouse CD64 (Clone X54-5/7.1)	BioLegend	139320
Anti-mouse CD80 (Clone 16-10A1)	BioLegend	104714
Anti-mouse CD86 (Clone GL-1)	BD Bioscience	560581
Anti-mouse CD152 (CTLA-4) (Clone UC10-4B9)	BD Bioscience	12-1522-82
Anti-mouse CD152 (CTLA-4) (Clone UC10-4B9)	BioLegend	106312
Anti-mouse CD197 (CCR7) (Clone 4B12)	BioLegend	120125

Anti-mouse CD274 (PD-L1) (Clone 10F.9G2)	BioLegend	124319
Anti-mouse CD357 (GITR) (Clone YGITR 765)	BioLegend	120222
Goat anti-rabbit (Clone NA)	Invitrogen	A27040
Anti-mouse FoxP3 (Clone FJK-16s)	Invitrogen/eBioscience	12-5773-82
Anti-mouse FoxP3 (Clone FJK-16s)	Invitrogen/eBioscience	17-577382
Anti-mouse Helios (Clone 22F6)	BioLegend	137213
Anti-mouse RORgt (Clone Q31-378)	BD Bioscience	562607
Anti-mouse IFNγ (Clone XMG1.2)	Invitrogen/eBioscience	25-7311-82
Anti-mouse IFNγ (Clone XMG1.2)	Invitrogen/eBioscience	11-7311-41
Anti-mouse IL-10 (Clone JES5-16E3)	Invitrogen/eBioscience	12-7101-82
Anti-mouse IL-12p40/p70 (Clone C15.6)	Invitrogen/eBioscience	554480
Anti-mouse IL-17A (Clone eBio17B7)	Invitrogen/eBioscience	45-7177-80
Anti-mouse IL-4 (Clone 11B11)	Invitrogen/eBioscience	17-7041-82
Anti-mouse TNF-a (Clone MP6-XT22)	BioLegend	506324
Anti-mouse F4/80 (Clone BM8)	Invitrogen/eBioscience	47-4801-82
Anti-mouse MERTK (Clone 2B10C42)	BioLegend	151507
Anti-mouse MHCII (Clone M5/114.15.2)	Invitrogen/eBioscience	56-5321-80
Anti-mouse MHCII (Clone M5/114.15.2)	Invitrogen/eBioscience	47-5321-82
Anti-mouse MHC II (Clone 2G9)	BD Bioscience	743876
Anti-mouse Siglec-H (Clone 511)	BioLegend	129611
Anti-mouse LAP (Clone Tw7-16B4)	Invitrogen/eBioscience	46-9821-82
Anti-mouse Ly6C (Clone HK1.4)	BioLegend	128025
Anti-mouse Ly6C (Clone HK1.4)	Invitrogen/eBioscience	45-5932-80
Anti-mouse Ly6G (Clone 1A8)	BioLegend	108467
Anti-mouse CX3CR1 (Clone SA011F11)	BioLegend	149025
Anti-mouse Siglec-F (Clone E50-2440)	BD Biosciences	740388
Anti-mouse Siglec-H (Clone 440c)	BD Biosciences	747675
Streptavidin (Clone NA)	BioLegend	405214
Streptavidin (Clone NA)	BioLegend	405249
Anti-mouse XCR1 (Clone ZET)	BioLegend	148220
Anti-human CD1a (Clone HI149)	BD Biosciences	555806
Anti-human CD1a (Clone HI149)	BioLegend	300127
Anti-human CD3 (Clone UCHT1)	Invitrogen/eBioscience	47-0038-42
Anti-human CD4 (Clone SK3)	Invitrogen/eBioscience	46-0047-42
Anti-human CD14 (Clone MΦP9)	BD Biosciences	345786
Anti-human CD25 (Clone M-A251)	BD Biosciences	562442
Anti-human CD40 (Clone 5C3)	BD Biosciences	555591

Anti-human CD40 (Clone 5C3)	BioLegend	334338
Anti-human CD80 (Clone L307,4)	BD Biosciences	560442
Anti-human CD83 (Clone HB15e)	Invitrogen/eBioscience	12-0839-42
Anti-human CD85k (ILT3) (Clone ZM4.1)	BioLegend	333015
Anti-human CD86 (Clone 2331 (FUN-1))	BD Biosciences	561128
Anti-human CD86 (Clone 2331 (FUN-1))	BD Biosciences	555657
Anti-human CD103 (Clone Ber-ACT8)	BioLegend	350211
Anti-human CD127 (Clone eBioRDR5)	Invitrogen/eBioscience	47-1278-42
Anti-human CD152 (CTLA-4) (Clone BNI3)	BD Biosciences	555853
Anti-human HLA-DR (Clone LN3)	Invitrogen/eBioscience	47-9956-42
Anti-human INF-g (Clone B27)	BD Biosciences	560371
Anti-human IL-4 (Clone 8D4-8)	eBioscience	25-7049-82
Anti-human IL-10 (Clone JES3-19F1)	BD Biosciences	554707
Anti-human IL-13 (Clone JES10-5A2)	BioLegend	501903
Anti-human IL-17a (Clone BL168)	BioLegend	512304
Anti-human LAP (Clone TW4-2F8)	BioLegend	349611
Anti-human FoxP3 (Clone PCH101)	Invitrogen/eBioscience	17-4776-41

Table 2: Primers used for quantitative PCR

Gene	Forward 5' – 3'	Reverse 3' – 5'
β2-microglobulin	GCCTGCCGTGTGAACCAT	TTACATGTCTCGATCCCACTTAACTAT
GAPDH	CAGCCTCAAGATCATCAGCA	TGTGGTCATGAGTCCTTCCAA
AMPKα1	TCGGCAAAGTGAAGGTTGGCA	TCCTACCACACTCAAGGCTCCGAA
PPARγ	CTCATATCCGAGGGCCAA	TGCCAAGTCGCTGTCATC
PGC1α	ACTGCAGGCCTAACTCCACCCA	ACTCGGATTGCTCCGGCCCT

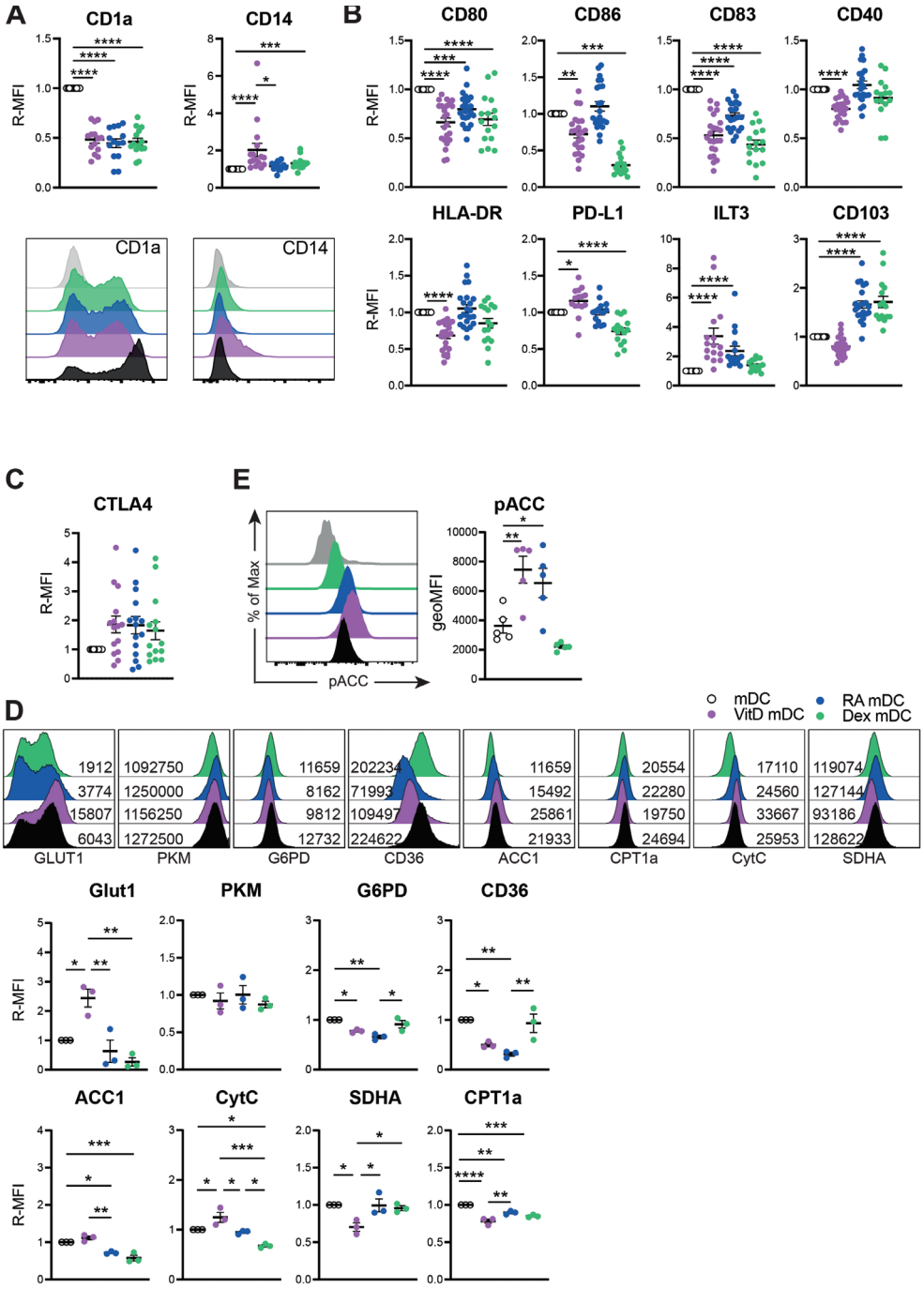

Legend on next page

Figure S1: Metabolic and phenotype characterization of tolerogenic human monocyte-derived DCs. Monocytes were isolated from PBMC with $CD14^+$ magnetic beads and differentiated in moDCs in the presence of GM-CSF + IL-4. On day 5 cells were treated with either VitD3, RA or Dex. On the 6^{th} day, 100 ng/mL of LPS were added and 24 hours later cells were harvested for functional assays. **(A)** quantification and representative histograms of the geometric mean fluorescence intensity (R-MFI) of CD1a (top left and bottom left) and CD14 (top right and bottom right) of tolDCs measured by flow cytometry and normalized by mDC (set as 1). **(B)** Quantification of the relative geometric mean fluorescence (R-MFI) of CD80, CD86, CD83, CD40, HLA-DR, PD-L1, ILT3 and CD103 normalized by mDC set as 1 (data used to generate heatmap in Figure 1A) in tolDCs. **(C)** tolDCs were co-cultured with allogeneic naïve T cells and intracellularly stained for CTLA-4. **(E)** Monocytes were isolated from PBMC with $CD14^+$ magnetic beads and differentiated in moDCs in the presence of GM-CSF + IL-4 and either VitD3, RA or Dex. On the 6^{th} day, 100 ng/mL of LPS were added and 24 hours later cells were harvested for analysis. Representative histogram staining (left) and quantification levels (right) of Ser79 phosphorylation in acetyl coA carboxylase (pACC). **(D)** Representative histograms for the intracellular staining of metabolic proteins (related to Figure 1H). Data are pooled from 15-22 donors **(A-C)**, 5 donors **(E)**, or 3 donors **(H)**. Statistics are One-Way Anova with Tukey HSD post-test. Data shown as mean ± SEM; *$p < 0.05$, **$p < 0.01$, ***$p < 0.001$, ****$p<0.0001$.

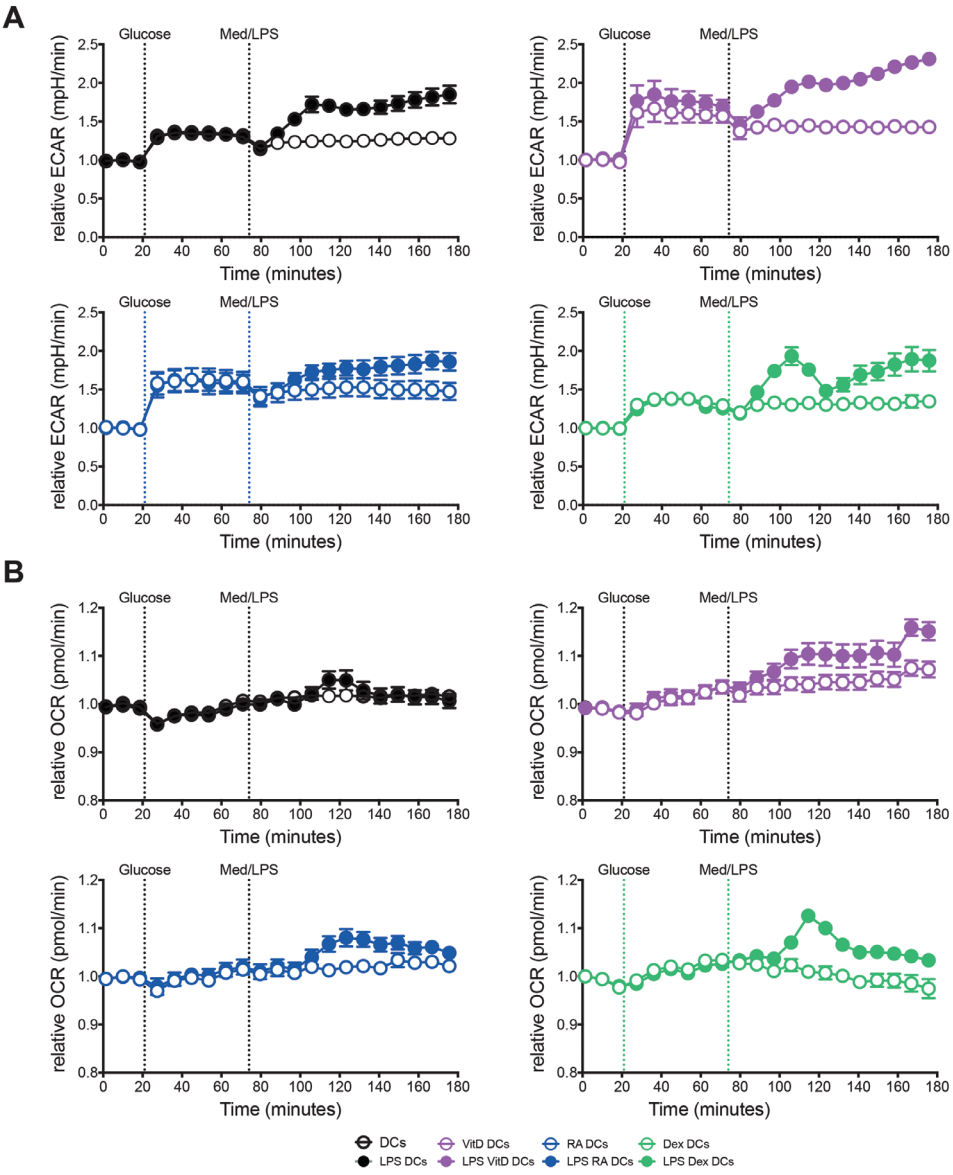

Figure S2: Tolerogenic DCs display increased ECAR and OXPHOS after LPS stimulation.
(A) Seahorse extracellular flux analysis. Real-time extracellular acidification rate (ECAR) of mDC (top left), VitD3-DCs (top right), RA-DCs (bottom left) and Dex-DCs (bottom right) after sequential injection of glucose and either media or LPS. **(B)** Seahorse extracellular flux analysis. Real-oxygen consumption rate (OCR) of mDC (top left), VitD3-DCs (top right), RA-DCs (bottom left) and Dex-DCs (bottom right) after sequential injection of glucose and either media or LPS. Data are pool of 3 donors.

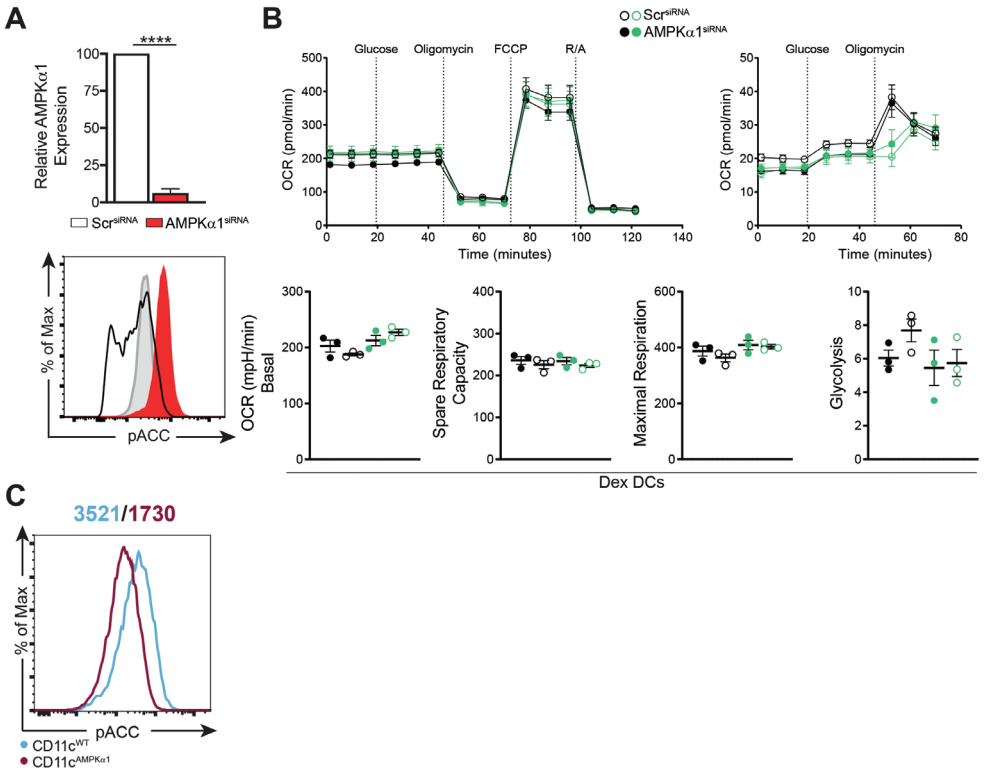

Figure S3: Dex-DCs display few metabolic alteration which are independent of AMPK signaling. **(A-B)** Monocytes were isolated from PBMC with CD14^{+} magnetic beads and differentiated in moDCs in the presence of GM-CSF + IL-4. On day 4 cells were transfected with small interference RNA (siRNA) against AMPKα1 and 24 hours later cells were treated with either RA or left untreated. On the 6th day, 100 ng/mL of LPS were added and 24 hours later cells were harvested. **(A)** Expression levels of AMPKα1 in moDCs silenced with scramble (white) or siRNA targeting AMPKα1 (red). **(B)** Seahorse extracellular flux analysis. Real-time oxygen consumption rate (OCR) (upper left) and extracellular acidification rate (ECAR) (upper right) in Dex-DCs. Basak OCR (bottom far right), spare respiratory capacity (SRC) (bottom right), maximal respiration (bottom left) and glycolysis (bottom far left) were quantified and are displayed. **(C)** Representative histogram staining of Ser79 phosphorylation in acetyl coA carboxylase (pACC) in GM-CSF-induced bone-marrow DCs (GMDCs). Data are pool of 4 donors **(A)** and representative of 1 out 4 **(B)** or 3 **(C)** independent experiments.

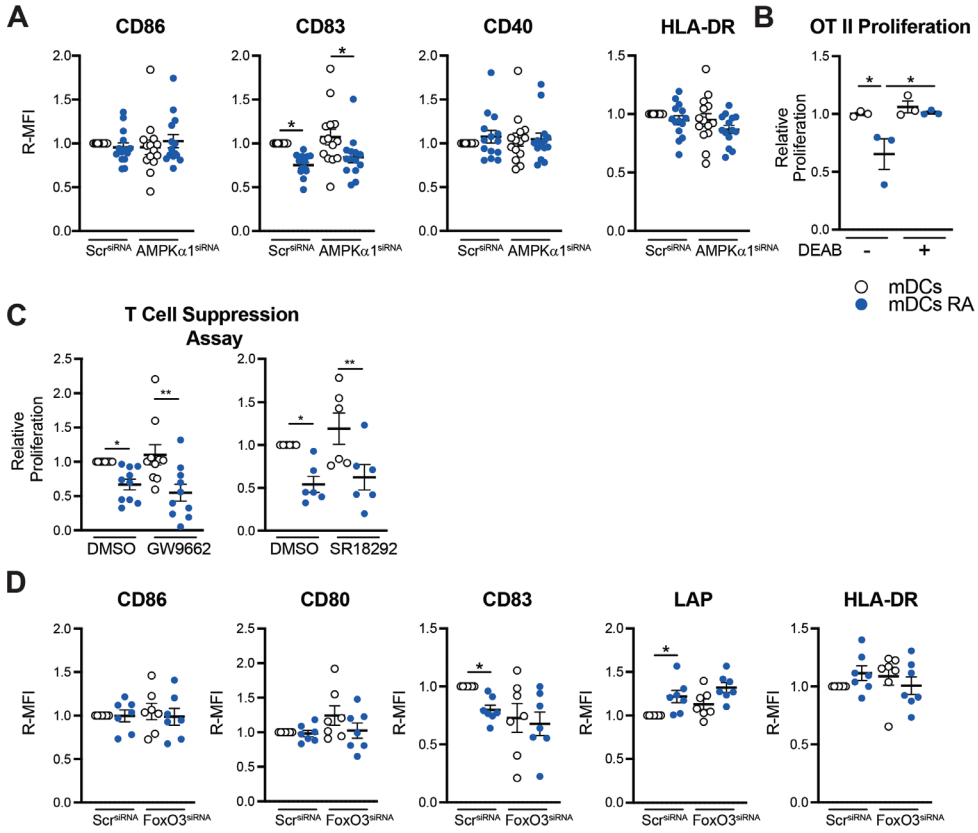

Figure S4: Phenotypic characterization of RA-DCs silenced for either AMPK or FoxO3.
Monocytes were isolated from PBMC with CD14⁺ magnetic beads and differentiated in moDCs in the presence of GM-CSF + IL-4. On day 4 cells were transfected with small interference RNA (siRNA) against AMPKα1 **(A)** or FoxO3 **(D)** and 24 hours later cells were treated with either RA or left untreated. On the 6th day, 100 ng/mL of LPS were added and 24 hours later cells were harvested. **(A)** Quantification of the relative geometric mean fluorescence (R-MFI) of CD86, CD83, CD40 and HLA-DR normalized by mDC set as 1 in RA-DCs silenced for AMPKα1. **(B)** GM-CSF-induced bone-marrow DCs (GMDCs) pre-treated with RALDH inhibitor N,N-diethylaminobenzaldehyde (DEAB) 30 minutes prior to RA treatment. 48 hours later, GMDCs were co-cultured with CTV-labelled OT-II T cells and proliferation was evaluated by flowcytometry. **(C)** moDCs were pre-treated with either DMSO, PPARγ (GW9662) or PGC1α (SR18292) inhibitors for 30 minutes prior to RA treatment and T cell suppression assay was performed by co culturing irradiated primed naïve T cells with CFSE-labelled memory T cells from the same donor. On the 6th day CFSE dilution was measured by flow cytometry. **(D)** Quantification of the relative geometric mean fluorescence (R-MFI) of CD86, CD80, CD83, LAP, and HLA-DR normalized by mDC set as 1 in RA-DCs silenced for FoxO3. Data are pooled from 7-13 donors **(A;C-D)** or 3 independent experiment with 1 mouse each **(E)**. Statistics are Two-Way Anova with Sidák's post-test. Data shown as mean ± SEM; *p < 0.05, **p < 0.01, ***p < 0.001, ****p<0.0001.

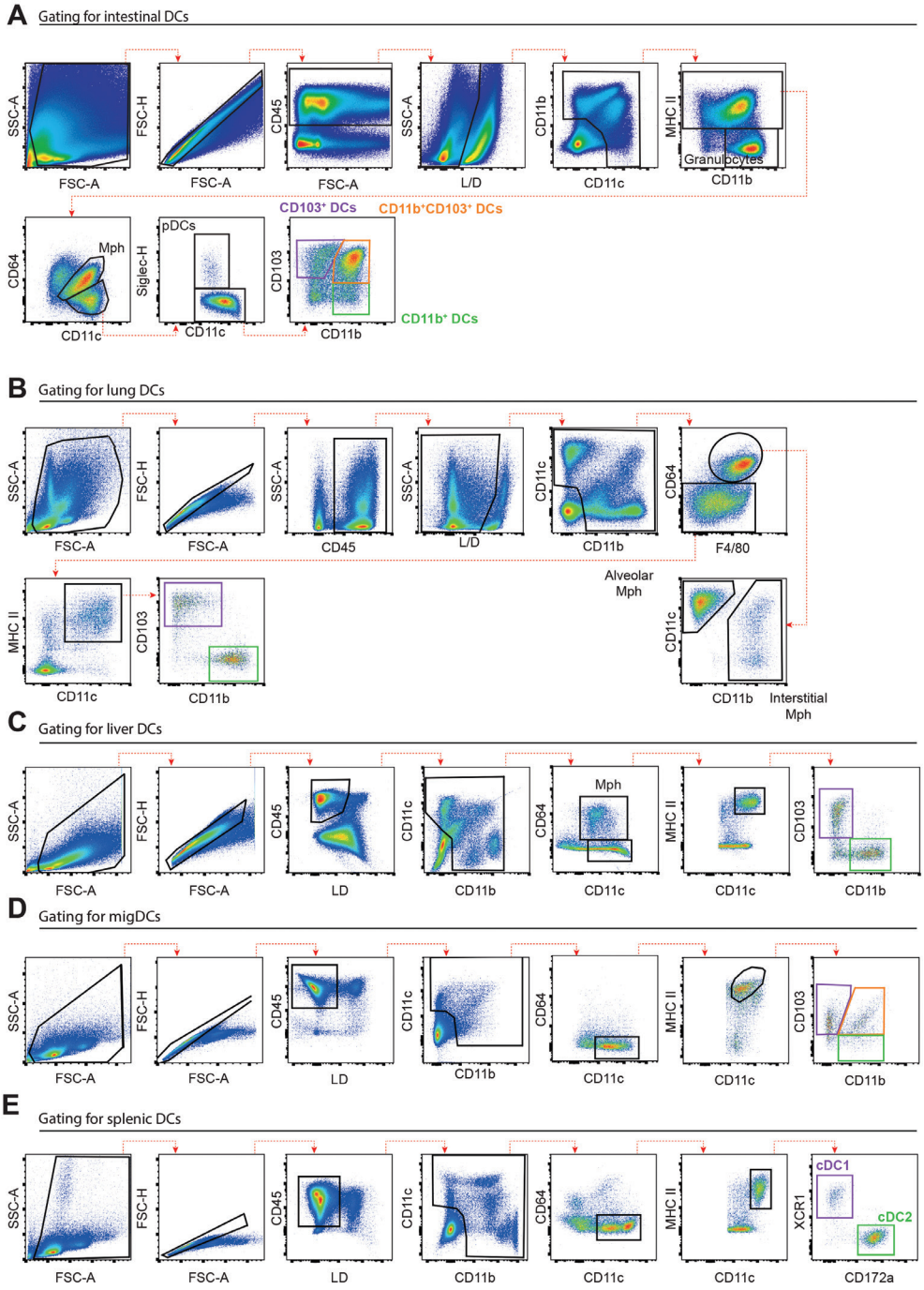
A
Gating for intestinal DCs
SSC-A
FSC-A
FSC-H
FSC-A
CD45
FSC-A
SSC-A
L/D
CD11b
CD11c
MHC II
Granulocytes
CD11b
CD103+ DCs
CD11b+CD103+ DCs
CD64
Mph
CD11c
pDCs
Siglec-H
CD11c
CD103
CD11b
CD11b+ DCs
B
Gating for lung DCs
SSC-A
FSC-A
FSC-H
FSC-A
SSC-A
CD45
SSC-A
L/D
CD11c
CD11b
CD64
F4/80
Alveolar
Mph
MHC II
CD11c
CD103
CD11b
CD11c
CD11b
Interstitial
Mph
C
Gating for liver DCs
SSC-A
FSC-A
FSC-H
FSC-A
CD45
LD
CD11c
CD11b
CD64
Mph
CD11c
MHC II
CD11c
CD103
CD11b
D
Gating for migDCs
SSC-A
FSC-A
FSC-H
FSC-A
CD45
LD
CD11c
CD11b
CD64
CD11c
MHC II
CD11c
CD103
CD11b
E
Gating for splenic DCs
SSC-A
FSC-A
FSC-H
FSC-A
CD45
LD
CD11c
CD11b
CD64
CD11c
MHC II
CD11c
XCR1
cDC1
cDC2
CD172a

Figure S5: Gating strategy used in different tissues to analyze *in vivo* DCs subsets.
Representative staining and gating strategies for CD103^{+} DCs, CD103^{+}CD11b^{+} DCs, CD11b^{+} DCs and macrophages in small intestine lamina propria (siLP) **(A)**, CD103^{+} DCs, CD11b^{+} DCs, alveolar and interstitial macrophages in lungs **(B)**, CD103^{+} DCs and CD11b^{+} DCs and Kupfer cells inn liver **(C)**, migratory CD103^{+} DCs, CD103^{+}CD11b^{+} DCs, CD11b^{+} DCs in mesenteric lymph nodes **(D)** and cDC1 and cDC2 in spleen **(E)**.

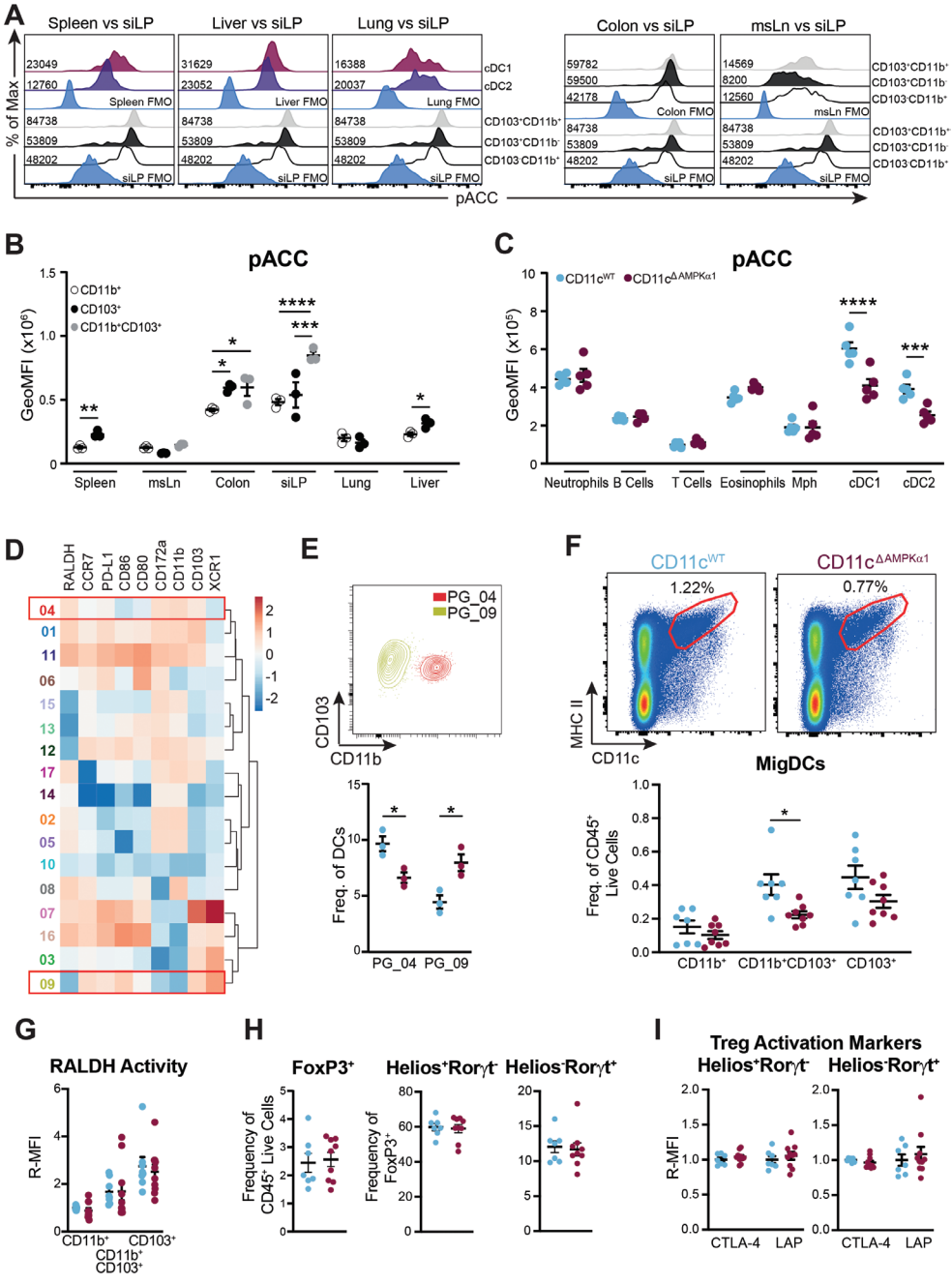
A
Spleen vs siLP
Liver vs siLP
Lung vs siLP
Colon vs siLP
msLn vs siLP
% of Max
pACC
cDC1
cDC2
CD103+CD11b+
CD103+CD11b-
CD103-CD11b+
Spleen FMO
Liver FMO
Lung FMO
Colon FMO
msLn FMO
siLP FMO
B
pACC
GeoMFI (x10^6)
CD11b+
CD103+
CD11b+CD103+
Spleen
msLn
Colon
siLP
Lung
Liver
C
pACC
GeoMFI (x10^5)
CD11c^WT
CD11c^ΔAMPKα1
Neutrophils
B Cells
T Cells
Eosinophils
Mph
cDC1
cDC2
D
RALDH
CCR7
PD-L1
CD86
CD80
CD172a
CD11b
CD103
XCR1
04
01
11
06
15
13
12
17
14
02
05
10
08
07
16
03
09
E
PG_04
PG_09
CD103
CD11b
Freq. of DCs
F
CD11c^WT
CD11c^ΔAMPKα1
1.22%
0.77%
MHC II
CD11c
MigDCs
Freq. of CD45+ Live Cells
CD11b+
CD11b+CD103+
CD103+
G
RALDH Activity
R-MFI
CD11b+
CD103+
CD11b+ CD103+
H
FoxP3+
Helios+Rorγt-
Helios-Rorγt+
Frequency of CD45+ Live Cells
Frequency of FoxP3+
I
Treg Activation Markers
Helios+Rorγt-
Helios-Rorγt+
R-MFI
CTLA-4
LAP

Figure S6: Mesenteric lymph nodes recapitulates the phenotype observed in small intestine lamina propria of CD11c$^{\Delta AMPK\alpha1}$ mice. Representative histograms **(A)** and geoMFI levels **(B)** for phosphorylation of Ser79 in acetyl-coA carboxylase (pACC) in DCs subsets amongst different tissues. **(C)** GeoMFI of pACC in different immune cells in spleen of naïve CD11c^{WT} and CD11c$^{\Delta AMPK\alpha1}$ mice. **(D)** Heatmap displaying expression of RALDH, activation and lineage markers from clusters identified in Figure 5E. **(E)** Contour plot of PG_04 (red) and PG_09 (ochre) displaying the expression of CD103 and CD11b (top) and frequency of PG_04 and PG_09 in CD11c^{WT} and CD11c$^{\Delta AMPK\alpha1}$ mice (bottom). **(F)** Representative dot plot for the gating of migratory DCs (migDCs - top) and frequency of CD45$^+$ live cells of CD103$^+$ DCs, CD103$^+$CD11b$^+$ DCs, CD11b$^+$ DCs (bottom) in the mesenteric lymph nodes (msLNs) of CD11c^{WT} and CD11c$^{\Delta AMPK\alpha1}$ mice. **(G)** Relative geoMFI (R-MFI) of RALDH activity in migDCs subsets in the msLNs of CD11c^{WT} and CD11c$^{\Delta AMPK\alpha1}$ mice. **(H)** Frequency of FoxP3$^+$ regulatory T cells (Tregs) within CD45$^+$ live immune cells (right), frequency of Helios$^+$RORgt$^-$ (tTregs) and Helios$^-$RORgt$^+$ (pTregs) within total Tregs population (middle and left, respectively) in msLns of CD11c^{WT} and CD11c$^{\Delta AMPK\alpha1}$ mice. **(I)** Quantification of CTLA-4 and latency-associated peptide (LAP) as proxy of TGF-b secretion by tTregs and pTregs in msLns of CD11c^{WT} and CD11c$^{\Delta AMPK\alpha1}$ mice. Student's t test was used to assess statistically significant differences. Mean ± SEM are indicated in the graphs;*p < 0.05, **p < 0.01, ***p < 0.001, ****p<0.0001.

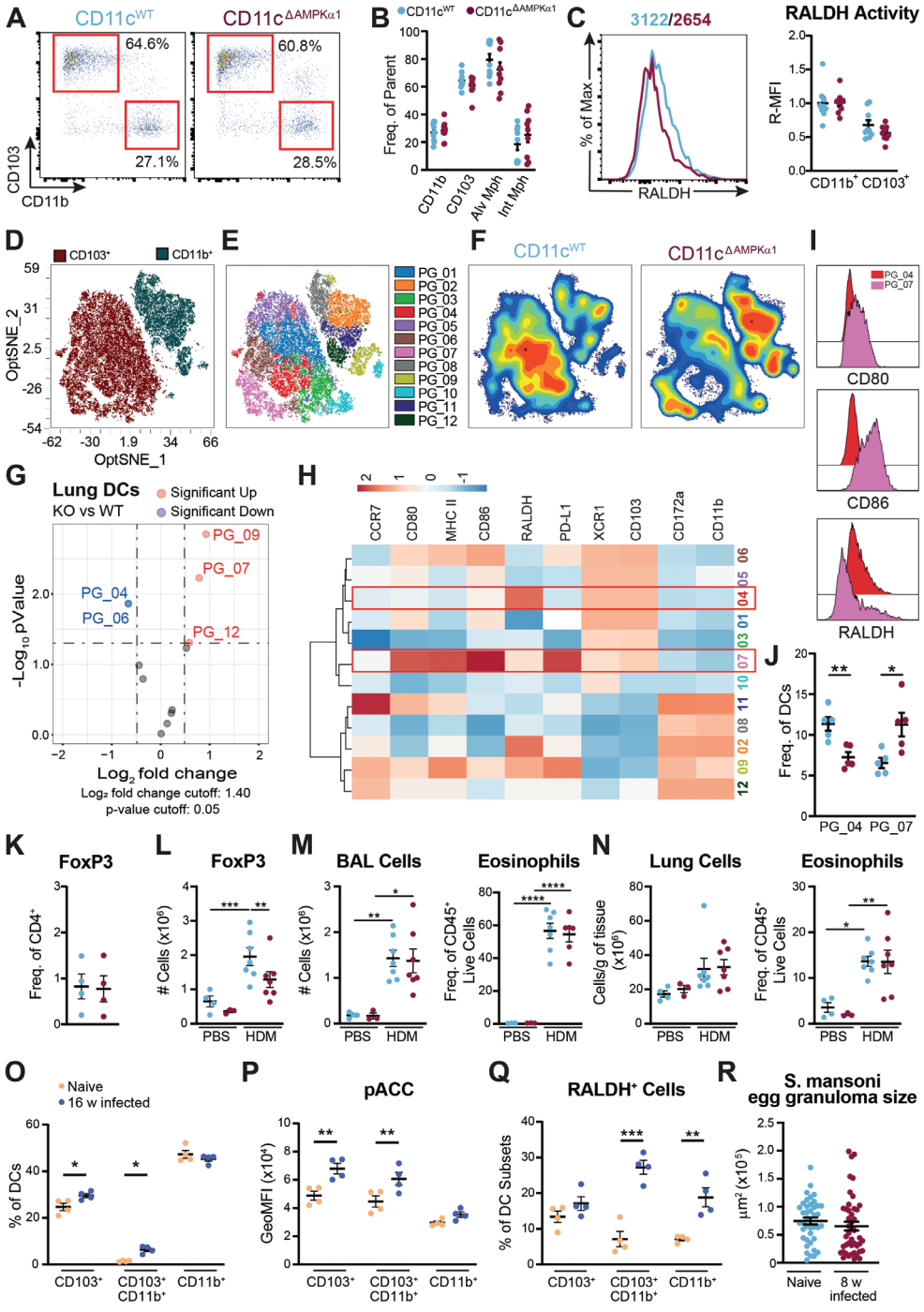
A
CD11c^WT
CD11c^ΔAMPKα1
64.6%
27.1%
60.8%
28.5%
CD103
CD11b
B
CD11c^WT
CD11c^ΔAMPKα1
Freq. of Parent
CD11b
CD103
Alv Mph
Int Mph
C
3122/2654
% of Max
RALDH
RALDH Activity
R-MFI
CD11b+ CD103+
D
CD103+
CD11b+
OptSNE_2
OptSNE_1
E
PG_01
PG_02
PG_03
PG_04
PG_05
PG_06
PG_07
PG_08
PG_09
PG_10
PG_11
PG_12
F
CD11c^WT
CD11c^ΔAMPKα1
I
PG_04
PG_07
CD80
CD86
RALDH
G
Lung DCs
KO vs WT
Significant Up
Significant Down
PG_09
PG_07
PG_04
PG_06
PG_12
-Log10 pValue
Log2 fold change
Log2 fold change cutoff: 1.40
p-value cutoff: 0.05
H
CCR7
CD80
MHC II
CD86
RALDH
PD-L1
XCR1
CD103
CD172a
CD11b
J
Freq. of DCs
PG_04
PG_07
K
FoxP3
Freq. of CD4+
L
FoxP3
Cells (x10^6)
PBS
HDM
M
BAL Cells
Eosinophils
Cells (x10^6)
Freq. of CD45+ Live Cells
N
Lung Cells
Eosinophils
Cells/g of tissue (x10^6)
Freq. of CD45+ Live Cells
O
Naive
16 w infected
% of DCs
CD103+
CD103+ CD11b+
CD11b+
P
pACC
GeoMFI (x10^4)
Q
RALDH+ Cells
% of DC Subsets
R
S. mansoni egg granuloma size
µm2 (x10^5)
Naive
8 w infected

Figure S7: AMPK signaling in DCs is dispensable for the inflammatory response in HDM disease model. (A) Representative dot plot for $CD103^+$ and $CD11b^+$ DCs in the lungs of $CD11c^{WT}$ and $CD11c^{\Delta AMPK\alpha1}$ mice. **(B)** Frequencies of DCs and macrophages subsets and **(C)** RALDH activity of DCs in the lungs of $CD11c^{WT}$ and $CD11c^{\Delta AMPK\alpha1}$ mice. **(C)** Representative histogram (left) and relative geometric MFI (R-MFI) of RALDH activity in siLP DC subsets. **(D)** Unbiased opt-SNE analysis of lung DC populations in which $CD103^+$ and $CD11b^+$ are indicated. **(E)** Phenograph clustering performed on lung DCs using RALDH, activation and lineage markers. **(F)** Contour plots overlaid on opt-SNE analysis as shown in **(D)** displaying distribution of cells for $CD11c^{WT}$ and $CD11c^{\Delta AMPK\alpha1}$ mice. **(G)** Volcano plot displaying the clusters as displayed in **(E)** with significant differences in frequency between $CD11c^{WT}$ and $CD11c^{\Delta AMPK\alpha1}$ mice. **(H)** Heatmap displaying expression of RALDH, activation and lineage markers from clusters identified in **(E)**. **(I)** Histograms displaying the activity of RALDH, or expression levels CD86 and CD80 in PG_04 (red) and PG_07 (pink). **(J)** Frequency of PG_04 (red) and PG_07 (pink) in $CD11c^{WT}$ and $CD11c^{\Delta AMPK\alpha1}$ mice. **(K)** Frequency of $FoxP3^+$ regulatory T cells in the lungs of $CD11c^{WT}$ and $CD11c^{\Delta AMPK\alpha1}$ mice. **(L-N)** $CD11c^{WT}$ and $CD11c^{\Delta AMPK\alpha1}$ mice were sensitized by intranasal application of house dust mite (HDM) and one week later challenged for 5 consecutive days. 3 days after the challenge, allergic airway inflammation was evaluated in bronchoalveolar fluids (BAL), lungs and lung-draining mediastinal LNs by flow cytometry. **(L)** Cell number of $FoxP3^+$ regulatory T cells (Tregs) in the lungs of $CD11c^{WT}$ and $CD11c^{\Delta AMPK\alpha1}$ mice. **(M-N)** Cell number (left) and eosinophilia (right) in the **(M)** BAL and **(N)** lungs of $CD11c^{WT}$ and $CD11c^{\Delta AMPK\alpha1}$ mice. **(O)** Frequency of DCs in the liver of naive (yellow) and 16 week infected WT mice (blue). **(P)** geometric MFI (GeoMFI) of phosphorylation level of acetyl-coA carboxylase-Ser79 (pACC) and **(Q)** frequency of RALDH positive cells in hepatic DC subsets from naïve (yellow) and 16 week infected WT mice (blue). **(R)** Quantification of size of individual egg granuloma in the liver from 8 week-infected $CD11c^{WT}$ and $CD11c^{\Delta AMPK\alpha1}$ mice. Data are a pool of 2 experiments with 7-9 mice **(A-C)**, 1 experiment using 5 mice per group **(D-K)**, 1 experiment using 4-7 mice per group **(L-N)**, 1 experiment using 4 mice per group **(O-Q)** or 1 experiment using 3-5 mice per group **(R)**. Two-Way Anova with Sidák's post-test was used to assess statistically significant differences. Mean ± SEM are indicated in the graphs;*p < 0.05, **p < 0.01, ***p < 0.001, ****p<0.0001.

Part 4

Discussion


AMPK

8

General discussion

Introduction

The metabolic status of an individual at both systemic as well as tissue level has a significant impact on the immune system. For example, excess of nutrients leads to chronic inflammation and metabolic dysfunction, while children suffering from undernutrition have a higher risk of dying from infectious diseases (1,2). Furthermore, the tumor micro-environment (TME) exerts immunosuppressive effects through local dysregulation of nutrient availability (3,4). This thesis aimed to generate new mechanistic insights into this intricate link between nutrient availability and immune responses by focusing on how nutrient-sensor AMPK in dendritic cells (DCs) translates metabolic cues from the environment to intracellular metabolic changes, thereby affecting the immune response. Through assessment of AMPK activity in tissue-resident DCs under various (pathological) conditions, by studying the effects of AMPK signaling in DCs *in vivo*, and through in depth analysis of the consequences of AMPK modulation in DCs *in vitro*, we now have a better understanding of how AMPK signaling in DCs contributes shaping the balance between immunity and tolerance. A summary of the key findings from each research chapter can be found in box 1.

Box 1: summary of main findings presented in this thesis

- The LKB1-AMPK/SIK signaling axis in hepatic DCs protects against obesity-induced metabolic dysfunction by limiting Th17 responses (chapter 4)
- AMPK activation induces tolerogenic moDCs that promote differentiation of regulatory T cells through RALDH activity, phospholipid breakdown, mitochondrial-fission induced fatty acid oxidation, and glucose catabolism (chapter 5)
- AMPK signaling in tumor-associated DCs promotes tumor growth and limits anti-tumor immunity (chapter 6)
- Retinoic-acid induces tolerogenic moDCs through AMPK-FoxO3 signaling (chapter 7)
- AMPK drives $CD103^+$ DCs to induce Treg responses *in vivo* (chapter 7)

AMPK signaling in DCs, a double-edged sword

The studies presented in this thesis reveal a role for AMPK signaling in promoting tolerance and suggest that AMPK activation in DCs could compromise the immune system in nutrient-restricted conditions. Hence, heightened AMPK signaling in DCs can potentially weaken the immune system and contribute to increased susceptibility to infectious diseases during under nutrition, and impaired anti-tumor immunity during tumor growth. In these contexts, inhibition of AMPK signaling in DCs could be of clinical interest. However, diminished AMPK signaling may not be beneficial in other settings, as absence of AMPK in DCs limits parasite expulsion and control of associated pathology (5,6) and increases susceptibility to developing inflammatory bowel disease (unpublished data). Hence, AMPK signaling in DCs is a double-edged sword, which has to be taken into consideration if this pathway were to be explored as target for clinical purposes.

Also in other immune cells AMPK has a dual role. For example, AMPK signaling dampens the primary antibody response of B cells, while supporting the function of memory B cells (7), AMPK signaling in tumor-infiltrating T cells can have anti- (8) and pro- tumorigenic (9) effects, and while most studies show an anti-inflammatory role for AMPK in macrophages (10,11), pro-inflammatory polarization can also depend on AMPK signaling (12). Taken together, these examples highlight the crucial role of AMPK in controlling the balance between immunity and tolerance.

Consequences of AMPK activation in DCs across tissues

Given the important role of AMPK in adapting cellular metabolic states to the tissue metabolic environment, and thereby DC function, a better understanding of how AMPK activation is regulated in different tissues and pathological contexts is key. Here, I aim to provide an overview of AMPK activity in DCs in murine tissues and how this affects immune responses in health and disease.

Given the fact that AMPK is activated during metabolic stress, AMPK signaling in DCs is expected to be low during homeostasis. In line with this, $CD11c^{\Delta AMPK}$ mice do not have any observable phenotype (data not shown). In chapter 7 we show that AMPK activity in DCs during homeostasis is similar among a variety of tissues, including the spleen, lung, and liver, with the notable exception of the colon and small intestine, where DCs display high levels of AMPK activity (Fig. 1A). Intestinal homeostasis requires a fine balance between inflammatory responses to pathogens and tolerance to commensal microorganisms, and it has been suggested that AMPK activity in gut-residing DCs may contribute to the immunosuppressive environment (13). Indeed, we showed that AMPK signaling is required for maintenance of, and RALDH activity in intestinal $CD103^{+}CD11b^{+}$ DCs, a subset of DCs with known tolerogenic properties. We hypothesize that AMPK activity in intestinal DCs is driven by retinoic acid (RA), derived from dietary Vitamin A, as we have seen that RA in *in vitro* moDCs induces AMPK activity (Chapter 7).

In addition to the immunosuppressive environment of the intestine, we showed in chapter 6 that the immunosuppressive TME can also promote AMPK signaling in DCs (Fig. 1B). AMPK signaling suppressed expression of various metabolic enzymes, lowered expression of CD86 on cDC1s, and prevented the accumulation of $GLUT1^{+}$ cDC1s with high expression of activation markers. Furthermore, tumor-infiltrating $CD8^{+}$ T cells secreted lower levels of TNF in $CD11c^{WT}$ compared to $CD11c^{\Delta AMPK}$ mice. Although the exact mechanisms are yet to be discovered, these studies suggest that AMPK signaling in tumor-associated (TA)-DCs contributes to immunosuppression, thereby supporting tumor growth. We have not explored the signals that induce AMPK activity, but a variety of metabolic characteristics of the TME can induce AMPK activation (4), including low glucose levels (14), hypoxia (15), and lactate (16).

In contrast to the presumably nutrient-deficient TME, limited AMPK activity is expected in nutrient-rich inflamed tissues of high fed diet (HFD)-fed mice (2). In chapter 4 we compared AMPK signaling in DCs from adipose tissue and liver from low fat diet (LFD)- and HFD-fed mice, and indeed, AMPK activity in DCs from these metabolic tissues remained low following a HFD (Fig. 1C). Correspondingly, loss of AMPK signaling in CD11c-expressing cells did not affect the metabolic dysfunctions caused by HFD, including weight gain, impaired glucose

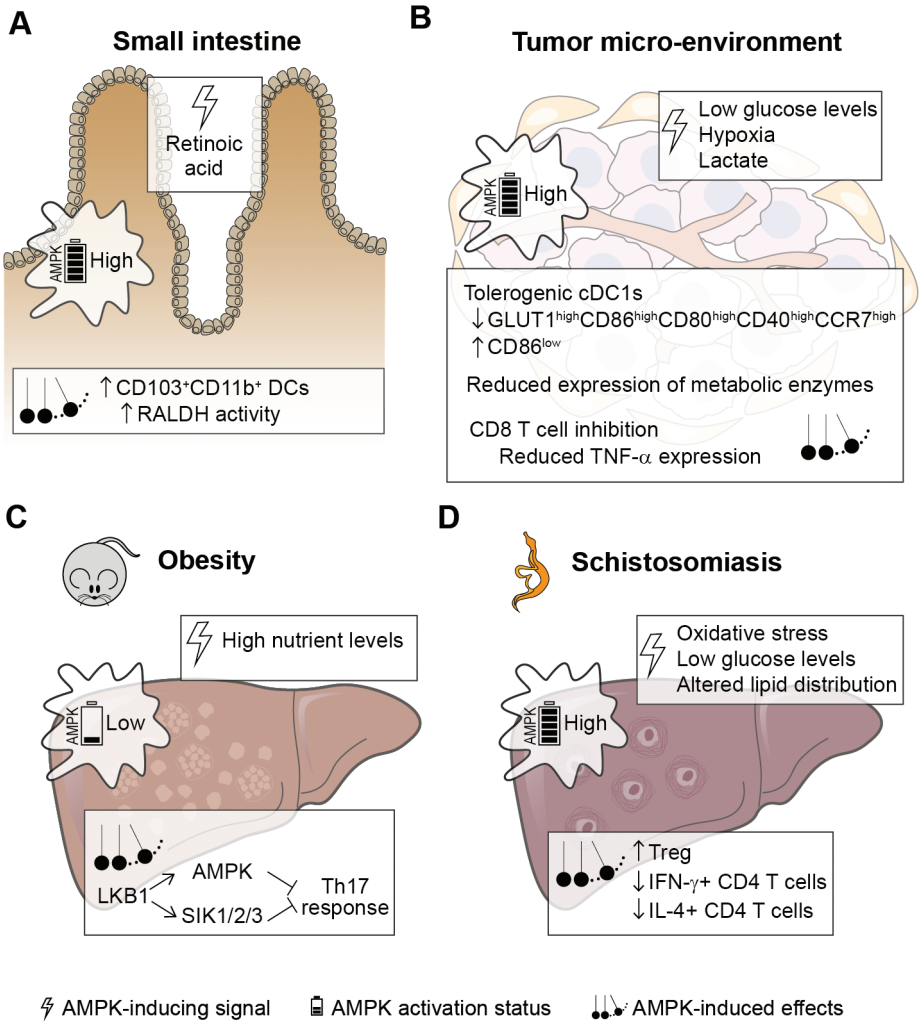

Figure 1: Dendritic cell AMPK activation *in situ*. Putative AMPK-inducing signals, AMPK activation status, and AMPK-induced effects in DCs residing in **(A)** the small intestine, **(B)** the TME, **(C)**, the liver during obesity, and **(D)** the liver during schistosomiasis.

homeostasis, and hepatic steatosis. In contrast, we did show that LKB1 in DCs, a direct upstream activator of AMPK, was required for limiting metabolic dysfunctions during obesity. Interestingly, we identified this effect to be dependent on LKB1-driven AMPK/SIK signaling to limit hepatic pathogenic Th17 accumulation. These data suggest that even in conditions where AMPK activity is not notably elevated, AMPK can apparently play important role in relaying signals from upstream kinase LKB1, albeit in combination with other AMPK-related kinases.

While DCs in the pro-inflammatory, nutrient-rich liver of obese mice do not exhibit high AMPK activity, hepatic DCs during schistosomiasis did show elevated AMPK activity compared to hepatic DCs from naïve mice (Fig. 1D) (chapter 7). Hence, AMPK activation in DCs is not restricted to certain tissues, but highly dynamic and dependent on the (metabolic) conditions. AMPK signaling in hepatic DCs contributed to regulatory T cell (Treg) accumulation, dampened IFN-γ and IL-4 secretion by CD4 T cells, and reduced attenuated egg granuloma size during schistosomiasis. Intriguingly, both HFD and schistosomiasis increased FoxP3$^+$ Tregs in the liver, but only during schistosomiasis AMPK signaling in DCs was involved in the Treg response. The Th2 response to egg-derived antigens in the liver (17) is accompanied by oxidative stress, elevated glycolytic enzyme expression in hepatocytes (possibly leading to reduced glucose levels in the environment), and altered lipid metabolism (18), potential inducers of the observed AMPK activation in hepatic DCs during schistosomiases (19).

The conclusions that can be drawn from studying AMPK signaling in DCs across various tissues under different pathological conditions are summarized in box 2. The tissue-specific factors that drive AMPK activation in DCs have not been addressed in this thesis. It is likely that the metabolic cues that promote AMPK signaling are diverse and context dependent. Within the TME, AMPK-induced tolerogenicity and metabolic stress-induced immunosuppression could be a side effect of the high metabolic demands of tumor cells. However, it can also be argued that it is favorable for tumors to have limited vascularization and scarce nutrient levels, accompanied by a metabolically immunosuppressive environment. Tumor cells, however, will most likely also outcompete DCs for nutrients in nutrient-rich conditions, thereby further increasing their proliferation rates. Additionally, taking into account that tumor cells also developed other strategies to suppress the immune system (e.g. MHC-I downregulation and secretion of anti-inflammatory molecules) (20), AMPK-induced suppression of anti-tumor immunity is most likely a beneficial side effect of metabolically highly active cancer cells, rather than a mechanism that evolved to promote tumor growth. Further understanding of this balance between nutrient supply and immune suppression, for example by comparing nutrient availability in high immunogenic vs. poor immunogenic tumors, may help to find therapeutic strategies to change the metabolic, immunosuppressive TME at the cost of tumor growth.

It is important to keep in mind that AMPK signaling is a dynamic process. AMPK activation status in intestinal DCs might be affected by food intake for example and AMPK activity may also differ at various locations within one tissue, e.g. nutrient gradients caused by poor vascularization in the tumor micro-environment may lead to various degrees of AMPK activity within tumor-associated DCs. Spatiotemporal control of AMPK activation in different (pathological) settings is a yet unexplored area that warrants further investigation, to fully understand the biology of AMPK signaling in DCs and to implement this knowledge for therapeutic purposes.

The downstream effects of AMPK signaling in DCs

Thus far it remained largely unknown how AMPK activation affects DC biology. In chapter 5 we explored the immunological consequences and downstream mechanisms of AMPK activation in DCs using human monocyte-derived DCs (moDCs), treated with AMPK-activator 991 (21). AMPK activation induced RALDH^{high} tolerogenic DCs that primed T cells towards a regulatory phenotype. Using an unbiased approach we showed that breakdown of phospholipids, mitochondrial fission-induced fatty acid oxidation, and glucose catabolism are important

Box 2: Dendritic cell AMPK signaling in murine tissues: main findings.

- Without a (metabolic) environment that induces AMPK activation, DC homeostasis and function are not affected by loss of AMPK
- AMPK activation in DCs is associated with, but not restricted to, immunosuppressive environments
- AMPK activation in DCs can regulate Treg, Th17, and Th2 responses, but always favors a tolerogenic rather than an immunogenic response.
- In conditions that do not elevate AMPK activation, AMPK can still control DC function in combination with other AMPK-related kinases

for AMPK-induced tolerogenicity. However, when AMPK activation *in situ* is driven by low glucose levels, it is unlikely that glycolysis would be upregulated. In line with this, we observed that AMPK-activated TA-DCs, residing in the TME of highly glycolytic B16 melanoma cells, expressed lower levels of enzymes involved in glycolysis and the TCA cycle, suggesting a reduction rather than increase in glucose oxidation (chapter 6). Discrepancies between *in vitro* and *in vivo* studies may be explained by the nutrient-rich medium in which moDCs are cultured, which does not reflect the physiological conditions of AMPK activation. On the other hand, AMPK activity in TA-DCs suppressed expression of ACC1, a key enzyme of fatty acid synthesis, suggesting that *in vivo* AMPK activation suppresses anabolic metabolism, while *in vitro* AMPK activation boost catabolic metabolism. This points towards a consistent shift from anabolic to catabolic metabolism upon AMPK activation. This shift can, depending on the context, be mediated by inhibition of fatty acid synthesis through downregulation and/or inhibition of ACC1, promotion of fatty acid oxidation through inhibition of ACC2 or induction of mitochondrial fission, enhanced glucose oxidation, and/or elevated catabolism of phospholipids.

Within the tumor, AMPK signaling in DCs affected cDC1s and CD8 T cells, but no difference in the intra-tumoral Treg compartment could be detected. On the other hand, DC-specific AMPK activation during schistosomiases promoted Treg abundance and was, interestingly, associated with higher RALDH activity, which is important for Treg induction by AMPK-activated moDCs *in vitro*. Although we did not address CD8 T cell priming using our human moDC model, this may indicate that the observed metabolic changes and tolerogenic properties induced by AMPK activation in moDCs *in vitro*, may reflect how AMPK regulates DC biology in the context of schistosomiasis, rather than cancer. In depth metabolic analysis of hepatic DCs during schistosomiasis may reveal whether increased phospholipid, fatty acid, and glucose catabolism could also play a role in promoting Treg responses by AMPK-activated DCs *in vivo*.

Our *in vivo* models show that loss of AMPK in DCs shifts the balance towards pro-inflammatory responses rather than tolerance. As AMPK is activated by metabolic stress, AMPK-deficient DCs still reside in a presumably metabolically harsh environment, which raises the question of which nutrient sources and metabolic pathways are used for DC activation upon AMPK loss. In the TME of CD11c$^{\Delta AMPK}$ mice we observed an increase in cDC1s with high expression of activation markers and elevated GLUT1 levels. Upregulation of nutrient transporters, in this case a glucose transporter, may allow these cells to more efficiently compete for nutrients, to better fuel the metabolic programs underpinning their activation.

Furthermore, intracellular lipid, protein, or glycogen storages may be used, mechanisms also described during early DC activation (22).

Taken together, our data provide new and functional information on the consequences of AMPK activation in DCs. How these findings translate to other immune cells, and how the metabolic environment affects these downstream events remains to be explored.

Future perspectives

The work in this thesis expands the field of immunometabolism with novel insights on the role of AMPK signaling in DCs. To ultimately be able to exploit these insights for DC-based immunotherapies continued efforts are needed that further address cellular and systemic metabolism. Key future research areas are summarized in box 3 and include further studies on spatiotemporal regulation of AMPK signaling in DCs *in situ*, tissue-specific metabolic demands of DCs, metabolic rewiring during development and activation of the different DC subsets, and metabolic crosstalk (e.g. nutrient exchange) between DCs and other (immune) cells. To drive this research forward we need to take full advantage of the latest models and methods that allow a deeper understanding of the interplay between metabolism and immune cells.

Box 3: Future research directions

- Spatiotemporal control of AMPK activity *in situ*
- Mechanisms of AMPK controlled immune responses
- AMPK as target for inflammatory and tolerogenic DC-based therapies
- Differences in metabolic reprogramming necessary for the activation and function of distinct DC subsets
- Tissue-specific metabolic demands of DCs
- Metabolic crosstalk between DCs and other (immune) cells
- Modulation of the metabolic environment for therapeutic purposes

Methods to study immunometabolism

Tools to study immunometabolism can be roughly divided into functional assays, including extracellular flux analysis and enzyme activity assays, flow cytometry approaches, and omics-based methods (transcriptomics, proteomics, metabolomics) (23). The scarcity of dendritic cells *in situ* make *ex vivo* functional assays difficult and therefore the quickly expanding flow cytometry and -omics toolbox is a boost for this field. Single cell transcriptomics data has been of great value for understanding immune cell ontogeny and inter- and intra-tissue heterogeneity, and also is a useful tool to obtain metabolic information (24). Mass spectrometry allows for quantification of metabolites, lipids, and proteins and has proven to be an important method for unravelling immunometabolic mechanisms, especially when these different omic-datasets are integrated (chapter 5). Furthermore, C13/N15 isotope labelling techniques can provide information about fluxes of various nutrients in different metabolic pathways, both *in vitro* and *in vivo*, and may help to define DC subset-specific metabolic rewiring. Imaging mass spectrometry can provide spatiotemporal information to connect nutrient availability to immune cell activation and metabolic status, which is particularly important for understanding

the dynamics of nutrient-sensing enzymes such as AMPK, that are highly-dependent of microenvironment (25). Spatial transcriptomics also contributes to this understanding, although AMPK is a kinase and hence addressing the phosphorylation of target proteins using imaging mass spectrometry provides better information on the AMPK activation status than a transcriptional profile (25). A highly valuable resource for system-based immune cell profiling are publicly available datasets, that are sometimes integrated in easy-to-access online databases. Examples include mouse single cell atlas with data from all major mouse organs called Immgen (24), a database containing transcriptomics data from murine mononuclear phagocytes derived from 38 different tissues (26), and the Chan Zuckerberg Cell by Gene discover that allows easy access to human single cell datasets (27).

Unlike to omics-based approaches, flow cytometry is limited by the number of markers and biased by the selected markers that can be analyzed. On the other hand, it is better accessible and can also provide data on dynamic processes, including activity of the metabolic pathways using SCENITH (28). Spectral flow cytometry allows for panels up to 40 markers and in combination with either SCENITH or Met-Flow, which contains antibodies targeting key metabolic enzymes and proteins, in depth metabolic information on multiple immune cell subsets can be obtained in one run (28,29). Flow cytometry can also be used to measure mitochondrial activity with metabolic dyes and to assess uptake of nutrients (30). A disadvantage of fluorescent labeling of nutrients is that it may affect their structure and thereby the cellular import route (31). Click-chemistry based staining, which only requires minor metabolite modifications and allows intracellular fluorescent labelling, may overcome this problem (32,33). Another interesting method is imaging flow cytometry. Adding subcellular spatial information to the fluorescently labelled markers can for example visualize DC-T cell interactions (34), which in combination with a met-flow panel can potentially lead to new insights into the metabolic crosstalk required for this interaction.

The quickly expanding immunometabolism toolbox, particularly those methodologies that provide spatial information or allow assessment of dynamic processes on single cell level, are key to better understand the metabolic processes inside immune cells, and are needed to improve immunotherapies (Fig. 2).

Models to study DC biology

In addition to innovating methods, proper model systems are needed. The extremely low numbers of DCs in blood and tissues complicate *ex vivo* experiments to study these cells. Hence, several *in vitro* human and murine DC models have been developed. Human moDCs, differentiated *in vitro* from PBMC-derived $CD14^+$ monocytes using GM-CSF and IL-4 are the most commonly used model for human DC studies (35). moDCs exhibit phenotypical and functional similarities with cDCs, but are transcriptionally related to $CD1c^+CD1a^+CD14^+$ inflammatory DCs and may not be representative for DC biology during homeostasis (36,37). Interestingly, recent developments in the immunometabolism field contributed to differentiation of highly immunogenic moDCs, induced through GM-CSF and inhibition of metabolic regulators PPARγ and mTORC1 (38). This study shows that in depth knowledge of developmental trajectories can lead to improved *ex vivo* differentiation methods that will hopefully lead to culture conditions that better resemble the different *in vivo* DC subsets.

DCs can also be generated from $CD34^+$ cells derived from human umbilical cord blood (39). $CD34^+$ hematopoietic progenitors can differentiate into cDC1s, cDC2s, and pDCs that closely resemble peripheral blood DC, using a cocktail of cytokines, growth factors, and Notch

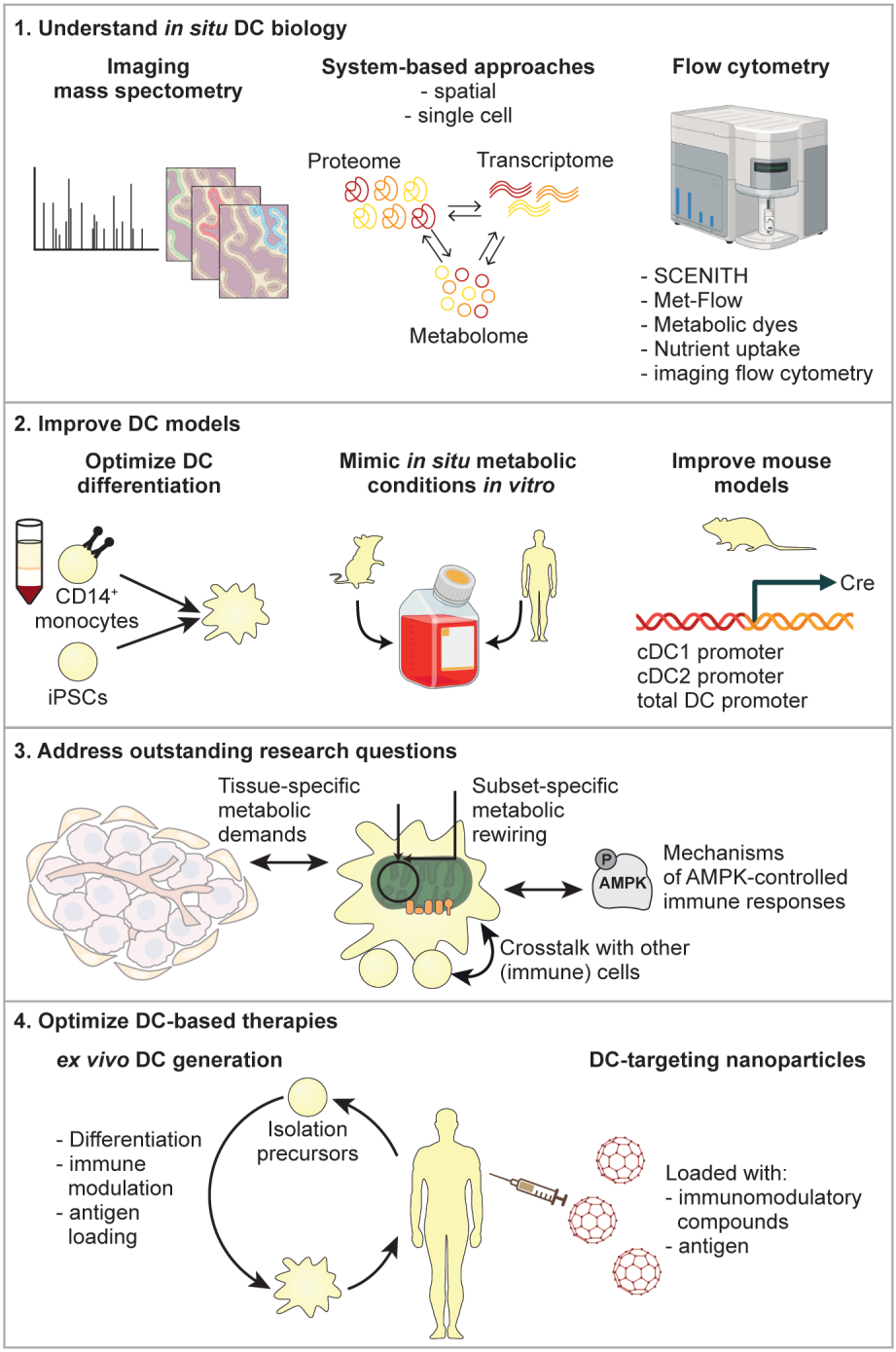

Figure 2: Tools to study DC metabolism and function. Methods and models to strengthen our fundamental knowledge on DC metabolism and immunity, to ultimately improve DC-based therapies. iPSCs = induced pluripotent stem cells.

ligand-expressing stromal cells. Unfortunately, in addition to a challenging cell culture protocol, differentiation can take up to 4 weeks, and cell numbers are low (40,41). Representative cDC1s (42), cDC2s (43), and regulatory DCs (44) can also be differentiated from induced pluripotent stem cells (iPSCs) that can be cultured in high cell numbers, but also require complicated cell culture conditions (45). Another possibility to achieve high cell numbers is the use of immortal cell lines. Several human myeloid leukemia cell lines have been used for DC differentiation, but the leukemic-origin of these cells results in several defects with regards to antigen presentation capacity (46,47).

An important step towards better understanding of how metabolism and immune cell function are linked is the use of cell culture conditions that better reflect the *in situ* environment of cells. Tissue-specific oxygen levels can be mimicked using microfluidic devices (48) and physiological medium allows for exposure to physiological relevant concentrations of carbon sources, salts, and other plasma components. Culturing moDCs in physiological oxygen concentrations (5%) did increase IL-12p40 secretion by DCs, but had no effects on CD8 T cell priming (49), suggesting that the use of atmospheric oxygen levels might be sufficient to mimic *in situ* DC biology *in vitro*. The effects of physiological medium on DC function are yet to be determined, but various studies show that metabolism and inflammatory responses observed in T cells *in vitro* are distinct and more similar to *in vivo* conditions when standard culture medium is replaced for physiological medium (50–52). Mimicking physiological conditions *in vitro* may lead to better representative models, in particular when addressing the role of nutrient-sensing enzymes such as AMPK.

Mouse models are extremely useful for *in vivo* studies. Adoptive transfer of DCs allows for *ex vivo* treatment and genetic manipulation of DCs, and the Cre-loxP system facilitates *in situ* targeting of DCs, albeit with limitations. The relatively new Xcr1-Cre strain is the best model for genetic manipulation of cDC1s (53), but a similar model for cDC2s does not exist, due to the variable expression of lineage-defining markers across tissues (54). CD11c-Cre is used to target total DCs and while the largest Cre-induced effects are indeed in the DC compartment, contribution of other CD11c-expressing cells, including macrophages or T cells, to an obtained phenotype cannot be excluded (55).

To move the DC field forward it is important to keep optimizing models and methods (Fig. 2). As monocyte to DC differentiation is relatively easy, commonly used, and enables high cell yields, newly obtained knowledge on immunological markers, metabolic conditions, and cytokine requirements for the distinct developmental trajectories should be used to optimize this model. iPSC-derived DCs are also a highly valuable model to study DC biology, but the use of this model has not received much traction yet amongst immunologists. Nevertheless, adapting to new protocols that better take into account the specific metabolic context in which DCs are cultured are likely to be critical to improve efficacy of DC-based therapies.

DCs as therapeutic intervention: targeting AMPK signaling?

The field of immunotherapy, the treatment of disease through stimulation or suppression of the immune system, is quickly expanding since the FDA approval of the first immune checkpoint inhibitor in 2011, but has a long history with earliest reports regarding the disappearance of tumors after infection, from ancient Egypt, 3000 years ago (56,57). The basis for modern science started in the 18th century and led to one of the first major immunotherapeutic breakthroughs in 1796: the discovery of protective immunity against smallpox after inoculation with common cowpox virus. Today, there is a broad spectrum of immunotherapeutic treatments, including

prophylactic and therapeutic vaccinations, immunosuppressants, antibody-based therapies, cytokine-treatments, and cell-based therapies (56,57). As antigen-presenting cells, DCs have the capacity to initiate a highly specific immune response and are therefore a very interesting target for cell-based therapies.

In 2010 the FDA approved the first (and thus far only) DC vaccination therapy, which aimed to treat prostate cancer. Autologous PBMC-derived APCs were activated *ex vivo* with a fusion protein consisting of a tumor antigen and GM-CSF and although clinical trial results were promising, it did not improve disease outcome in clinical settings (56,58). Since then, multiple approaches have been developed to improve DC therapy. *Ex vivo* generation of DCs from monocytes and *in vivo* targeting of DCs using nanoparticles are strategies that use immunomodulatory compounds to change the *in situ* immune response (Fig. 2) (59).

Clinical trials have proved the safety of tolerogenic moDCs for treatment of inflammatory diseases (59,60) and immunogenic moDCs for treatment of cancer (61,62), but efficacy is generally still limited. Problems include reduced fitness of patient-derived monocytes, limited duration of the tolerogenic state, insufficient antigen presentation capacity, and impaired migratory abilities (59–62). Delivering antigens and immunomodulatory compounds to DCs *in vivo* would overcome some of these problems. Although various nanoparticles are already approved for therapy (63), therapies using DC-based nanoparticles are still in early stages (64). Results from clinical trials are promising, but optimization of the nanoparticles itself, the delivery methods, and the desired cell-specificity, are examples of aspects that need to be improved (64). Important additional variables that impact efficacy for both approaches include effects of the micro-environment (e.g. the immunosuppressive TME may overrule the enhanced inflammatory capacity of the treated-DCs) and the selection of the type of antigen, adjuvant, or immunomodulatory compound.

Results from this thesis indicate that AMPK activation may be a promising strategy for the generation of therapeutic tolerogenic DCs. Furthermore, inhibiting AMPK activity may boost inflammation of DC-based cancer therapies by providing protection against metabolic stress in the TME. Further studies into AMPK signaling in DCs, as part of larger efforts to better delineate how nutrient availability, DC metabolism, and DC function are connected, will hopefully contribute to improvement of DC-based therapies and better treatment of immune-driven diseases.

References

1. Rytter MJH, Kolte L, Briend A, Friis H, Christensen VB. The immune system in children with malnutrition - A systematic review. PLoS One. 2014;9(8).
2. Christ A, Lauterbach M, Latz E. Western Diet and the Immune System: An Inflammatory Connection. Immunity. 2019;51(5):794–811.
3. Chang CH, Qiu J, O'Sullivan D, Buck MD, Noguchi T, Curtis JD, et al. Metabolic Competition in the Tumor Microenvironment Is a Driver of Cancer Progression. Cell. 2015;162(6):1229–41.
4. Arner EN, Rathmell JC. Metabolic programming and immune suppression in the tumor microenvironment. Cancer Cell. 2023;41(3):421–33.
5. Patente TA, Brombacher EC, Heieis GA, Pelgrom LR, Zawistowska-Deniziak A, Otto F, et al. Metabolic sensor AMPK licenses CD103+ dendritic cells to induce Treg responses. bioRxiv. 2023;
6. Nieves W, Hung LY, Oniskey TK, Boon L, Foretz M, Viollet B, et al. Myeloid-Restricted AMPKα1 Promotes Host Immunity and Protects against IL-12/23p40–Dependent Lung Injury during Hookworm Infection. The Journal of Immunology. 2016;196(11):4632–40.
7. Brookens SK, Cho SH, Basso PJ, Boothby MR. AMPKα1 in B Cells Dampens Primary Antibody Responses yet Promotes Mitochondrial Homeostasis and Persistence of B Cell Memory. The Journal of Immunology. 2020;205(11):3011–22.
8. Pokhrel RH, Acharya S, Ahn JH, Gu Y, Pandit M, Kim JO, et al. AMPK promotes antitumor immunity by downregulating PD-1 in regulatory T cells via the HMGCR/p38 signaling pathway. Mol Cancer. 2021;20(1).
9. Rao E, Zhang Y, Zhu G, Hao J, Persson XMT, Egilmez NK, et al. Deficiency of AMPK in CD8 + T cells suppresses their anti-tumor function by inducing protein phosphatase-mediated cell death. Oncotarget. 2015;6(10):7944–58.
10. Phair IR, Nisr RB, Howden AJM, Sovakova M, Alqurashi N, Foretz M, et al. AMPK integrates metabolite and kinase-based immunometabolic control in macrophages. Mol Metab. 2023;68.
11. Sag D, Carling D, Stout RD, Suttles J. Adenosine 5′-Monophosphate-Activated Protein Kinase Promotes Macrophage Polarization to an Anti-Inflammatory Functional Phenotype. The Journal of Immunology. 2008;181(12):8633–41.
12. Liu PS, Chen YT, Li X, Hsueh PC, Tzeng SF, Chen H, et al. CD40 signal rewires fatty acid and glutamine metabolism for stimulating macrophage anti-tumorigenic functions. Nat Immunol. 2023;24(3):452–62.
13. Round JL, Mazmanian SK. The gut microbiota shapes intestinal immune responses during health and disease. Nat Rev Immunol. 2009;9(5):313–23.
14. Zhang CS, Hawley SA, Zong Y, Li M, Wang Z, Gray A, et al. Fructose-1,6-bisphosphate and aldolase mediate glucose sensing by AMPK. Nature. 2017;548(7665):112–6.
15. Dengler F. Activation of ampk under hypoxia: Many roads leading to rome. Int J Mol Sci. 2020;21(7).
16. Zhou Y, Liu X, Huang C, Lin D. Lactate Activates AMPK Remodeling of the Cellular Metabolic Profile and Promotes the Proliferation and Differentiation of C2C12 Myoblasts. Int J Mol Sci. 2022;23(22):1–16.
17. Wilson MS, Mentink-Kane MM, Pesce JT, Ramalingam TR, Thompson R, Wynn TA. Immunopathology of schistosomiasis. Immunol Cell Biol. 2007;85(2):148–54.
18. von Bülow V, Gindner S, Baier A, Hehr L, Buss N, Russ L, et al. Metabolic reprogramming of hepatocytes by Schistosoma mansoni eggs. JHEP Reports. 2023;5(2).
19. Steinberg GR, Hardie DG. New insights into activation and function of the AMPK. Nat Rev Mol Cell Biol. 2022;24:255–72.

20. Kim SK, Cho SW. The Evasion Mechanisms of Cancer Immunity and Drug Intervention in the Tumor Microenvironment. Front Pharmacol. 2022;13.

21. Bultot L, Jensen TE, Lai YC, B Madsen AL, Collodet C, Kviklyte S, et al. Benzimidazole derivative small-molecule 991 enhances AMPK activityand glucose uptake induced by AICAR or contraction in skeletal muscle. Am J Physiol Endocrinol Metab. 2016;311:706–19.

22. Thwe PM, Pelgrom L, Cooper R, Beauchamp S, Reisz JA, D'Alessandro A, et al. Cell-Intrinsic Glycogen Metabolism Supports Early Glycolytic Reprogramming Required for Dendritic Cell Immune Responses. Cell Metab. 2017;26(3):558-567.e5.

23. Artyomov MN, Van den Bossche J. Immunometabolism in the Single-Cell Era. Vol. 32, Cell Metabolism. Cell Press; 2020. p. 710–25.

24. Gainullina A, Mogilenko DA, Huang LH, Todorov H, Narang V, Kim KW, et al. Network analysis of large-scale ImmGen and Tabula Muris datasets highlights metabolic diversity of tissue mononuclear phagocytes. Cell Rep. 2023;42(2).

25. Moffitt JR, Lundberg E, Heyn H. The emerging landscape of spatial profiling technologies. Nat Rev Genet. 2022;23(12):741–59.

26. Han X, Wang R, Zhou Y, Fei L, Sun H, Lai S, et al. Mapping the Mouse Cell Atlas by Microwell-Seq. Cell. 2018;172(5):1091-1107.

27. Jones RC, Karkanias J, Krasnow MA, Pisco AO, Quake SR, Salzman J, et al. The Tabula Sapiens: A multiple-organ, single-cell transcriptomic atlas of humans. Science. 2022;376(6594).

28. Argüello RJ, Combes AJ, Char R, Gigan JP, Baaziz AI, Bousiquot E, et al. SCENITH: A Flow Cytometry-Based Method to Functionally Profile Energy Metabolism with Single-Cell Resolution. Cell Metab. 2020;32(6):1063-1075.

29. Heieis GA, Patente TA, Tak T, Almeida L, Everts B. Spectral flow cytometry reveals metabolic heterogeneity in tissue macrophages. BioRxiv. 2022;

30. Brombacher EC, Patente TA, Quik M, Everts B. Characterization of Dendritic Cell Metabolism by Flow Cytometry. In: Sisirak V, editor. Dendritic Cells Methods in Molecular Biology. Humana Press; 2023. p. 219–37.

31. D'Souza LJ, Wright SH, Bhattacharya D. Genetic evidence that uptake of the fluorescent analog 2NBDG occurs independently of known glucose transporters. PLoS One. 2022;17(8)

32. Pelgrom L, Davis G, O'shoughnessy S, Van Kasteren S, Finlay D, Sinclair L. QUAS-R: Glutamine (Q) Uptake Assay with Single cell Resolution reveals metabolic heterogeneity with immune populations. BioRxiv. 2022;

33. Laval T, Demangel C. Click-chemistry-based protocol to quantitatively assess fatty acid uptake by Mycobacterium tuberculosis in axenic culture and inside mouse macrophages. STAR Protoc. 2023;4(1).

34. Markey KA, Gartlan KH. Imaging Flow Cytometry to Assess Antigen-Presenting-Cell Function. Curr Protoc Immunol. 2019;125(1).

35. Sallusto F, Lanzavecchia A. Efficient Presentation of Soluble Antigen by Cultured Human Dendritic Cells Is Maintained by Granulocyte/Macrophage Colony-stimulating Factor Plus Interleukin 4 and Downregulated by Tumor Necrosis Factor alpha. J Exp Med. 1994;179:1109–18.

36. Sander J, Schmidt S V., Cirovic B, McGovern N, Papantonopoulou O, Hardt AL, et al. Cellular Differentiation of Human Monocytes Is Regulated by Time-Dependent Interleukin-4 Signaling and the Transcriptional Regulator NCOR2. Immunity. 2017;47(6):1051-1066.

37. Schultze JL, Aschenbrenner AC. Systems immunology allows a new view on human dendritic cells. Semin Cell Dev Biol. 2019;86:15–23.

38. Erra Diaz F, Mazzitelli I, Bleichmar L, Melucci C, Thibodeau A, Dalotto Moreno T, et al. Concomitant inhibition of PPARγ and mTORC1 induces the differentiation of human monocytes into highly immunogenic dendritic cells. Cell Rep. 2023;42(3).

39. Balan S, Ollion V, Colletti N, Chelbi R, Montanana-Sanchis F, Liu H, et al. Human XCR1+ Dendritic Cells Derived In Vitro from CD34+ Progenitors Closely Resemble Blood Dendritic Cells, Including Their Adjuvant Responsiveness, Contrary to Monocyte-Derived Dendritic Cells. The Journal of Immunology. 2014;193(4):1622–35.
40. Balan S, Arnold-Schrauf C, Abbas A, Couespel N, Savoret J, Imperatore F, et al. Large-Scale Human Dendritic Cell Differentiation Revealing Notch-Dependent Lineage Bifurcation and Heterogeneity. Cell Rep. 2018;24(7):1902-1915.
41. Kirkling ME, Cytlak U, Lau CM, Lewis KL, Resteu A, Khodadadi-Jamayran A, et al. Notch Signaling Facilitates In Vitro Generation of Cross-Presenting Classical Dendritic Cells. Cell Rep. 2018;23(12):3658-3672.
42. Silk KM, Silk JD, Ichiryu N, Davies TJ, Nolan KF, Leishman AJ, et al. Cross-presentation of tumour antigens by human induced pluripotent stem cell-derived CD141 XCR1 dendritic cells. Gene Ther. 2012;19(10):1035–40.
43. Sontag S, Förster M, Seré K, Zenke M. Differentiation of Human Induced Pluripotent Stem Cells (iPS Cells) and Embryonic Stem Cells (ES Cells) into Dendritic Cell (DC) Subsets. Bio Protoc. 2017;7(15).
44. Cai S, Hou J, Fujino M, Zhang Q, Ichimaru N, Takahara S, et al. iPSC-Derived Regulatory Dendritic Cells Inhibit Allograft Rejection by Generating Alloantigen-Specific Regulatory T Cells. Stem Cell Reports. 2017;8(5):1174–89.
45. Flosdorf N, Zenke M. Dendritic cells generated from induced pluripotent stem cells and by direct reprogramming of somatic cells. Eur J Immunol. 2022;52(12):1880–8.
46. Rasaiyaah J, Noursadeghi M, Kellam P, Chain B. Transcriptional and functional defects of dendritic cells derived from the MUTZ-3 leukaemia line. Immunology. 2009;127(3):429–41.
47. Santegoets SJAM, van den Eertwegh AJM, van de Loosdrecht AA, Scheper RJ, de Gruijl TD. Human dendritic cell line models for DC differentiation and clinical DC vaccination studies. J Leukoc Biol. 2008;84(6):1364–73.
48. Palacio-Castañeda V, Velthuijs N, Le Gac S, Verdurmen WPR. Oxygen control: the often overlooked but essential piece to create better in vitro systems. Vol. 22, Lab on a Chip. Royal Society of Chemistry; 2022. p. 1068–92.
49. Futalan D, Huang CT, Schmidt-Wolf IGH, Larsson M, Messmer D. Effect of oxygen levels on the physiology of dendritic cells: implications for adoptive cell therapy. Mol Med. 2011;17(9–10):910–6.
50. Kaymak I, Luda KM, Duimstra LR, Ma EH, Longo J, Dahabieh MS, et al. Carbon source availability drives nutrient utilization in CD8+ T cells. Cell Metab. 2022;34(9):1298-1311.
51. Leney-Greene MA, Boddapati AK, Su HC, Cantor JR, Lenardo MJ. Human Plasma-like Medium Improves T Lymphocyte Activation. iScience. 2020;23(1).
52. Ma EH, Verway MJ, Johnson RM, Roy DG, Steadman M, Hayes S, et al. Metabolic Profiling Using Stable Isotope Tracing Reveals Distinct Patterns of Glucose Utilization by Physiologically Activated CD8+ T Cells. Immunity. 2019;51(5):856-870.
53. Mattiuz R, Wohn C, Ghilas S, Ambrosini M, Alexandre YO, Sanchez C, et al. Novel Cre-Expressing Mouse Strains Permitting to Selectively Track and Edit Type 1 Conventional Dendritic Cells Facilitate Disentangling Their Complexity in vivo. Front Immunol. 2018;9.
54. Anderson DA, Dutertre CA, Ginhoux F, Murphy KM. Genetic models of human and mouse dendritic cell development and function. Nat Rev Immunol. 2021;21(2):101–15.
55. Caton ML, Smith-Raska MR, Reizis B. Notch-RBP-J signaling controls the homeostasis of CD8- dendritic cells in the spleen. J. Exp. Med. 2007;204(7):1653–64.
56. Dobosz P, Dzieciątkowski T. The Intriguing History of Cancer Immunotherapy. Front Immunol. 2019;10.
57. Oiseth SJ, Aziz MS. Cancer immunotherapy: a brief review of the history, possibilities, and challenges ahead. J Cancer Metastasis Treat. 2017;3(10):250.

58. Kantoff PW, Higano CS, Shore ND, Berger ER, Small EJ, Penson DF, et al. Sipuleucel-T Immunotherapy for Castration-Resistant Prostate Cancer. New England Journal of Medicine. 2010;363(5):411–22.

59. Ness S, Lin S, Gordon JR. Regulatory Dendritic Cells, T Cell Tolerance, and Dendritic Cell Therapy for Immunologic Disease. Front Immunol. 2021;12.

60. Passeri L, Marta F, Bassi V, Gregori S. Tolerogenic dendritic cell-based approaches in autoimmunity. Int J Mol Sci. 2021;22(16).

61. Najafi S, Mortezaee K. Advances in dendritic cell vaccination therapy of cancer. Biomedicine and Pharmacotherapy. 2023;164.

62. Poirier A, Tremblay ML. Pharmacological potentiation of monocyte-derived dendritic cell cancer immunotherapy. Cancer Immunology, Immunotherapy. 2022;72:1343–53.

63. Anselmo AC, Mitragotri S. Nanoparticles in the clinic: An update. Bioeng Transl Med. 2019;4(3).

64. Cifuentes-Rius A, Desai A, Yuen D, Johnston APR, Voelcker NH. Inducing immune tolerance with dendritic cell-targeting nanomedicines. Nat Nanotechnol. 2021;16(1):37–46.

Appendices

Nederlandse samenvatting

De rol van dendritische cellen in het immuunsysteem

Het immuunsysteem beschermt het menselijk lichaam tegen zowel lichaamseigen (bv. cellen met een afwijking, zoals tumorcellen) als lichaamsvreemde (bv. virussen en bacteriën) ziekteverwekkers en bestaat uit de aspecifieke/algemene afweer en de specifieke afweer.
Een ziekteverwekker wordt in eerste instantie herkend door cellen van de aspecifieke afweer. Dit zijn onder andere **Dendritische Cellen (DCs)**, de cellen die centraal staan in dit proefschrift. DCs kunnen ziekteverwekkers herkennen en worden dan geactiveerd. Een geactiveerde DC kan vervolgens het specifieke immuunsysteem activeren. Cellen van het specifieke immuunsysteem kunnen heel gericht ziekteverwekkers herkennen en vernietigen. Belangrijke cellen van deze tak van het immuunsysteem zijn T cellen. Een geactiveerde DC gaat een interactie aan met naïeve T cellen, die zich vervolgens vermenigvuldigen en ontwikkelen tot een bepaald subtype.

Sommige subtypes, de **pro-inflammatoire T cellen**, brengen een ontstekingsreactie/ inflammatie op gang. Pro-inflammatoire T cellen zijn belangrijk bij de afweer tegen bijvoorbeeld virussen maar kunnen ook bijdragen aan ontstekingsreacties in bijvoorbeeld auto-immuun ziekten. Een naïeve T cel kan zich ook ontwikkelen tot een **regulatoire T cel**. Een regulatoire T cel onderdrukt het immuunsysteem en is bijvoorbeeld belangrijk om een ontstekingsreactie te stoppen of om auto-immuunreacties tegen te gaan. Welk type T cel ontwikkelt wordt grotendeels bepaald door DCs.

DC activering hangt nauw samen met omgevingsfactoren

Net als bij T cellen zijn er ook meerdere typen DCs. De omgeving waarin een DC zich bevindt op het moment dat deze een ziekteverwekker tegenkomt, is van grote invloed op hoe een DC geactiveerd wordt en welk type T cel ze gaan stimuleren. Zo zijn er immuun-gerelateerde omgevingsfactoren en metabool-gerelateerde omgevingsfactoren; beide spelen een belangrijke rol bij DC activering.

Immuun-gerelateerde omgevingsfactoren

Als er net een infectie heeft plaatsgevonden ontstaat er een pro-inflammatoire omgeving. Deze omgeving stimuleert activering van **immunogene DCs**. Een immunogene DC promoot de ontwikkeling van pro-inflammatoire T cellen (Fig. 1A). DC activering kan ook plaatsvinden in een anti-inflammatoire omgeving. Dit zorgt voor **tolerogene DCs** die de ontwikkeling van regulatoire T cellen bevorderen (Fig. 1B). De dikke darm is een voorbeeld van een anti-inflammatoire omgeving. In de dikke darm zitten namelijk veel nuttige bacteriën en regulatoire T cellen zorgen ervoor dat ons immuunsysteem niet een ontstekingsreactie start tegen deze bacteriën.

Metabool-gerelateerde omgevingsfactoren

Met metabool-gerelateerde omgevingsfactoren bedoelen we onder andere de hoeveelheid voedingsstoffen en het type voedingsstoffen (bijvoorbeeld suikers, eiwitten of vetten) die aanwezig zijn in de omgeving van een cel. De metabole omgeving is heel belangrijk voor DCs, omdat DC activering nauw verwant is aan de energiehuishouding binnen in de cel, het **intracellulaire metabolisme**.

Voor activering van een immunogene DC is heel veel glucose nodig (Fig. 1A). Glucose wordt verbrand in de cel om er energie uit te halen, een proces dat we **glycolyse** noemen. Glucose wordt ook gebruikt voor **vetzuursynthese**, een metabole route die zorgt voor de opbouw van vetzuren. Metabole processen die leiden tot de opbouw van voedingsstoffen noemen we **anabole processen**, en daarom wordt ook wel gezegd dat immunogene DCs een anabool metabolisme hebben. Vetzuursynthese is essentieel voor DCs om pro-inflammatoire T cellen te stimuleren.

In tegenstelling tot immunogene DCs halen tolerogene DCs hun energie niet uit glucose, maar uit vetzuren (Fig. 1B). **Vetzuurafbraak** levert meer energie op dan glycolyse, maar is een trager proces. Dit **katabole proces** (afbraak van voedingsstoffen) blijkt belangrijk te zijn voor tolerogene DCs om regulatoire T cellen te activeren.

Het verschil in functie tussen immunogene en tolerogene DCs wordt dus deels veroorzaakt door een verschil in intracellulair metabolisme en een juiste combinatie van immuun-gerelateerde en metabool-gerelateerde omgevingsfactoren is dus cruciaal om de juiste immuunrespons in gang te zetten.

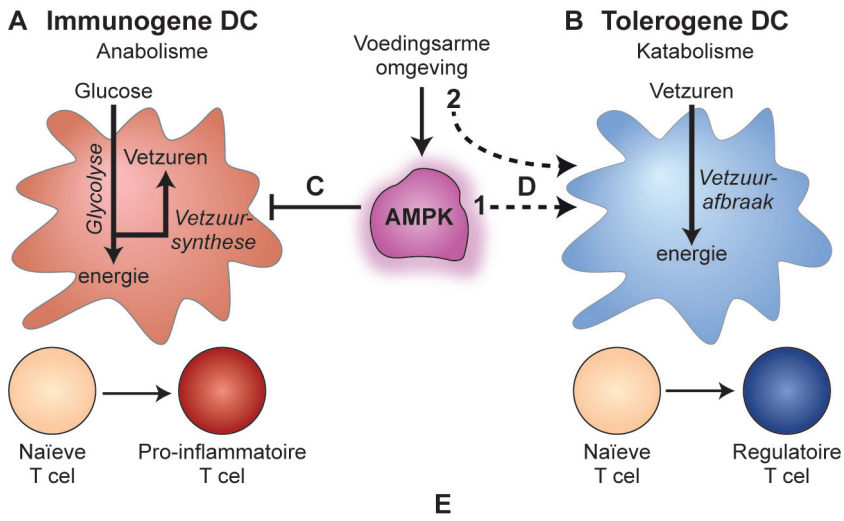

Figuur 1: AMPK signalering in dendritische cellen: onderzoeksvragen. (A) Immunogene DCs promoten de ontwikkeling van naïeve T cellen tot pro-inflammatoire T cellen. Hiervoor verbranden DCs veel glucose en hebben ze een anabool metabolisme nodig, gekenmerkt door vetzuursynthese. **(B)** Tolerogene DCs promoten de ontwikkeling van regulatoire T cellen uit naïeve T cellen. Katabole processen zoals vetzuurafbraak zijn hiervoor belangrijk. **(C)** Onderzoek heeft aangetoond dat actief AMPK de activering van immunogene DCs remt. **(D+E)** Dit zijn de belangrijkste onderzoeksvragen uit dit proefschrift.
→ promotie —| remming - - → hypothese

Metabole sensor AMPK verbindt de metabole omgeving met intracellulair metabolisme

Intracellulair metabolisme hangt dus nauw samen met de metabole condities buiten de cel. Dit wordt gereguleerd door enzymen in een cel die de hoeveelheid voedingsstoffen in de directe omgeving van de cel kunnen waarnemen, zogenoemde metabole sensors. Een belangrijke metabole sensor die actief wordt als er te weinig voeding in de omgeving is, is **AMP-activated protein kinase (AMPK).** Als reactie op het energietekort remt AMPK anabole processen die energie kosten, zoals vetzuursynthese. Daarnaast stimuleert AMPK katabool metabolisme dat energie oplevert, zoals vetzuurafbraak. Door het promoten van katabool in plaats van anabool metabolisme zorgt AMPK ervoor dat een cel kan overleven in een voedingsarme omgeving.

In veel verschillende celtypen is aangetoond dat AMPK een belangrijke schakel is tussen de metabole omgeving en het intracellulaire metabolisme, maar er is nog weinig onderzoek gedaan naar de rol van AMPK in DCs. Wat wel opvalt is dat AMPK activatie metabole processen die belangrijk zijn voor tolerogene DCs (vetzuurafbraak) stimuleert en processen die belangrijk zijn voor immunogene DCs (vetzuursynthese) remt. Of AMPK ook daadwerkelijk belangrijk is voor de deze processen in DCs en daarmee ook voor de regulatie van immunogene en/of tolerogene DCs is onbekend.

Het onderzoek in dit proefschrift

Over de rol van AMPK op DC activering is dus weinig bekend, maar gezien de invloed van metabole omgevingsfactoren en intracellulair metabolisme op DC activering is het niet onwaarschijnlijk dat AMPK hier invloed op heeft. Bovendien is wel aangetoond dat als je tijdens het stimuleren van immunogene DCs ook AMPK activeert, je de activering van immunogene DCs remt (Fig. 1C). Door AMPK activatie krijgt de DC een soort signaal dat er niet voldoende voedingstoffen aanwezig zijn en dit zorgt voor remming van immunogene DC activering. Hoe het komt dat AMPK activatie immunogene DCs remt en of deze DCs ook tolerogeen worden, en dus een ander type T cel stimuleren, is echter nog niet onderzocht. De eerste belangrijke onderzoeksvraag van dit proefschrift gaat hierover (Fig. 1D+E). Onze hypothese is namelijk dat AMPK activatie leidt tot katabool metabolisme (met name vetzuurafbraak) en dat dit ervoor kan zorgen dat AMPK activatie tolerogene DCs promoot.

Daarnaast denken wij dat AMPK een link kan vormen tussen de metabole omgeving en de DC activering. Het is namelijk zo dat in een voedselrijke omgeving, bijvoorbeeld in het vetweefsel van mensen met obesitas, immuuncellen continu actief zijn. Deze voedselrijke omgeving zorgt voor een chronische ontsteking wat type II diabetes kan veroorzaken. Een voedselarme omgeving daarentegen is geassocieerd met onderdrukking van het immuunsysteem. Dit kan bijvoorbeeld gebeuren in een tumor omgeving, waar snel delende tumorcellen alle voedingsstoffen gebruiken en er een te kort kan ontstaan voor immuuncellen. Immuuncel activatie verloopt dan niet goed met als gevolg dat de tumorcellen niet herkend en vernietigd kunnen worden. Een voedselrijke omgeving is dus geassocieerd met over-activatie van immuuncellen, waaronder DCs, en een voedselarme omgeving kan zorgen voor onderdrukking van het immuunsysteem. De tweede onderzoeksvraag van dit proefschrift gaat over de mogelijk verbindende rol van AMPK tussen de metabole omgeving en de activering van DCs (Fig. 1D+E). Zou AMPK bijvoorbeeld actief worden in de DCs die zich in de voedselarme tumor-omgeving bevinden en kan dit bijdragen aan tolerogene tumor-DCs en onderdrukking van de anti-tumor immuunrespons?

Belangrijkste resultaten

De verschillende hoofdstukken in dit proefschrift vormen samen een antwoord op deze vragen. We hebben hierbij gekeken naar de rol van AMPK signalering in immunogene DCs (hoofdstuk 4) en de rol van AMPK in tolerogene DCs (hoofdstuk 5, 6 en 7).

In **hoofdstuk 4** (Fig. 2A) kijken we naar hoe AMPK signalering immunogene DCs beïnvloedt in een muizen model voor obesitas. Hier zien we dat LKB1 (een eiwit dat AMPK activeert), door middel van AMPK en SIK activatie (SIK is een soort broertje van AMPK) het immuunsysteem onderdrukt en daarmee voor een betere glucose huishouding zorgt. In DCs in de lever van muizen met obesitas zien we dat deze LKB1-AMPK/SIK signaalroute niet goed werkt. Daardoor ontstaat er een pro-inflammatoire response die mogelijk kan leiden tot type II diabetes als gevolg van obesitas.

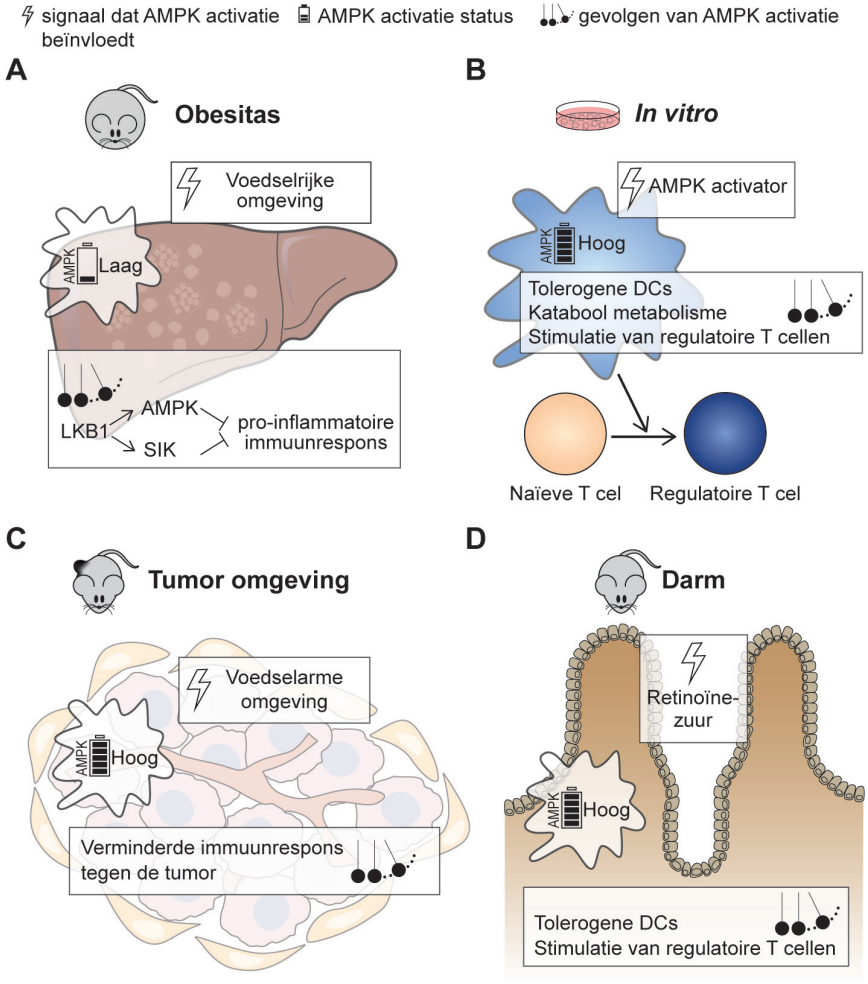

Figuur 2: belangrijkste resultaten van de onderzoekhoofdstukken in dit proefschrift. Grafische samenvatting van de belangrijkste resultaten uit **(A)** hoofdstuk 4 **(B)** hoofdstuk 5 **(C)** hoofdstuk 6 en **(D)** hoofdstuk 7.

In **hoofdstuk 5** (Fig. 2B) zien we hoe AMPK activatie in DCs leidt tot tolerogene DCs *in vitro* (in een kweekschaal). Deze AMPK-geactiveerde DCs stimuleren de ontwikkeling van regulatoire T cellen uit naïeve T cellen. We laten zien dat dit komt doordat AMPK katabole metabole processen in de cel stimuleert, zoals vetzuurafbraak, die cruciaal zijn voor de ontwikkeling van tolerogene DCs.

In **hoofdstuk 6** (Fig. 2C) bestuderen we DCs uit tumoren van muizen. We zien dat DCs uit de tumor-omgeving een verhoogde AMPK activatie hebben ten opzichte van DCs uit de milt. Als we tumoren laten groeien in muizen die genetisch gemanipuleerd zijn zodat AMPK afwezig is in hun DCs, zien we dat de tumoren kleiner zijn ten opzichte van de controle groep (waar wel AMPK activatie plaats vindt in tumor-infiltrerende DCs). Het lijkt er dus op dat de tumor-omgeving voor AMPK activatie in DCs zorgt en daardoor ontstaan tolerogene DCs die geen immuunrespons tegen de tumor in gang kunnen zetten. Zonder AMPK lijkt er een betere anti-tumor immuunrespons te zijn en worden tumoren minder groot. Hoe dit precies werkt moet nog verder worden uitgezocht.

In **hoofdstuk 7** (Fig. 2D) kijken we naar DCs in de darmen van muizen, net als de tumor-omgeving een anti-inflammatoire omgeving. Hier tonen we aan dat de AMPK activering hoger is in DCs die zich in de darm bevinden dan in DCs uit andere organen. Dit komt mogelijk door de aanwezigheid van retinoïnezuur, een metaboliet dat veel voorkomt in de darm en dat *in vitro* kan leiden tot tolerogene DCs, door middel van AMPK activatie. Uit onze experimenten blijkt ook dat AMPK signalering in DCs ook *in vivo* (in muizen) een belangrijke rol speelt bij de stimulatie van tolerogene DCs en de ontwikkeling van regulatoire T cellen.

Conclusie

In dit proefschrift hebben we aangetoond dat AMPK signalering leidt tot onderdrukking van immunogene DCs en ontwikkeling van tolerogene DCs. Ook laten we zien dat dit komt doordat AMPK katabool metabolisme promoot (vraag 1). Uit onze experimenten blijkt dat AMPK activatie in DCs afhankelijk is van de omgeving waar een DC zich bevindt. AMPK activatie *in vivo* vindt plaats in een anti-inflammatoire omgeving en kan leiden tot tolerogene DCs die de ontwikkeling van regulatoire T cellen stimuleren. AMPK is dus een centrale schakel die op basis van signalen uit de metabole omgeving de T cel stimulerende eigenschappen van DCs reguleert (vraag 2).

Deze kennis kan mogelijk toegepast worden bij de ontwikkeling van immuuntherapieën. Zo worden er bijvoorbeeld therapieën ontwikkeld om patiënten met een auto-immuunziekte te behandelen met in het lab gekweekte tolerogene DCs. Onze resultaten suggereren dat AMPK activatie een methode is om tolerogene DCs te produceren. Ook immunogene DCs worden gekweekt in het lab voor bijvoorbeeld de behandeling van kanker. Onze data laat zien dat het mogelijk nuttig kan zijn om AMPK te remmen in deze DCs, zodat de DCs die in een tumor-omgeving terecht komen minder gevoelig zijn voor de voedselarme omgeving.

Kortom, AMPK is een belangrijke schakel tussen de metabole omgeving en DC activering en manipulatie van deze metabole sensor kan mogelijk leiden tot nieuwe en verbeterde immuuntherapieën.

Curriculum Vitae

Eline Constance Brombacher was born on the 17th of September 1993 in Monnickendam, The Netherlands. She obtained her Gymnasium diploma at RSG Sneek in 2011 after which she took a gap year and travelled for eight months. In 2012 Eline started her Bachelor's in Biomedical Sciences at Utrecht University. During this program she participated in the Honors Program where she wrote a proposal to involve students in the development of online teaching material, supervised by Dr. Van Mil. After graduation in 2015 she started the Master's program Cancer Stem Cells and Developmental Biology at Utrecht University and was enrolled at the U/Select Master's Honors Program. Eline's first research internship was at the group of Professor Burgering, UMC Utrecht, where she studied the role of FOXOs on metabolic regulation of small intestinal organoid differentiation, supervised by Dr. Rodríguez Colman. In January 2017 she moved to Zurich, Switzerland, for her second internship. She studied lateral plate mesoderm development in zebrafish embryos under supervision of Dr. Prummel in the group of Prof. Mosimann at the University of Zurich. Eline obtained her Master's degree cum laude in 2017. After graduation she worked at ETH Zurich in the group of prof. Zamboni and studied how breast cancer heterogeneity affects responses to mitochondria-targeting drugs. In April 2019 Eline started her PhD in the group of Dr. Everts at the department of Parasitology, Leiden University Medical Center. Here, she studied how nutrient-sensor AMPK regulates dendritic cell immunity and tolerance. Results of her studies are described in this thesis. Since September 2023 Eline is working as a university teacher in molecular cell biology at the Center for Molecular Medicine, UMC Utrecht.

List of publications

1. **Brombacher E.C.**, Patente T.A., van der ham A.J., Moll T.J.A., Otto F., Verheijen F.W.M., Zaal E.A., de Ru A.H., Tjokrodirijo R.T.N., Berkers C.R., van Veelen P.A., Guigas B., Everts B. *AMPK activation induces RALDH^{high} tolerogenic dendritic cells through rewiring of glucose and lipid metabolism.* bioRxiv, 2023.

2. Van der Zande H.J.P.*, **Brombacher E.C.***, Lambooij J.M., Pelgrom L.P., Zawistowska-Deniziak A., Patente T.A., Heieis G.A., Otto F., Ozir-Fazalalikhan A., Yazdanbakhsh M., Everts B.$^{\#}$, Guigas B.$^{\#}$ *Dendritic cell-intrinsic LKB1-AMPK/SIK signaling controls metabolic homeostasis by limiting the hepatic Th17 response during obesity.* JCI Insight, 2023. 8(11):e157948. *shared first authorship, $^{\#}$shared senior authorship

3. Tzung K., Lalonde R.L., Prummel K.D., Mahabaleshwar H., Moran H.R., Stundl J., Cass A.N., Le Y., Lea R., Dorey K., Tomecka M.J., Zhang C., **Brombacher E.C.**, White W.T., Roehl H.H., Tulenko F.J., Winkler C., Currie P.D., Amaya E., Davis M.C., Bronner M.E., Mosimann C., Carney T.J.*A median fin derived from the lateral plate mesoderm and the origin of paired fins.* Nature, 2023. 618: p. 543–549.

4. **Brombacher E.C.***, Patente T.A.*, Quik M., Everts B. *Characterization of Dendritic Cell Metabolism by Flow Cytometry.* Methods Mol Biol. 2023. 2618. *shared first authorship

5. Patente T.A., **Brombacher E.C.**, Heieis G.A., Pelgrom L.R., Zawistowska-Deniziak A., Otto F., Ozir-Fazalalikhan A., van der Ham A.J., Guigas B., Barbuto J.A.M., Everts B. *Metabolic sensor AMPK licenses CD103+ dendritic cells to induce Treg responses.* bioRxiv, 2023.

6. Prummel K.D., Crowell H.L, Nieuwenhuize S., **Brombacher E.C.**, Daetwyler S., Soneson C., Kresoja-Rakic J., Ronner M., Kocere A., Ernst A., Labbaf Z., Clouthier D.E., Firulli A.B., Sánchez-Iranzo, H., Naganathan S.R., O'Rourke R., Raz E., Mercader N., Burger A., Felley-Bosco E., Huisken J., Robinson M.D., Mosimann C. *Hand2 delineates mesothelium progenitors and is reactivated in mesothelioma.* Nature Communications, 2022. 13 (1677).

7. Ludikhuize M.C., Meerlo M., Gallego M.P., Xanthakis D., Burgaya Julià M., Nguyen N.T.B., **Brombacher E.C.**, Liv N., Maurice M.M., Paik J., Burgering B.M.T., Rodriguez Colman M.J. *Mitochondria define intestinal stem cell differentiation downstream of a Foxo/Notch Axis*. Cell Metabolism, 2020. 32(5).

8. **Brombacher E.C.** & Everts B. *Shaping of Dendritic Cell Function by the Metabolic Micro-Environment.* Frontiers in Endocrinology, 2020. 11.

9. Prummel K.D., Hess C., Nieuwenhuize S., Parker H.J., Rogers K.W., Kozmikova I., Racioppi C., **Brombacher E.C.**, Czarkwiani A., Knapp D., Burger S., Chiavacci E., Shah G., Burger A., Huisken J., Yun M.H., Christiaen L., Kozmik Z., Müller P., Bronner M., Krumlauf R., Mosimann C. *A conserved regulatory program initiates lateral plate mesoderm emergence across chordates.* Nature Communications, 2019. 10(1).

10. Felker A. Prummel K.D., Merks A.M., Mickoleit M., **Brombacher E.C.**, Huisken J., Panáková D., Mosimann C. *Continuous addition of progenitors forms the cardiac ventricle in zebrafish*. Nature Communications, 2018. 9(1).

11. de Goede P.D., Wefers J., **Brombacher E.C.**, Schrauwen P., & Kalsbeek A. *Circadian rhythms in mitochondrial respiration.* Journal of Molecular Endocrinology, 2018. 60(3)

Dankwoord

Met veel plezier kijk ik terug op mijn PhD, een leuke, maar soms ook moeilijke tijd. In dit dankwoord hoop ik iedereen die me de afgelopen jaren heeft gesteund te bedanken, want zonder jullie had ik dit proefschrift niet kunnen schrijven.

Bart, wat heb ik het getroffen met een PhD positie in jouw lab. Immuunmetabolisme bleek een fascinerend onderzoeksveld te zijn en jij een hele fijne baas. Onze één-op-één meetings waren hoogtepuntjes van mijn week en ik heb veel geleerd van je wetenschappelijke kennis en inzichten. Ik hoop dat we ook in de toekomst nog eens kunnen tennissen of samen vogels mogen bewonderen.

Bruno, thank you for being my personal AMPK-expert. I could always knock on your door with a question and highly valued your input on my projects. Maria, ook jou wil ik bedanken voor de fijne gesprekken en je kritische vragen tijdens meetings.

Thiago and Karin, I feel honored to have the two of you as my paranymphs. Thiago, my thesis would be nothing without you. Your knowledge, dedication and friendship are of incredible value to me and I miss being a well-oiled silencing/harvest/section machine with you.
Karin, met niemand kan ik zo goed sparren over werk en wetenschap als met jou. Daarnaast ben je ook ontzettend lief, attent en sta je altijd voor me klaar. Dankjewel voor je vriendschap.

Patrick, wat heb ik genoten van onze tijd als collega's. De LKB1-secties zijn één van de beste herinneringen aan mijn PhD. Jouw openheid, vriendelijkheid en wetenschappelijke inzichten zijn bewonderingswaardig. Luìs, thank you for your humor, your biochemistry knowledge and all the good times we had in the lab. Just remember: DC > Mφ. Marjolein, dank voor de fijne gesprekken en de talloze keren dat jij me hebt geholpen bij een te krappe planning. Alwin, dank voor alle hulp in het lab (en de daarbij behorende grapjes). Frank, ook jij bedankt voor alle experimentele hulp en de bereidheid om in te springen waar nodig. Graham, I keep on being amazed by your immunology knowledge. Joost, dank voor het delen van jouw grote hoeveelheid kennis en kunde. Joana, I highly enjoyed all the discussions we had. Anna, thanks for all the fun in the lab. Marion, als ik iemands pipeteerskills vertrouw ben jij het wel. Roos, dank voor al je vrolijkheid en de gezellige koffie momentjes. Nikolas, the borrels would not have been the same without you. Dennis, zo leuk om jou te leren kennen, je bent een topper. And many thanks to all the other colleagues that contributed to my memorable time at PARA.

Lieve Ropo's, van dagelijkse snaps tot ploegvakanties, samen dingen vieren, maar ook ruimte voor verdriet. Ik hoop dat onze vriendschap altijd zo gezellig én zo vertrouwd mag blijven. Lieve Magriet, wat ben jij toch een heerlijk mens. Je enthousiasme, interesse en gezelligheid zijn me zo dierbaar. Sjikkies van het RSG, met niemand kan ik zo lachen als met jullie. Bij ieder zeiltochtje, etentje of slaapfeestje staan de tranen van het lachen me in de ogen. Lieve Stampkrüg, dank voor de immer gezellige eet- en spelletjesavonden, het luisteren naar mijn verhalen over muizen en jullie steun van de afgelopen jaren. Lieve pipetjes, een vriendschap gesterkt door Hester en een voorliefde voor eten. Ik kijk uit naar de vele all-you-can-eat dinertjes die nog gaan komen. Lieve mensen van het CMM-onderwijsteam, dank voor het

warme welkom. Ik voel me helemaal op mijn plek bij jullie. Ook heel veel dank voor alle vrienden en familie die ik nu niet bij naam heb kunnen benoemen, maar die ik wel regelmatig spreek of zie voor een wijntje, een wandelingetje of een potje tennis.

Lieve familie Jansma, heerlijk vind ik de dagen die we doorbrengen met elkaar. Dank voor jullie warmte en gezelligheid. Een extra bedankje voor Sare, want zonder jou had dit boekje niet zo'n mooie voorkant gehad.
Lieve Aart en Marijke, vanaf moment één hebben jullie mij met open armen ontvangen. Jullie staan niet alleen voor Jornel, maar ook voor mij altijd klaar. Ik kan me geen fijnere schoonouders wensen.

Lieve Willem en Nynke, dat wij als gezin altijd voor elkaar klaar staan is de afgelopen jaren wel gebleken. Ik waardeer onze gesprekken vol openheid, interesse en humor en ben dankbaar voor de band die wij hebben.
Lieve pap en mam, altijd zijn jullie positief, jullie gastvrijheid kent geen grenzen en niets is onmogelijk. Deze bewonderenswaardige eigenschappen maken moeilijke tijden draaglijk en inspireren me bij alles wat ik doe. Ik ben zo trots op jullie! Dank voor jullie onvoorwaardelijke steun.

Lieve Jornel, maatje van me. Bij niemand voel ik me zo thuis als bij jou. Dank voor wie je bent en voor alle liefde en steun die je me geeft. Ik ben trots op hoe wij het samen doen en kijk uit naar al het moois dat nog gaat komen.